Development and Characterisation of Multifunctional One-Dimensional Fibres Reinforced Composite Coatings

by

XIAOCHAO JI

A thesis submitted to

the University of Birmingham

for the degree of

DOCTOR OF PHILOSOPHY

School of Metallurgy and Materials

College of Engineering and Physical Sciences

The University of Birmingham

August 2018

Synopsis

Nanocomposite coatings are attractive due to their unique mechanical, physical and multifunctional properties, which can address the limitations of conventional monolithic structures to achieve an excellent combination of strength, stiffness, toughness, and some other functional properties. However, limited work has been carried out on the one-dimensional (1D) nanofibers reinforced composite coatings. Therefore, the aim of this project was to develop novel multifunctional 1D fibres reinforced composite coatings through the design of novel hybrid plasma technologies combining plasma enhanced chemical vapor deposition (PECVD) technique and the advanced active screen plasma (ASP) co-sputtering and co-alloying technique.

In this study, a novel *in-situ* low temperature (below 500ºC) hybrid plasma technology combining active-screen plasma co-sputtering and PECVD has been developed to cost-effectively generate vertically aligned carbon nanotubes (VACNTs) films in a gas mixture of C_2H_2, H_2 and Ar. Co-sputtering of stainless-steel (SS) and silver (Ag) for the deposition of catalyst films was achieved by purposely designed active screen settings consisting of 316 SS mesh cylinder with double top lids within a PECVD facility. The co-sputtering rate can be effectively enhanced by the hollow-cathode effect in between the double lids. It has been revealed by SEM and TEM that SS and Ag nanoparticles have acted as a catalyst for the growth of VACNTs with a multiwalled structure and an average diameter around 30 nm. The VACNT film is superhydrophobic and can be easily changed to superhydrophilic by doping nitrogen via a post-nitriding treatment. All the VACNT films have exhibited excellent antibacterial activity mainly through a physical damage mode.

A two-step approach has been employed to develop VACNTs reinforced composite coatings. First, a modified composite catalyst was deposited by introducing noble Ag particles, which inhibit the growth of CNTs, in order to decrease the density of the VACNT film to facilitate the penetration of the matrix material for the nanocomposite coating. Second, based on the low-density VACNT film, a well-designed CNTs reinforced diamond-like carbon (DLC) composite coating can be formed using the PECVD. The DLC-CNTs composite coating is conductive mainly due to the CNT reinforcements as well as the Ag catalyst particles.

The Ag wires reinforced composite coatings have been deposited through a one-step approach using the advanced hybrid plasma technology combining ASP co-sputtering and plasma carburising in a plasma ambient of CH_4 (1.5%) and H_2 (98.5%). Ag wires are aggregates of Ag nanoparticles with an average diameter of around 2 μm which are embedded in the matrix formed with stainless-steel, Ag, and carbon. The composite coating presents excellent friction reduction effect and antibacterial activity. However, no Ag wires could be formed in the plasma ambient of N_2 (25%) and H_2 (75%). Instead, the as-formed composite surfaces are composed of an antibacterial surface layer and a hard S-phase case underneath due to the diffusion of nitrogen, which could provide the composite surfaces with long-lasting antibacterial activity and excellent wear resistance.

Acknowledgements

First, I want to express my deepest appreciation to Prof. Hanshan Dong and Dr. Xiaoying Li for giving me the chance to develop my research in the Surface Engineering Group. I also want to thank Prof. Wei Zhang from National Key Laboratory for Remanufacturing, China, for his support.

I would like to extend my acknowledgement to Dr. Helong Yu, Dr. Linhai Tian, Dr. Yangchun Dong, Dr. Rachel Sammons, Dr. Kaijie Lin, Dr. Zhenxue Zhang, Dr. Santiago Corujeira Gallo, Dr. Yulung Chiu, Dr. Shangfeng Du, Dr. Rengen Ding, Dr. Jing Wu, Dr. Shaojun Qi for their valuable discussions and technical supports.

I would like to thank all the colleagues of the SE group for their help and advice.

Equal thanks to constant help and support from the staffs in the School of Metallurgy and Materials, specially Mr. Paul Stanley, Mrs. Theresa Morris, for their help with SEM and TEM techniques. Also grateful to Dr. Daniel Reed for his help with Raman spectroscopy and XRD.

Finally, I must express my deepest gratitude to my parents, for their unconditional love and support served as a driving force for me to hold on.

Publications

- ***X. Ji***, W. Zhang, X Li, H. Yu, H. Dong. A novel hybrid method combining ASP with PECVD for *in-situ* low temperature synthesis of vertically aligned carbon nanotube films[J]. ***Diamond and Related Materials***, 2017, 77: 16-24.
- R. Ahmed, ***X Ji***, RMH Atta, AA Rifat, H Butt. Morpho butterfly-inspired optical diffraction, diffusion, and bio-chemical sensing [J]. ***RSC Advances***, 2018, 8(48): 27111-27118
- K. Lin, X. Li, H. Dong, S. Du, Y. Lu, ***X. Ji***, D. Gu. Surface modification of 316 stainless steel with platinum for the application of bipolar plates in high performance proton exchange membrane fuel cells[J]. ***International Journal of Hydrogen Energy***, 2017, 42(4): 2338-2348.
- H. Yu, W. Zhang, H. Wang, ***X. Ji***, Z. Song, X. Li, B. Xu. In-situ synthesis of TiC/Ti composite coating by high frequency induction cladding[J]. ***Journal of Alloys and Compounds***, 2017, 701: 244-255.
- H. Yu, W. Zhang, H. Wang, Y. Yin, ***X. Ji***, K. Zhou. Comparison of surface and cross-sectional micro-nano mechanical properties of flame sprayed NiCrBSi coating[J]. ***Journal of Alloys and Compounds***, 2016, 672: 137-146.
- W. Zhang, L. Zhang, ***X. Ji***, H. Yu, M. Wei. Finite element analysis of micro-cutting mechanism for solid particle erosion[J]. ***Materials Review***, 2015, 14: 144-147

Contents

List of Figures

List of Tables

Chapter 1 Introduction and objectives

Composite materials are promising for addressing the limitations of conventional monolithic materials to achieve an excellent combination of strength, stiffness, toughness and some other functional properties [1]. Bulk composite materials can be classified based on the shape and size (i.e. dimension) of the reinforcements. Similar to bulk composite materials, nanocomposite coatings can also be grouped by the dimension of the reinforcements. Some advanced two-dimensional (2D) and three-dimensional (3D) structures have been developed in the past decades in order to produce nanocomposite coatings with attractive properties [2]. However, limited work has been carried out on one dimensional (1D) nanocomposite coatings because of the technical challenges involved although novel nanofiber reinforced nanocomposite coatings may possess some extraordinary properties due to their unique structure.

Many 1D materials have been investigated in the past decades, including carbon nanotubes (CNTs), Ag wires, Cu wires, TiO_2 wires etc. These 1D materials could act as reinforcements for the deposition of 1D nanocomposite coatings. However, it is difficult to control the dispersion of the 1D reinforcements during the deposition process. To overcome this problem, different strategies have been developed to achieve the well-designed nanocomposite coatings, such as premixing approach, one-step approach, and two-step approach, etc. [3-7]. In this study, both one-step and two-step approaches have been explored to fabricate the well-reinforced nanocomposite coating structures, using advanced plasma-based techniques.

CNTs are the most investigated 1D material. The unique cylindrical nanostructure provides CNTs with some excellent properties. However, the harsh synthesis conditions are the bottleneck for the growth of CNTs. Therefore, it is timely to explore

a new method for low temperature *in-situ* synthesis of CNTs. In order to form the CNTs reinforced composite coating, a two-step deposition approach has been developed. Great effort has been made to control the growth of CNTs to acquire well-designed CNT arrays for the formation of 1D nanocomposite coatings; composite catalyst films are used to reduce the density of the vertically aligned CNTs (VACNTs) films to facilitate the fabrication of the 1D nanocomposite coatings.

Metal wires are commonly synthesised by a solution-based process which is only suitable for the premixing approach to deposit 1D nanocomposite coatings. Limited work has been carried out to produce metal wires reinforced composite coatings through a one-step approach because it is difficult to control the growth of metal wires and the formation of the matrix at the same time. In this research, a promising one-step approach to fabricate the Ag wires reinforced composite coatings has been investigated.

Therefore, the aim of this PhD research project was to develop 1D fibres (aligned CNTs and metal wires) reinforced composite coatings with multifunctional properties. Accordingly, the scientific and technological objectives are as follows:

- To develop cost-effective techniques for the deposition of iron group catalyst thin films for the growth of CNTs, including the sputtering and solution-based processes.
- To synthesise VACNT films at relative low temperature and control the density of the VACNT films using the composite catalyst films developed from this study.
- To characterise the morphology, chemical states, microstructure of the VACNT films.

- To explore the feasibility of fabricating the well-designed CNTs reinforced composite coatings.
- To characterise the microstructure and evaluate the properties of the CNTs reinforced composite coatings and investigate the mechanisms behind microstructural evolution and property enhancement.
- To develop and characterise the multifunctional Ag wires reinforced composite coatings using the active screen plasma technique.
- To investigate the properties of the Ag wires reinforced composite coatings and formation mechanism of the metal wires.

Chapter 2 Literature review

2.1 Development of nanocomposite coatings

In recent years, surface functional coatings are widely used in industry for decorative, protective, or other functional purposes. The functionalities of the coatings can be tailored depending on the practical applications. Typical functionalities of most coatings are wear resistance, corrosion resistance, self-cleaning, anti-bacterial, conductive, thermal resistance, etc. To achieve these functions, novel coating structures can be designed and produced by some advanced coating techniques. The development of coating architectures can be summarised into four generations as shown in Figure 2. 1. Although not exhaustive, this provides a guideline for the development of the coating architectures. The ultimate target for developing novel functional coatings is to meet the ever-increasing property requirements, long lasting, and cost-effectiveness.

The first-generation coatings are metal, ceramic or polymer-based single component coatings. However, their functions are limited due to the simple structure, and hence composite structures were developed to improve their properties. Typical structures for the second-generation coatings are multicomponent and multilayer structures, which can combine properties from the different components. The design of the third-generation composite coatings is based on nanoscale effects. The emergence of novel hybrid techniques has made it possible to tune the coating structures in nanoscale. Nanoparticles reinforced composite structure [8, 9], superlattice structure [10] and gradient structure [11, 12] are the typical third-generation architectures. The combined control of structures and compositions can provide advantages for the composite coatings, such as reduction in lattice mismatch, phase transformation, and grain growth. These nanocomposite coatings may have low internal stress, high hardness and

toughness, strong adhesion, and high thermal stability. For the fourth generation, researchers intend to develop adaptive composite coatings which are sensitive to such environmental factors as temperature, force, irradiation, and voltage. The structures need to provide the coatings abilities to change their properties to meet the requirements under different severe operating conditions. Future studies are needed to develop novel architectures to achieve advanced functional coatings with smart functions under multiple cycles of operating variation.

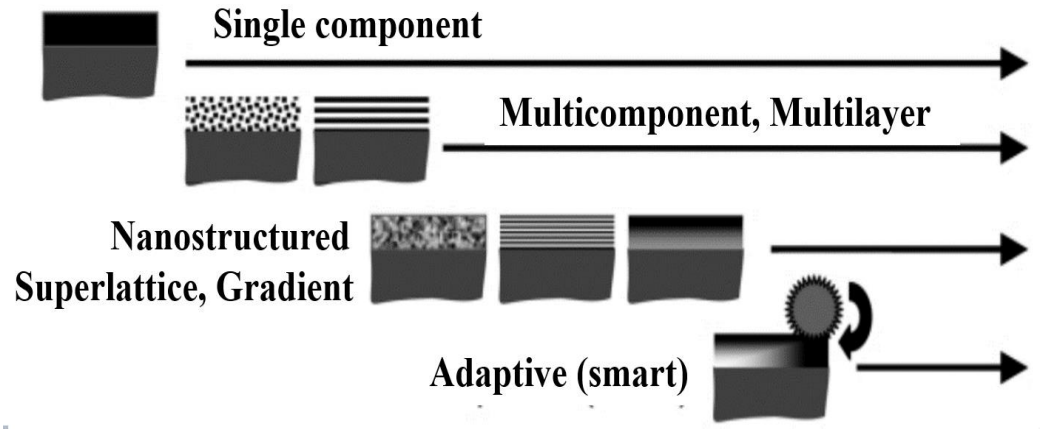

Figure 2. 1 Historical development of functional coating architectures [13]

Composite structures are promising for addressing the limitations of conventional monolithic structures to achieve an excellent combination of strength, stiffness, toughness, and some other functional properties [14]. To have a better understanding of the composite structures, a comparison between the composite coatings and the traditional bulk composite materials is made in Figure 2. 2. The structures of the bulk composite materials can be classified based on the dimension of the reinforcements, such as the zero-dimensional (0D) particle reinforcement, one-dimensional (1D) short fibre reinforcement, two-dimensional (2D) laminate reinforcement and three-dimensional (3D) continuous fibre reinforcement. For the composite coating structures, typical multicomponent structure, multilayer structure, and multigrain structure are

corresponding to the 0D, 2D and 3D composite structures. However, few studies have been carried out on the 1D composite coating structures because it is difficult to fabricate a well-dispersed nanofiber reinforced composite coating. The 1D nanofibers reinforced bulk polymers, ceramics, and metals have a lot of unique properties, and hence it is technologically important to develop the novel 1D nanocomposite coatings in view of their potential properties for practical applications.

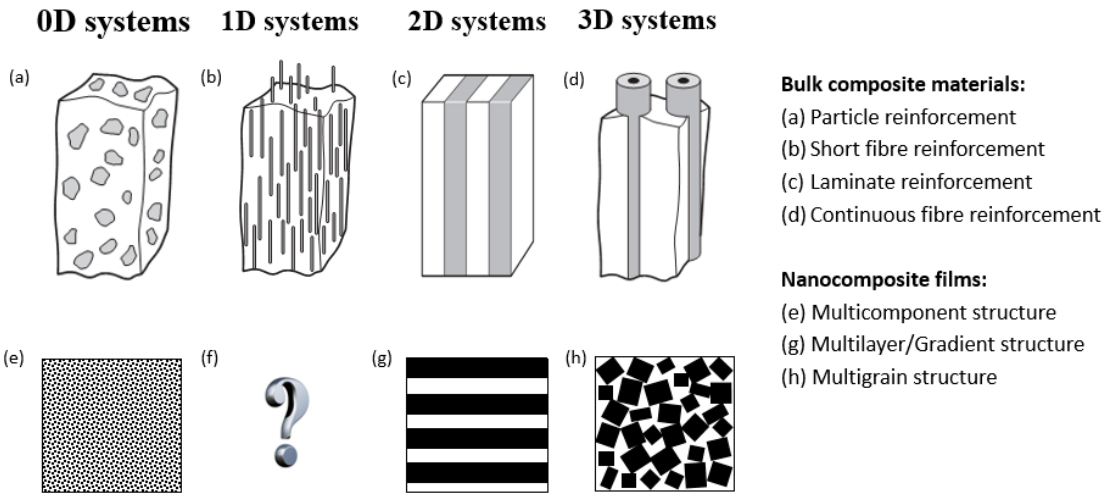

Figure 2. 2 Comparison of the structures of bulk composite materials and nanocomposite coatings

There have been many exciting developments in the field of nanocomposite coatings. The above novel composite coating structures should have great potential for scientific research and practical applications. For example, a new combination of surface properties could be developed by exploring novel 1D coating architectures, which formed the theme of this PhD project.

2.2 Carbon nanotubes

One-dimensional (1D) nanomaterials have been extensively studied due to their unique properties and potential applications. A broad range of the 1D nanomaterials have been

explored, and notable materials include carbon nanotubes, silicon nanotubes, and some metal oxides nanorods, such as TiO_2, ZnO, MgO and SnO_2 [15-18]. Among these 1D nanomaterials, carbon nanotubes are the most promising 1D nanomaterial, which was first identified by Iijima in 1991 when investigating the carbon soot deposited by the arc discharge method. Transmission electron microscopy images clearly showed the multiwalled tube structures with diameters in nanoscale, which is named multiwalled carbon nanotubes (CNTs). The work on multi-wall carbon nanotubes (MWCNTs) by Iijima is an important milestone in the history of CNTs research, which has been driving the study of 1D nanomaterials in the past years [2][19].

The new types of carbon nanotubes, such as single-walled carbon nanotubes (SWCNTs), double-walled carbon nanotubes (DWCNTs), vertically aligned carbon nanotubes (VACNTs), coiled carbon nanotubes, etc. have made the study of carbon nanotubes a flourishing subject. Their growth mechanism, atomic structures and properties were well studied to explore potential applications of CNTs. Their excellent mechanical strength, electrical conductance and thermal resistance make CNTs interesting for a broad range of applications, such as composite materials [14, 20], nanoscale electronic, physical and biosensors [21-23], field emission devices [24, 25], energy storage [26, 27], electrodes [28, 29], etc. However, most of these potential applications are still being tested in a laboratory scale.

In this study, it is intended to use CNTs as the 1D reinforcements for the new nanocomposite coatings to be developed. Thus, it is important to fully control the growth of the CNTs for the subsequent deposition of the composite coatings. The synthesis methods, growth temperature, catalysts, substrates are key issues for the deposition of the CNTs.

2.2.1 Synthetic strategies

Various methods have been developed to synthesise CNTs including arc discharge [30, 31], laser ablation [32, 33] and chemical vapour deposition (CVD) [34, 35]. The arc discharge technique utilises the electric arc between two graphite electrodes to synthesise CNTs within an inert gas ambience. A high current in the range of 50~120A is applied and high temperature (>3000°C) plasma is generated between the two graphite electrodes. Carbon atoms vaporize from the graphite electrodes and then condense to form CNTs and other carbonaceous by-products. Laser ablation technique has similar growth mechanism to arc discharge technique. A laser source is applied to vaporize carbon atoms from the graphite target at high temperature, and then CNTs and other by-products are formed in the inert gas ambience. Due to the high deposition temperature, arc discharge and laser ablation methods are effective to produce high quality CNTs or even SWCNTs. However, CNTs synthesised by arc discharge and laser ablation are usually randomly curved and post-treatment is needed to remove the impurities. Meanwhile, harsh reaction conditions act as barriers to the scale-up production of CNTs by arc discharge and laser ablation methods.

Only CVD methods are feasible for the mass production and tailored synthesis of CNTs. In the CVD process, transition metals are used as catalysts to crack the hydrocarbon gases. The cracked carbon atoms are dissolved into the catalyst nanoparticles and then precipitate to form the CNTs. This catalytic process makes it possible to synthesise CNTs at a relatively low temperature (<1000°C). Various CVD techniques have been established for the growth of CNTs, including simple thermal CVD and hybrid CVD systems such as laser-assisted CVD and plasma enhanced CVD. Typical thermal CVD equipment is made of a vacuum chamber and a heating source, and hydrocarbon gases are cracked by thermal energy only from the heater, resulting in a high deposition

temperature. Schematic diagrams of the simple hot-wall CVD and hot-wire CVD are shown in Figure 2. 3.

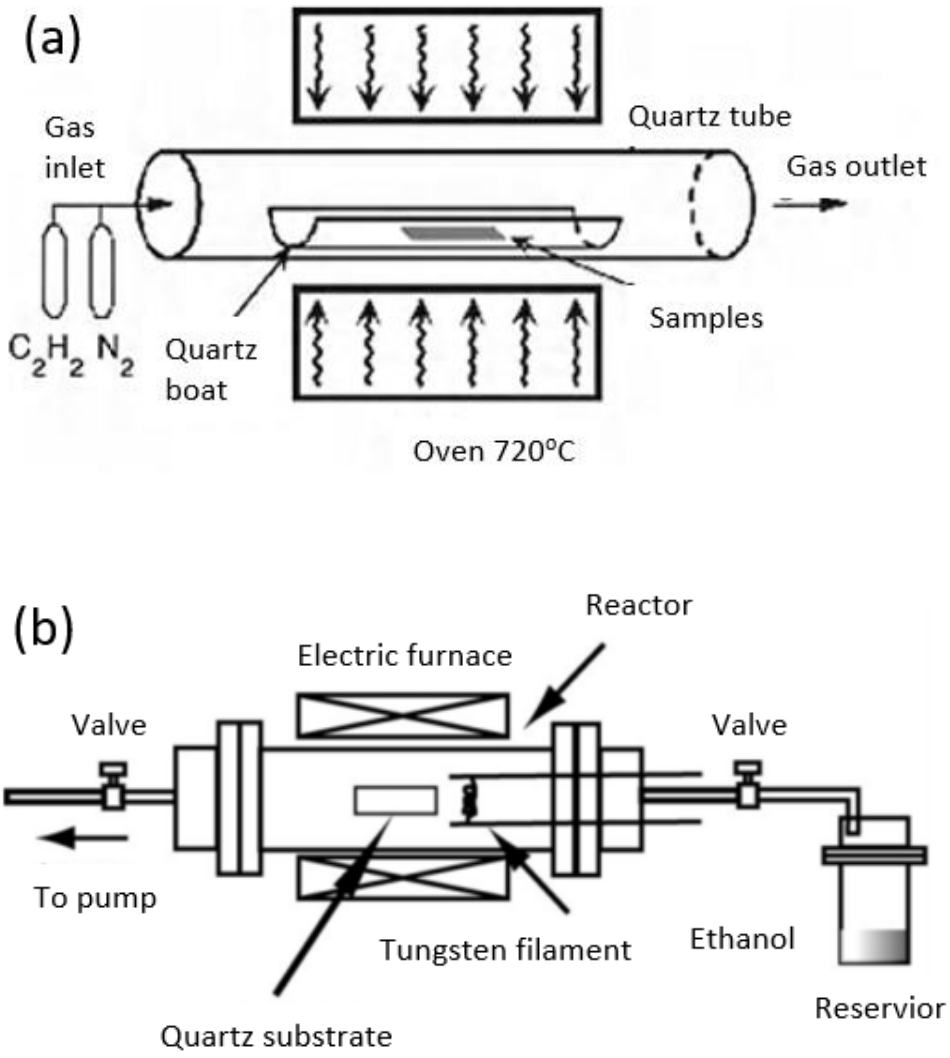

Figure 2. 3 Schematic diagrams of thermal CVD devices: (a) hot-wall CVD [36]; (b) hot-wire CVD [37]

Although the growth temperature for the thermal CVD methods is lower than that for arc discharge and laser ablation methods, it is still higher than 600°C, which may cause significant degradation or even damage to some thermal sensitive substrates, such as glasses for field emission displays [38, 39]. Thus, hybrid CVD systems have been developed which are capable of improving the quality and yield of CNTs compared to

the conventional thermal CVD. The plasma enhanced CVD is an important approach to lower the synthesis temperature of CNTs because plasma can assist the cracking of the hydrocarbon gases. Based on the plasma sources, there are two types of plasma enhanced CVD (PECVD) which are radio frequency PECVD (rf PECVD) and direct current PECVD (dc PECVD). During the synthesis process, hydrocarbon sources (methane, acetylene, ethylene, and benzene) with other precursor (argon, hydrogen, ammonia) are fed into the vacuum chamber, and the plasma is generated between the anode and the cathode electrodes. Charged and neutral species can be formed in the plasma field which makes the growth process very complex [40]. The CNTs synthesised by thermal CVD are usually curved, but vertical and straight CNTs can be produced in the plasma enhanced process (See Figure 2. 4). The growth process is very complex and in addition to the working parameters such as temperature, flow rate, gas ratio (CH_4/H_2) and pressure, the intensity of plasma, the microstructure of the catalyst and the substrates also play important roles in the growth of CNTs.

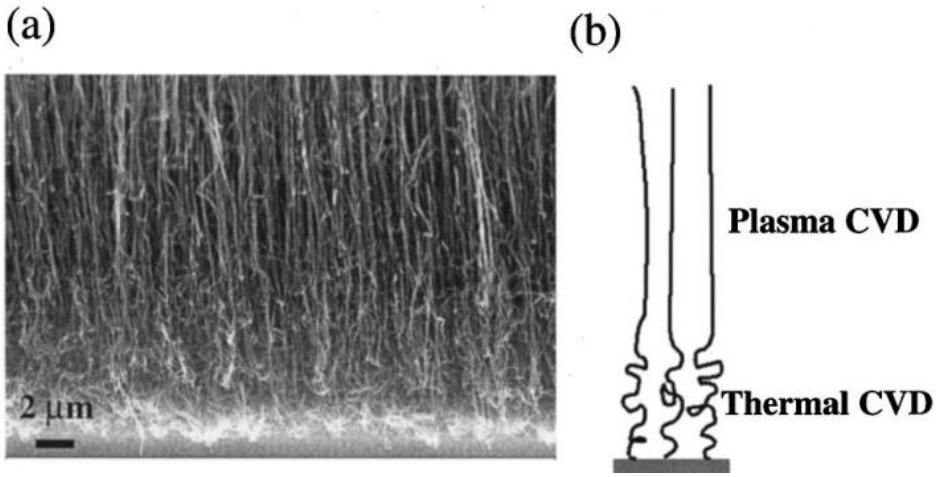

Figure 2. 4 CNTs grown by an alternating thermal and plasma process, curled in the thermal CVD process and straight in the plasma CVD process. (a) SEM image of as-grown CNTs; (b) schematic diagram of the CNT structure in the alternating process [41]

Recently, some work has been dedicated to the low temperature growth of MWCNTs by PECVD. The reported synthesis temperature is below 400^{o}C and could be as low as room temperature [42-44]. In spite of the progress, the plasma heating effect can cause a temperature difference between the sample surface and the bottom of the plate electrode, where the temperature is usually monitored. Meyyappan [45] questioned the reported growth temperature because the measured temperatures depend on the methods used and the locations selected. Thus, low temperature synthesis of CNTs is still difficult.

Wang *et al.* [44, 46] synthesised vertically aligned CNTs and CNFs by RF PECVD at 140^{o}C and 180^{o}C. Ni or bimetal FeNi thin films were sputtered as catalysts. Gas flow of CH_4, Ar and H_2 as 10:90:10 sccm was introduced into the chamber while keeping the pressure at 128 Pa. The plasma power for the deposition was between 30 W and 80 W. Wang *et al.* [44] also indicated that the low temperature growth mechanism is different from that occurring at high-temperature growth. The thermal energy supplied in low temperature treatments would not be sufficient and the amorphous catalyst particles could not be transformed into crystalline phases. Thus, the as deposited CNFs showed rough edges and contained many defects.

Hofmann *et al.* [42, 47, 48] utilised a DC PECVD to selectively grow vertically aligned CNFs at about 120^{o}C. A Ni nanofilm was prepared by magnetron sputtering and the plasma was ignited with a voltage of 600 V and a current flow of 30 mA; the thermocouple was mounted in the substrate. They suggested that the plasma dissociated the hydrocarbon gas and improved the adsorption and diffusion of carbon atoms. Besides, the etching effect can also decrease the formation of amorphous carbon and keep the activity of the catalyst nanoparticles. Carbon atoms can diffuse along the surface, making it possible to form graphitic planes at such a low temperature.

Boskovic *et al.* [49] used an industrial RF PECVD unit to synthesise carbon nanofibers at room temperature. CH_4 and H_2 (30:50 sccm) were used as carbon source and Ni powders (4-7 μm) were used as catalysts. Two typical Raman spectra bands (D and G band) of the room-temperature CNFs were found to be close to that of the CNTs grown by hot-filament CVD at 450°C, but broader than that of the commercial MWCNTs. Boskovic *et al.* [49] have pointed out that the activation energy for carbon atoms to diffuse through the Ni catalyst in a plasma environment is lower (0.54 eV) than in a thermal CVD process (1.5 eV). The heating effect of the RF plasma on the supersaturated Ni can make the local temperature close to the melting temperature of the Ni-C eutectic.

In most cases, the low temperature growth of CNTs is conducted at about 400°C. The modified PECVD with a mesh electrode was reported to synthesise CNTs at relatively lower temperatures [30, 50-54]. Kang *et al.* [50] used a mesh electrode to add an additional potential. Aligned CNTs were produced at about 450°C, but the function of the mesh electrode was not clearly explained. Kojima *et al.* [51] utilised microwave PECVD (2.45 GHz) equipment with a grid electrode between the anode and cathode, which produced VACNTs at 400°C. Kojima *et al.* [51] believed that the grid electrode would suppress the damage by ion bombardment. Jang *et al.* [52] tried to reduce the ion bombardment effect during the growth of CNTs by a mesh electrode, which was connected to the cathode. The CNTs produced with the mesh electrode showed reduced diameters and increased lengths with reduced defects and amorphous carbon impurities. Show *et al.* [53, 55, 56] selectively grew VACNTs using a photolithography method. A typical schematic of the modified PECVD is shown in Figure 2. 5. A grounded stainless-steel grid was placed between the anode and the cathode. They claimed that the ion flux and ion bombardment were not helpful for the growth of CNTs. Ionic

species can be trapped by the grounded electrode while the neutral carbon atoms and carbon radicals can get through the grid and impact on the substrate surface, and then the amorphous carbon (a-C) could be suppressed and high purity VACNTs were produced.

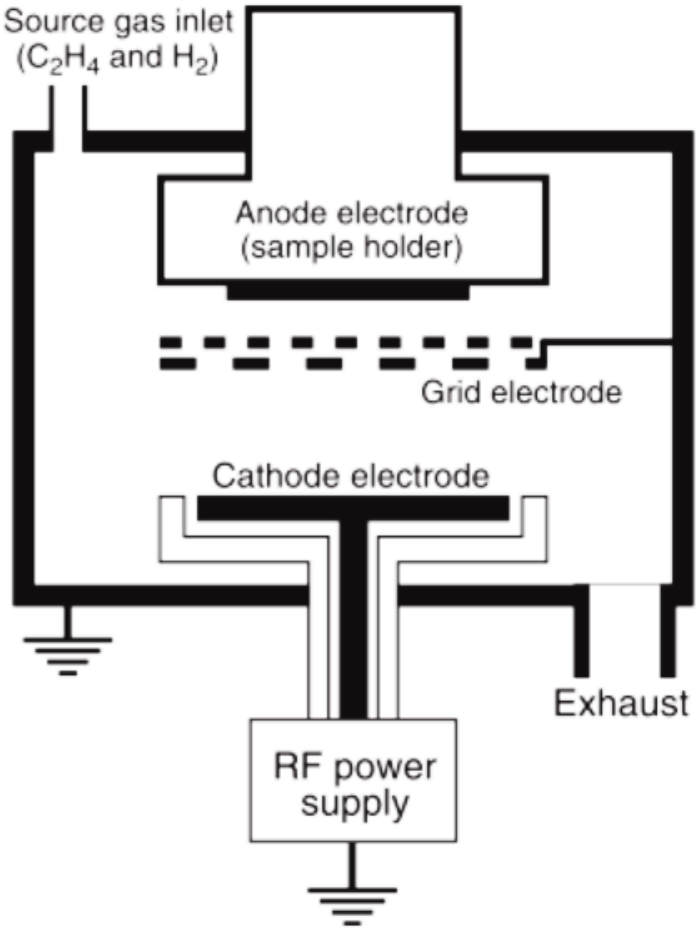

Figure 2. 5 Schematic of a modified PECVD with a mesh electrode for the growth of CNTs [50]

2.2.2 General growth aspects

During the growth of CNTs, the substrate supports the catalysts, which is one of the key factors for the growth of high quality CNTs, and the interaction between the substrate and the catalyst can greatly influence the nanostructure and growth mechanism of CNTs. Silicon wafers are most commonly used as the substrate for the

growth of CNT_S because of their ultra-flat surface. Some researchers [54, 57] indicated that nickel silicide can be formed by the reaction between the nickel catalysts and the Si substrate. Therefore, buffer layers or underlayers are used to prohibit the reaction between the substrates and the catalysts. SiO_2 [58], Al_2O_3 [59, 60], TiN [44], Ti [61, 62] films are often used as the buffer layers. The material of the buffer layer can help the formation of small particles of catalyst and improve their wetting ability. Cassell *et al.* [63] reported that a Cr buffer layer to support the Ni catalyst can increase the growth rate and improve the alignment and uniformity of CNTs. The interaction between the catalysts and the buffer layer can help to adhere the catalyst to the substrate and alter the growth mechanism [64].

2.2.3 Catalysts

Catalysts play a crucial role in the growth of CNTs. There are three main steps for CNTs growth in a typical CVD process: (i) decomposition of the hydrocarbon gases, (ii) diffusion of the carbon atoms through the catalyst and (iii) precipitation of the carbon atoms to form CNTs [65]. The diffusion and precipitation processes of the carbon atoms are complex, and various catalysts are used to produce CNTs. Iron group elements (Fe, Ni, Co) are widely used as catalysts. Their binary or multimetal alloys sometimes can provide advantages for CNTs growth. Al, Mo, Cu, etc. were added to promote the diffusion and precipitation rate of the process and to make the growth of CNTs more controllable and efficient. On the other hand, some metal free catalysts are explored in order to reduce the detrimental effects of metal particles, which unavoidable change the intrinsic property of CNTs (e.g., chemical, electronic, thermal stability and toxicity) and study the growth mechanism in depth [66, 67].

Besides the composition of the catalyst, the film thickness also affects the growth of CNTs [68, 69]. Wei *et al.* [68] found that there was a strong relation between the film

thickness and CNTs density and the growth can only start in a limited range of film thickness. The diameter of the nanotube is related to the catalyst particle size and the pre-treatment process used to form catalyst nanoparticles has an effect on the size and shape of the particles. Jung *et al.* [70] pointed out that prolonged pre-treatment not only increased the particle size but also changed the crystalline state of the nanoparticles, which decreased the density, uniformity and nucleation rate of the CNTs.

2.2.4 Novel methods for catalysts preparation

There are a variety of methods to prepare catalysts for CNTs growth, such as physical vapour deposition (PVD) [71, 72], electron beam evaporation, sol-gel methods[73], metal organic CVD [74], etc. Sputtering and evaporating are two of the most used approaches, because they can control the density, uniformity, size and shape of the catalyst particles.

Active screen plasma (ASP) was first developed for plasma nitriding [75, 76]. However, the ASP technique has recently been used to achieve a hybrid treatment combining nitriding and sputtering metal particles at the same time [77, 78]. The hybrid process could be simplified as a sputtering process to deposit nanolayer catalyst films by using 100% hydrogen as a reaction gas. Due to the low sputtering rate, it could easily control the thickness of the catalyst films. Furthermore, the CNTs could be synthesised *in-situ* by placing an active screen setup in a CVD system. The potential of advanced ASP technique for the growth of CNTs has been explored in this research.

2.2.5 Composite coatings reinforced with CNTs

Various methods can be used to produce carbon nanotubes reinforced bulk composite materials with different matrices (polymer, metal, and ceramic), such as casting,

sintering, hot pressing, etc. However, little work has been carried out on the nanofiber reinforced composite coatings due to the complexity of the process.

The incorporation of CNTs imparts structural and functional properties to the composite coatings. A few reports were focused on the CNTs reinforced composite coatings. However, achieving a homogeneous dispersion of CNTs in the matrix during deposition is a primary challenge. Tan *et al.* [79] prepared the Ni-CNTs composite coatings using brush plating in an attempt to improve the wear resistance of Ni coating, but more pores were produced compared to the brush plated pure Ni coating. Schittenhelm *et al.* [80] deposited the SWCNTs-amorphous diamond composite coatings using pulsed laser deposition. The as deposited SWCNTs-amorphous diamond showed a scratch hardness up to 25 GPa.

Composite coatings with CNTs reinforcements are gaining importance because CNTs could serve to increase toughness and to reduce internal stresses. Kinoshita *et al.* [5] investigated the mechanical properties of a DLC-CNTs composite coatings deposited with PECVD. The toughness of the composite coatings was improved. However, DLC did not naturally impregnate the CNTs because of the unsuitable process (see Figure 2. 6). Using substrates spray-coated with CNTs, Chiba *et al.* [81] proved that the CNTs reinforced structure can reduce the internal stress of DLC films by 1.5 GPa, which can act as a stress buffering layer.

Besides CNTs, some other nanofibers can also be used as reinforcement. Li *et al.* [82] prepared SiC nanowires reinforced SiC composite coatings which improved the wear resistance at high temperature (800^{o}C) of the conventional carbon/carbon composites.

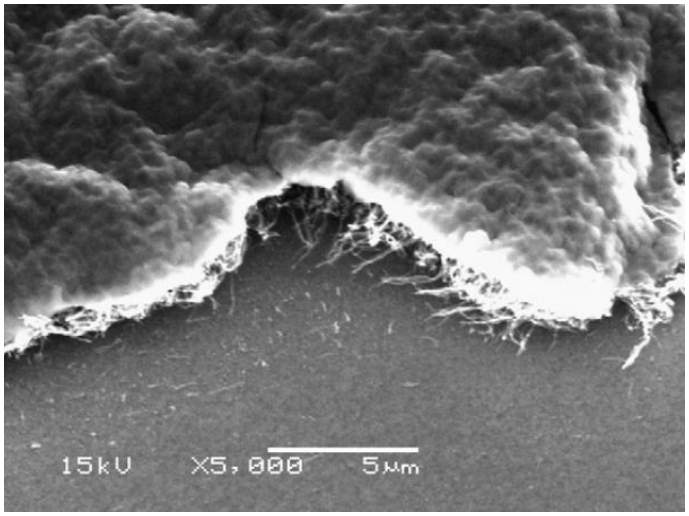

Figure 2. 6 SEM image of the DLC-CNTs composite coating showing that DLC did not impregnate into the CNTs film [53]

From the literature review described above, it is apparent that CNTs are promising reinforcements for the 1D nanofibers reinforced nanocomposite coatings. However, the inherent shortcomings of the deposition process will limit the formation of the nanocomposite coatings, such as growth control of CNTs and complex interactions between reinforcements and the matrix. Thus, it is important to develop feasible and cost-effective techniques to achieve the well-designed composite structures.

Herein, one approach is to control the growth of CNTs, an active screen plasma technique is applied to prepare several types of composite catalyst films, which provides a convenient way to affect the density of the CNT films. Some efforts have been dedicated to the low temperature synthesise of vertically aligned CNT film. Another approach is to use both physical vapor deposition (PVD) and chemical vapor deposition (CVD) methods to investigate the feasible process for the deposition of the 1D CNTs reinforced composite coatings.

2.3 Fundamentals of plasma physics

Plasma technology is applied in this study for the growth of CNTs and the sputtering processes. Different plasma power sources (RF and DC) and electrical configuration (Active screen) were used in varied circumstances in order to control the status of plasma for the specific depositions. Thus, it is necessary to have a knowledge on the simple principle of plasma in order to understand the mechanisms of the plasma interactions during the deposition processes.

2.3.1 Plasma

Plasmas can be generated by electrical discharges, and are known as the fourth state of matter. During the ionization process, electrons are striped from atoms and molecules due to high energy, which can be electrical energy, thermal energy, or light energy. The plasma field consists of positive ions and negative electrons, and excited molecules collisions between the charged particles and neutral particles are continuously happening in the plasma field and new charged particles are created, which creates the avalanche of the charged particles and initiates the electrical breakdown.

2.3.2 Glow discharge

Glow discharge between two plate electrodes depends on voltage, dimensions, and pressure. In 1889, Paschen derived a relationship between the breakdown voltage, pressure, distances between two electrodes, and the applied voltage, what is known as the Paschen's Law [83]. There are always free electrons within a vacuum chamber due to cosmic rays, and so when a voltage is applied on the electrodes, free electrons will be accelerated to move towards the anode plate.

Collisions between the electrons and neutral atoms will cause ionization, while positive ions and more electrons (secondary electrons) are generated. If the collision processes

are continuous and self-sustainable, then the breakdown starts, and the critical voltage is called breakdown voltage. The breakdown voltage is related to the collision probability, plate distance, and gas pressure. If the pressure is too low or the distance is too small, then the probability of collision between the electrons and the neutral atoms is low. Thus, as the gas pressure and plate distance increase, the collision probability will be increased, and therefore the breakdown voltage can be lowered.

Once the glow discharge initiates, positive ions and electrons are moving respectively towards the cathode and the anode plates. When the electric current generated by the discharge flow is dense enough, visible light will be emitted from the plasma. As shown in Figure 2. 7, several luminous and dark zones can be viewed between cathode and anode. The colours of the luminous zones are mainly depending on the type of gas and the pressure [84].

The first zone next to the cathode is called Aston dark space, which contains a negative charge layer and a strong electric field. In this region, electrons are accelerated away from the cathode, and the low density of plasma makes this region dark. The zone next to the Aston dark space is called cathode glow zone, in which the ion density is very high. The thickness of the cathode glow zone depends on the working gases and pressure. The dark zone next to the cathode glow zone on the anode side is named the cathode dark space, which has a high density of ion and strong electric field. The Aston dark space and the cathode dark space form a double layer electric field. The brightest zone of the discharge next to the cathode glow zone is negative glow zone. The electric field in this region is low compared to the cathode glow zone. Electrons have been accelerated through the Aston dark zone and the cathode dark zone and then excite the neutral atoms within the negative glow zone. The electrons are slowed down due to the

collisions and their energies are no longer high enough for the excitation of plasma, and thus a dark zone named Faraday dark space is formed next to the negative glow zone.

The positive column zone is next to the Faraday dark space and near the anode, and the electric field is weak in this region. The anode glow zone next to the positive column is the boundary of the anode sheath, which is brighter than the positive column. Between the anode glow zone and the anode is the anode dark space, where the electric field is stronger than that in the positive column.

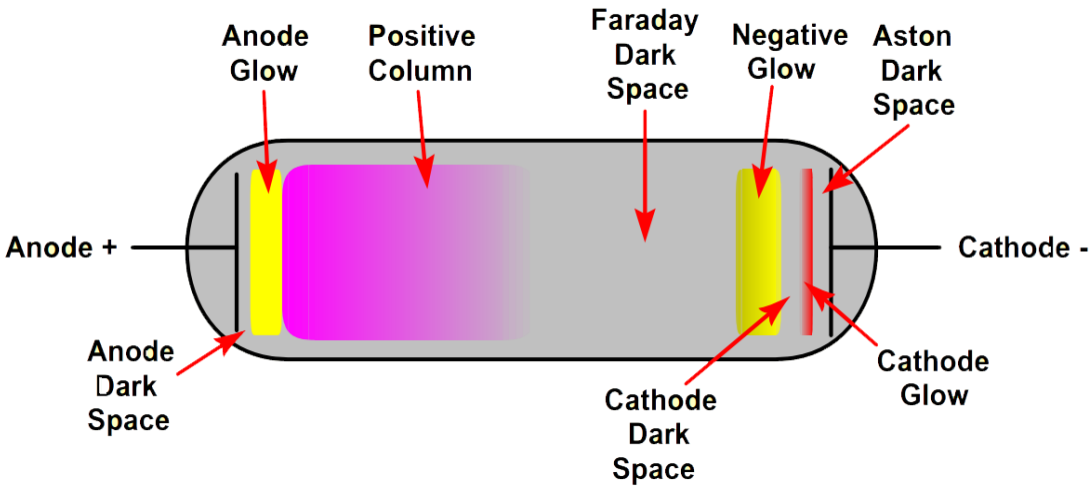

Figure 2. 7 The physical appearance of the glow discharge between two plates [84]

Hollow cathode effect describes the glow discharge process that occurs within a small metal hole cathode. The glow discharge can be extremely strong under certain conditions. For two plate cathodes, when the distance between them is about the same dimension as the hole, the discharge voltage between the plates will increase, leading to a high density of electrons and ions. The hollow cathode effect can, not only enhance the ionization efficiency during the glow discharge, but also generate a large amount of thermal energy. Thus, hollow cathodes have been employed in the sputtering deposition processes. It can act as a heater or improve the efficiency of the sputtering process.

This brief introduction to the DC plate glow discharge serves the purpose of controlling the growth of the CNTs and the nanocomposite coatings.

2.3.3 Active screen plasma surface engineering

Surface engineering is widely used to improve the surface properties of bulk materials, such as metals, polymers, ceramics, and some new materials. A wide range of functional properties is developed by the surface engineering techniques, such as high hardness, excellent wear resistance, corrosion resistance, electronic and thermal resistance. Surface engineered components have been used in many industrial sectors, such as automotive, aerospace, electronics, biomedical, etc. which forms a large market in the UK. Various advanced heat sources are applied for surface treatments, such as electric, plasma, arc, laser, induction, etc. Among those sources, plasma is the most versatile one and has been used in a range of surface engineering techniques.

2.3.3.1 Development of active screen plasma technique

Active screen plasma is an advanced surface engineering technology, which has been developed from the direct current (DC) plasma technique. It is known that plasma nitriding has some advantages over the conventional gas nitriding and bath nitriding in terms of reduced energy consumption and environmental impact [85]. However, normal DC plasma nitriding process has inherent shortcomings, such as edging effect and arcing. This is because the specimen is connected to the cathode with a high potential and plasma forms directly on the surfaces. The active screen technique has been developed to overcome these disadvantages [86]. The comparison between the DC plasma and the AS plasma systems is shown in Figure 2. 8. In the AS plasma system, a metal screen is connected to the cathode, and the specimen is surrounded by the active screen at the floating potential during the nitriding process. Plasmas are formed on the metal active screen and interact with the specimens indirectly. Thus, the edging effect

and arcing associated with DC plasma can be addressed because the plasmas are formed on the active screen, no bias is applied to the specimens and the specimens are uniformly heated by the radiation from the screen.

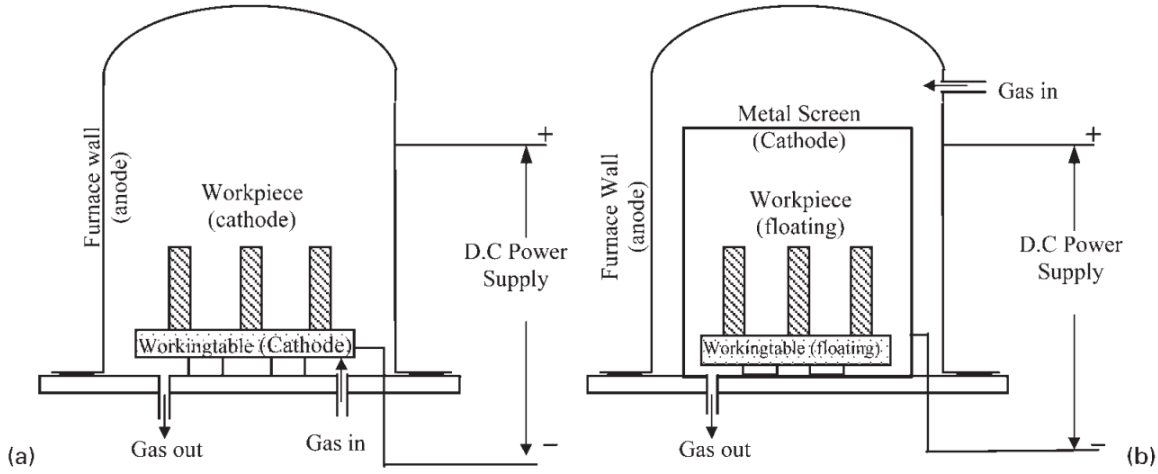

Figure 2. 8 Schematic diagrams of the settings comparison between the direct current plasma and active screen plasma systems [75]

Active screen plasma technology has been developed rapidly in the past ten years and found practical use in plasma nitriding (PN), plasma carburising (PC), and plasma carbonitriding processes applied to components from several industrial sectors. A variety of studies on the active screen plasma treatments were focused on ferrous materials, such as low alloy steels [85, 87, 88] and stainless steels (austenitic, ferritic, duplex) [76, 89, 90]. Most of these plasma treatments are used for surface hardening [91] and the improvement of wear resistance [85] and corrosion resistance [92]. Santiago *et al.* [93] proved that the austenitic stainless steel treated by ASPC produced similar surface hardness and layer thickness compared with the samples treated by DCPC. Li *et al.* [92] carefully evaluated the corrosion resistance of stainless steel treated by ASPN, and the results indicated that the stainless steel samples treated by

ASPN at a lower temperature (420°C) can enhance their corrosion resistance. However, when the stainless-steel samples were treated at high temperature (500°C), their corrosion resistance was decreased because of the precipitation of the chromium nitrides. Thus, the treatment temperature plays an important role in the ASP treatments.

2.3.3.2 Mechanism of active screen plasma technique

As discussed above, the active screen plasma process is different from the direct current plasma process. Researchers have found that there is a deposition layer formed on the surface after the ASPN treatment, which is related to the mechanism of the ASP process. Li *et al.* proposed a 'sputtering and deposition' model to explain the mass transfer during the ASPN process based on the 'sputtering and recondensation' model for DCPN [85, 92]. In a typical DCPN process, iron particles are sputtered from the cathodic sample surface, FeN is formed in the cathode potential drop region and then the formed FeN particles drop on the sample surface. Nitrogen atoms released from the decomposing of FeN will diffuse into the α-Fe lattice. In the ASPN process, there is no sputtering on the sample which is in a floating potential. Sputtering only occurs on the active screen and Fe atoms and iron nitrides ($Fe_{2-3}N$ and Fe_2N) particles are transferred to the sample surface. Iron nitrides are formed in the active nitrogen atmosphere which are extremely unstable thermodynamically, while the decomposed nitrogen will diffuse into the sample.

Figure 2. 9 shows the schematic diagram of a modified model of the 'sputtering and deposition' process. Zhao *et al.* [87] proposed that the particles serve as a nitrogen carrier for the nitriding process. Nitrogen ions react with the particles and then desorbed and diffused into the substrate when the particles are attached to the sample surface. Saeed *et al.* [94] made a comparison between the DCPN and the ASPN processes and verified the 'sputtering and deposition' model in the ASPN process. They further

modified the model based on the results from optical emission spectroscopy, and it was confirmed that the sputtering from the sample is not necessary. Nitriding can be achieved at floating potential, and $N_mH_n^+$ was considered as the dominant nitriding species because they observed the line emission from NH. Santiago *et al.* [86] utilised XRD to investigate the sputtered layers on glass and they found that stable iron nitrides were formed on the inert glass. However, these iron nitrides were easily decomposed on metal samples which is important for the nitriding process. Santiago *et al.* [95] also used the electron backscattered diffraction (EBSD) technique to investigate the sputtered particles, and found that particles remained only on some grains on the sample surface. This is because the crystal orientation of the grains can influence the diffusion rate of nitrogen and hence the decomposition of the back-deposited iron nitrides.

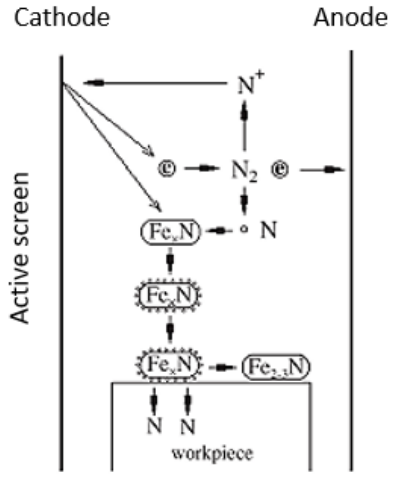

Figure 2. 9 Schematic diagram of the active screen nitriding process [87]

Due to the 'sputtering and deposition' process, the ASPN process is feasible to treat non-conductive materials, such as polymer [96] and ceramic [97]. It has been shown that the ASPN treated polymeric materials had enhanced hardness, elastic modulus and wear resistance. Recently, researchers from the University of Birmingham have further developed the ASPN technique into a novel duplex treatment combining a nitriding

process for the formation of a hard S-phase layer and a sputtering process for the deposition of a functional coating.

2.3.3.3 Novel duplex active screen plasma treatment

The mechanism of the sputtering and deposition during the ASPN process is still not fully understood. However, it is confirmed that materials sputtered from the active screen can interact with nitrogen and form a coating on the sample surface. Generally, stainless-steel active screen is used for the ASPN treatments of iron-based metals, such as stainless-steel, low alloy steel, and cast iron. Li *et al.* [85] found that in the ASPN process, Ti or Cu contained layer can be formed on the surface of the samples when the top active screen lids contained Ti or Cu.

Inspired by this deposition process, some novel functional composite surfaces were developed. Dong *et al.* [98] developed a highly durable antimicrobial stainless-steel surface alloyed with N and Ag by ASPN method. Composite active screen lid made by silver and stainless-steel was used during the ASPN process, and it was found that a silver impregnated composite layer was formed on the surface of the sample followed by a thick hard S-phase underneath layer. This novel composite surface showed excellent antimicrobial property due to the silver nanoparticles within the surface layer, and high wear resistance because of the hard S-phase supporting layer. Dong *et al.* [77] also employed the ASPN technique to fabricate a composite surface which contained a copper-rich layer and an S-phase layer. The double layer structure has made it possible to fabricate a long-lasting antimicrobial bio-functional composite surface. The ASPN duplex treatment provides a feasible way to produce composite surfaces in one-step, and the composition of the functional layer can be adjusted by changing the active screen lids.

Lin *et al.* carried out a series studies of stainless steel bipolar plates for proton exchange membrane fuel cells [99-101], and the ASPN duplex treatment method was applied for the modification of the stainless-steel bipolar plates. Silver, niobium, and platinum were used as alloying elements to modify the surface electrical conductivity of the bipolar plates. Besides, the duplex treatments can also improve the corrosion properties of the stainless-steel bipolar plates by increasing the corrosion potential and the passive current density and decreasing the corrosion current density.

In some cases, the hollow cathode effect was utilised to increase the sputter rate. Akio *et al.* [102] used a titanium double screen settings for the deposition of the TiN coating and the S-phase layer. The distance between the two screens was 10mm and this structure was feasible to produce more ions and active species on the screens to enhance the sputtering process.

The ASPN duplex deposition method provides a way to produce composite surfaces in one-step. The composition of the functional surface layer can be tailed by changing the active lids, which could provide an easy way for the deposition of the multifunctional composite surfaces to be developed from this research.

Inspired by the previous work on the active screen plasma technology, it is known that the active screen plasma process provides a feasible way for the duplex plasma deposition to form multifunctional composite surfaces with a functional surface coating and an underneath S-phase layer. However, most of the co-alloying processes were carried out in a plasma ambient of nitrogen and hydrogen. In this study, the active screen plasma co-alloying processes were also conducted in a plasma ambient of methane and hydrogen in order to achieve the metal wires reinforced composite coatings.

2.4 Spontaneous growth metal wires

Different strategies have been developed to synthesise the 1D metal wires, such as spontaneous growth [103], template-based growth [104], and lithography [105]. While some of them have been developed extensively, others attracted limited attention. In this study, the growth method is different from the template-based and the lithography methods, which are widely utilised for the preparation of one-dimensional (1D) wires. Therefore, the spontaneous growth of the 1D structures is discussed first in order to explore the formation mechanism of the metal wires produced in this study.

The spontaneous growth of wires is commonly driven by the reduction of Gibbs free energy or chemical potential, and it can be typically categorized into (a) vapor phase growth and (b) solution-based growth. Anisotropic growth is required for the formation of the 1D structure which means that the crystal grows faster along one direction than others.

Due to the different growth media, the solution-based growth process differs from the vapor phase growth process. For the solution-based process to synthesise Ag nanowires, $AgNO_3$ is commonly used as precursor dissolved in ethylene glycol which also acts as a reduction agent. $PtCl_2$ can be used as growth seeds [106]. Polyvinyl pyrrolidone (PVP) is introduced into the solution as a capping agent which can block some growth surface and result in the formation of the uniform Ag nanowires. Sun *et al.* indicated that [2 1 1] and [0 1 1] were the growth direction of the Ag nanowire and the HRTEM images verified that the twined Ag nanowire was single crystalline [106].

The mechanism for the solution-based growth of Ag nanowires can be explained as follows. First, Pt nanoparticle seeds were formed by reducing $PtCl_2$ using ethylene glycol at elevated temperature. Then $AgNO_3$ and PVP were added into the reaction system for the nucleation and growth of the Ag nanowires. In this process, the as grown

Pt nanoparticles acted as nuclei for the growth of the Ag nanowires because they have similar crystal structures and lattice parameters. The reduction of $AgNO_3$ with ethylene glycol generates Ag nanoparticles for the nucleation process. PVP as a polymeric surfactant prevent the aggregation of the Ag particles which can chemically absorb onto the surface of the Ag nanoparticles and assist to form the rod-like Ag nanowires. The specific role of PVP in the formation process is still not fully understand. Bonet *et al.* explained that PVP can kinetically affect the growth rates of different faces in the adsorption and desorption process [107].

Actually, large Ag particles were also formed through the homogeneous nucleation process. Thus, it should note that the nanoparticle seeds and PVP are key to the formation of the Ag nanowires. Silvert *et al.* pointed out that the concentration of PVP can determine the morphologies and aspect ratio of the final Ag nanowires, otherwise the Ag nanowires were predominated by the seeds [108, 109]. Besides, the relatively slow reduction rate of $AgNO_3$ also helpful for the anisotropic growth of the Ag nanowires.

Zhang *et al.* proved the formation of the five-fold-twinned Ag crystals through the wet-chemistry synthesis, while a higher concentration of PVP will lead to a thinner and more symmetrical pentagonal nanowire compare to the thick rods. The surfactant mechanism does not consider the crystal configuration and cannot explain the five-fold twinned crystal structure. Thus, a strain-restriction mechanism proposed that internal strain exists in the lattice is responsible for the anisotropic growth. It indicates that the elongation of the decahedra in the axial direction will not increase the internal strain, while the growth in the lateral direction is inhibited. This can explain the appearance of the pentagonal five-fold-twinned nanowire and reveal the anisotropic growth of the 1D structures. However, the actual function of PVP still needs further investigation

[110].

Unlike the dissolution condensation process, the Ag wires formation process in this study can be referred to an evaporation condensation process. However, limited reports have been carried out to synthesise Ag wires through the evaporation condensation process. Evaporation condensation process for the growth of metal wires is commonly driven by the reduction of Gibbs free energy due to the recrystallization or a reduction in supersaturation [111]. Oxide-assisted growth, vapor-liquid-solid, vapor-solid growth, are three typical synthetic strategies of the vapor phase growth of the 1D structure.

Lee *et al.* addressed the oxide-assisted growth mechanism for the growth of Si nanowires. SiO_2 is decomposed through the thermal evaporation process and the precipitated Si nanoparticles act as nuclei for the growth of Si nanowires. They suggested that the temperature gradient offers the driving force for the growth of the nanowires [112]. The nuclei were isolated at the surface at the first stage and then accumulated and grown normal to the substrate. Nuclei were formed with Si cores and an amorphous SiO_2 outer layer. No catalytic nanoparticles were found in the nanowire, while a lot of defects were generated within the Si crystalline core.

It is considered that the surface SiO_2 shell layer has a catalytic effect for the formation of the nanowires which retard the lateral growth. The SiO_2 vapor is continuously evaporated to form nuclei at the tip of the nanowires. However, these nuclei have different crystalline orientations and nonpreferred orientations growth will be terminated. Besides, fault stacking of the nuclei leads to partial dislocation and microtwins within the nanowires. In the present study, as there was no oxygen in the reaction ambient, the oxide-assisted growth mechanism cannot be used to explain the formation of Ag wires. However, some of the nucleation processes are helpful to understand the formation of the Ag wires.

The vapor-liquid-solid process has been widely used to explain the growth of nanowires or nanotubes through a gas phase reaction. Wagner *et al.* first proposed the VLS mechanism to explain the growth of single crystalline whiskers in the 1960s [113]. During the VLS growth process, the anisotropic growth of the 1D structures is supported by the presence of the liquid/solid interface. Real-time observation of the growth of Ge nanowire in an *in-situ* TEM showed that there are three stages of the growth which are metal alloying, crystal nucleation and axial growth. Ge vapor generated due to the high temperature in the system, and liquid droplets formed through the condensation and dissolution of the Ge vapor. With the increase of the alloy droplet, nucleation of the Ge nanowires starts around the Au catalyst nanoparticles.

The continuous diffusion and condensation of the Ge vapor will nucleate at the liquid/sold interface to form the nanowire. The elongation of the nanowires is attributed to the driving force from the nucleation at the interface. While the diameter of the nanowires is related to the sizes of the catalyst particles [114]. In this case, the melt temperature of Ag (961.8 °C) is much higher than the deposition temperature (420 °C). Thus, no liquid alloy phase could form during the growth process. Besides, catalyst nanoparticles are required through the VLS route to synthesise the 1D structures. However, no catalyst seeds were found in the as grown Ag wires, indicating that VLS mechanism cannot be used to explain the growth mode in this sputtering process.

The vapor-solid mechanism was applied to explain the growth of metal nanowires through noncatalytic and template-free processes [115]. The metal vapor is generated through evaporation and then condense on the substrate for the crystallization. At the beginning of the crystallization process, there is a competition between different crystallographic planes depending on their surface free energies. Once the specific favoured advancing plane is determined, the anisotropic growth of the nanowire begins.

The feed metal nanoclusters will strike on the favourable plane continuously to form the nanowire. It is considered that the supersaturation ratio of the condensing nanoclusters significantly affects the formation of the 1D structures. Low supersaturation ratio leads to the anisotropic growth of nanowires, while bulk crystals will generate with a medium supersaturation ratio. High supersaturation ratio can enable the crystal growth in two favourable directions to form square-shaped nanostructures [115].

The oxide-assisted, VLS and VS growth of 1D structures have been briefly discussed. However, the oxide-assisted and VLS mechanism seem not suitable to explain the growth of Ag wires synthesised in the present work. To our understanding, the formation process of the Ag wires can be ascribed to a VS growth process but more complex. Since the formation was carried out in an ambient of methane and hydrogen, whilst Ag and stainless-steel were co-sputtered during the deposition.

2.5 Development of antibacterial surfaces

Microorganisms have existed on our planet for over million years, which have developed the excellent adaptive ability to the surfaces of the colonisation. Globally, over 700,000 lives are lost each year by antimicrobial-resistant infections [116]. Bacterial adhesion and formation of biofilms on the surfaces of various exteriors like cell phone, food package, surgery tools etc. can cause serious problems in our society from the perspective of economical and health [117]. Thus, there has been strong global demands for advanced materials and surfaces for antibacterial applications in our daily life.

2.5.1 Bacteria

Bacteria are prokaryotes which consist of a single cell with some simple internal structures. There are different criteria that are used to classify bacteria, such as their

cell walls, shape, or the genetic makeup. The Gram staining method is always the first step for the identification of a bacteria which was developed by Hans Christian Gram in 1884. Gram staining procedures of bacteria are shown in Figure 2. 10, in which bacteria are identified by the composition of the cell walls. Bacteria can be broadly categorized into Gram-positive and Gram-negative bacteria. Gram-positive bacteria have a thick peptidoglycan layer which can be stained by crystal violet (purple dye); Gram-negative bacteria have a thin layer of peptidoglycan which can be removed by alcohol and losing the stained colour [118].

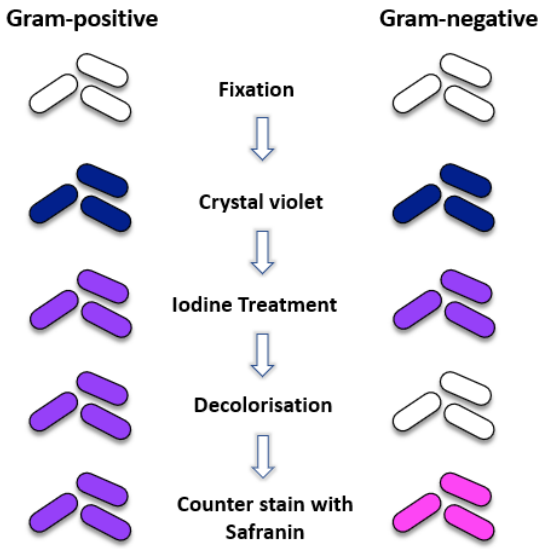

Figure 2. 10 Procedure of the Gram staining and colour change of Gram-positive and Gram-negative bacteria

Schematic diagrams of the cell wall structures of the Gram-positive and Gram-negative bacteria are shown in Figure 2. 11. The cell wall of the Gram-negative bacteria is composed of an outer membrane connected by lipoproteins to the thin layer of peptidoglycan (7-8 nm) in the periplasmic space between the outer and the inner lipid membranes. Porins in the outer membranes are channels to transport small hydrophilic molecules through the membrane, and lipopolysaccharide molecules are linked to the

outer leaflet of the outer membrane. Figure 2. 11 (b) shows the cell wall structure of the Gram-positive bacteria. Lack of an outer membrane, whilst a thick cell wall composed of a thick peptidoglycan layer (30-100 nm) which is attached to lipoteichoic acids and teichoic acids, while lipoteichoic acids are extended to the inner cell membrane. Only one lipoprotein layer is located between the cell membrane and the peptidoglycan layer. It has shown that the cell wall of the Gram-negative bacteria is structurally and chemically more complex compare than the Gram-positive bacteria [119].

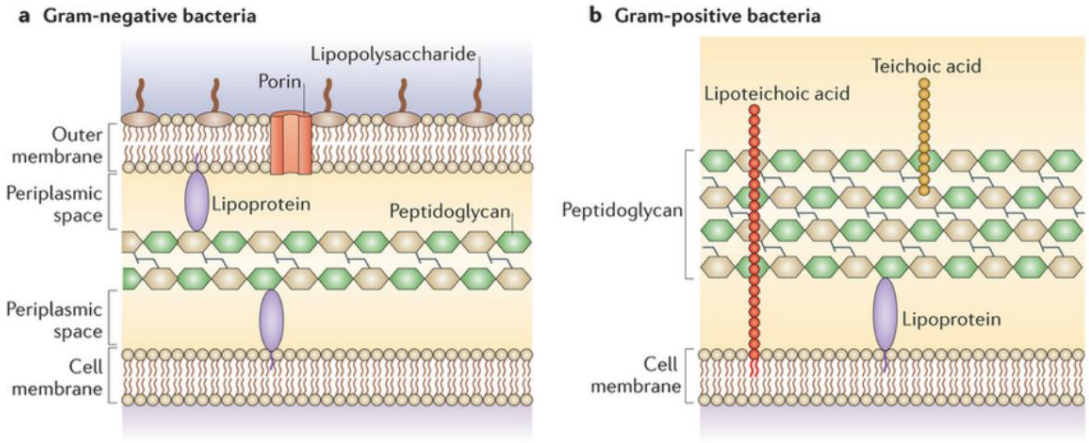

Figure 2. 11 Schematic diagram of the cell wall structures of the Gram-negative and Gram-positive bacteria [119]

Some bacteria commonly used in the antibacterial researches are summarized in Table 2. 1 according to their shape, size, source, and infection. Most of the Gram-negative bacteria have a rod-like shape around 2 μm long and 1 μm in diameter. Rod-like Gram-positive bacteria are longer than the rod-like Gram-negative bacteria. The only exception is the coccal like Gram-positive bacteria which have a smaller size with a diameter of about 0.6 μm. The size of the bacteria can affect their interactions with the antibacterial surfaces.

The selected bacteria are typically cultured on the surface of solid nutrient media which normally consist of a mixture of protein digests, inorganic salts, and agar. Examples of the enriched media which can support the growth of different bacteria include tryptic soy agar, chocolate agar, sheep blood agar. Bacteria grow on these solid media as colonies, and a colony is formed with a mass of bacteria all originating from a single mother cell, and hence the bacteria in the same colony are genetically alike. Bacteria in the biofilms have a complex arrangement of cells, while colonies are formed which have networks of channels for diffusion of nutrients.

There are four main growth phases of bacteria which are lag phase, log growth phase, stationary phase, and death phase. The lag phase is a period before the initiation of cell division. During this period, DNA, enzymes, and macromolecules are synthesised within the cell for reproduction, and cells may double or triple in size due to the preparation. When the cells are ready, bacteria start to divide at a maximum rate and then remain constant. This period is called the log phase because the logarithm of the number of bacteria increases linearly with time, and cells are most active during this period. The growth of bacterial population will be ceased eventually during the stationary phase due to the exhaustion of available nutrients. The number of dying bacteria balance the number of the new born bacteria to stabilize the bacterial population. When the number of dying bacteria starts to exceed that of the new born bacteria, viable cells starts to decline exponentially during the death phase.

Table 2. 1 Bacteria commonly used in antibacterial research [116]

Bacteria	Gram	Size	Shape	Source	Infections
Staphylococcus aureus	+	0.6 μm	Coccal	Nose, respiratory tract, skin	Abscesses, sinusitis, food poisoning
Staphylococcus epidermidis	+	0.6 μm	Coccal	Catheters, intravascular devices	Endocarditis, nosocomial infections
Enterococcus faecalis	+	0.6–2 μm	Coccal	Gastrointestinal tract	Urinary tract infection, endocarditis
Bacillus subtilis	+	~ 7 μm long, ~ 0.7μm in diameter	Rod	Soil, gastrointestinal tract	Ear infection, urinary tract infection
Listeria	+	~ 1 μm long, ~ 0.5 μm in diameter	Rod	Uncooked meats and vegetables, raw milk	Food poisoning
Clostridium perfringens	+	~ 6 μm long, ~ 0.8 μm in diameter	Rod	Intestines of humans, raw meat	Abdominal pain, diarrhoea
Escherichia coli	-	2 μm long, ~ 0.6 μm in diameter	Rod	Gastrointestinal tract, animals	Diarrhoea, urinary tract
Porphyromonas gingivalis	-	1.5 μm long, 1 μm in diameter	Rod	Gastrointestinal tract, respiratory tract, colon, oral cavity	Pathogenesis of periodontitis
Pseudomonas aeruginosa	-	2 μm long, ~ 0.7 μm in diameter	Rod	Water, soil	Infections in immune-compromised hosts
Pseudomonas fluorescens	-	2 μm long, ~ 0.6 μm in diameter	Rod	Plants, soil, water	Affects patients
Klebsiella pneumoniae	-	2 μm long, 0.5 μm in diameter	Rod	Mouth, skin, intestinal tract	Upper and lower respiratory tract infections
Salmonella	-	~ 3 μm long, ~ 1 μm in diameter	Rod	Eggs, meat, poultry	Typhoid fever, food poisoning, gastroenteritis, enteric fever

2.5.2 Antibacterial strategies

The main strategy to combat the growth of bacteria is to inhibit the initial adhesion of the cells and prevent the formation of the bacterial biofilm because once the biofilm is formed, it is considerably difficult to control the bacteria colonies. Intensive efforts have been made on the deposition of novel long-lasting antibacterial surfaces or on the improvement the antibacterial performances of the existing surfaces through modification of the surface architectures.

To prevent the formation of biofilm and further bacterial infections, the bacteria biofilm should be inhibited at the initial stage when the bacteria contact the surface. However, the efficacy of the antibiotic in killing the bacteria is limited to the surface layer of the biofilm, with limited effect on the bacteria located at the bottom layers, which will provide long periods for the bottom bacteria to develop antibiotic resistance to the specific antibiotic agents. Thus, it is essential to prevent the formation of biofilms by effectively killing the bacteria once they contact the surface.

In order to inhibit the attachment of bacteria and the formation of biofilms, efforts have been focused on developing new generation surfaces, such as novel functional surface coatings, or surface functionalisation through the chemical or physical process [120]. There are several types of antimicrobial coatings that can prevent infections, which apply nanoparticles as antibacterial agents that are toxic to microorganisms, or some polymer-based surfaces and other functional materials.

2.5.2.1 Chemical approach

Inorganic antibacterial agents, such as silver, copper, zinc oxide, and titanium dioxide, have been reported to have intrinsic properties to kill a wide range of bacteria. Due to the complex interactions between the bacteria and the antimicrobial agents, there are

different possibilities for these agents to distract the biological processes. It is difficult to give a general statement about the antibacterial mechanism of the bacteria-killing actions.

It was reported that silver ions can inactivate the thiol group in enzymes to kill the cells [121]. Jeon *et al.* prepared the Ag-SiO_2 thin film through a sol-gel method which has excellent antibacterial effect against *E. coli* and *S. aureus*. Ag ions were metalized and trapped in the SiO_2 matrix and showed 99.9% killing rate after 24h contact [122]. Lee *et al.* tested the antibacterial performance of the Ag loaded coating on magnetic colloidal particles. It is thought that the release rate of the antibacterial Ag ions depended on the supply of the zerovalent Ag in the film [123]. Reactive oxygen species were observed in some cases due to the silver ions [124]. Choi *et al.* reported that reactive oxygen species (including singlet oxygen, superoxide, hydrogen peroxide and hydroxyl radical) generated by Ag can damage cellular constituents and affect cell functions, leading to the death of cells [125].

Copper is reported to bind with some proteins to cause oxidative stress inside the cell and damage the surface. Besides, copper can degrade the integrity of the cell membrane, leading to leakage of nutrients and subsequent death of cells. Kuo *et al.* studied the effect of Cu content on the antibacterial effect of the Cu-Cr-N nanocomposite coating by DC reactive magnetron sputtering. Cu ions can be released when the sample was contacted with water which will damage enzymes on the cell surfaces [126]. Yao *et al.* prepared a Cu doped TiO_2 composite coating through micro-arc oxidation. The chemical state of Cu was investigated by XPS and Cu^{2+} was identified in the TiO_2 coating. The doping of Cu provided excellent antibacterial activities for the composite coating against both *E. coli* and *S. aureus*.

TiO_2 and ZnO can produce photocatalytic reactive oxygen species in the presence of UV light [127, 128]. Adams *et al.* found that light was a significant factor to promote the generation of reactive oxygen species, although growth inhabitation was also supported in dark environment [127]. TiO_2 is reputed with excellent antibacterial activity to both Gram-negative and Gram-positive bacteria. Rincon *et al.* indicated that the Gram-negative *E. coli* was more sensitive than the Gram-positive *B. subtilis* to the effect of TiO_2 [129]. However, Fu *et al.* found that TiO_2 has a higher killing rate to Gram-positive bacteria than to Gram-negative bacteria [130]. These results indicate that the sensitivity of bacteria to TiO_2 is determined by the specific interact conditions.

ZnO has been reported to be environmentally friendly material and is widely used as an additive ingredient due to its antibacterial property. Applerot *et al.* coated ZnO nanoparticles on the surface of glass using ultrasound irradiation method, which presented an excellent antibacterial effect against *E. coli* (Gram-negative) and *S. aureus* (Gram-positive). The antibacterial property of ZnO is attributed to the production of reactive oxygen species which can cause oxidative injury to the bacterial cell [131, 132]. Hu *et al.* deposited a zinc incorporated TiO_2 composite coating by plasma electrolytic oxidation method and discovered that the antibacterial activity of the Zn-incorporated coatings is enhanced compared with the Zn-free coatings, and the antibacterial effect is ascribed to the release of zinc ions [133].

2.5.2.2 Physical approach

In addition to these chemical antibacterial approaches, some living organisms both animals and plants have developed some fascinating antibacterial surfaces through million-year evolution to prevent colonization from the pathogens, such as the gecko skin, cicada wing, and dragon fly wing [134]. Researchers have been inspired by these nature bactericidal surfaces that can kill bacteria coming in contact with them. Recently,

some studies have been carried out to mimic these nature surfaces for developing the new-generation of bio-inspired antibacterial surfaces [135].

It was reported that the bactericidal effects of the insect surfaces are owing to the sharp nanostructures on the surface [116]. Usually, nanorods with diameter of 50-250 nm, and height of 80-250 nm can penetrate or rupture the bacteria cell wall and cause leakage of nutrients, thereby leading to cell death. This contact killing mechanism has provided an effective approach to tackle the antibiotic-resistant bacteria [135].

Recent studies have been carried out to investigate the relationship between the nanostructures, surface wettability and antibacterial performance of the natural surfaces. Watson *et al.* reported that the hair-like structures of the gecko skin showed an antibacterial action to Gram-negative bacteria *P. gingivalis.* The superhydrophobic property of the skin inhibits the growth of the bacteria, and the stretching effect can cause damage to the cell wall [136].

Ivanova *et al.* reported that the cicada wing has a surface full of nanoneedles with a 60 nm diameter tip and a height of 200 nm. The superhydrophobic nature of the surface has not prohibited the adhesion of the bacteria, but the nanostructured surface has the ability to kill the bacteria upon contact [137]. Figure 2. 12 shows the *P. aeruginosa* (Gram-negative) cells on the surface of the cicada wing. The cells were penetrated by the nanopillars thus leading to the death of the bacteria. This image verified that the nanostructured surface was effective antibacterial too killing the bacteria through the physical approach [137].

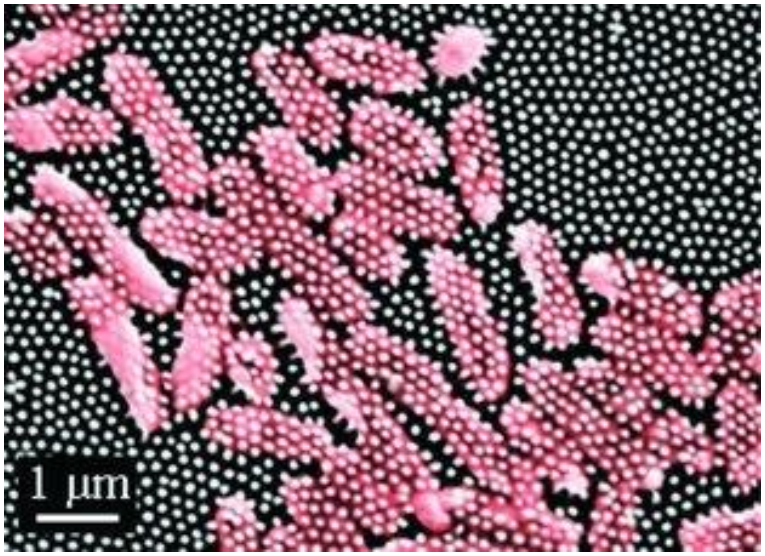

Figure 2. 12 SEM image of the *Pseudomonas aeruginosa* cells on the surface of a cicada wing. The nanopillars are penetrated through the cells [137]

Jafar *et al.* pointed out that the killing-effect of the cicada wing is also related to the thickness difference between Gram-negative bacteria and Gram-positive bacteria. The peptidoglycan cell wall of Gram-positive bacteria is 4-5 times to that of the Gram-negative bacteria which makes it difficult to be penetrated. This implies that the rigidity of the cell walls significantly influences the survival ability of bacteria upon contact with the nanostructures [138].

Dragonfly wing has randomly distributed nanostructures on the surface, which was found to be efficient to kill both Gram-negative bacteria and Gram-positive bacteria [139]. Kyle *et al.* found that the nanoscale topographies on the periodical cicada, annual DD cicada, and sanddragon dragonfly can rupture and kill adhered *S. cerevisiae*. They indicated that there is a connection between the geometry of the surface and cell death. High adhesion between cells and the surface led to a high degree of rupturing for a specific nanostructured surface [140]. These findings from the natural antibacterial

surfaces are useful for designing antimicrobial structures for large-scale cost-effective applications.

Inspired by the nanostructure of the natural antibacterial surfaces, researchers have developed some novel nanostructured surfaces to evaluate their antibacterial performances. Reactive ion etching method is a feasible way to fabricate nanostructured surface due to the etching effect. Hasan *et al.* employed the deep reactive ion etching to fabricate nanostructures on the Si surface, with pillars 220 nm in diameter. The surface was superhydrophobic with a contact angle of 154^{o}. Antibacterial tests showed that 83% of *E. coli* and 86% of *S. aureus* were killed after 3 h contact with the surface [139].

Fisher *et al.* prepared a diamond nanocone surface to mimic the cicada fly wing. The nanodiamond films were fabricated by the microwave plasma chemical vapor deposition at about 850 °C which was modified by bias-assisted reactive ion etching to form the nanocone surfaces [141]. The results indicated that the nonuniform and low-density array exhibited a better antibacterial activity compared to the uniform and high-density array. The radius of the sharp tips of the nanocones ranged from 10 to 40 nm with a base width of 0.35 to 1.2 μm. It has verified that these tailor surfaces were effective to kill a broad range of microorganisms [141].

Nanoneedles of black silicon surfaces have been fabricated by reactive ion etching which demonstrated excellent bactericidal activity against *P. aeruginosa*. May *et al.* used SEM and fluorescence microscopy to observe the killed bacteria, and the results indicated that the needle-like surface exhibited a higher antibacterial efficacy than the flat control surface [142].

Beside these nanostructure surfaces formed by reactive ion etching, it has been reported that sharp nanowires such as TiO_2 nanowires, ZnO nanowires, CNTs, and surfaces with other types of nanowires were also effective in killing microorganisms.

Diu *et al.* prepared the TiO_2 nanowire surfaces with an alkaline hydrothermal method, and the diameter of these nanowires is around 100 nm. It has been found that these nanowires have enhanced the bactericidal effect against motile bacteria (*E. coli*) than that against the non-motile bacteria (*S. aureus*) due to more interactions between bacteria and the nanowires. Both brush and niche types of TiO_2 nanowire surface were verified to be effective to kill bacteria [143].

Chat *et al.* fabricated TiO_2 nanotubes on the surface of Ti foil using an anodization process. They found that the annealing temperature directly affected the antibacterial performance and photocatalytic dye degradation of the nanostructure surface. Gram-positive bacteria *B. atrophaeus* ATCC 9372 was applied for antibacterial tests. A higher antibacterial efficacy can be achieved from the combination of TiO_2 and UV illumination than from the UV illumination only [144].

Wang *et al.* prepared ZnO nanowire arrays with different orientations and used confocal laser scanning microscopy (CLSM) to investigate the antibacterial activity of the ZnO nanowires. The results showed that the antibacterial activity was strongly dependent on the ZnO nanoarray orientations with the randomly oriented ZnO nanoarrays exhibiting the superior antibacterial activity than the well-defined ZnO nanoarrays. The CLSM images showed that cell membranes were significantly damaged by the nanowires which can penetrate through the cells [145].

Densely packed ZnO nanowire arrays were synthesised using a solution-based method with the diameter of about 100 nm. The biological property of the densely packed ZnO

nanowires was tested with the neuronal cell line, neonatal rat cardiomyocytes, and cardiac muscle cell line. The results revealed that the ZnO nanowire arrays had significant inhibitory effects against these cells in comparison to the control surfaces, including gold, glass, and polystyrene [146].

Kang *et al.* first provided direct evidence that SWCNTs have a strong antibacterial effect which can cause physical membrane damage, leading to the release of intracellular content. SEM images showed that the morphology (outer membrane) of *E. coli* changed after exposed to SWCNTs, while the control bacteria maintained their outer membrane structures [147]. Besides, Kang *et al.* found that SWCNTs are more toxic against bacteria compare to that of MWCNTs. While bacteria expressed high levels of gene products after contacted with both MWCNT and SWCNT, yet compared with MWCNT, SWCNT can lead to a higher quantity and larger magnitude of gene expression [148].

Liu *et al.* reported that the individually dispersed CNTs were more toxic than the CNT aggregates against both Gram-negative and Gram-positive bacteria, such as *E. coli*, *P. aeruginosa*, *S. aureus*, and *B. subtilis*. The CNTs can be imagined as "nano darts" which can penetrate the cell walls of bacteria and lead the cell death. They inferred that the activity of the CNTs is related to the dispersion, concentration, and speed of the nano-darts [149].

To study the interactions between single CNT and the bacteria membrane, Liu *et al.* carried out the piercing experiments on the cell walls using an AFM tip with a diameter of 2 nm. The results exhibited that no physical damage can be caused under the low load condition as shown in Figure 2. 13, indicating that the antibacterial effect conferred

by the single CNT is due to the accumulation of interactions between the CNT and the cell membrane [150].

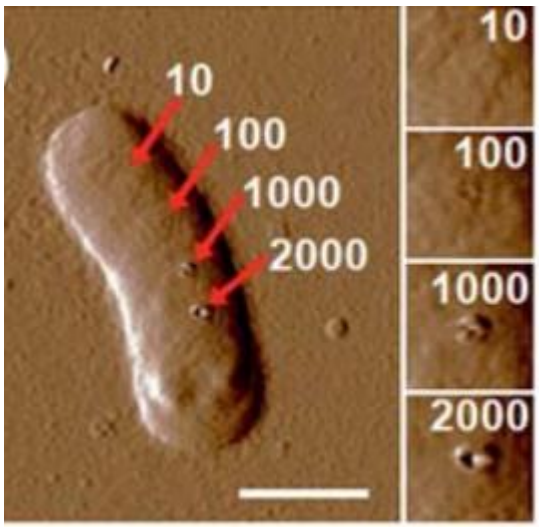

Figure 2. 13 AFM image of *E. coli* after piercing by a 2 nm AFM tips under different load (10 nN – 2000 nN). Scale bar is 1μm [150]

Literature indicates that global demands for advanced antibacterial surfaces have increased significantly over the past years. In this study, two types of functional surfaces (Ag impregnated and VACNTs) have been developed and their antibacterial performances were specifically investigated respectively. The Ag impregnated surfaces with long-lasting antibacterial activity have great potential for applications due to the novel composite structures. Meanwhile, further explorations on the bio-inspired VACNT films are required to have a better understanding of the physical killing mechanism.

Chapter 3 Experimental procedures

3.1 Low temperature synthesis of carbon nanotubes

3.1.1 Substrate materials

Commercial silicon wafers and AISI316 stainless steel (Ø25×6 mm) were used as the substrate materials for the deposition of carbon nanotubes (CNTs). The N-type silicon wafer (100) was approximately 500 μm thick with the electrical resistivity in the range of 5-10 Ωcm. The chemical composition of the stainless-steel sample is shown in Table3.1. All samples were ultrasonically cleaned with acetone for 10 min and dried before the deposition.

3.1.2 Preparation of catalyst

3.1.2.1 Sputtering deposition

A DC Klöckner Ionon 40 kW furnace was used for the deposition of catalyst films for the growth of carbon nano tubes (CNTs). Figure 3. 1 shows the schematic diagram of the furnace and the active screen settings. The worktable was connected to the cathode electrode and the bell-shaped chamber was grounded. An AISI316 stainless steel mesh cylinder was installed on the worktable and connected to the cathode. The top of the active-screen consisted of two lids with an interlayer distance of 6mm in order to form a hollow cathode effect to enhance the sputtering during treatment. The bottom lid was made of a meshed AISI316 stainless steel plate and the top lid was made of stainless steel or silver for the deposition of different catalyst films.

The samples were loaded onto a ceramic base in order to electrically insulate the samples from the worktable (cathode). Hence, the samples were kept at a floating potential during the process and a thermocouple was used to measure the temperature of the samples. Catalyst films were formed by the nanoparticles sputtered from the top

active screen lids. The sputtering deposition process was enhanced by the hollow cathode effect generated between the two top active screen lids. The distance between the sample surface and bottom lid was set to 15 mm.

The deposition of the catalyst thin films was carried out at temperatures between 200^{o}C to 400^{o}C. The working pressure was adjusted to 4 mbar by feeding hydrogen gas. The deposition time of the processes was ranged from 10 min to 60 min. The specific deposition conditions are described in the result section. The thin film contained the elements sputtered from the active screen lids, which are suitable catalysts for the growth of carbon nanotubes. Beside the deposition of catalyst thin films on the substrate materials, the sputtered stainless-steel nanoparticles can also serve to grow the freestanding carbon nanotubes.

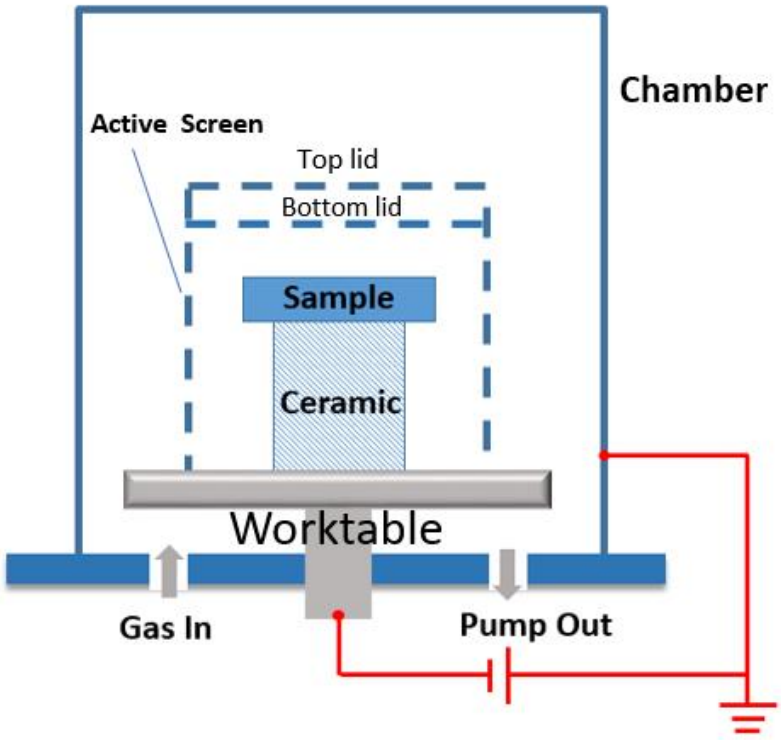

Figure 3. 1 Schematic diagram of the active screen settings in the DC Klöckner Ionon 40 kW furnace

Table 3. 1 Chemical composition of the AISI316 stainless steel

Element	Cr	Ni	Mo	Mn	Si	C	P	S	Fe
Content(wt. %)	17.2	11.7	2.2	1.3	0.6	0.06	0.026	0.014	Balanced

3.1.2.2 Solution method

Solution-based methods can provide another way for the preparation of catalysts through the chemical reactions in the solution. In this study, iron nitrate was used for the formation of an iron catalyst. The iron nitrates were dissolved in ethanol firstly and then spread and dried on the flat sample surfaces. For small particle samples made of Ni and hollow glass beads, to make the iron nitrates uniformly attached to the surface of the particles, the particles were fully immersed in the solution and dispersed by ultrasonic vibration for 10 min. The iron nitrates can be decomposed into iron oxide, and then reduced to iron nanoparticles due to hydrogen (see Equation 1 below).

$$Fe(NO)_3 \xrightarrow{Heating} Fe_2O_3 \xrightarrow{H_2} Fe \quad (1)$$

3.1.3 Synthesis of carbon nanotubes

3.1.3.1 Synthesis of VACNTs films

A commercial plasma enhanced chemical vapour deposition system (PECVD, P500+) was used to synthesise carbon nanotubes. Figure 3.2 shows the cross-section view of the PECVD system, which contains a stainless-steel vacuum chamber, a pumping system, a power control system and two RF electrodes (worktables) mounted at the top and bottom of the chamber. The diameter of the worktables is 250 mm and the distance between the two electrodes was set as 100 mm. Electrode heaters were installed on both worktable with temperature sensors and controllers, and the worktables can be heated separately. The RF power (2 kW) supply can be switched between the top and the

bottom electrodes as required. Various gases and metal organic precursors can be fed into the main chamber as reactive gases, such as hydrogen, nitrogen, argon, methane, and acetylene.

Figure 3. 2 Cross-sectional view of the P500+ PECVD system

For the low-temperature growth of carbon nanotubes, an active screen was set up on top of the samples during the growth process. The schematic diagram of the active screen settings within the PECVD system is shown in Figure 3. 3. Whilst one active screen lid was used for the synthesis of VACNTs films, two active screen lids were needed for the *in-situ* synthesis of CNTs (i.e. both catalysts and CNTs were produced in the P500+ PECVD system). Samples were loaded on the bottom worktable, and the

distance between the lid and the samples was set to be 10 mm. Two categories of the sample were used: the plate-like samples were put on the worktable directly, and the powder samples were packaged within Al foils to prevent them from being blown away during the vacuum process.

The basic processes of the synthesis of CNTs are described as follows. First, the chamber was pumped down to a base pressure of 1×10^{-5} mbar to avoid the interference of the residual air. After that, the samples were heated to the working temperatures ranging from 350ºC to 500ºC. Then a gas mixture of Ar and H_2 was fed into the chamber with the flow rates of 50 standard cubic centimetres per minute (sccm) and 30 sccm, and then plasma was turned on for about 10 min with an RF power of 300 W to clean the sample surface and remove the oxidation layer on the catalyst films.

When the temperature stabilized, C_2H_2 was fed into the chamber, as the carbon source, at a flow rate of 5 sccm. During the growth process, the hydrocarbon gas was diluted by Ar (50 sccm) and H_2 (10~30 sccm). The gas pressure and the power played an important role in the growth of CNTs and hence were optimized for the growth of high quality CNTs. The gas pressure inside the chamber was controlled by adjusting the throttle valve in the range from 0.1 mbar to 5 mbar, and the working power varied between 10 W to 100 W. After the deposition, the power was shut down and the hydrocarbon gas was stopped, while the samples were exposed to the ambient of Ar and H_2 (50 sccm and 20 sccm), and cooled down to room temperature for collection.

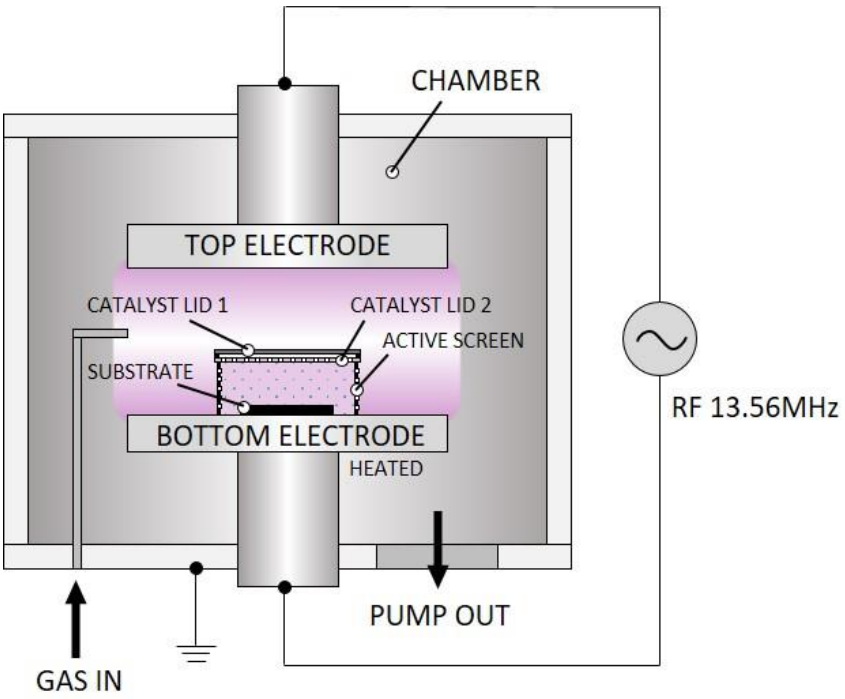

Figure 3. 3 Schematic diagram of the active screen settings used to synthesise CNTs with the P500+ PECVD system

3.1.3.2 Synthesis of free-standing carbon nanotubes

The P500+ PECVD system was also employed to synthesise freestanding carbon nanotubes (FSCNTs). As has been shown in Figure 3.3, two parallel active-screen catalyst lids (stainless-steel) were mounted on the bottom worktable in order to enhance the sputtering of the catalyst lids via so-called hollow cathode effect.

Similar to the preparation of catalysts for VACNTs (Section 3.1.2.1), two types of catalyst particles were used to grow freestanding carbon nanotubes: stainless steel and the nitrates of iron, nickel, and cobalt. Alike the synthesis of VACNTs, the active screen device with double catalyst lids was installed directly in the P500+ PECVD system and the hollow cathode effect was used to sputter stainless steel catalyst particles. Ar and H_2 (50 sccm and 30 sccm, respectively) were fed into the chamber after the base pressure was reached. The RF power source was 500 W and the chamber pressure was

adjusted using the throttle valve to generate a hollow cathode effect between the two active screen lids. The catalyst nanoparticles were deposited onto the surface of the silicon wafer substrate.

The nitrates of iron, nickel, and cobalt were used as the second type of catalyst. The nitrates were dissolved in ethanol and then spread and dried on the surface of silicon wafers. The nitrates decomposed during the CNTs growth process, following Equation2.

$$Me(NO)_3 \xrightarrow{Heat} MeO \xrightarrow{H_2} Me + H_2O \quad (Me=Fe,Co,Ni) \tag{2}$$

The deposition process for FSCNTs using stainless steel catalysts and chemical nitrates catalysts is the same as that for the deposition of the VACNTs films (see Section 3.1). However, the as-grown carbon nanotubes were deposited on the substrates and they were collected as reinforcement for the composite coatings.

3.2 Deposition of CNT reinforced diamond-like carbon (DLC) film

3.2.1 Deposition of DLC film

The deposition of DLC films was carried out also using the P500+ RF PECVD. Figure 3. 4 shows the schematic diagram of the settings for the deposition of the DLC films. Samples were directly placed on the bottom worktable. During the deposition process, the chamber was evacuated to 1×10^{-5} mbar, and then Ar (50 sccm) was fed into the chamber. The heater in the bottom worktable was turned on to heat the samples. When the temperature reached 170°C, CH_4 (10 sccm) was fed into the chamber. The chamber pressure was controlled to around 0.1 mbar using a throttle valve. When the temperature and pressure were stable, the radio frequency plasma was turned on, and the power varied from 50 W to 500 W to study its influence on the formation of the DLC films.

Once the deposition finished, both gas flows and power were stopped, and the chamber was cooled down to room temperature for the collection of the treated samples.

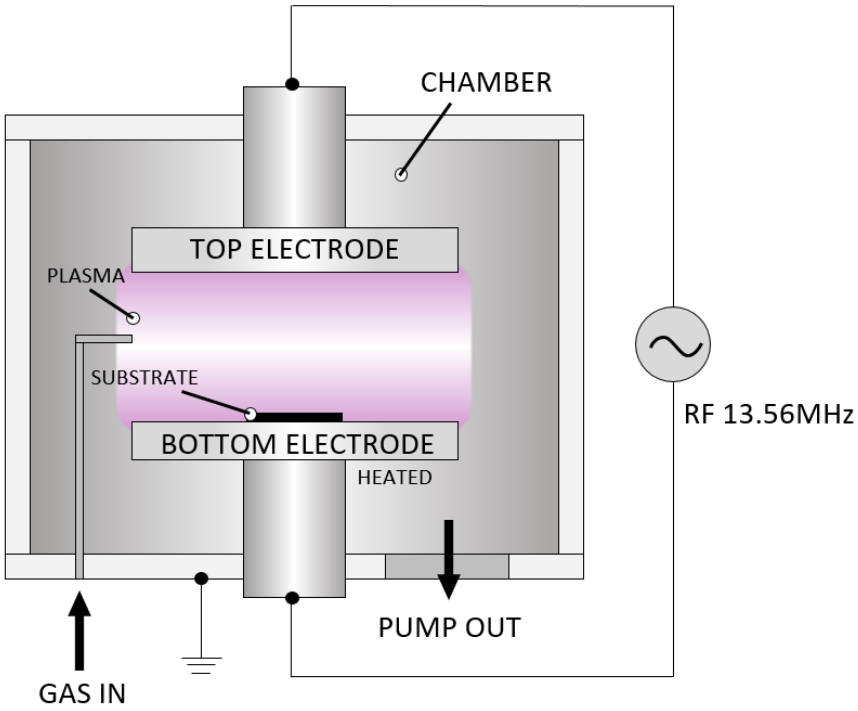

Figure 3. 4 Schematic diagram of the P500 rf PECVD settings for the deposition of DLC films

3.2.2 Deposition of DLC-CNT composite coating

Basically, there are two steps for the deposition of DLC-CNT composite coatings when using the deposition processes mentioned in Section 3.1. First, several types of catalyst films were fabricated, such as stainless steel (SS) and Ag-SS catalyst films, and all the catalyst films were deposited at 200°C for 10 min. The VACNT films were synthesised based on these catalyst films subsequently, and the synthesis was carried out at 500°C for 1 h at 30 W, and C_2H_2 was used as the carbon source. Second, the as-deposited VACNT films were placed on the bottom worktable of the P500 PECVD for the deposition of the DLC coating, and the deposition process was similar to that described in Section 3.2.1.

3.3 Deposition of metal fibre reinforced composite coatings

3.3.1 Active screen plasma co-alloying process

Some metal wires reinforced composite coatings were also deposited using the DC Klöckner Ionon 40 kW furnace adapted with the additional active screen settings similar to that described in Section 3.1.1. The schematic diagram of the deposition processes is illustrated in Figure 3. 5. Samples were kept at a floating potential by using insulating ceramic holders. The two lids were spaced 6 mm apart to form desirable hollow cathode effect for the enhancement of the sputtering process. The distance from the sample surface to the bottom lid was set as 20 mm. The materials for the top active screen lid were selected based on the type of the metal wires to be produced, and in this study silver and copper plates were employed to investigate the formation of the metal wires during the plasma deposition process.

The chamber was evacuated to a pressure of 0.07 mbar before a gas mixture of CH_4 and H_2 (1.5% and 98.5%) was fed into the chamber and the power was turned on under the voltage of 600V. The chamber together with the samples was heated by the plasma formed on the active screen. The gas pressure was 1 mbar during the heating process. When the temperature reached 420°C, the pressure was increased to 3 mbar for the formation of the metal wires reinforced composite coating for 18 h. The coatings were deposited on the substrate of AISI 316 stainless steel (Ø25.4×5 mm) as described in Section 3.1.1.

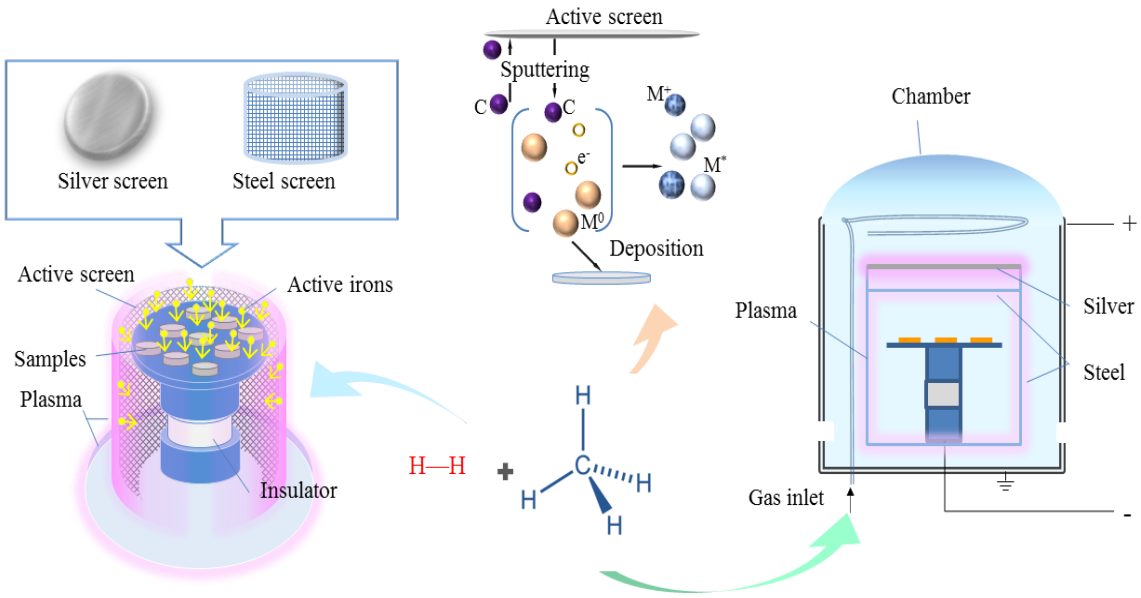

Figure 3. 5 Synthesis of metal wires reinforced carbon composite coating deposited by AS co-alloying process

3.3.2 Double glow plasma co-alloying process

AISI 316 stainless steel samples (Ø25.4×5 mm) were prepared as the substrate with the surface being roughened by 1200 grit SiC paper to increase the bonding between the substrate and the coating to be deposited. Samples were ultrasonically cleaned in acetone for 10 min and then dried prior to the deposition.

The deposition of the functionally graded composite surfaces was carried out also using the DC plasma furnace (Klöckner 40 kW, Luxembourg) but with some special modification. Besides the DC power connected to the bottom electrode for the control of the bias on the samples, an additional TruPlasma 3005 DC power source was installed to separately control the bias on the silver plate and the stainless-steel active screen. The schematic diagram of the settings is shown in Figure 3. 6. It can be seen that samples were placed on the top of the bottom electrode which is connected to the main cathode. The silver plate and the stainless-steel active screen were connected to the additional cathode of the TruPlasma 3005 DC power. The distance between the

silver plate and the stainless-steel lid was fixed at 15 mm, while the distance between the sample surface and the stainless-steel lid can be adjusted to optimise the composite coatings produced.

The typical duplex plasma deposition process can be described as follows. The vacuum chamber was pumped down to 0.07 mbar, and then a gas mixture of N_2 and H_2 (25% and 75%) was fed into the chamber. When the pressure reached 1 mbar, the bottom main power was turned on to clean and to heat the samples. When the temperature reached about 50°C below the setting temperature, the TruPlasma 3005 DC power was turned on to start the sputtering process. The bias on the bottom electrode was then decreased to the setting value. After the deposition, both powers were turned down at the same time, and the treated samples were then cooled down with the furnace to the room temperature.

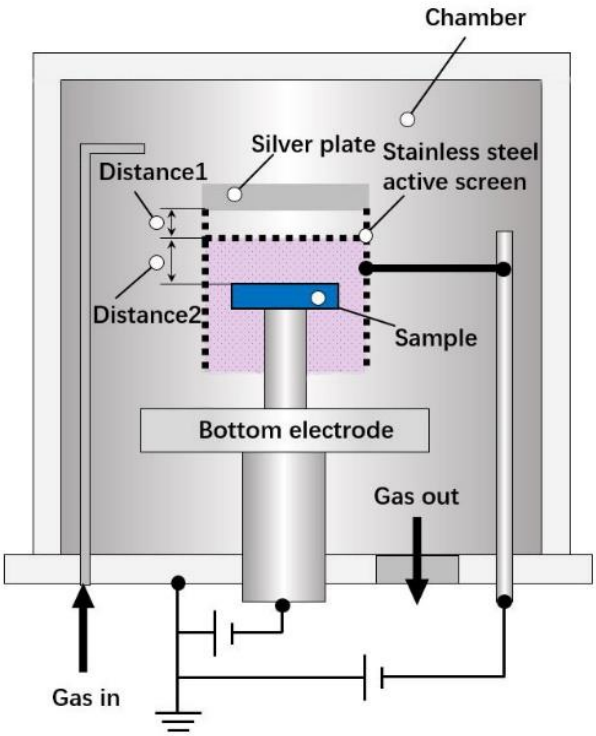

Figure 3. 6 Schematic diagram of the settings of the duplex plasma treatment device for the deposition of the functionally graded Ag impregnated composite surface

3.4 Characterisation techniques

3.4.1 Scanning electron microscopy (SEM)

A scanning electron microscope (JEOL 7000) was utilised to investigate the surface and cross-section morphologies of as-deposited samples. Both secondary electron (SE) mode and back scattering (BS) mode were utilised to observe the samples. Energy dispersive X-ray spectroscopy (EDS, Oxford Instrument) was used to analyse the composition of the samples, and both point and mapping acquisition modes were applied depending on the requirement. The accelerating voltages, working distance, and spot size were adjusted to achieve optimal quality of the SEM images.

The cross-section samples were cut and mounted with conductive Bakelite by the Opal 400 mounting machine. After grinding and polishing, the samples were etched by an etchant (HNO_3 25% + HCl 50% + H_2O 25%) to investigate their microstructures. Some of the samples were coated with Pt nano layer to improve their conductivity using a mini sputtering coater. Samples were attached to the holder using the conductive carbon tape.

3.4.2 Transmission electron microscope (TEM)

A transmission electron microscope (TEM, Oxford JEOL 2100 LaB_6) coupled with EDS was employed to analyse the nanostructure and composition of the CNTs produced at an acceleration voltage of 200 kV. EDS measurements were conducted to measure the composition of the coatings. The bright field TEM images and the selected area diffraction patterns were collected for analysing the microstructure and phases of the samples.

CNTs were scratched off from the samples for TEM specimen preparation. The Cu grid with a holey carbon film was wetted by ethanol to collect the CNTs for the TEM

observation.

3.4.3 Raman spectroscopy

Raman measurements were carried out at room temperature using a Renishaw inVia Raman Microscope with a 488 nm excitation Ar^+ laser. The target areas on the VACNT films or DLC coatings were focused by an optical microscope (20X). The laser power was set to be 3.5W, and each spectrum was acquired by accumulating 10 scans. The spectral lines were smoothened and analysed using WiRE software.

3.4.4 X-ray diffraction (XRD)

A Bruker D8 Advance X-ray diffractometer (Cu Kα, λ = 0.154 nm) was used to investigate the binding and phase structures of the composite coatings developed from this research. Glancing angle detects settings were used to analyse the phase structures of the thin composite layers. The acquired spectra were analysed using X'pert Highscore Plus based on the PDF2-2004 ICDD database.

3.4.5 Glow discharge optical emission spectroscopy (GDOES)

Glow discharge optical emission spectroscopy (GDOES) was utilised to obtain the composition depth profiles of the composite coatings. Figure 3. 7 shows the schematic diagram of the operation mechanism of the GDOES. During the measurement, the sample was attached to the cathode (Figure 3. 7 (a)), a high direct voltage (DC) was applied between the anode and the cathode, and a glow discharge (Ar plasma) was formed in the anode tube due to the high voltage. Ar ions were generated and accelerated to collide on the sample surface (Figure 3. 7 (b)). The sputtered atoms emit lights which are measured by the detector. Their wavelengths are related to the specific elements in the sample. The intensity of the emitted lights can be used to quantify the compositions in the sample (Figure 3. 7 (c)).

The samples with two flat surfaces are required to cover the sealing ring during the tests, and the diameter of the measured round area is about 2.5 mm.

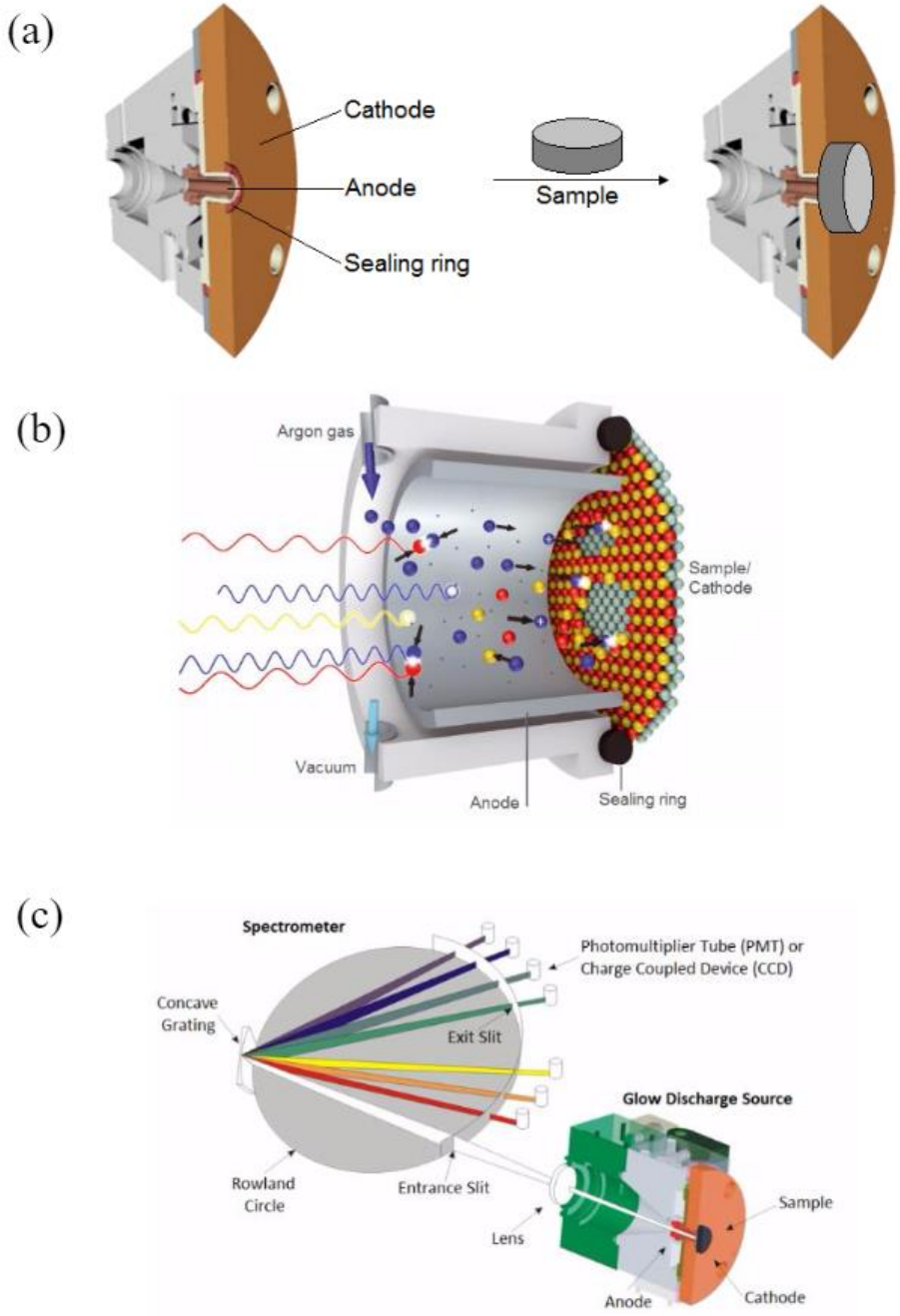

Figure 3. 7 Schematic diagrams of the detect mechanism of GDOES: (a) anode and cathode positions; (b) plasma etching process; (c) detecting process

3.4.6 X-ray photoelectron spectroscopy (XPS)

The surface composition and the chemical states of the elements were investigated by X-ray photoelectron spectroscopy (XPS, Thermo Scientific ESCALAB 250Xi, Figure 3. 8), with an Al Kα (1486.8 eV) source, using a spot size of 500 μm and a binding energy step size of 0.05 eV. Full range spectra and the high-resolution spectra of the specific elements were detected for the characterization of different composite coatings. To decrease the influence of oxygen in the ambient, the surfaces were etched by Ar ions for 60s in order to characterise the chemical status of the elements within the composite surfaces.

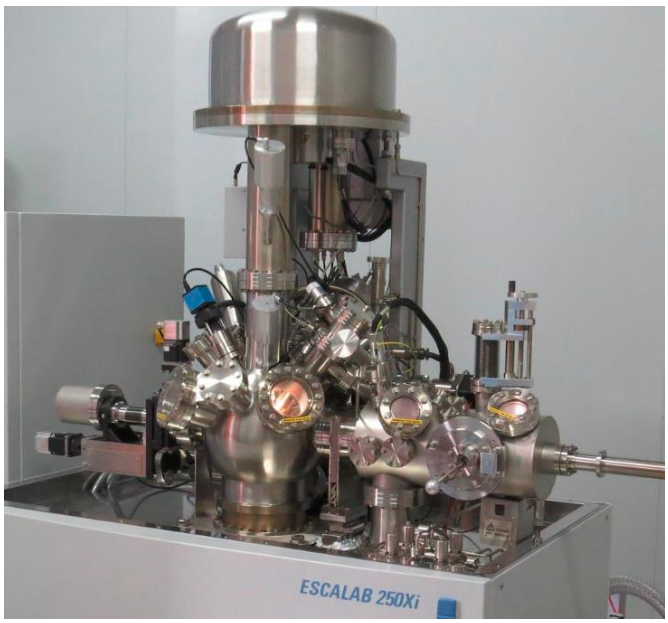

Figure 3. 8 Thermo Scientific ESCALAB 250Xi X-ray photoelectron spectroscopy

3.4.7 Atomic force microscope (AFM)

A multimode AFM (Veeco, Digital Instruments) was applied to investigate the surface morphologies of the as-deposited catalyst films (see Figure 3. 9). The contact mode was applied for the measurement of the surface morphologies of the samples. A 10 μm×10 μm area was scanned while both 2D images and 3D images were acquired to characterise the samples with a size smaller than 5 mm × 5 mm.

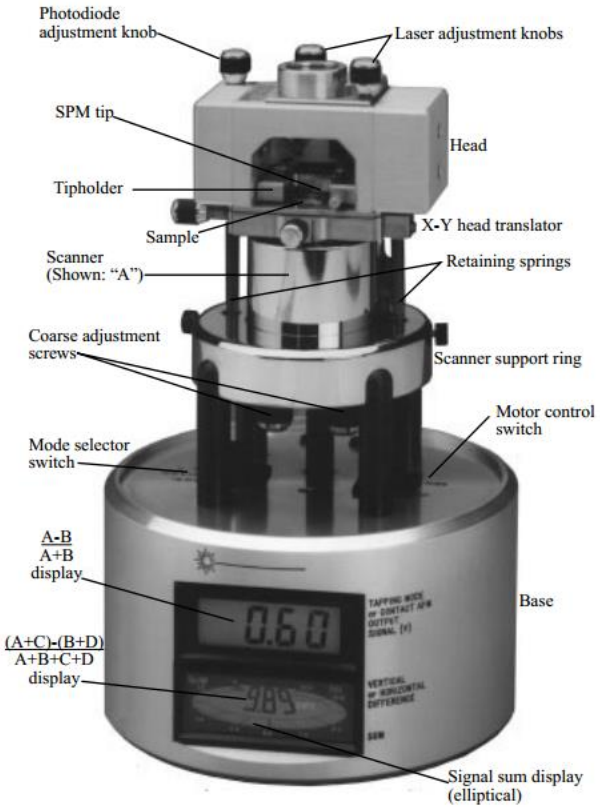

Figure 3. 9 The Veeco multimode AFM

3.5 Property evaluation methods

3.5.1 Hardness testing

The microhardness of the composite coatings was measured by a calibrated Mitutoyo MVK hardness tester with a Vickers diamond indenter. The indent load varied from 10 g to 1000 g and the dwell time was 10 s. The two diagonals of the indentation crater were measured to calculate the hardness value. Three measurements at the same load were carried out and the average hardness and its standard deviation error were reported.

Nanoindentation tests were also carried out to evaluate the nano-hardness and Young's modulus of the DLC coatings. A calibrated Agilent Nano Indenter G200 nanoindentation with a pyramidal indenter was utilised for the measurement of the mechanical properties of the deposited coatings. The maximum indent depth was set to

be 900 nm, and the continuous stiffness measurement mode was applied. The load and depth during the loading and unloading processes were recorded for the calculation of the nanohardness and Young's modulus.

3.5.2 Wettability testing

The wettability of the treated sample surfaces was investigated by the Biolin Scientific Theta contact angle meter (Theta Optical Tensiometer) as shown in Figure 3. 10. During the tests, a sample was put on the flat platform, and the sample edge was focused by an optical microscope from the side. The instrument was calibrated each time before the test. Distilled water (γ_{tot} = 72.8 mN m^{-1}, γ_d = 21.8 mN m^{-1}) was filled in the syringe and precautions were taken to ensure no air bubbles in the needle. The dropout volume was around 2.5 μl with a dropout rate of 0.5 μl/s. The droplets were recorded by the optical microscope for the analysis. The baseline of the interface was automatically recognised, and the contact angles were calculated by the software. Each sample was measured three times to calculate the average contact angle.

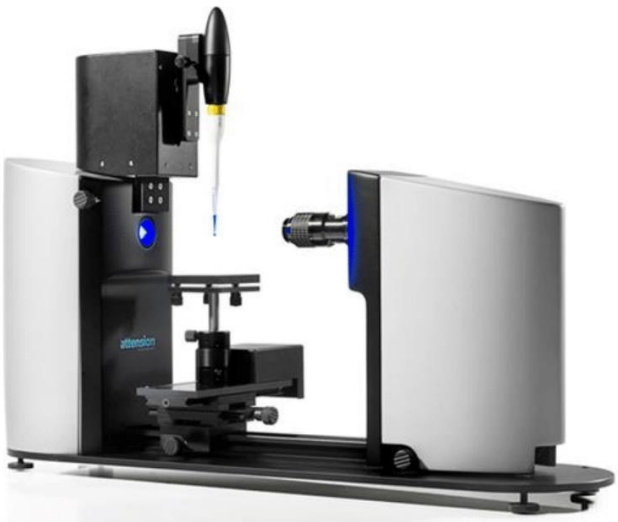

Figure 3. 10 Theta optical tensiometer for measuring the static contact angles

3.5.3 Antibacterial tests

Antibacterial tests were carried out following the JIS Z 2801:2000 bacterial

enumeration standard. All samples were sterilized by autoclaving before the antibacterial tests. The test bacteria were cultured in Tryptone soya agar. The basic procedures of the antibacterial tests are schematically shown in Figure 3. 11. The first step was to dilute the bacteria in broth to decrease the optical density to 0.05 (about 10^7 cells/ml), and then the diluted suspensions were pipetted on the surface of the samples, which were covered by sterile glass coverslips to get equal contact areas for the tests. Samples were then put inside the Petri dishes to incubate for 5h at room temperature. Even though the wettability of the contact between the droplets and the surfaces (e.g. hydrophobic and superhydrophobic surfaces), the contact time in this case was long enough for the fully contact and all the liquid was limited within the glass coverslip to ensure the same contact area. To collect the bacteria, the samples were washed with 10 ml of sterile phosphate buffered saline (PBS) within a sterile container. The dislodge process was carried out with a vortex mixer for 10s and the diluted bacteria suspension (100 µl) was pipetted on the Tryptone soya agar plate. After incubation at 37°C for 24 h, the number of the colony forming units (CFU) were counted (δ_{CFU}) to calculate the surviving numbers of the bacteria δ_t using the following equation:

$$\delta_t = \delta_{CFU} \times 10^3 \ (cells/ml) \tag{3}$$

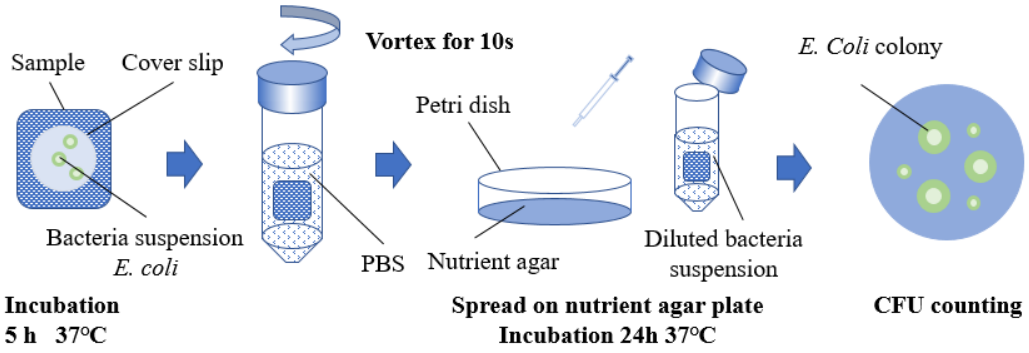

Figure 3. 11 Schematic diagrams of the procedures of the antibacterial test

3.5.4 Tribological tests

A series of tribological tests were carried out to investigate the tribological properties of some composite coating using a reciprocating ball-on-plate CETR UMT-3 tribometer (see Figure 3. 12) under a load of 5 N at 5 Hz for 10min. The length of the wear tracks was 3 mm and Si_3N_4 ceramic balls (Ø 3.8mm) were used as the counterpart. To stimulate the body fluid environment, some of the tests were carried out under wet conditions with the Ringer's solution containing NaCl, KCL, $CaCl_2$ and $NaHCO_3$.

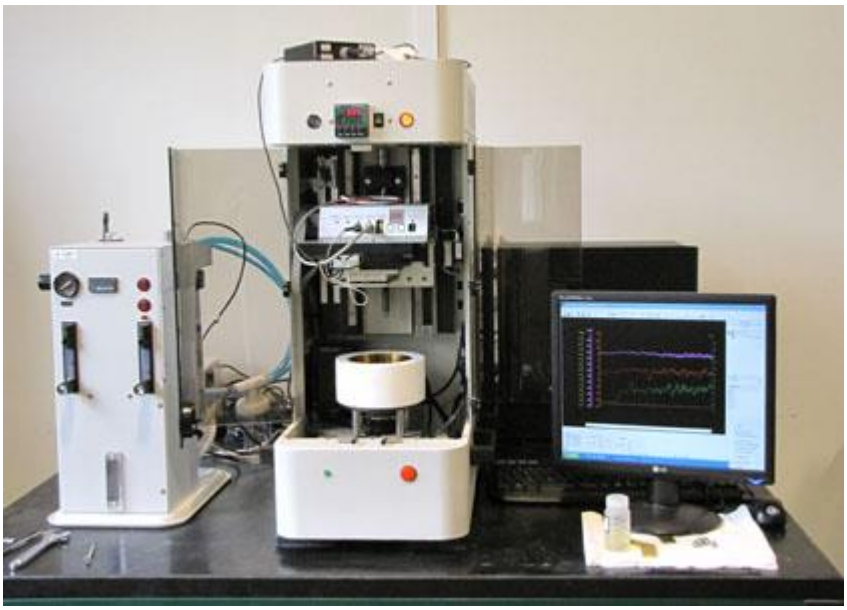

Figure 3. 12 The CETR UMT-3 tribology and mechanical testing machine

3.5.5 Sheet resistance measurement

An RTS-9 four-point probe apparatus (Figure 3. 13 (a)) was used for the sheet resistance measurement of the deposited nanocomposite thin films. Figure 3. 13 (b) shows the measurement apparatus and the arrangements of the four probes. During the measurements, a current passed through the two of the probes which induced a voltage on another two probes, using the readings of voltage and current, the sheet resistance can be calculated using Equation 4, where $\rho_{\square}$ is the sheet resistance, V is voltage, and

I is current. The measurement is relatively simple, but some adjustment of current is needed to obtain the reliable reading when measuring samples with very high or very low resistances. For the high resistance sample, the current is reduced to avoid an excessively high voltage on the surface. For a sample with very low resistance, high current may cause current heating and in turn increasing the measured resistance.

$$\rho_{\square} = \frac{\pi}{\ln(2)} \frac{V}{I} \tag{4}$$

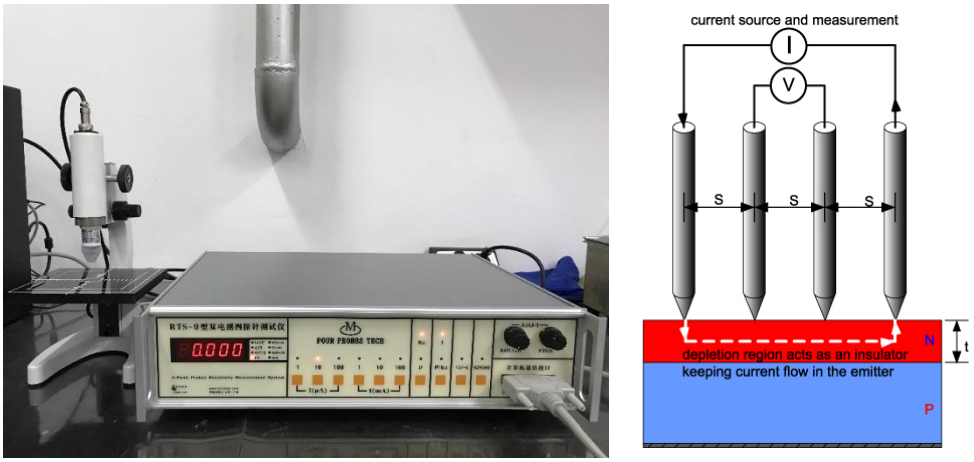

Figure 3. 13 (a) RTS-9 Four-point probe measurement system; (b) schematic diagram of the mechanism of the four probes test

Chapter 4 Results and interpretation

4.1 Synthesis of catalyst films

4.1.1 Stainless steel catalyst films

As discussed in Section 2.2.3, catalyst films play an important role in the growth of carbon nanotubes. Therefore, as described in Section 3.1.2, a series of work has been conducted to develop advanced catalyst films through developing novel active screen plasma technique using the DC Klöckner Ionon 40 kW furnace. The microstructure and the thickness of catalyst films are affected by the deposition parameters, such as temperature, time, pressure, and distance between two active screen lids. Thus, some preliminary work was conducted to deposit stainless steel catalyst films in order to identify the optimal deposition parameters. To this end, stainless steel catalyst films were deposited using the deposition conditions summarised in Table 4. 1. Two 316 stainless-steel (SS) active screen lids were used to prepare the SS catalyst films and the distance between the two active screen lids was 6 mm. The sputtering processes were carried out at 4 mbar in the ambient of H_2 for the generation of strong hollow cathode effect for the sputtering process.

Table 4. 1 Summary of the conditions for the deposition of stainless-steel catalyst films

Code	Substrate	Temperature	Time	Pressure	Gas
C1	Si	200°C	10min	4 mbar	H_2
C2	Si	400°C	10min	4 mbar	H_2

The typical surface morphologies of the as-deposited catalyst films are shown in Figure 4. 1. The appearances of these two catalyst films are very similar mainly due to the similar sputtering conditions. Granular surfaces were formed on the Si surface with uniformly distributed nanoparticles with the size ranging from 10 nm to 50 nm.

Figure 4. 2 shows a 2D AFM image of the 316 SS catalyst film deposited at 200°C for 10 min, and a line scan profile is superimposed showing a maximum amplitude of 2.19 nm. The average roughness of this area is about 2.6 nm and the deduced active site density is approximately $10^{11}/cm^2$.

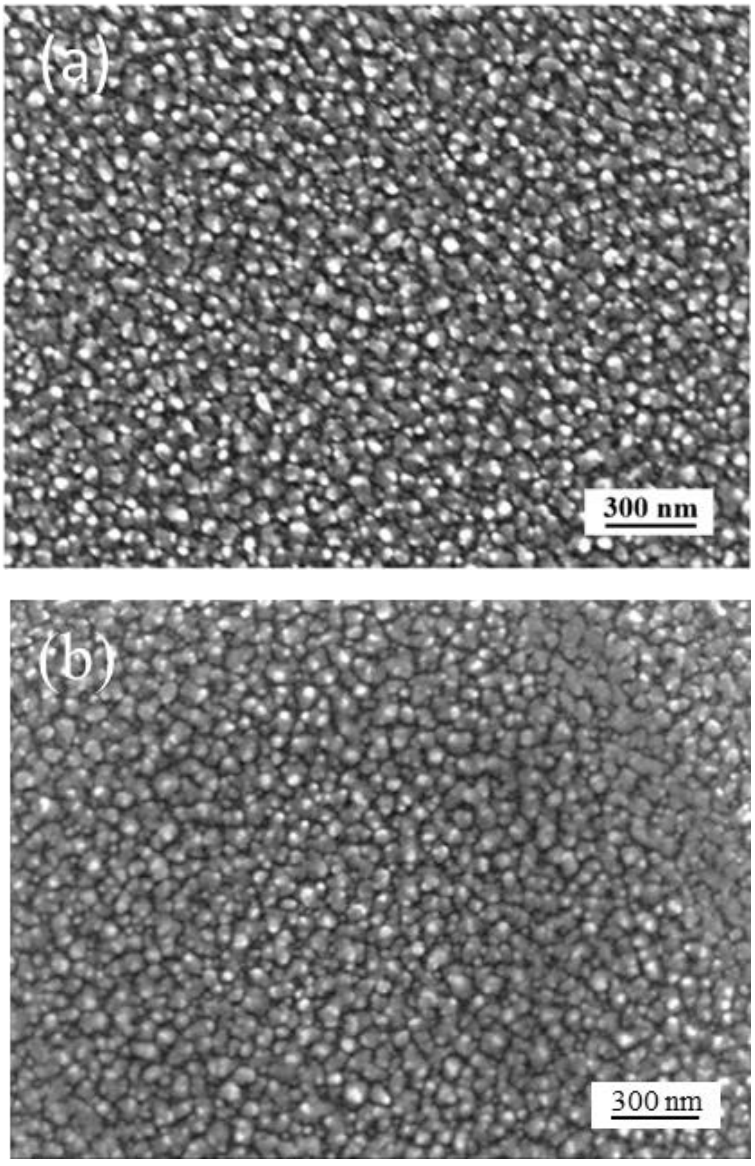

Figure 4. 1 SEM surface morphology of the catalyst films deposited for: (a) C1; (b) C2

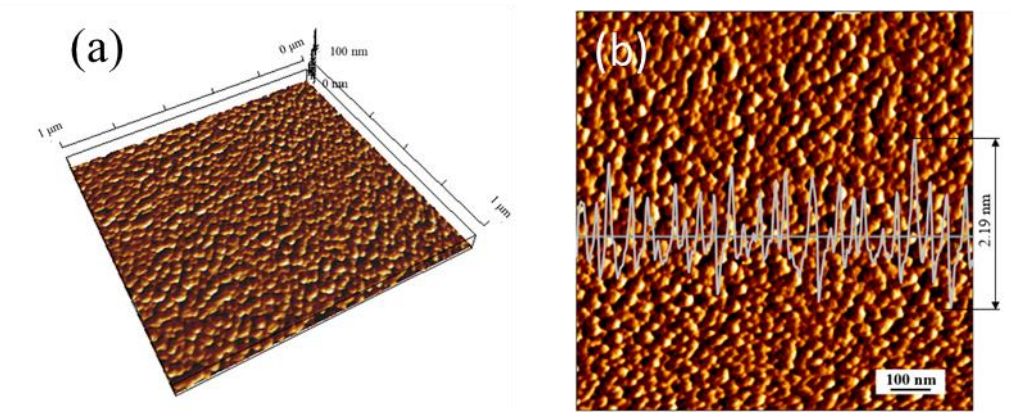

Figure 4. 2 AFM images of the surface morphology of the 316 SS catalyst film: (a) 3D image; (b) 2D image with a profile

XRD was employed to characterise the structures of the catalyst films. Considering the thinness of the catalyst films, glancing angle scan mode was applied. Figure 4. 3 shows the diffraction pattern of the SS catalyst films. Three major peaks near 43º, 51º and 75º are corresponding to γ (111), γ (200) and γ (220), were observed which implies that the catalyst films are mainly formed with austenitic stainless-steel nanoparticles.

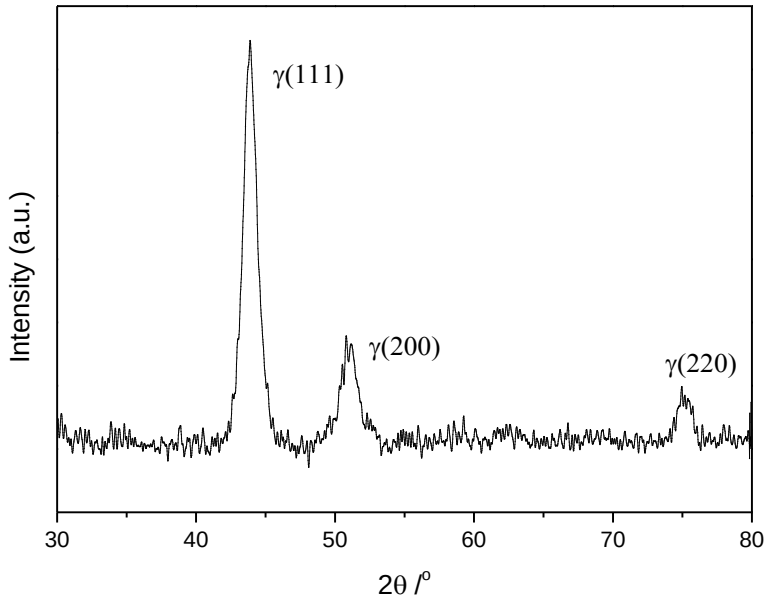

Figure 4. 3 XRD diffraction patterns for the catalyst film deposited at 200°C for 10 min on Si and showing typical γ(111), γ(200) and γ(220) peaks

To measure the thicknesses of the catalyst films, a small part of the Si substrate was covered during the deposition, and a step was formed after removing the cover. Thus, the thickness of the catalyst film is equivalent to the with the height of the step formed. The results revealed that the thickness of the catalyst films is increased with the increase of the deposition temperature and time. When deposited for 10 min, the thickness of the catalyst films deposited at 200°C (C1 sample) and 400°C (C2 sample) is about 20 nm and 40 nm, respectively.

4.1.2 Ag-SS catalyst films

Beside the SS catalyst films, Ag impregnated composite catalyst films were also prepared using an active screen co-sputtering or co-alloying process. As described in Section 3.3.1, the equipment used is the same (DC Klöckner Ionon 40 kW plasma furnace) as for the deposition of SS catalyst film. However, the active-screen settings are different with the top 316 SS mesh lid (used for the deposition of SS catalyst film) was replaced by a solid Ag lid (for the deposition of composites catalyst films) although with the bottom lid made of 316SS mesh lid. The hollow cathode effect generated between the Ag lid and the SS lid can be used to intensify the sputtering nanoparticles from the 316 SS mesh lid and from the solid Ag lid, thus forming so-called co-sputtering or co-alloying. Consequently, the composite thin films consist of both stainless steel and Ag nanoparticles.

Noble Ag particles do not have any catalytic effect for the growth of CNTs and hence can be used to tailor the density and morphology of the CNT film to be grown from the composite catalyst films.

Figure 4. 4 (a) depicts the SEM images of the Ag impregnated stainless-steel catalyst films (i.e. composite catalyst films). Unlike the SS catalyst films, some large particles

are uniformly distributed on the surface of the composite catalyst films. These large particles can be identified by EDX as silver particles indicating a higher sputter rate of silver than SS. The average size of these large Ag particles is about 132nm which is measured from Figure 4. 4 (b). Figure 4. 4 (c) shows the high-resolution secondary electron (SE) image of the catalyst film while Figure 4. 4 (d) is the back-scattering (BS) electron image of the corresponding area. It can be deduced by comparing the SE and BS images that both SS (black coloured) and Ag (white-coloured) particles were formed on the surface of the composite film. It also can be seen that beside the large Ag particles, some small Ag particles were also formed during the sputtering process which would affect the growth of CNTs.

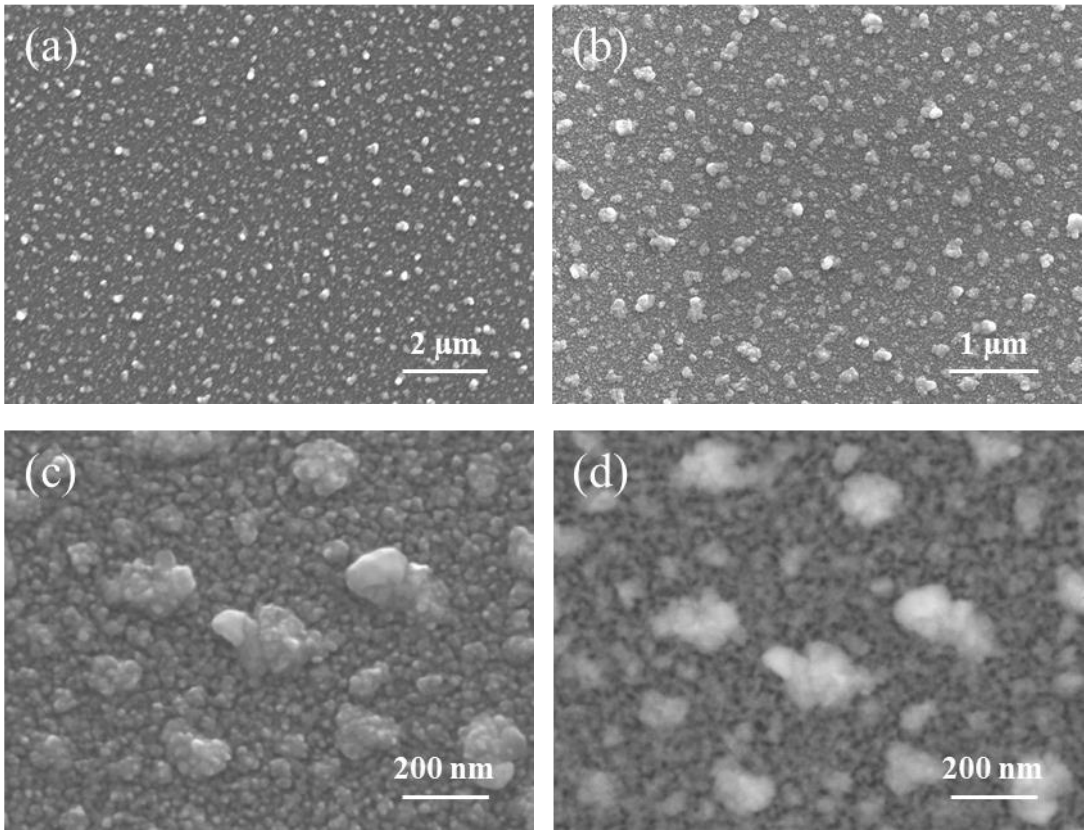

Figure 4. 4 SEM images of the Ag-SS composite catalyst film: (a) & (b) low magnificent SE images; (c) high magnificent SE image; (d) BS image of the corresponding area in (c)

4.2 Synthesis of carbon nanotubes

CNT films

As described in Chapter 3, the synthesis of carbon nanotubes was carried out using a commercial radio frequency (rf) P500+ PECVD system (Figure 3.3). It is known that the growth of carbon nanotubes is affected by the deposition conditions (such as temperature, pressure, power) and the status of the catalysts. In this study, limited by the capacity of the equipment all the syntheses were conducted at temperatures below 500^{o}C. The relatively low growth temperature made it difficult to effectively grow CNTs. Thus, several growth trials were carried out to explore the feasible deposition settings and conditions. It has been found that it is impossible to grow CNTs without the use of the active screen setting, which may be due to the strong plasma etching effect during the growth process. Thus, the purposely designed active screen settings as described in Chapter 3 were used to promote the growth of CNTs.

Figure 4. 5 shows the SEM surface morphologies produced by the unsuccessful trials, and the corresponding deposition conditions are summarised in Table 4. 2, indicating that the growth of CNTs only happens under some specific conditions. Figure 4. 5 (a) shows the surface morphology of the sample deposited at 300^{o}C using the C1 catalyst film (see Table 4. 1). The growth of CNTs could be activated by thermal energy within the system but the carbon source cannot be cracked when the temperature is too low. The intensity of the plasma, which is correlated with the power applied to the electrode, has a strong etching effect on the surface of the sample shown in Figure 4. 5 (a).

Figure 4. 5 (b) shows the surface topographical characteristics of the sample after processing under the power of 100 W. It can be seen that the original continuous catalyst film was damaged and numerous etching craters were formed on the Si substrate. No CNTs were synthesised on the rough surface under this harsh condition.

The percentage of the carbon source also affect the growth of the CNTs, and too high a percentage of carbon source can provide an excessive amount of carbon which will contaminate the catalyst particles and inhibit the growth of the CNTs. Figure 4. 5 (c) shows that the catalyst film is covered by a layer of carbon with few short CNTs.

In addition, the status of the catalyst film also affects the growth of the CNTs. Large catalyst particles will form from a thick catalyst layer, which would inhibit the growth of CNTs. Figure 4. 5 (d) shows the morphology of the sample surface when using a thick catalyst film. Large particles were formed without the growth of CNTs; some CNTs were synthesised with small catalyst nanoparticles in the tips. Thus, further studies have been carried out using thin catalyst films.

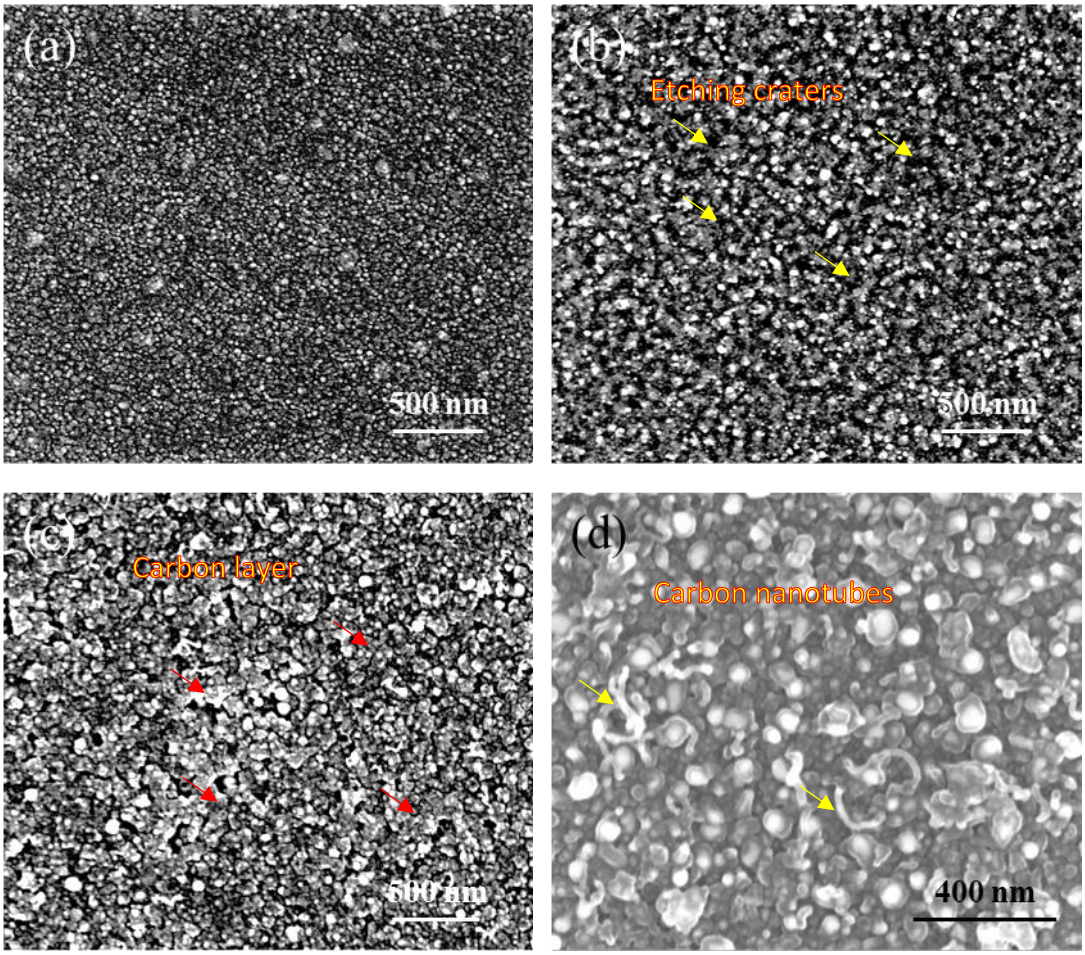

Figure 4. 5 SEM images of the carbon nanotube samples from unsuccessful trials: (a) F3: 300°C; (b) F4: 100 W; (c) F5: C_2H_2 10 sccm; (d) F6: ~100 nm

After a number of trials, it has been found that the feasible deposition parameters for the growth of CNTs would be high temperature, low power, low percentage of carbon source and thin stainless-steel catalyst film. The parameters for the successful depositions of the VACNT films are shown in Table 4. 2. The surface morphologies of the as-deposited CNT films are shown in Figure 4. 6. It can be seen that the substrate is fully covered by carbon nanowires, and the average diameter of the CNTs is around 28 nm when measured from Figure 4. 6 (b).

Figure 4. 6 (c) shows the TEM image of the as-deposited CNTs on F1 sample, and the tubular structure is distinguished from the nanowires. Black nanoparticles can be observed at the tips of the CNTs, which could be attributed to the catalyst nanoparticles. These results indicate that CNTs have been successfully synthesised under the temperature of 500°C and the power of 30 W. To observe the 3D structures of the CNT films, a film was fractured and the cross-sectional view of the VACNT film is shown in Figure 4. 7. It can be seen that CNTs are vertically aligned and densely packed with a thickness of about 1 μm.

Table 4. 2 Deposition parameters for the growth of CNTs

Code	Catalyst	Power	Temperature	Time	Pressure	C_2H_2	Ar	H_2	Result
F1	~20nm	30W	500 ℃	30 min	200 Pa	5 sccm	50 sccm	30 sccm	√
F2	~20nm	30W	500 ℃	100 min	130 Pa	5 sccm	50 sccm	30 sccm	√
F3	~20nm	30W	300 ℃	30 min	200 Pa	5 sccm	50 sccm	30 sccm	×
F4	~20nm	100W	500 ℃	30 min	200 Pa	5 sccm	50 sccm	30 sccm	×
F5	~20nm	30W	500 ℃	30 min	200 Pa	10 sccm	50 sccm	30 sccm	×
F6	~100nm	30W	500 ℃	30 min	200 Pa	5 sccm	50 sccm	30 sccm	×

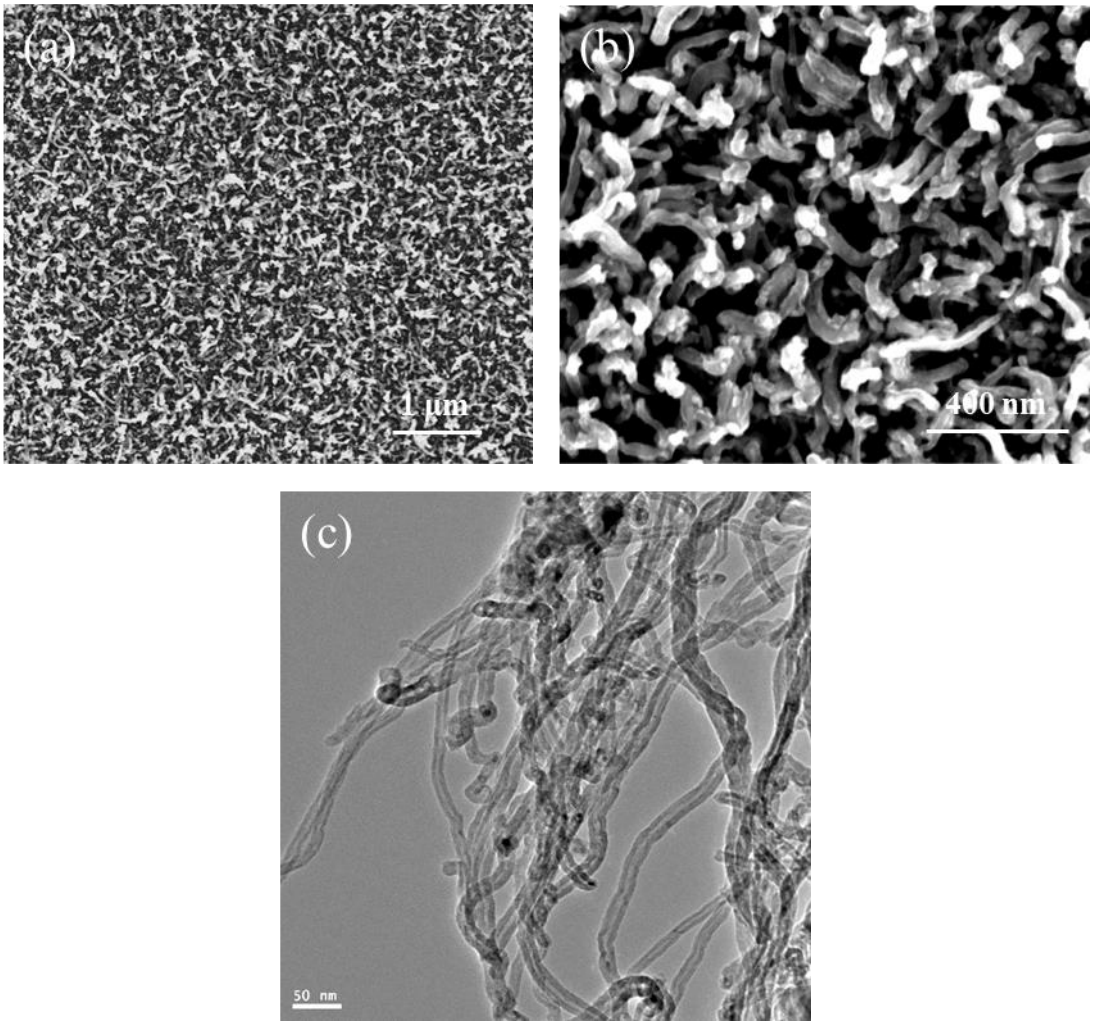

Figure 4. 6 SEM surface images (a & b) and (c) TEM microstructure image of the VACNT films deposited under F1 conditions

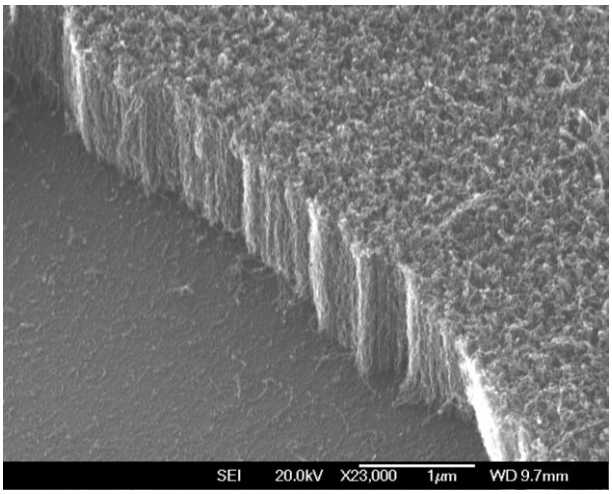

Figure 4. 7 Cross-sectional view of the VACNT film deposited under F2 conditions

Figure 4. 8 shows the VACNT film grown from Ag-SS catalyst films. CNTs can be clearly observed in the secondary electron image shown in Figure 4. 8 (a). Large Ag particles around 200 nm are embedded in the VACNT film, which would play a role in decreasing the density of the VACNT film. It is interesting to find that when observed using the backscattering mode, no CNTs could be seen (see Figure 4.8 (b)); in addition to the large Ag particles as observed from the secondary electron image (Figure 4.8 (a)), some small Ag particles can be also observed.

This is mainly because secondary electrons are emitted mainly from the surface atoms and hence are highly sensitive to the topographical characteristics of the surface. Consequently, even very fine CNT_S can be clearly seen from the secondary electron (SE) image. On the other hand, backscattering image (BS) is formed due to the backscattered electrons from the atoms in the surface region, which is highly related to the atomic mass of these atoms (i.e. chemical composition). It is known that the atomic mass of CNTs (in essence carbon) is much lower than that of Ag. Therefore, more backscattered electrons will be produced from the Ag particles than from the CNTs, thus leading to the bright contrast of the Ag particles in relative to the CNTs. This is the reason why these small Ag particles could be shown by the BS image even if they are embedded in the CNTs. These small Ag particles could directly prohibit the growth of CNTs and thus decrease the density of the VACNT films.

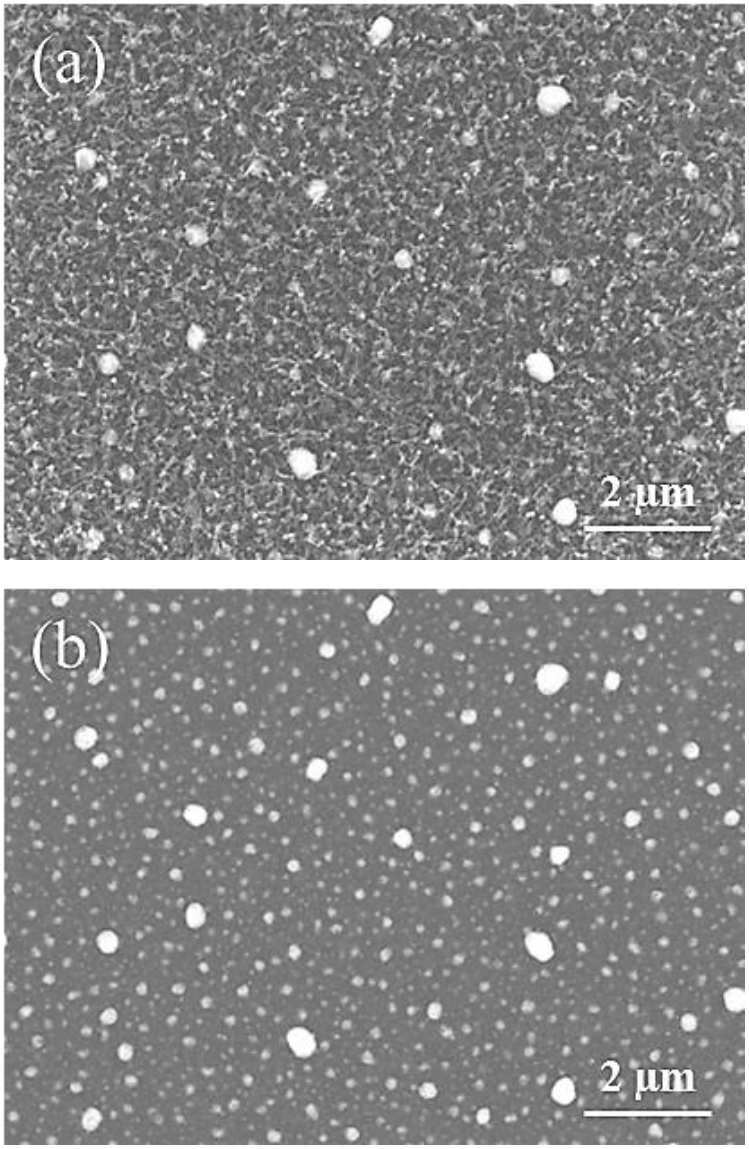

Figure 4. 8 SEM images of the VACNT film grown from the Ag-SS catalyst film: (a) SE image; (b) BS image

Free standing CNTs

In addition to the VACNT film, free-standing CNTs also can be produced using the similar PECVD deposition process, which could be useful for other applications. This would however require different catalyst preparation methods.

The first method for the generation of stainless-steel catalyst nanoparticles is similar to the method as described in Section 4.1.2 but instead of forming a continue layer of catalyst film, some stainless-steel catalyst nanoparticles with weak bonding to the

substrate were produced by increasing the distance between the bottom active screen lid and the substrate for the growth of free-standing CNTs under the condition of F2. The as-deposited free standing CNTs were shown in Figure 4. 9 (a) and it can be seen that curly CNTs are randomly distributed on the substrate.

The second method for the preparation of catalyst nanoparticles is a chemical process. $Fe(NO_3)_3$ (1g) powders were dissolved in 100 ml ethanol and then the solution was sprayed and dried on the surface of a Si substrate. The deposition of CNTs was carried out also under the conditions of F2. The as-grown free standing CNTs are shown in Figure 4. 9 (b). It can be seen that the growth of the CNTs is not uniform as evidenced by the fact that some CNTs are much longer than others. This implies the variation in the catalytic activity of these chemical catalysts. Most probably, the agglomeration of the catalysts would have influenced the decomposition of $Fe(NO_3)_3$ and the growth of the CNTs.

The chemical process also provides a convenient and cost-effective way to prepare catalysts on different surfaces. Figure 4. 10 and Figure 4. 11 are two typical examples to show that the chemical process can be applied to prepare catalysts on micron scale balls. The balls were immersed in the $Fe(NO_3)_3$/ethanol solution (0.01 g/ml) and then dispersed by ultrasonic vibration for 10 min. The dried balls were used to fabricate the CNT coated composite balls under the F2 conditions. Figure 4. 10 shows the morphologies of the CNT-Ni composite balls fully covered by the densely packed CNTs.

Figure 4. 11 shows that a VACNT film can be synthesised on the surface of hollow glass balls. Unlike the homogenous CNTs on the Ni balls, some of the CNT are agglomerated on the surface of the glass ball (Figure 4.11 (a)) mainly due to the

agglomeration of the catalysts. The cross-section view of the CNT covered glass ball was captured at the cracked area (Figure 4. 11 (b)). The thickness of the wall of the glass ball is 400 nm and the thickness of the densely packed VACNTs is around 1 μm. These CNTs covered glass balls could be potentially used as microwave absorbing materials.

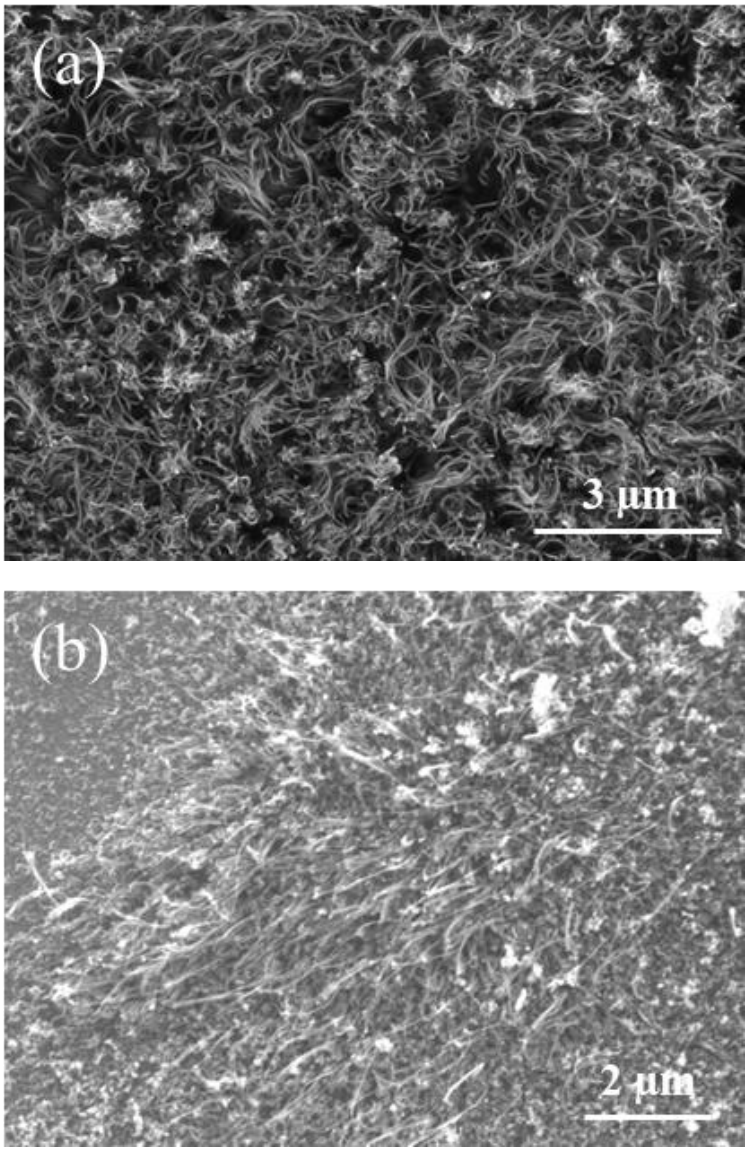

Figure 4. 9 SEM images of the free-standing CNTs grown from (a) sputtered catalysts and (b) chemically formed catalysts

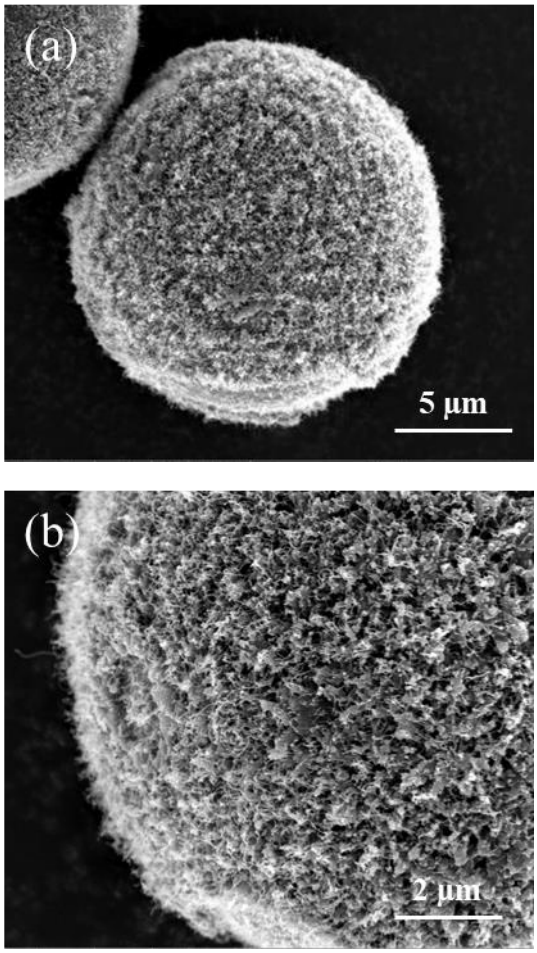

Figure 4. 10 SEM images of the CNT-Ni composite balls

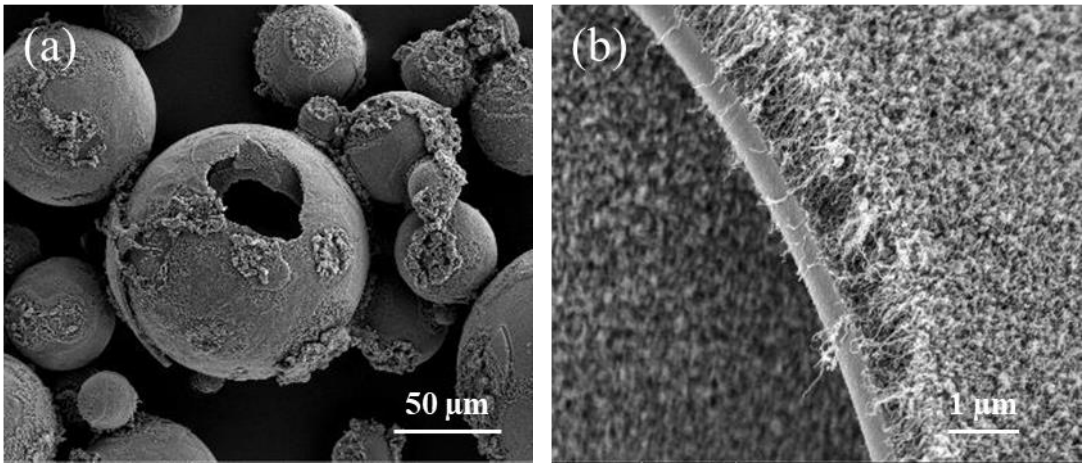

Figure 4. 11 SEM images of the CNT-glass ball composite structures. (a) a general view of the hollow glass balls; (b) cross-section view of the composite structure

4.3 Low temperature *in-situ* synthesis of VACNT films

The carbon nanotubes reported in the last section are produced using two steps separately: (i) the formation of catalyst film using ASP or chemical reaction and (ii) the growth of CNTs using PECVD. Unlike the two-step growth process, a novel low temperature *in-situ* synthesis of CNTs has been developed to deposit CNTs and the results are reported in this section. Here, the synthesis of CNTs is conducted immediately after the preparation of SS catalyst film within the same PECVD equipment. A series of experiments were carried out to evaluate the influence of deposition conditions (Table 4. 3) on the growth of VACNT films.

Table 4. 3 The conditions for the *in-situ* deposition of CNTs

Code	Power	Temperature	Time	Pressure	C_2H_2	Ar	H_2
N1	30W	400 ℃	100 min	100 Pa	5 sccm	50 sccm	30 sccm
N2	30W	450 ℃	100 min	100 Pa	5 sccm	50 sccm	30 sccm
N3	30W	500 ℃	100 min	100 Pa	5 sccm	50 sccm	30 sccm
N4	30W	500 ℃	100 min	200 Pa	10 sccm	50 sccm	30 sccm

4.3.1 Morphologies

Figure 4. 12 shows the surface morphologies and cross-section views of the VACNT films grown at 400℃, 450℃ and 500℃. It can be seen from Figure 4. 12 (a)&(c)&(e) that the CNTs at the top surfaces of the films are sparsely packed with curly ends, while the CNTs are densely packed in the middle and bottom area (Figure 4. 12 (b)&(d)&(f)) as a result of the interactions between the neighbour CNTs by Van der Waals forces. It is clear from the cross-sections of the CNT films that the CNTs are in general well-aligned and perpendicular to the interface between the CNT films and the substrate.

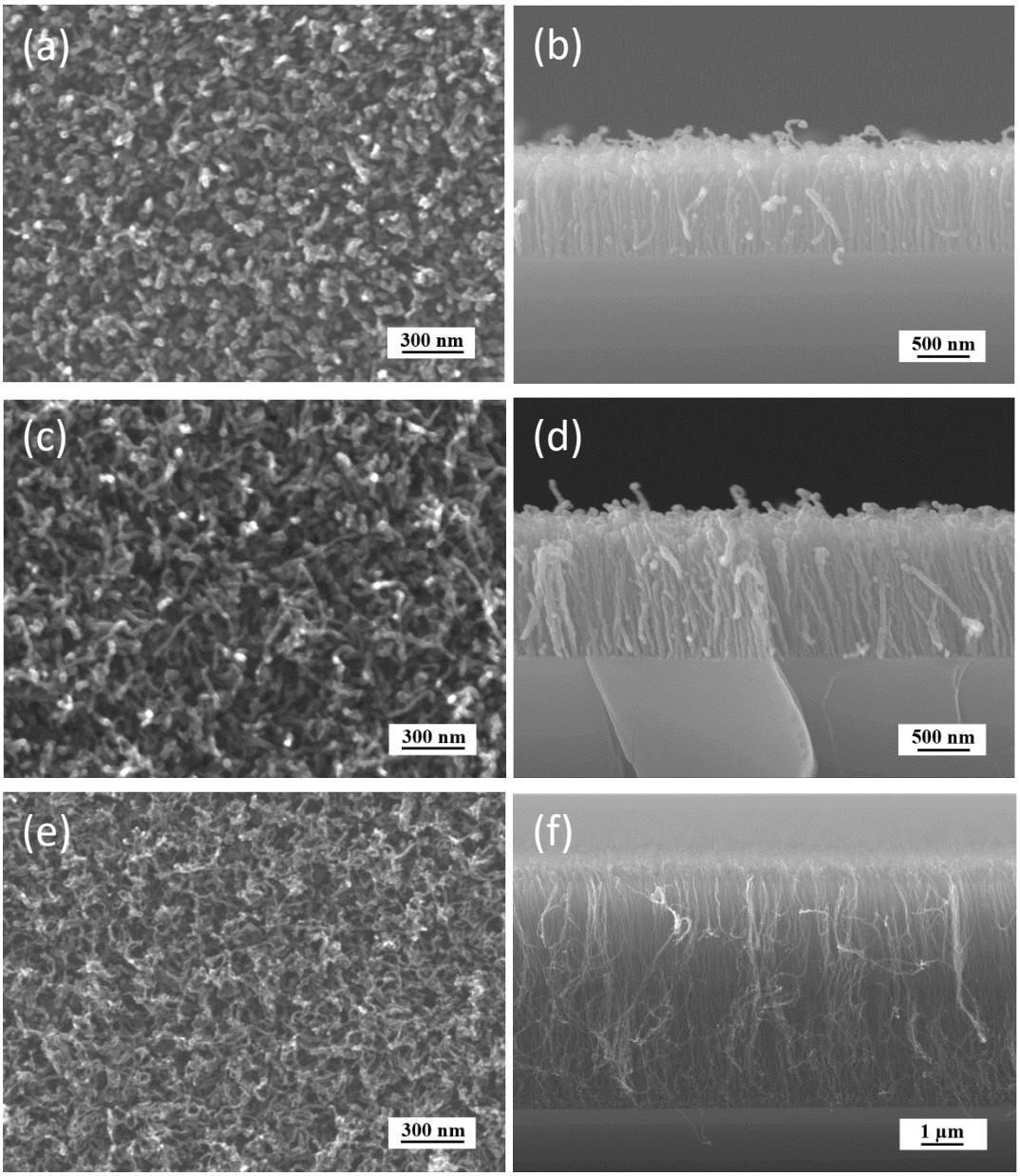

Figure 4. 12 SEM images of VACNT films deposited at different temperatures: (a) & (b) at 400℃; (c) & (d) at 450℃ and (e) & (f) at 500℃

The growth of the CNTs is directly influenced by the catalyst films. This is evidenced by the fact that the density of the VACNTs is closely related to the catalyst nanoparticles. This is supported by the observation that the bright dots at the CNT tips are catalyst nanoparticles, which implies a tip growth mode. The growth speed of the VACNT films is found to be closely related to the deposition temperature. The corresponding growth speed of the VACNT films formed at 400℃, 450℃ and 500℃

is about 9, 15 and 60 nm/min respectively. However, no CNTs were formed under the same deposition conditions when the ASP setting was removed from the PECVD chamber. This clearly indicates that the ASP setting has played a critical role in the low temperature *in-situ* growth of VACNTs.

4.3.2 Chemical state of VACNTs film

The surface chemical states of the VACNTs film (N2, 450℃) were analysed by X-ray photoelectron spectroscopy (XPS). The spectra shown in Figure 4. 13 were obtained from the top surface before and after etching by argon ions for 50s. Figure 4. 13 (a) shows two survey spectra from the as-deposited surface and the etched surface.

The overlapped low-resolution spectra were resolved to analyse the components of C, Fe and Ni. The C-C peak at 284.6 eV appeared in both spectra. However, a shoulder peak at 286.2 eV corresponding to C-O is more clearly detected from the as-deposited surface (see Figure 4. 13 (b)), which indicates that carbon in the surface interacted with oxygen when exposed in the air after deposition.

Almost no peaks of Fe or Ni were detected from the surface without etching, but obvious Fe $2p_{1/2}$, Fe $2p_{3/2}$ peaks, and a weak Ni 2p peak were detected after etching, as shown in Figure 4. 13 (c) & (d). The etching process was effective to remove the carbon coated on the catalyst nanoparticles. The existence of Fe and Ni spectra indicates that the catalysts were still stainless-steel nanoparticles, which is consistence with the XRD result.

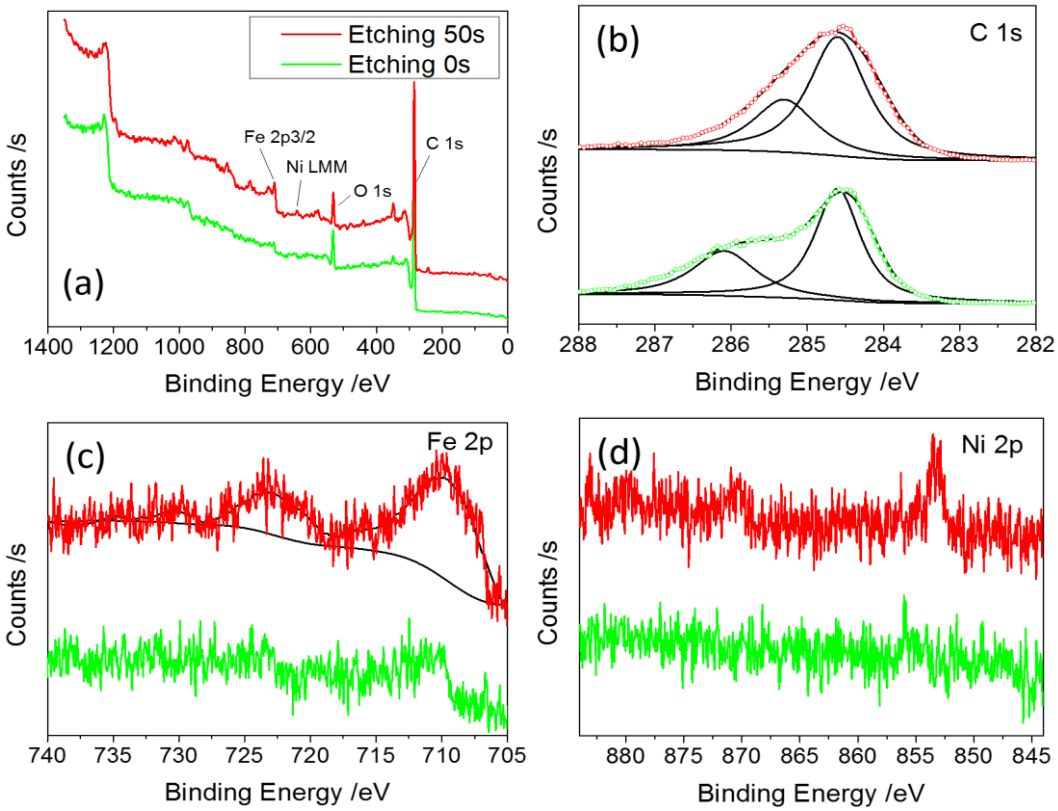

Figure 4. 13 (a) XPS survey spectra of VACNTs film deposited at 450℃ after etching for 0 s and 50 s; (b) high resolution C 1s spectra; (c) high resolution Fe 2p spectra; (d) high resolution Ni 2p spectra

4.3.3 TEM results

CNTs were scratched off from the films and the structural details of the CNTs were further studied by TEM. Figure 4. 14 (a)&(b)&(c) show the TEM images of the CNTs grown at 400℃, 450℃ and 500℃, respectively. Tubule structures with black dots embedded in the tips of the CNTs can be observed. These black dots are considered as the catalyst nanoparticles deposited by ASP in the catalyst preparation stage.

Although the size of the catalyst nanoparticles appeared at the tip of the CNTs is smaller than that of the CNTs, the structure and diameter of the CNTs formed are closely related to the shape and size of the catalyst nanoparticles. However, it is also noted by comparing the CNTs shown in Figure 4. 14 (a)&(b)&(c) that the lower the growth temperature, the stubbier the CNTs formed. Clearly, growth temperature has also

played an important role in the growth of CNTs.

Close observation also showed that all the CNTs are multi-walled. Figure 4. 14 (d) shows a high-resolution TEM image of a CNT synthesised at 450℃, which clearly presents the wall structure. The interlayer distance (about 0.34 nm) is consistent with that of the graphitic layers. It has been reported that the diameters of CNTs are highly related to the growth temperature, the plasma density and the structure of the catalyst particles [151].

In this study, the effect of growth temperature on the diameter of CNTs formed was studied by using the same plasma density and catalyst film. Figure 4. 14 (e) compares the diameter distribution measured from the TEM images of the CNTs formed at different temperatures. It can be seen that the diameter of the CNTs decreased with increase in the growth temperature and the average diameter for the CNTs formed at 400℃, 450℃ and 500℃ is 28 ± 3.6 nm, 23 ± 3.1 nm, and 16 ± 2.8 nm, respectively. This is mainly because a higher deposition temperature can offer more kinetic energy for the growth of CNTs. This will promote the diffusion and precipitation of the carbon atoms, which makes the growth of CNTs faster and hence thinner.

The chemical composition of the deposited CNTs (S2, 450℃) was measured using EDS during TEM analysis. The selected area is shown in Figure 4. 15 and the EDS spectrum is shown in Figure 4. 16. The element concentrations of the CNTs are listed in the EDS spectrum. As expected, it contained a high amount of carbon although the experimental error is large for such a light element as carbon.

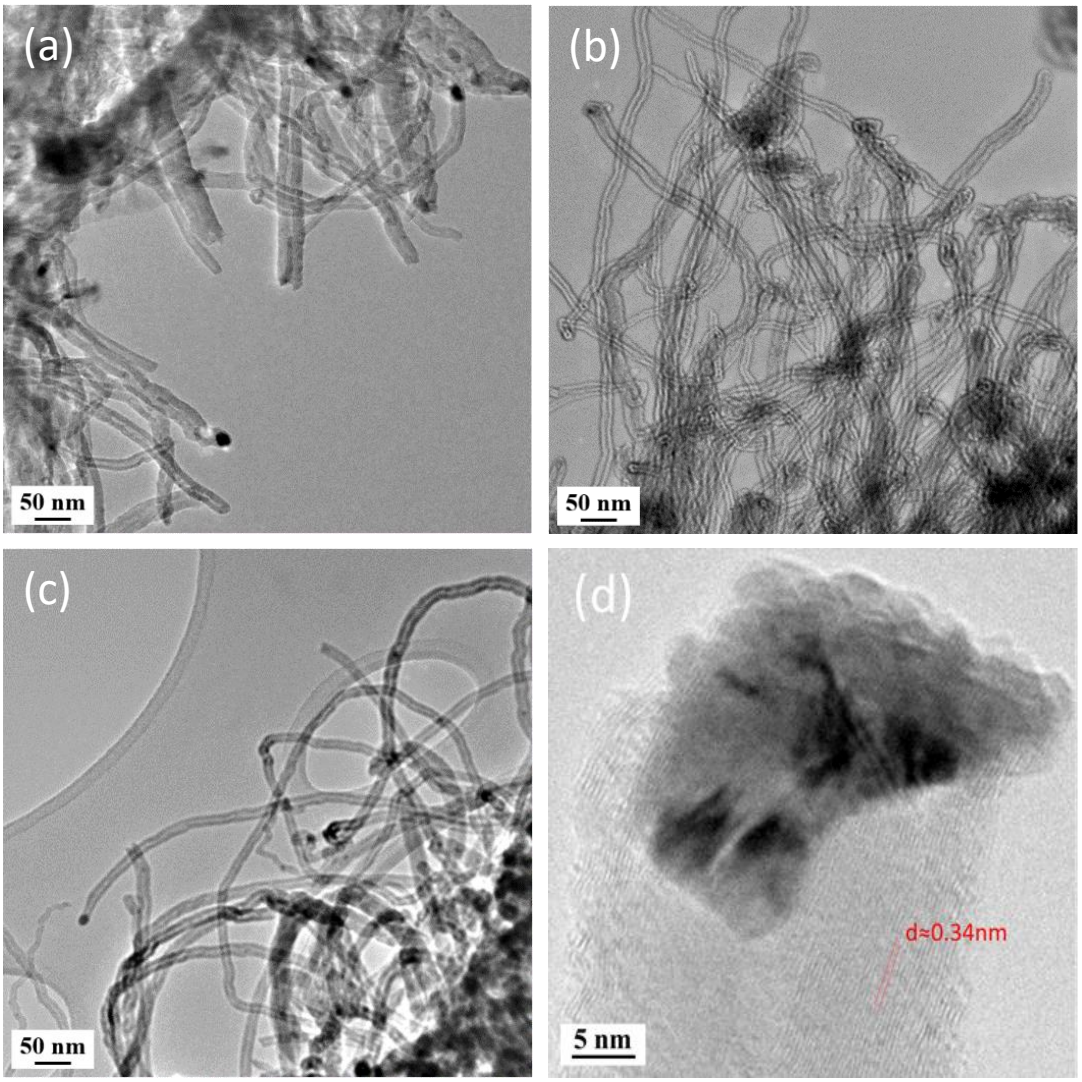

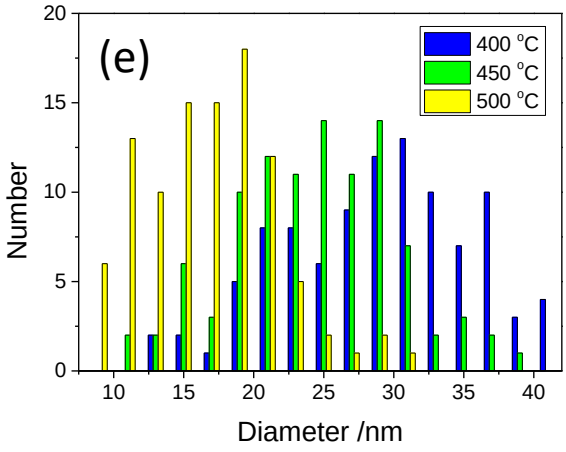

Figure 4. 14 TEM images of CNTs grown at temperature of (a) 400℃, (b) 450℃, (c) 500℃, (d) high resolution image of single carbon nanotube grown at 450℃, and (e) summary of the diameter distribution of CNTs grown at different temperature

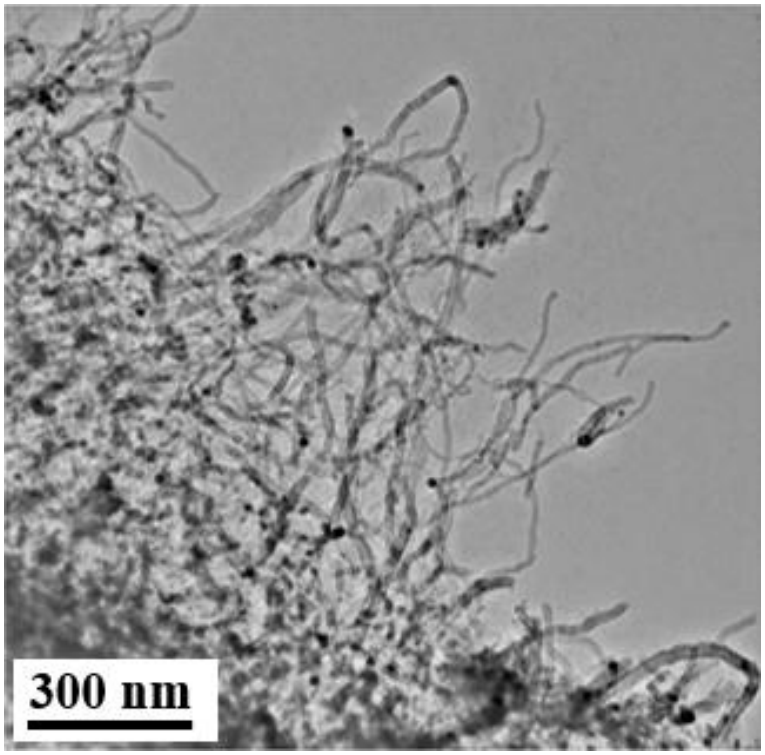

Figure 4. 15 TEM of the selected area for the EDS measurement of CNTs deposited at 450℃

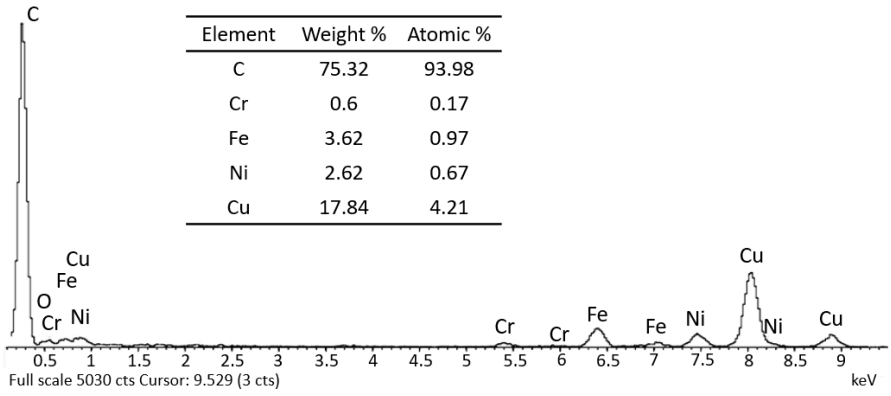

Element	Weight %	Atomic %
C	75.32	93.98
Cr	0.6	0.17
Fe	3.62	0.97
Ni	2.62	0.67
Cu	17.84	4.21

Figure 4. 16 EDS spectrum of the CNTs deposited at 450℃, element concentrations are illustrated in the inserted table

4.3.4 Raman results

Raman spectroscopy was used to evaluate the structure and quality of the CNTs produced by the novel *in-situ* low-temperature plasma process. The Raman spectra of as-deposited VACNT films are shown in Figure 4. 17. Typical D, G, 2D, D+G and 2D'

bands can be detected from all these samples, but the peak intensities varied with the synthesis conditions.

D band at around 1350 cm^{-1} is referred as the disorder band which originates from the defects [152]. G band at around 1600 cm^{-1} was caused by the vibration of graphitic carbon atoms. The band at around 2700 cm^{-1} is known as 2D or G' band, which is indicative of the stacked graphene layers and their intensity is correlated to the thickness of the walls. D bands and 2D bands are proportionately increasing with the walls of the nanotubes. The positions and intensities of these bands are affected by the features of the CNTs, such as defects, impurities, wall thickness and element doping [153].

In this study, it can be seen from Figure 4. 17 that the D band drifted to left with the increase of deposition temperature. The intensity ratios of the D band to the G band (I_D/I_G) for the CNTs formed at different temperatures are around 0.7. However, when the hydrocarbon gas flow raised from 5sccm to 10sccm (S4), the I_D/I_G ratio increased to 0.97 and the intensity of the 2D band increased. The D band and G band are shifted close to each other, which may be due to the generation of more defects or even amorphous carbon during the process.

The intensities of D+G bands and 2D' bands in all spectra are similar. D+G bands have similar information and behaviour to that of the D bands [154]. 2D' bands are too small to evaluate their variations, which have little help in distinguishing the CNTs [154]. No peaks were found in the low-frequency areas and the absence of the radial breathing mode (RBM) also verify that the as-grown CNTs are MWCNTs. Outer layers of MWCNTs can restrict the breathing mode, which is the primary difference of Raman spectra between SWCNTs and MWCNTs [155].

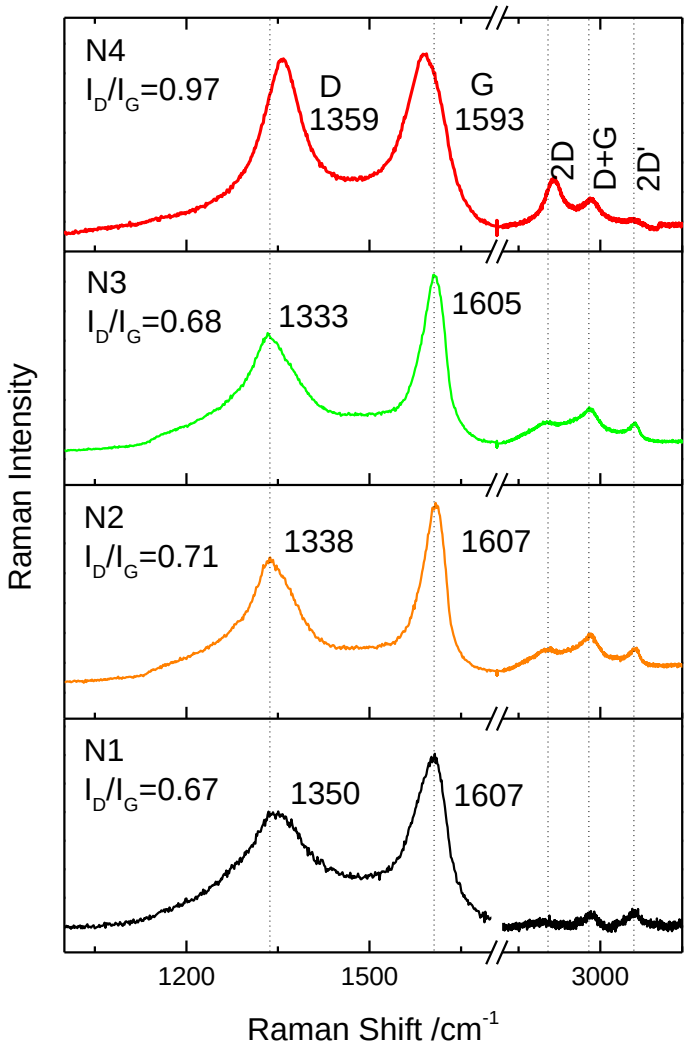

Figure 4. 17 Raman spectra of the VACNT films synthesised at different conditions

4.4 Bio-inspired antibacterial VACNT surfaces

4.4.1 VACNT films for antibacterial evaluation

Three types of vertically aligned carbon nanotubes films were selected for evaluation of their antibacterial performances. The deposition process is similar to that mentioned earlier. Two types of SS catalyst films were deposited on silicon wafers by the ASP technique for the growth of VACNT films. To investigate the effect of Ag, Ag

impregnated catalyst film was also prepared. The VACNT films were grown using these three catalyst films, and the growth parameters are summarised in Table 4. 4. All these catalyst films and VACNT films were also fully characterised due to the slightly different deposition conditions used.

Table 4. 4 Growth parameters of VACNT films by PECVD

Code	Catalyst	Temperature	Time	Pressure	C_2H_2	Ar	H_2	N-dope
S1	Ag+SS	450 ℃	60 min	100 Pa	5 sccm	50 sccm	30 sccm	-
S2	SS	450 ℃	60 min	100 Pa	5 sccm	50 sccm	30 sccm	-
S3	SS	450 ℃	60 min	100 Pa	5 sccm	50 sccm	30 sccm	√

SS and Ag impregnated catalyst films were effectively deposited by the ASP technique, and their surface morphologies are shown in Figure 4. 18. Figure 4. 18 (a) shows that SS nanoparticles are uniformly distributed on the surface. The surface of the Ag impregnated SS catalyst film is shown in Figure 4. 18 (b), and some larger Ag particles are randomly spread within the catalyst film. Beside these obvious large Ag particles, small Ag nanoparticles were also generated and uniformly distributed in the catalyst film. As discussed before, these Ag particles can influence the growth of the CNTs. Thus, the Ag-SS catalyst film was used for comparison.

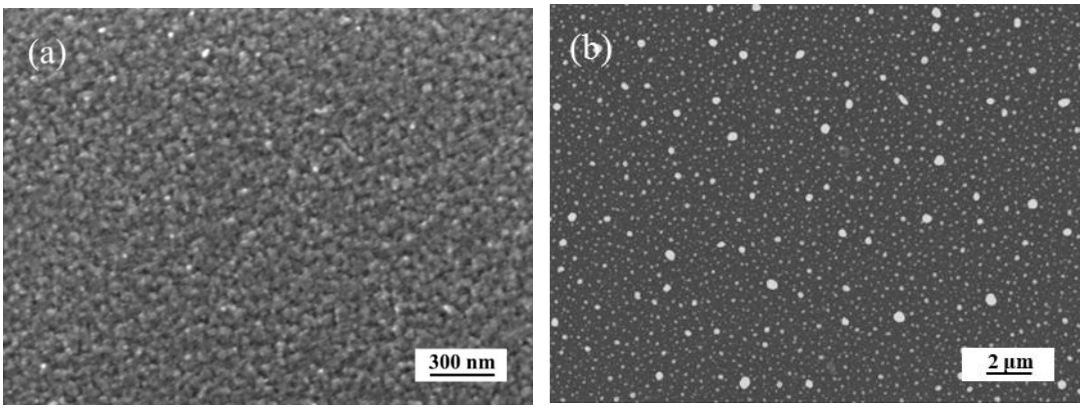

Figure 4. 18 Surface morphologies of as-deposited catalyst films. (a) SE image of SS catalyst film; (b) low magnification BS image of Ag-SS catalyst film

The surface morphologies of the three types of VACNT films are shown in Figure 4. 19. It can be seen that the density of the VACNTs grown from the Ag-SS catalyst film (Figure 4.19 (a)) is lower than that grown from the SS catalyst film (Figure 4.19 (b)) due to the existence of the Ag particles. Besides, CNTs grown from the SS catalyst film are vertically aligned because of the Van der Waals forces between the CNTs during the growth process, while CNTs grown from the Ag-SS catalyst film are relative curl. Post-nitriding was carried out for a VACNT film and it seems that the nitriding process has little influence on the microstructure of the VACNT film, and the nitrogen doped VACNT film (Figure 4.19 (c)) has a similar appearance to that of the as-deposited VACNT film (Figure 4.19 (b)).

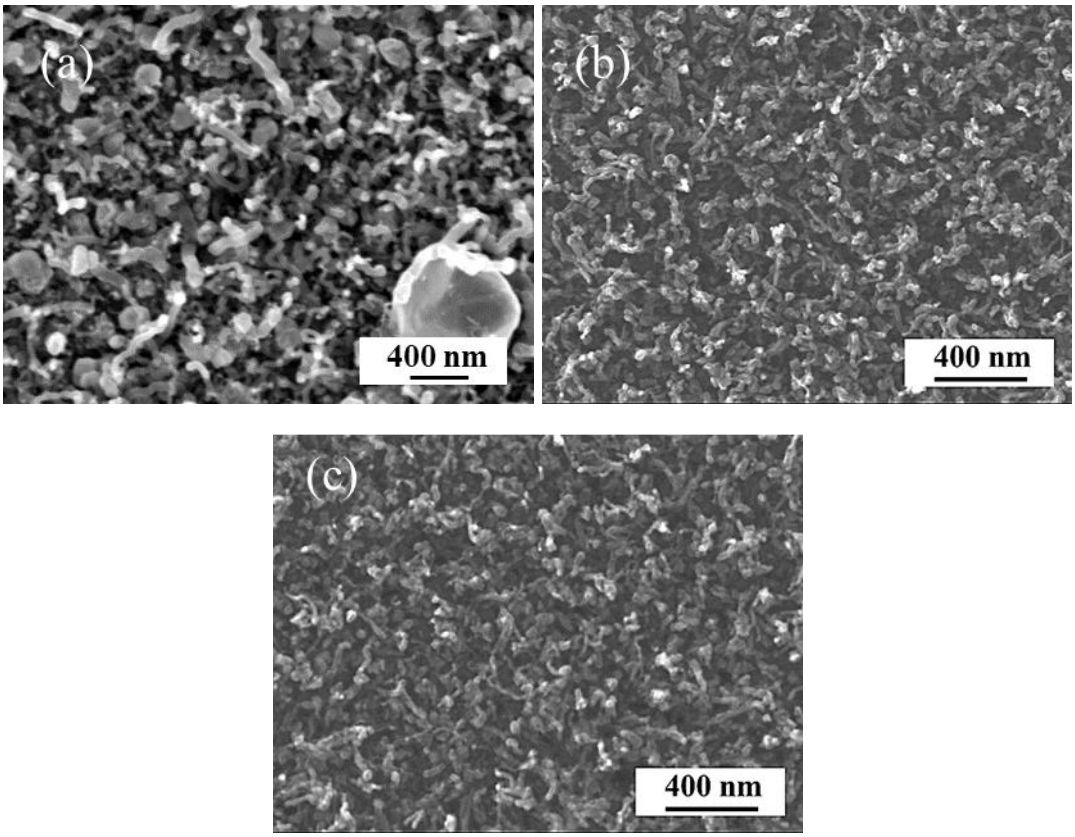

Figure 4. 19 SEM images of the surface morphologies of VACNT films: (a) Ag-VACNT film; (b) Pristine VACNT film; (c) Nitrogen-doped VACNT film

CNTs were scratched from the VACNT films to prepare the TEM samples, which were used to characterise the microstructure of the as-deposited CNTs. Figure 4. 20 shows the TEM images of the nitrogen-doped CNTs. It can be seen that the CNT has a multiwalled tubule structure with a nanoparticle embedded at the tip of the CNT. The diameter of the CNT is about 22nm, and the interlayer distance between the two walls is about 0.34 nm which is consistent with that of the graphitic layers. The TEM microstructures of the nitrogen-doped and the pristine CNTs are very similar. This is because the nitrogen plasma may cause some etching to the surface of the CNTs, but this cannot be distinguished from the TEM images.

However, there are two types of carbon wires grown from the Ag-SS catalyst film. In addition to the MWCNTs grown from the SS catalysts as mentioned before, another type of solid thick carbon fibre was also formed during the growth process as shown in Figure 4. 20 (b). The diameter of these solid carbon fibres is close to 100 nm which is much thicker than the carbon nanotubes. This may be due to the interference between the SS catalyst and the noble Ag nanoparticles.

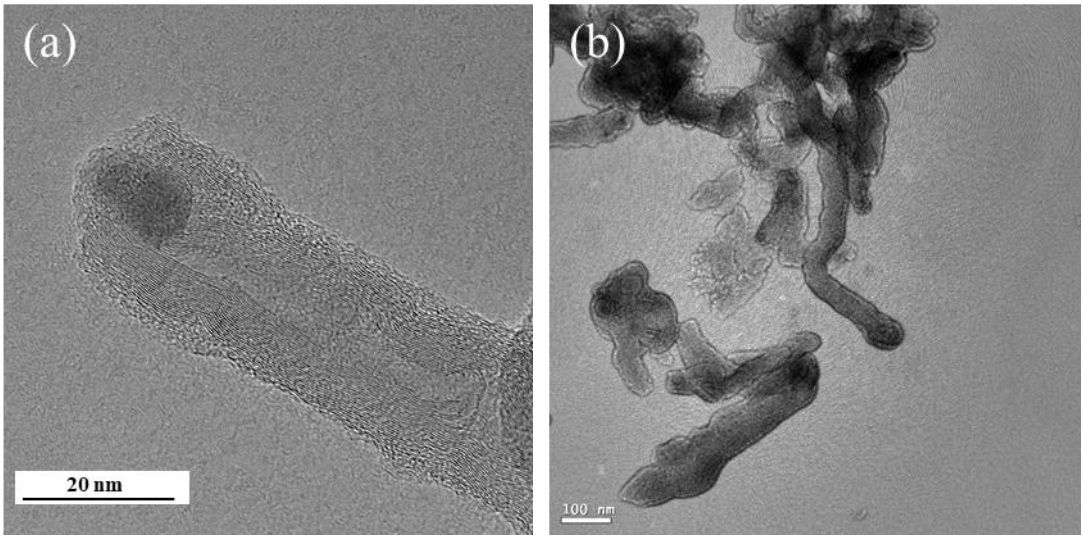

Figure 4. 20 (a) High-resolution TEM image of a nitrogen-doped CNT and (b) TEM image of the CNTS grow from Ag-SS catalyst films

4.4.2 Raman spectra of the VACNT films

Raman spectroscopy was utilised to investigate the structures of the deposited CNT films. Typical Raman D, G, 2D, and D+G peaks were detected as shown in Figure 4. 21. The position and intensity of these peaks reflect the features of the deposited CNTs. The D peak originates from the defects and disorder bonds within the CNTs, which is located around 1355 cm^{-1}. The G peaks of these three VACNT films are located around 1596 cm^{-1}, which is generated from the vibrations of the graphitic carbon atoms.

Besides, D+G and 2D peaks were also detected from all three VACNT films located around 2695 cm^{-1} and 2960 cm^{-1}, which are correlated to the stacked carbon layers and their intensities are in direct proportion to the walls of the nanotubes. The multi-walled structure of the CNTs prohibits the breathing mode Raman spectra belongs to single wall CNT at low frequency areas.

The intensity ratio (I_D/I_G) of the D peak to the G peak can be used to evaluate these CNTs. The intensity ratio of the nitrogen doped VACNT film is 1.01, which is higher than that of the VACNT and the Ag-VACNT which are 0.85 and 0.84, respectively. This could be attributed to the etching effect of the nitrogen plasma, which affected the carbon bonds on the CNTs and increased the content of sp^3 bonds.

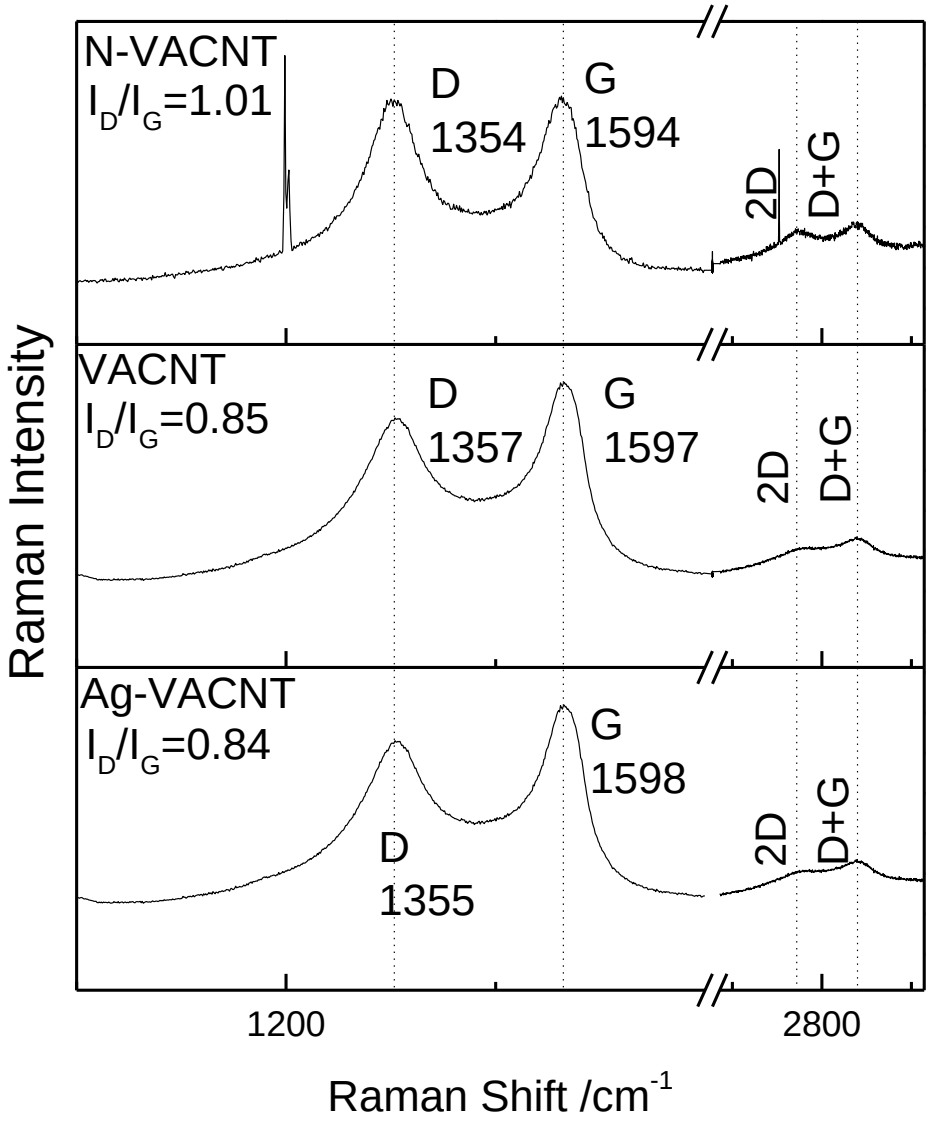

Figure 4. 21 Raman spectra of as-deposited VACNT films, and the I_D/I_G ratios are shown in the images

4.4.3 Wettability of the VACNT films

The wettability of VACNT surfaces may have an influence on their antibacterial effect because it can affect the dispersion of the bacteria aqueous and the spreading and attachment of bacteria. Wettability is commonly influenced by the chemical status and surface morphologies of the samples. Hence the wettability of the VACNTs produced from the research has been studied and Figure 4. 22 shows the contact angles of the VACNT films and the Si substrate.

The VACNT film exhibits a superhydrophobic wettability and its contact angle is around 160°. This is mainly due to the vertically aligned nanostructures of the CNTs which can prohibit or retard the wetting process. The nitrogen plasma etching process can affect the surface chemical status of the CNTs [156, 157]. These active sites can significantly change the wettability of the CNTs, and it is of great interest to find that after the nitrogen plasma treatment the wettability of the VACNT film was converted from superhydrophobic to superhydrophilic with a contact angle around 15°. The Ag-VACNT film showed a contact angle about 110°, probably because the VACNT film is not densely packed.

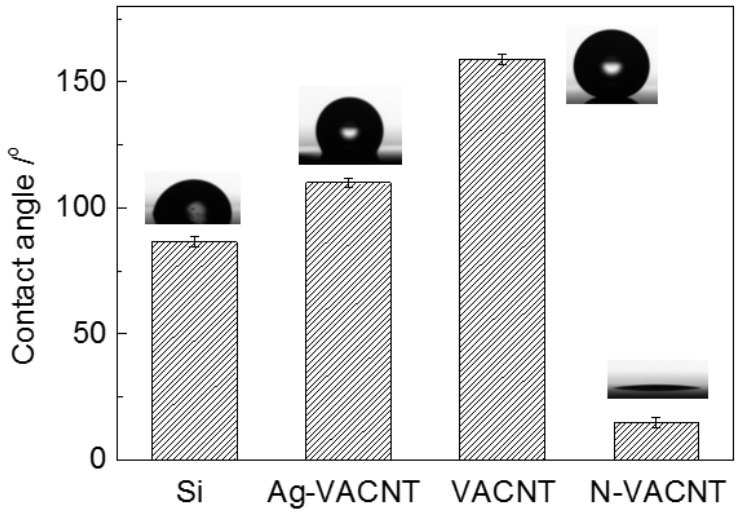

Figure 4. 22 Wettability of the Si substrate and three types of VACNT films

4.4.4 Antibacterial performances of the VACNT films

The spread plate method was used to investigate the antibacterial effects of the VACNT films to Gram-negative bacteria *E. coli* and Gram-positive bacteria *S. epidermidis*. Detailed experimental procedures have been described in the experimental section. After 5h contact between *E. coli* and the CNT surfaces, the colony forming units (CFU) of the alive *E. coli* were counted to evaluate their antibacterial performance. The optical images of the CFUs are shown in Figure 4. 23.

Typically, a noble surface can be used as control sample. As the VACNT film were grown on Si. Thus, slides of Si were applied as control sample in this case. It can be seen that the control surface generates more CFUs than that of the VACNT surfaces. This indicates that the control Si surface has a low inactivation rate of *E. coli* while all the VACNT related surfaces have led to a low surviving of *E. coli,* and their antibacterial efficacies are presented in Figure 4. 24. Over 99% of *E. coli* was killed after 5h contact, indicating that all these three VACNT films possess a high antibacterial efficacy.

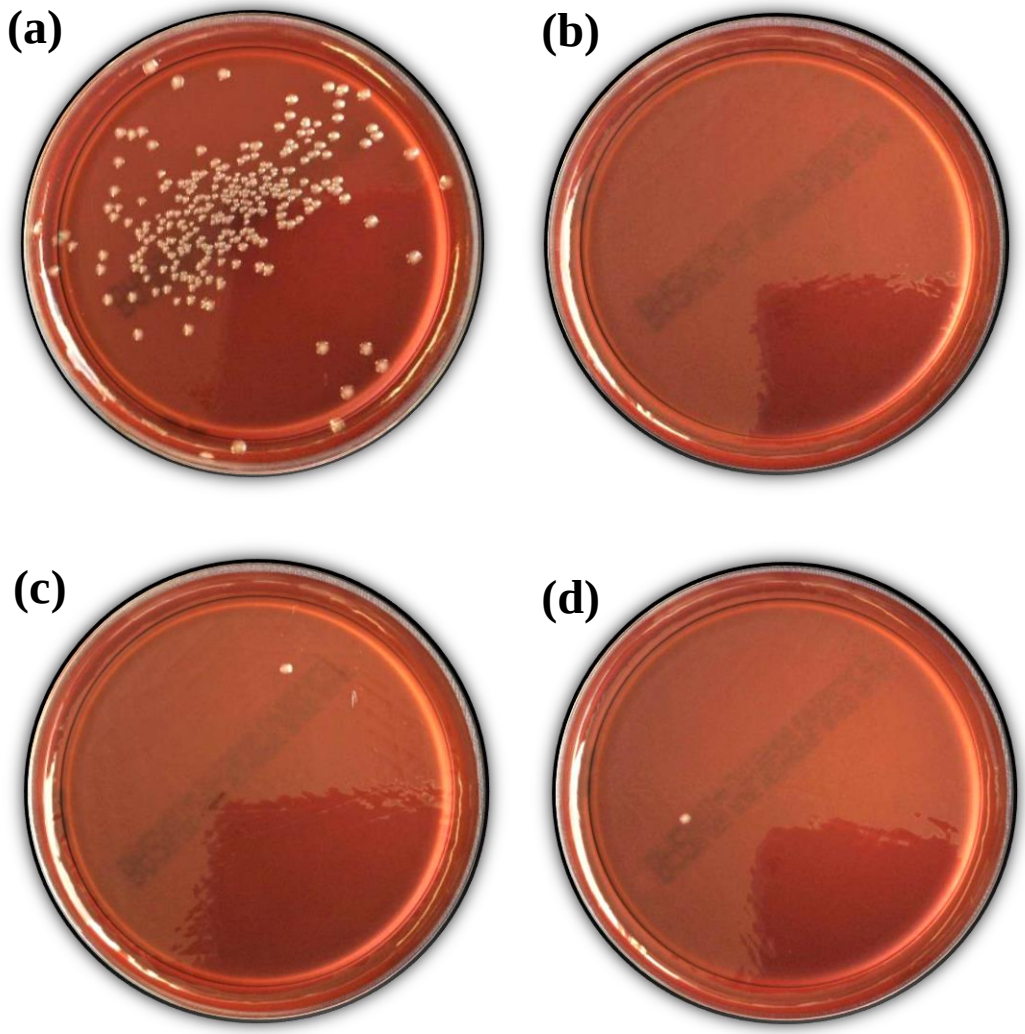

Figure 4. 23 Colony forming units (CFU) on the tryptone soya agar plates after the antibacterial tests with *E. coli*. (a) Si; (b) Ag-VACNT; (c) VACNT; (d) N-VACNT

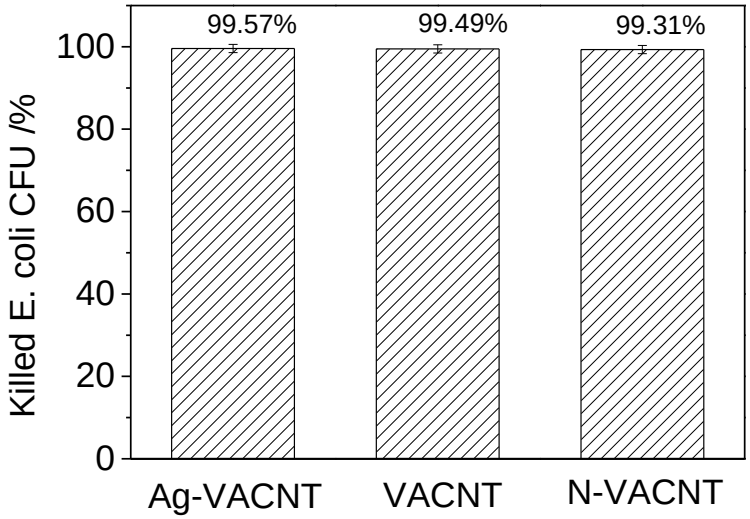

Figure 4. 24 Antibacterial efficiencies of the as-deposited VACNT films to *E. coli* after 5 h contact

It is well known that Ag is a widely used antibacterial agent. However, almost no difference in antibacterial efficacy was found between these three VACNT films. Both the pristine VACNT and the N-VACNT surfaces exhibit similar antibacterial performance comparable to that of the Ag impregnated VACNT surface after 5h contact.

Figure 4. 25 shows the colony forming units (CFU) of the alive Gram-positive S. epidermidis after 5h contact tests. Unlike the *E. coli tests*, there are still many colonies on the tryptone soya agar plates, indicating that some of the S. epidermidis were survived after 5h contact with these VACNT films. The kill rates of Ag-VACNT, pristine VACNT, and N-VACNT films are 90.7%, 88.2% and 88.8% (see Figure 4. 26), respectively. This indicates that the killing rate of these VACNT films to Gram-positive bacteria is relatively lower than to the Gram-negative bacteria after 5h contact.

In this case, the Ag impregnated VACNT film presents better antibacterial performance than that of the other two VACNT films. This is in line with the widely reported

antibacterial effect of Ag. However, it is also noted that although the wettability of the nitrogen-doped VACNT film is totally different from that of the pristine VACNT film, these two VACNTs showed almost the same antibacterial efficacy to the S. epidermidis. The similar kill rate suggests that the wettability of these CNTs does not play a main role in the antibacterial process.

The one-way analysis of variance (ANOVA) is applied to determine if there is any statistically significant difference of antibacterial effect to S. epidermidis between the three VACNT films. The multiple comparison results are shown in Table 4. 5. The results have verified that there are significant differences between the Si substrate and the three VACNT films. However, the differences between the Ag-VACNT and the other two types of VACNT films are not significant at the 0.05 level. However, more tests should be carried out to ensure the reliability of the statistical significance.

Clearly, the VACNT film exhibits high bactericidal effect to both Gram-negative and Gram-positive bacteria and the possible antibacterial mechanisms will be discussed in the next chapter.

Table 4. 5 Multiple comparisons of the S. epidermidis CFUs remained in the soya agar plates after the antibacterial tests

Groups		Mean Difference (I-J)	Std. Error	Sig.	95% Confidence interval	
					Lower Bound	Upper Bound
0	1	868.000*	117.162	.001	458.79	1277.21
	2	874.000*	117.162	.001	464.79	1283.21
	3	893.000*	117.162	.001	483.79	1302.21
1	0	-868.000*	117.162	.001	-1277.21	-458.79
	2	6.000	117.162	1.000	-403.21	415.21
	3	25.000	117.162	.997	-384.21	434.21
2	0	-874.000*	117.162	.001	-1283.21	-464.79
	1	-6.000	117.162	1.000	-415.21	403.21
	3	19.000	117.162	.999	-390.21	428.21
3	0	-893.000*	117.162	.001	-1302.21	-483.79
	1	-25.000	117.162	.997	-434.21	384.21
	2	-19.000	117.162	.999	-428.21	390.21

*. The mean difference is significant at the 0.05 level. Group 0 is Si substrate; Group 1 is VACNT film; Group 2 is N-VACNT film; Group 3 is Ag-VACNT film.

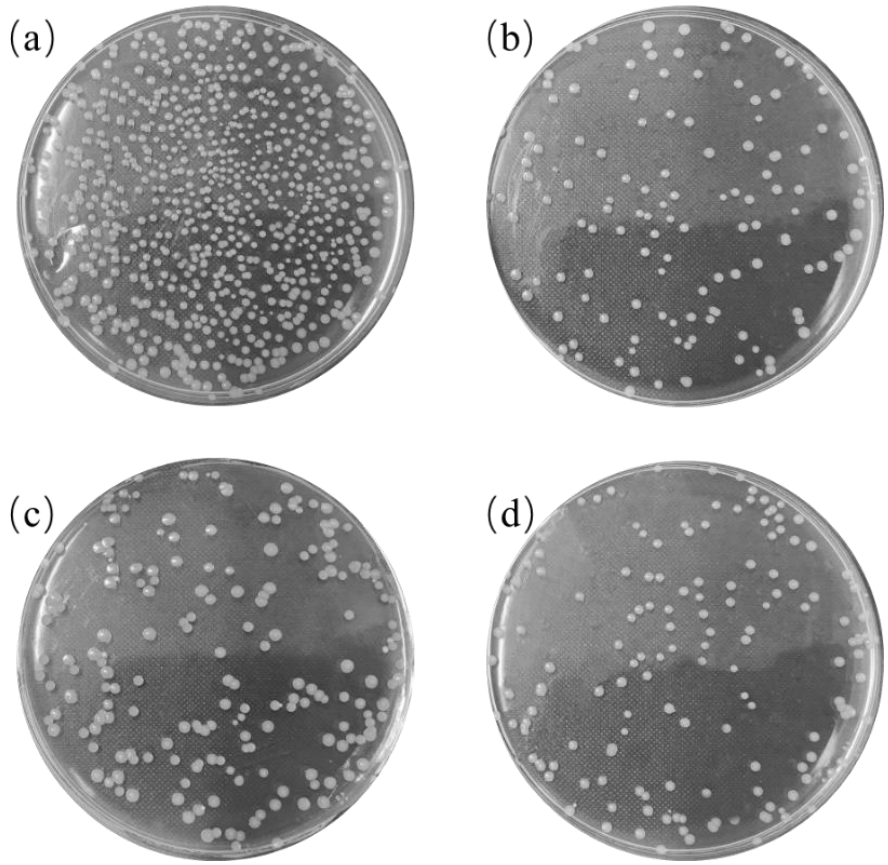

Figure 4. 25 Colony forming units (CFU) on the tryptone soya agar plates after the antibacterial tests with S. epidermidis. (a) Si; (b) Ag-VACNT; (c) VACNT; (d) N-VACNT

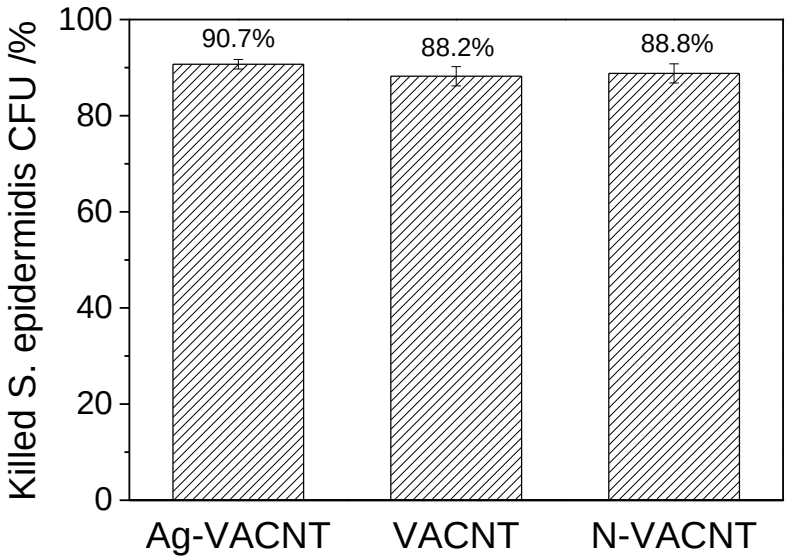

Figure 4. 26 Antibacterial efficiencies of the as-deposited VACNT films to S. epidermidis after 5 h contact

4.5 Synthesis of DLC films and CNT reinforced composite coatings

4.5.1 Deposition of diamond-like carbon films (DLC)

Diamond-like carbon films have been deposited by the rf PECVD (P500+) and the deposition process is described in the experimental session. It is known that DLC film has a high hardness and a high level of internal stress. The internal stress, an important factor in determining the stability and the life of the coating, is typically generated due to the high collision energy of the ions during the deposition process. To study the effect of the energy of the ions on the microstructure and performance of DLC films, a series of experiments have been carried out at different bias. The experimental details are described in Chapter 3 and the parameters are summarised in Table 4. 6.

Table 4. 6 Parameters for the deposition of DLC coatings by PECVD

Code	Bias	Temperature	Time	CH_4	Ar	Substrate
D1	50 V	170℃	1 h	1.5%	98.5%	Si
D2	100 V	170℃	1 h	1.5%	98.5%	Si
D3	150 V	170℃	1 h	1.5%	98.5%	Si
D4	200 V	170℃	1 h	1.5%	98.5%	Si
D5	250V	170℃	1 h	1.5%	98.5%	Si
D6	300V	170℃	1 h	1.5%	98.5%	Si
D7	350V	170℃	1 h	1.5%	98.5%	Si

Thickness measurement

As mentioned briefly in Chapter 3, the thickness of the DLC coating is measured by partially covering the substrate with a small piece of Si wafer as cover slip. A step is formed after deposition by removing the cover slip and the thickness of the DLC coatings can be measured using a laser confocal microscopy. Figure 4. 27 (a) shows a 3D optical image of the coating step.

Figure 4. 27 (b) summarises the average thicknesses of the DLC coatings deposited under different biases. The thicknesses of the DLC coating increased from 0.95 µm to 1.8 µm with increasing the plasma bias from 50V to 350V. The results indicate that the higher bias leads to a thicker film because the ions can achieve more kinetic energy during the deposition process.

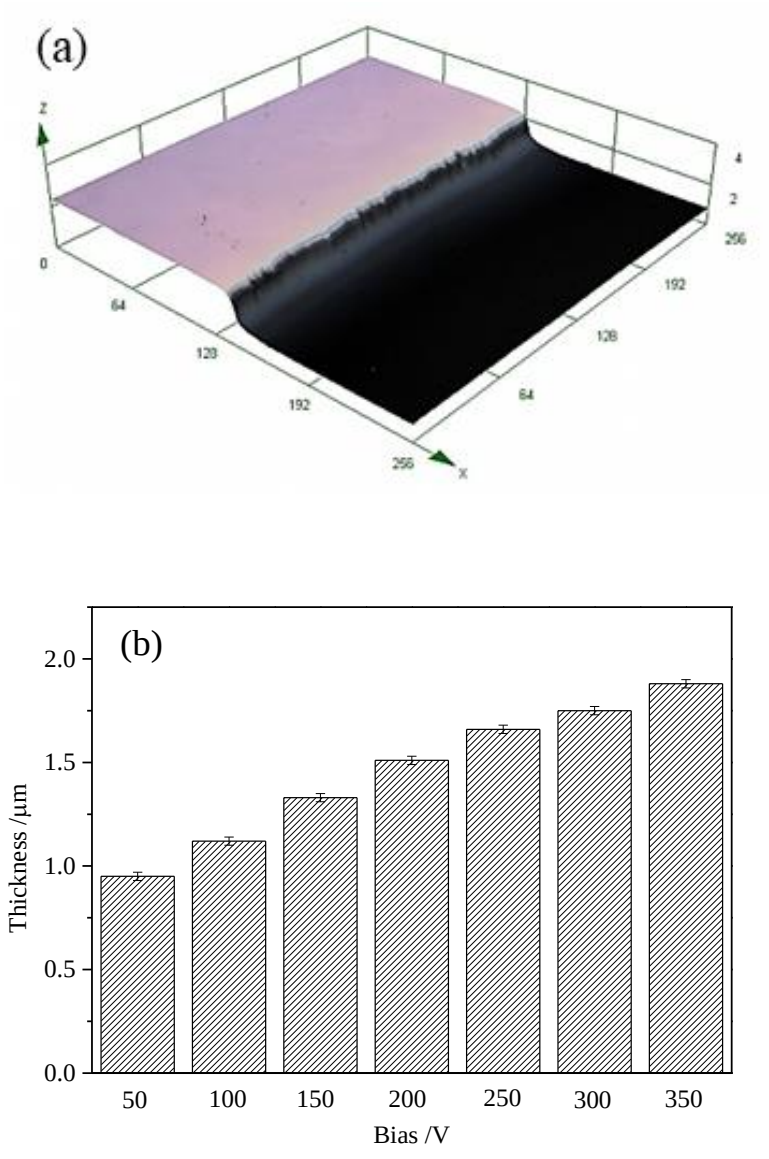

Figure 4. 27 (a) Optical image of the coating step used for measurement of the coating thickness; (b) Thicknesses of the DLC coatings deposited as a function of voltages

XPS study of chemical states of DLC coatings

The chemical states of the DLC coatings were studied by XPS. All the sample surfaces were cleaned by acetone before the measurements, and then the C 1s spectrum was acquired from each coating. Figure 4. 28 shows the XPS results of the DLC coatings deposited using different biases. Figure 4. 28 (a) shows the combined C 1s spectra of the DLC coatings because the chemical states of the DLC coatings are related to the position of their C 1s peaks. It is found that all the peaks are between 283 eV and 286 eV, while some peak shifts can be observed.

The relationship between the C 1s peak positions and the deposition bias is complex. The C 1s spectrum is influenced by several different bonding states and the C 1s peak is decomposed into four component peaks, including the peaks for sp^3 bonded carbon at around 285.3 eV, sp^2 bonded carbon at around 284.4 eV, sp^2 carbon satellite at around 285.7 eV, and the C=O bond at around 288.3 eV. To have a better understanding of the DLC coating, the C 1s spectrum for some specific coating is decomposed and the results are shown in Figure 4. 28 (b)-(h). The C 1s peak is mainly formed with the sp^3 bonded carbon peak and the sp^2 bonded carbon peak, and the intensity of these peaks are different for the DLC coatings deposited at different biases. In addition, a small C=O peak can be found in all of the spectra which may be due to the reactions between the carbon coating and the oxygen in the atmosphere.

Nanohardness and modulus of the DLC coatings

Nano indentation tests were applied to evaluate the uniformity of the mechanical properties of the as-deposited DLC coatings. The continuous stiffness measurement (CSM) mode is employed to obtain nanohardness and elastic modulus continuously during the nanoindentation test from the surface. Four or more indentations were

carried out on each coating and distance between two neighbour indentation points is 500 µm, while the maximum indentation depth is 0.9 µm.

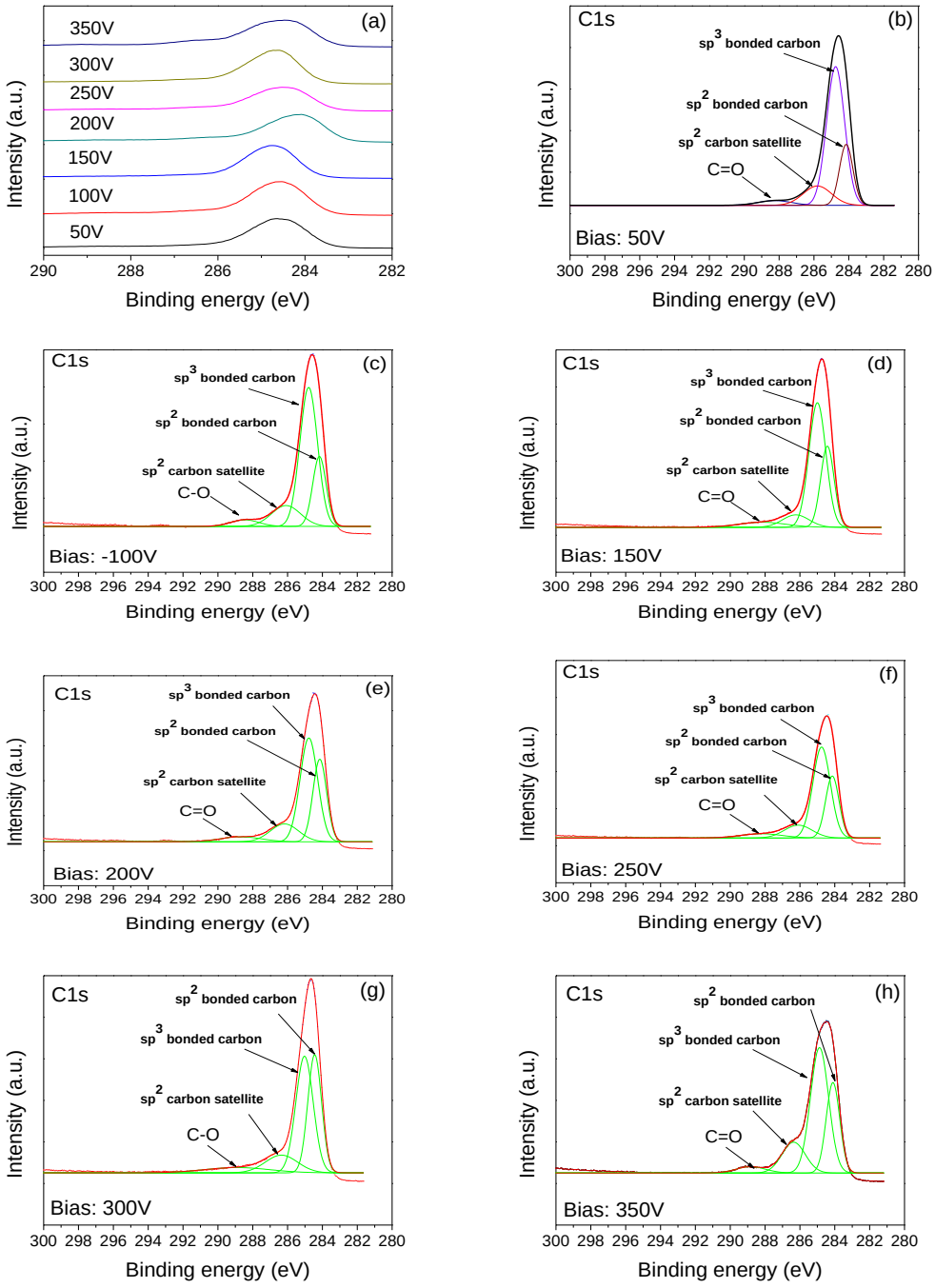

Figure 4. 28 XPS results of the DLC coatings deposited under various bias, (a) combined C 1s spectra of the DLC coatings; (b)-(h) C 1s spectra of the DLC coating deposited under different bias and fitted with four peaks

Figure 4. 29 shows the depth-dependent hardness of the DLC coatings deposited under different biases. It can be seen that the measured hardness varies with the penetration depth during the continuous stiffness measurements. The hardness rapidly increased to a peak value before gradually decreasing to a plateau. All the hardness curves exhibit similar trends. The half-width area of the hardness peak is used to calculate the average hardness of each indentation. The hardness curves measured from different positions of the DLC coatings deposited at specific biases. The consistency of these hardness curves was used to evaluate the uniformity of the DLC coatings.

Figure 4. 30 summarises the average hardness and elastic modulus of the DLC coatings. The coatings exhibit a high hardness and elastic modulus around 20 GPa and 200 GPa, respectively. The reason for the abnormal hardness and elastic modulus of the coating deposited at 300V is not clear and most probably some unknown technical problems occurred during the deposition process. The hardness of the DLC coatings increased from ~19 GPa to ~23 GPa when the bias increased from 50 V to 150 V, then there was no improvement in hardness when the bias increased further. The average hardness of the DLC coatings is around 23 GPa, indicating that the deposition bias has little impact on the hardness of the DLC coating.

Hardness variances of the DLC coatings reflect the change in the uniformity of their mechanical properties. As the deposition bias rises, the elastic modulus of the DLC coatings increased first and then decreased. The DLC coatings deposited at 150V and 200 V showed smaller variances of hardness and elastic modulus compared to the DLC coatings deposited at other bias voltages. Thus, the optimal deposition bias should be between 150V and 200 V.

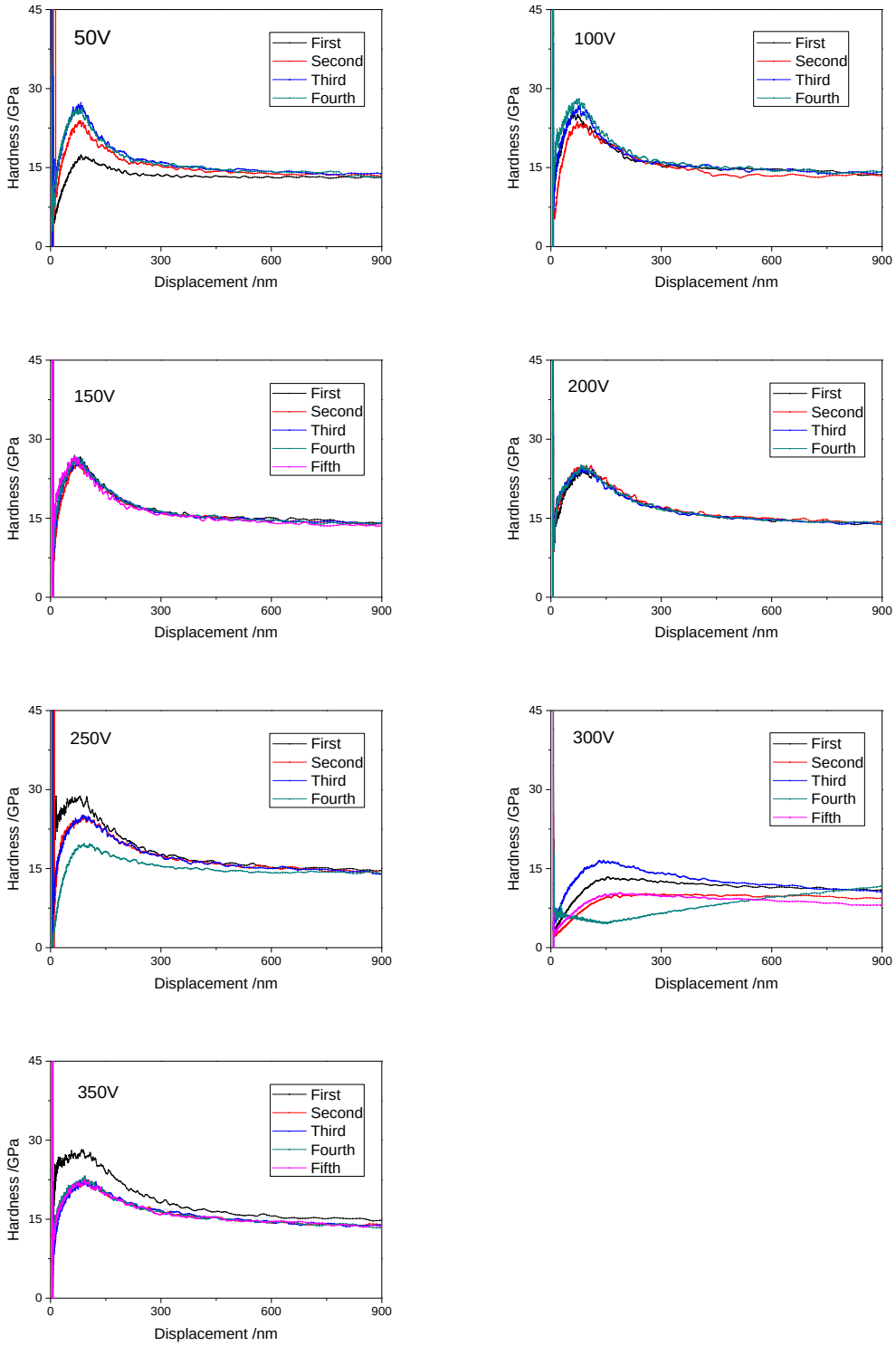

Figure 4. 29 Nanohardness of the DLC coatings deposited using different bias voltage, measured by continuous stiffness measurement method. Four or five indentations were carried out at different positions to investigate the uniformity of the DLC coatings

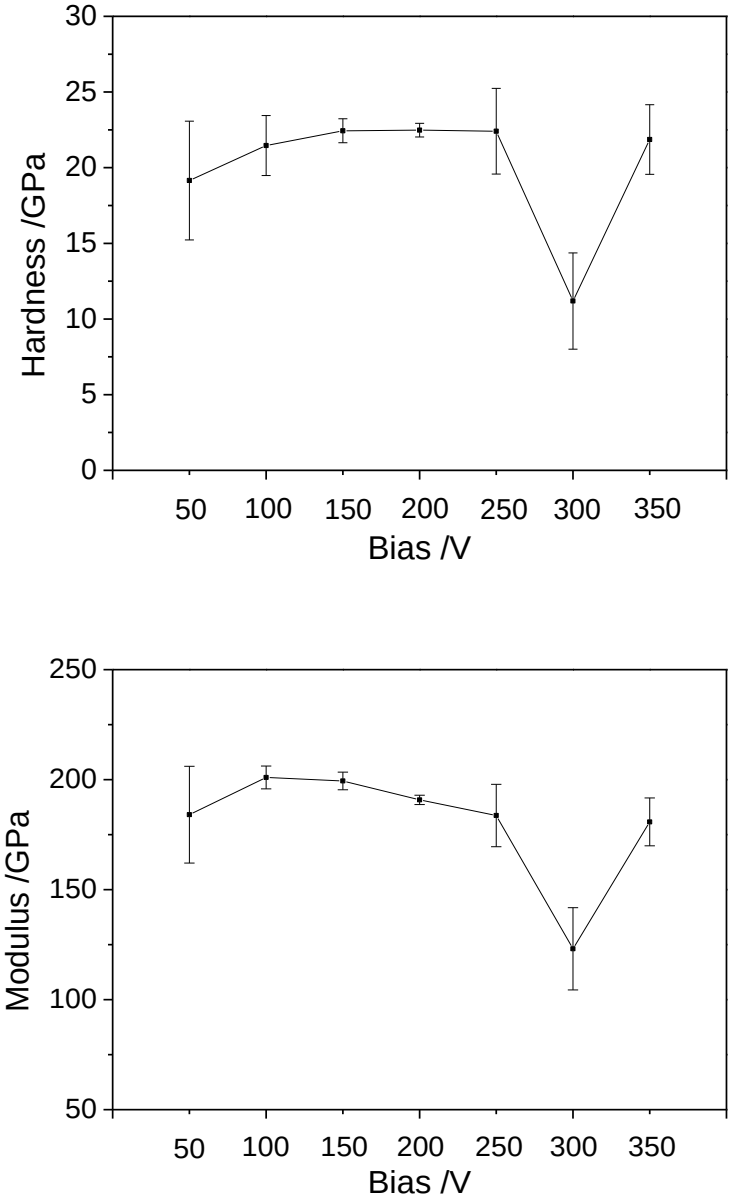

Figure 4. 30 Average hardness and elastic modulus of the DLC coatings deposited under different bias

Residual stress measurement

The Stoney equation is widely used to calculate the residual stress of a coating by measuring the curvature of the substrate [158, 159]. In this study, DLC coated Si sheet samples were cut into 5 mm in width and 20mm in length and a 12.5 mm length profile was measured at the centre of the surface area on each sample. Three measurements were carried out on each sample. The Stoney equation can be written as follow:

$$\sigma = \frac{E_s t_s^2}{6t_c(1-\nu_s)R} \quad (5)$$

where σ is the residual stress within the coating, E_s the Young's modulus of substrate, ν_s the Poisson ratio of substrate, t_s the thickness of substrate, t_c is the thickness of coating, and R is the radius of curvature. In this study, E_s = 140 MPa, ν_s = 0.25, t_s = 620 μm.

The measured profiles were fitted to quadratic curves ($y = A + Bx + Cx^2$) for the calculation of the radius of curvatures by the following equation:

$$R = \frac{|y''|}{(1+y'^2)^{3/2}} \approx |y''| = 2C \quad (6)$$

Considering the hardness results of these samples, the residual stresses of the DLC coatings deposited at 150V, 200V, and 250V were measured and calculated (Figure 4. 31). All the residual stresses measured from the DLC coatings are compressive internal stresses, which increased with increase of the deposition bias. The coating deposited at 150V showed a very low residual stress with an average value of 330 MPa, while the internal stress of the DLC coating deposited at 200V and 250V are around 605 MPa and 1022 MPa, respectively. This is mainly because high deposition bias can lead to high accelerating energy for the ions during the deposition process, thus leading to high impact and hence high internal stress. High compressive stress within a DLC coating may cause premature failure under external compressive loading.

Tribological tests

Tribological tests were carried out using a 2 N load, at 5 Hz and for 30 min, with a SiC ball (Φ 3.96 mm) as the counterpart. Beside the DLC coating, the Si wafer substrate was also tested for comparison. Figure 4. 32 shows the friction coefficients of the DLC coating and the Si substrate. The DLC coating has a friction coefficient of around 0.28,

which is much smaller than that (0.62) of the Si substrate. Besides, the friction coefficient of the DLC coating is relatively stable, indicating that no cracks or delamination of the coating occurred during the tribological test.

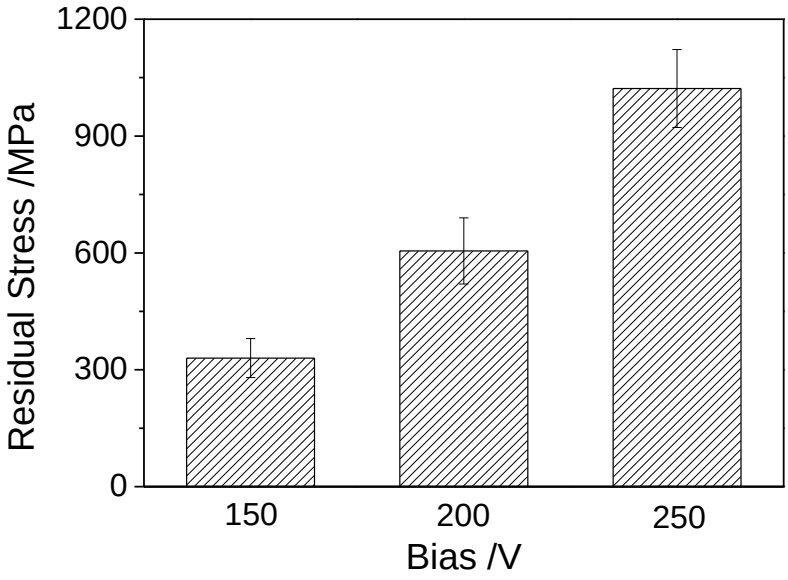

Figure 4. 31 Residual stress of the DLC coating deposited at different bias

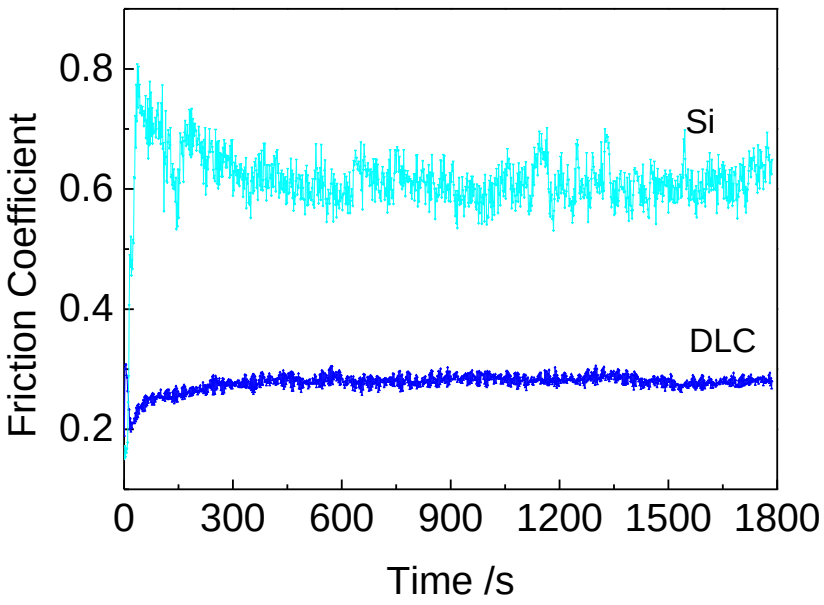

Figure 4. 32 Friction coefficients of Si and DLC coating

Wear tracks formed on the Si and the DLC coating are shown in Figure 4.33. Deep scratch grooves can be seen in the Si surface while the DLC coating shows a shallow and smooth wear track. Figure 4. 33 (c)&(d) present the wear marks on the SiC balls after sliding against the Si substrate and the DLC coating, respectively.

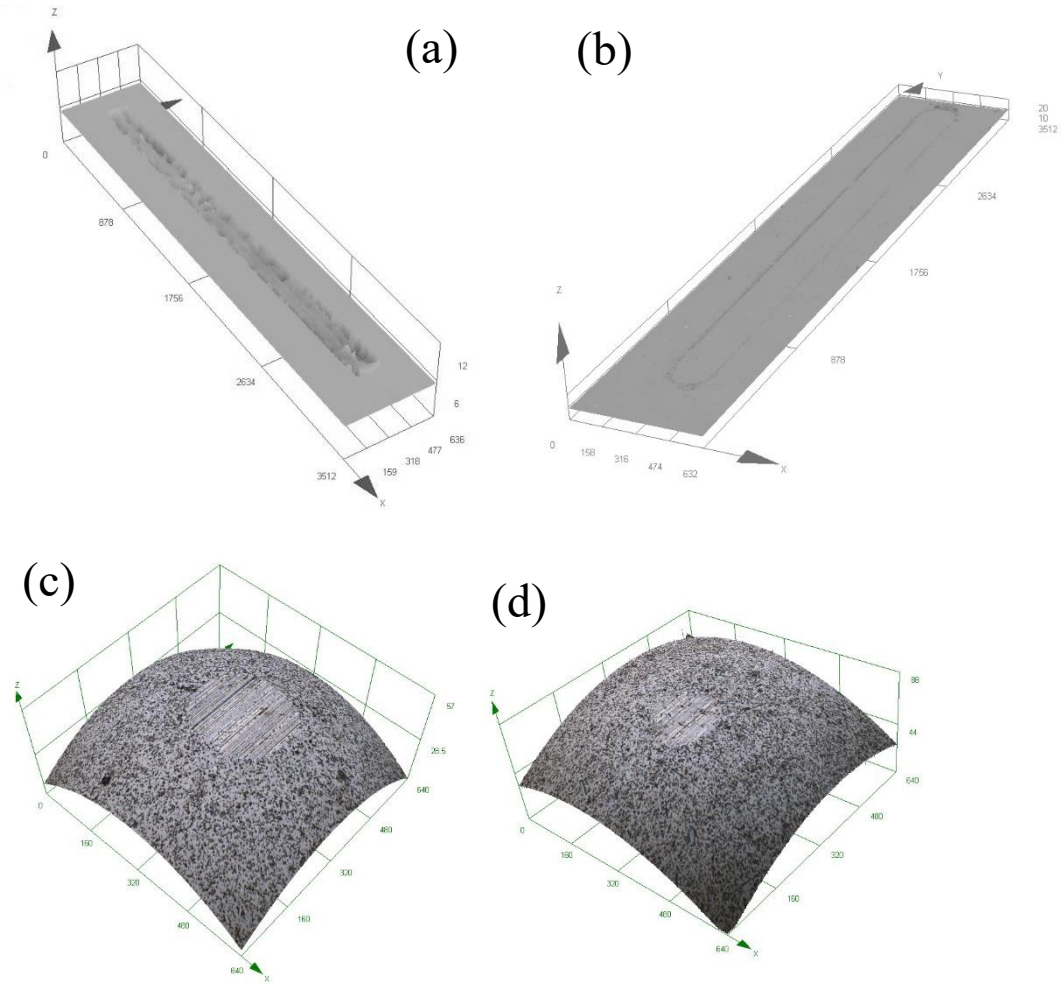

Figure 4. 33 Wear tracks on (a) Si and (b) DLC coating, and the corresponding wear marks on the Si_3N_4 balls: (c) against Si and (d) against DLC coating

Wear volumes were measured by a laser confocal microscope to calculate the wear rate of the Si substrate and the DLC coating. As shown in Figure 4. 34, the wear rate of the Si substrate (about 5.4×10^{-6} mm^3/Nm) is about 54 times higher than that of the DLC coating (1.02×10^{-7} mm^3/Nm). This is in line with the coarser wear groove and larger

wear mark formed on the SiC ball after sliding against the Si substrate as against the DLC coating.

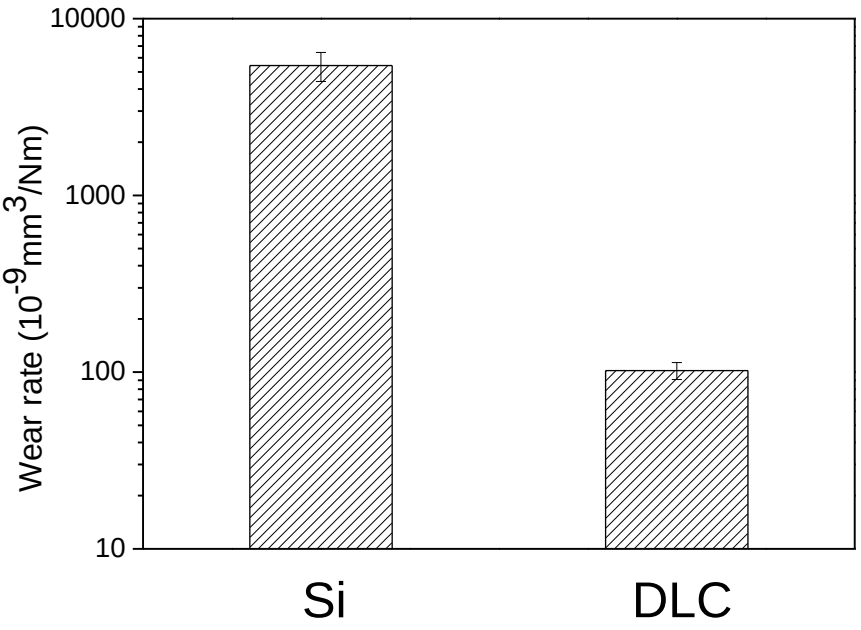

Figure 4. 34 Wear rate of the Si substrate and the DLC coating

Delamination of stressed thin coatings by buckling or cracking is common to some metallic and ceramic coatings. In this study, sinusoidal stress relief patterns were also observed in the DLC coatings deposited by PECVD. As reported above, the DLC coating has shown an excellent friction reduction effect and no cracks are observed in the coating during the wear tests. However, due to the high internal stress between the DLC coating and substrate, some stress relief patterns were generated on the DLC coating after several days' exposure to atmospheric air.

Figure 4. 35 shows a stress relief pattern on the DLC coating deposited at 150 V. Wrinkles are spread over the selected area which are buckled into the shape of 'telephone cord'. It was reported that the stress relief patterns initiate at the edge of the film, or at some interior defects, or at the exterior defect sites. Figure 4. 36 exhibits the

initiation of the stress relief patterns caused by the exterior defect sites. Some contamination particles were generated during the deposition process which caused defects and stress concentration. Figure 4. 36 (b) shows the progress of the sinusoidal stress relief patterns. Buckling patterns were generated at the defect sites and then extended outward. The width of the buckling tip is small initially and subsequently increased with the release of the internal stress.

These sinusoidal buckles were formed to relief compressive strain energy within the system or due to the thermal expansion mismatch between the DLC coating and the Si substrate. Several studies have been carried out to explain how and why the telephone cord buckles are generated and models are established to describe the relationship between the morphologies of the buckles and the internal stress of the coatings [160-162]. However, the generation mechanism of the telephone cord stress relief pattern is still not fully understood.

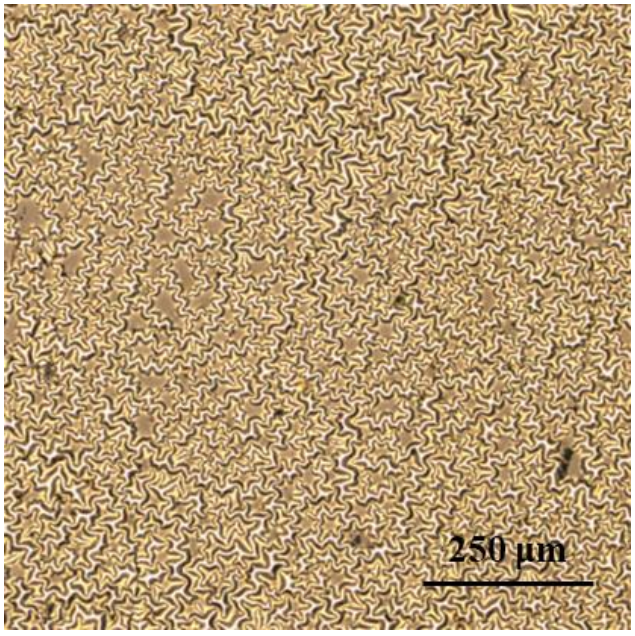

Figure 4. 35 Buckles and wrinkles generated in the DLC coating deposited at 150V on a Si substrate

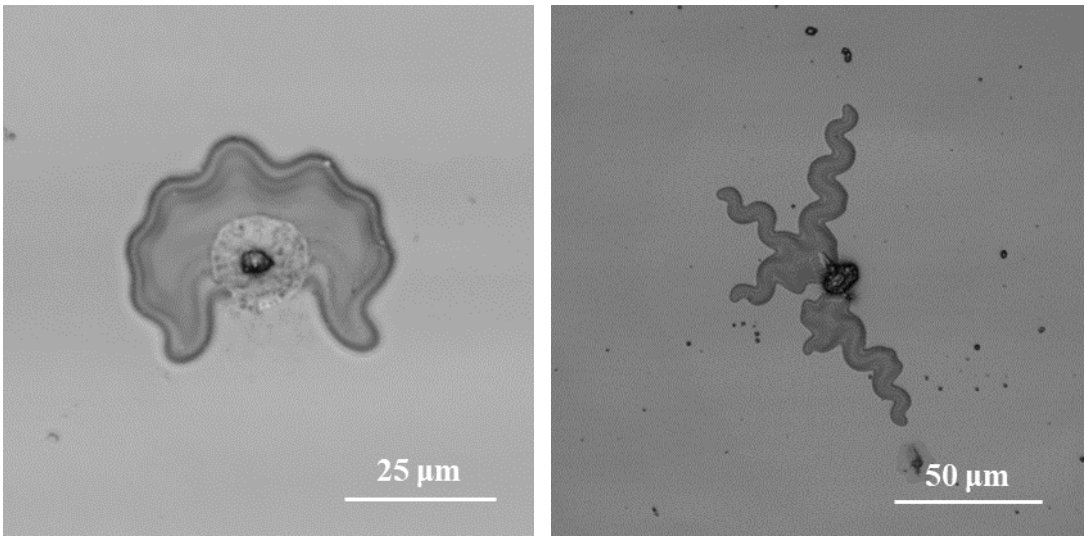

Figure 4. 36 Initiations of the wrinkles in the DLC coating deposited at 150V. The stress relief patterns were generated from the defect sites

The continuous growth of the buckles will lead to the delamination of the DLC coating. Figure 4. 37 shows the surface morphologies of the DLC coating after the stress relief delamination. The areas in pink colour are the DLC coating while the black areas are the Si substrate. Some parts of the DLC coating are delaminated from the Si substrate and belt skeletons of the stress relief pattern remain on the substrate.

Figure 4. 37 (b) presents a 3D image of the belt skeleton and some coating debris are left on the surface. It can be seen that the coatings between the belts are fully delaminated from the substrate while the zigzag belts generated from the sinusoidal stress relief pattern are still there. The colour variation is related to the thickness of the belts, indicating the lamellar cracking in the stress relief pattern area.

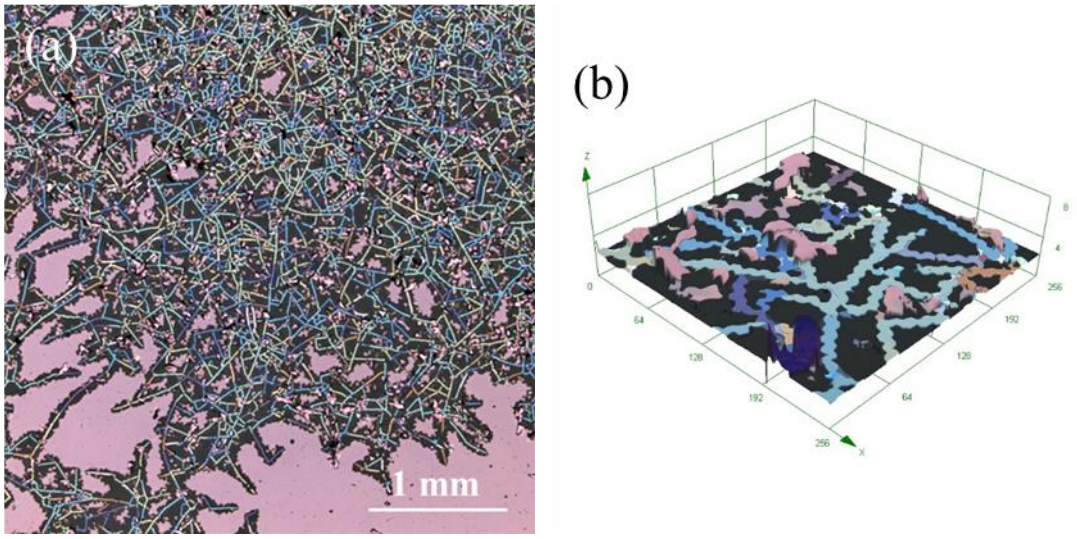

Figure 4. 37 Optical images of the morphologies of the DLC coating after the stress relief delamination. (a) overview of the DLC coating after delamination; (b) 3D image of the belt skeleton of the DLC coating

4.5.2 Challenge with the CNT reinforced composite coating

As discussed in Chapter 2, carbon nanotubes reinforced bulk composite materials have been developed for addressing the limitations of conventional monolithic structures to achieve an excellent combination of strength, stiffness, toughness, thermal conductivity, electrical conductivity, and some other novel functional properties. In this study, research work has been carried out to explore the feasibility of producing CNT reinforced composite coatings.

As mentioned in Section 2.2.5, some studies have already been conducted on the fabrication of the CNT reinforced composite coatings, and the main problem is that it is difficult to achieve a homogeneous dispersion of CNTs within the matrix during the deposition process. In this study, several advanced deposition methods have been employed to synthesise the well dispersed CNT reinforced composite coatings based on the VACNT films.

4.5.2.1 Density control of the VACNT films

The two-step strategy is applied to fabricate the CNTs reinforce composite coatings. and two types of catalyst films (SS, Ag-SS) were deposited on Si with the DC Klöckner Ionon 40 kW furnace, in order to achieve VACNT films with different density. The sputtering processes were similar to that described in Section 4.1.1. The morphologies of the as-deposited catalyst films are shown in Figure 4. 38. SS nanoparticles are relatively uniform and well distributed on the surface with the size of about 20 nm (See Figure 4. 38 (a)). Some large Ag particles were coated on the Ag-SS catalyst film which can be seen in Figure 4. 38 (b), due to the high sputter rate of silver

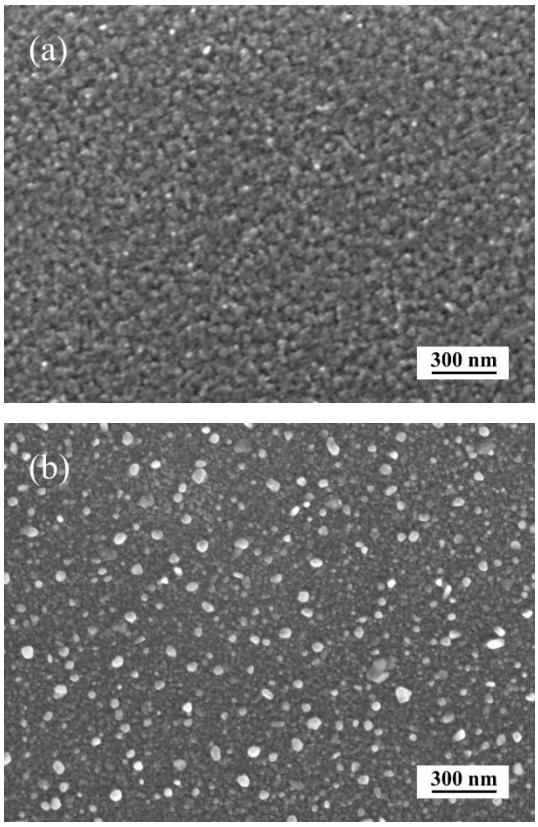

Figure 4. 38 Catalyst films deposited by active screen plasma technique: (a) SS catalyst film; (b) Ag-SS catalyst film

VACNT films were grown based on these catalyst films using the PECVD. The syntheses were carried out at 450℃ for 100 min under power of 30 W, and acetylene

was used as carbon source, diluted by argon and hydrogen, and their corresponding flow rate were 5 sccm, 50 sccm, and 10 sccm. The specific deposition sequences are same as that described in Section 4. 2. Besides, there are also some small silver particles sputtered on the surface which are difficult to be distinguished from the SS particles. Noble silver does not have a catalytic function for the growth of CNTs. Thus, the existence of silver particles could prohibit the growth CNTs and decrease the density of the VACNT films.

The as-grown VACNT films are shown in Figure 4. 39, and the VACNT film grown from SS catalyst film presents a densely packed structure due to the Van der Waals forces between the CNTs. The length and diameter of the CNTs are around 1 μm and 30 nm, respectively. Almost no gaps can be found between the CNTs, which makes it difficult for coating materials to penetrate into the film.

The CNTs synthesised from the Ag-SS catalyst film are shown in Figure 4. 39 (c) and (d). Large silver particles and CNTs can be seen on the surface, and in this case the density of the CNTs is much lower than that of the CNTs grown from the SS catalysts. These CNTs are not as straight as the CNTs grown from the SS catalyst film due to the gaps. Since silver is inert for the growth of CNT, not only the large silver particles, but also the small silver particles which prohibit the growth of CNTs and provide vacancies for the fabrication of the nanocomposite coatings.

It provides a convenient way to decrease the density of CNTs by adding inert elements in the catalyst film, as compared to other potential methods, such as patterning [24] and other post-treatments [163].

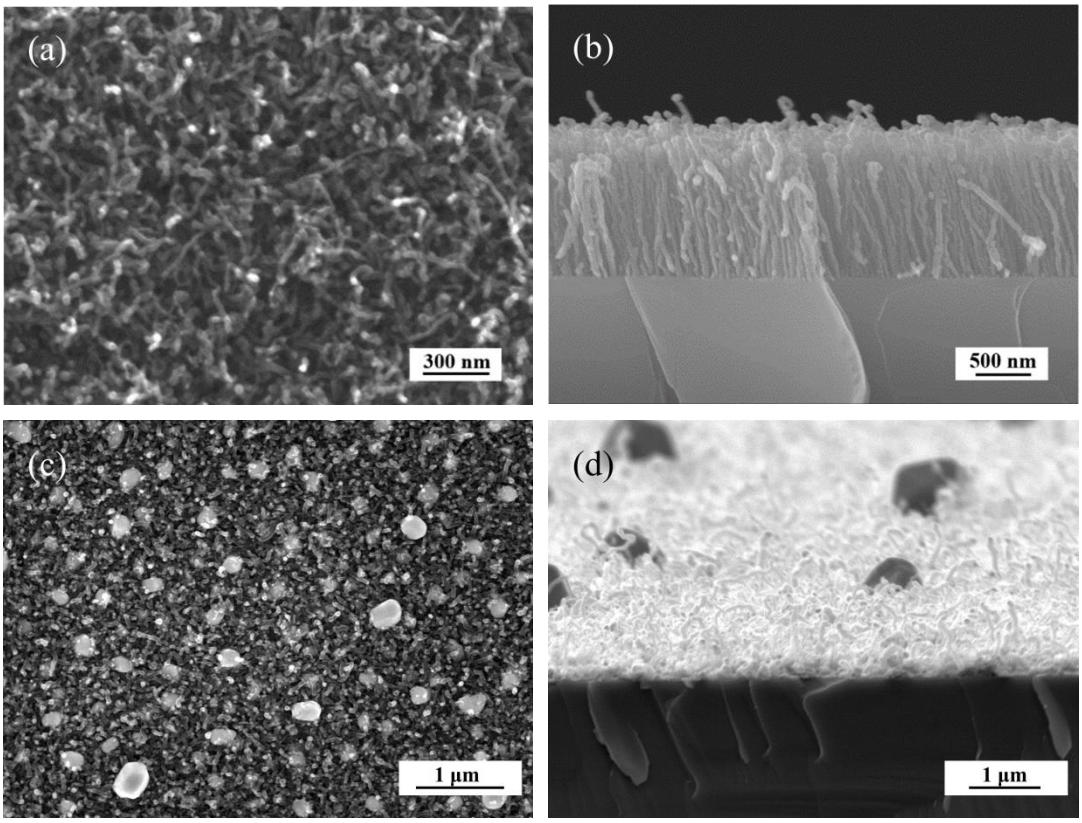

Figure 4. 39 SEM images the CNT films grown from SS catalyst film ((a), (b)) and Ag-SS catalyst film ((c), (d))

4.5.2.2 TEM of the CNTs for the 1D composite coating

TEM images of the as-deposited CNTs are shown in Figure 4. 40. Microstructures of the corresponding CNTs are similar to that as-described in Section 4.3.3 and Section 4.4.1. CNTs grown from the SS catalyst films also present a clear tubular structure, and black dots are embedded at the tip of the CNTs (Figure 4.40 (a)). The diameters of these CNTs are ranged from 10 nm to 50 nm and the average diameter is 23 nm.

On the other hand, both CNTs and carbon nanofibers (CNFs) are grown from the Ag-SS catalyst films. Figure 4. 40 (b) shows the CNTs synthesised from the Ag-SS catalyst film which have a similar structure to that of the CNTs grown from the SS catalyst film. Besides, there is another type of CNF, which has a solid nanostructure rather than a tube nanostructure (Figure 4. 40 (c)). The diameters of the CNFs are around 50 nm

which is thicker than that of the CNTs. A bottom growth mode is supposed to explain the formation of the CNFs in Chapter 5.

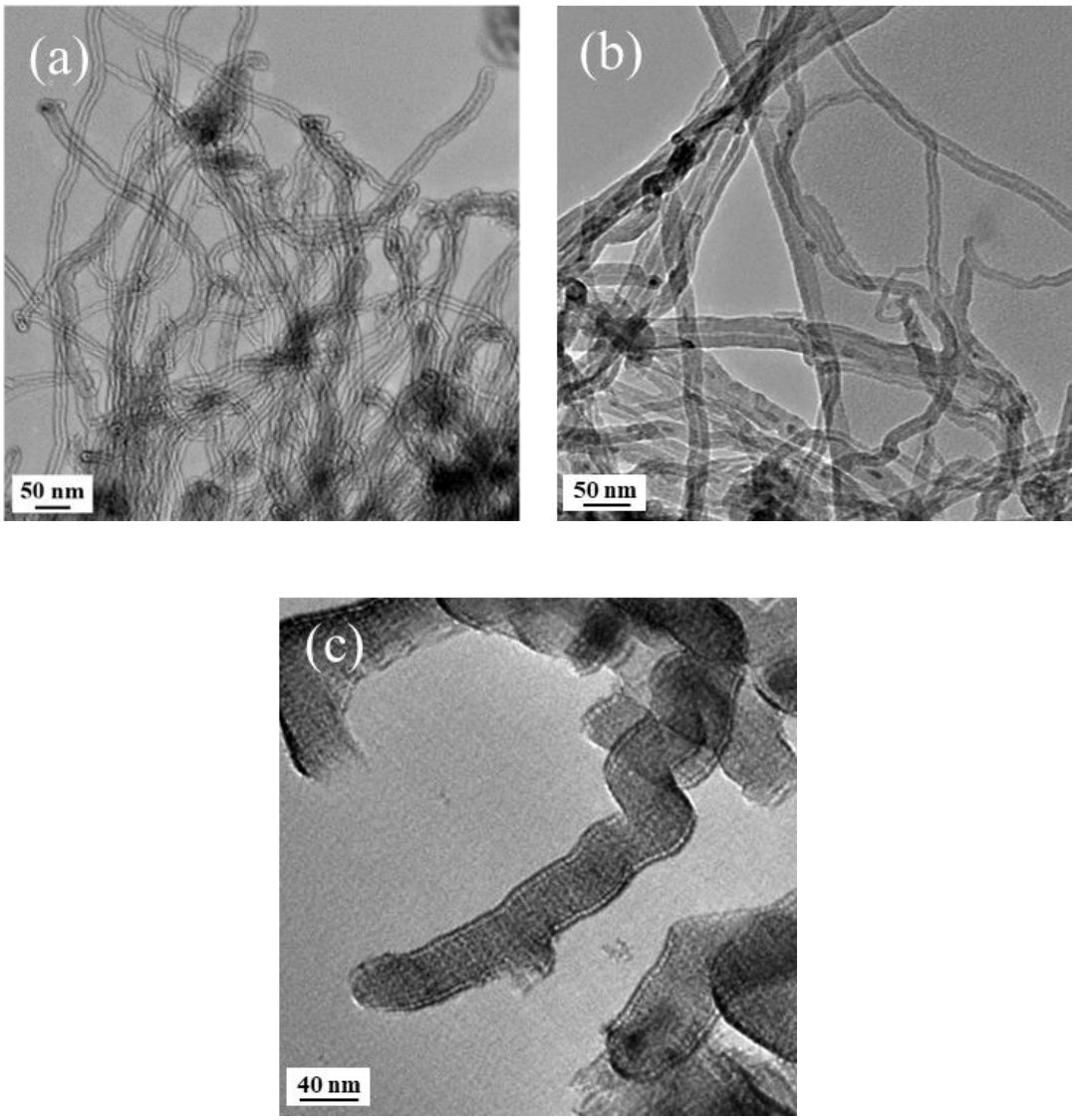

Figure 4. 40 TEM image of the CNTs grown from SS catalyst film (a) and from Ag-SS catalyst film (b & c)

4.5.2.3 Raman spectra of the VACNT films for the 1D composite coating

Raman spectra of the two types CNTs grown from SS and Ag-SS catalyst films are shown in Figure 4. 41, which present typical features of multiwalled CNTs. Two dominant Raman features, the disorder induced D band (1350 cm^{-1}) and the tangential

G band (1600 cm^{-1}) can be viewed from the Raman spectra of both CNT layers. The D band to G band intensity ratio (I_D/I_G) of these two CNT –layers grown from the SS and the Ag-SS catalyst films are 0.71 and 0.85, respectively. The higher intensity ratio of the CNTs grown from Ag-SS catalyst film implies more defects within the CNTs, which may be caused by the interference of silver particles.

It is known that the Raman features are detected from the vibrations of the carbon atoms: the D band comes from a double resonance process and the G band is assigned to the in-plane vibration of C-C bonds. The D band and G band from the CNT grown from the Ag-SS catalyst shift closer to each other, which is also related to the defects.

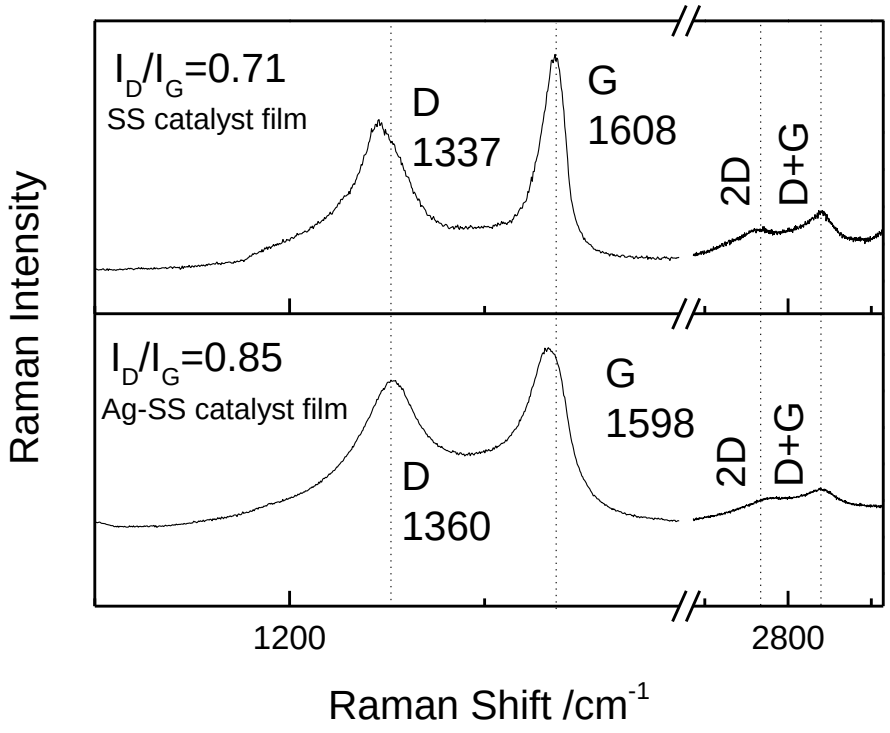

Figure 4. 41 Raman spectra of the VACNT films grown from stainless steel catalyst film and Ag impregnated stainless steel catalyst film

4.5.2.4 Exploration of CNT reinforced composite coating

Subsequently, the CNT films were used as substrates for the fabrication of the CNT reinforced composite coatings through different approaches. Pt-CNT coatings were deposited for 3 min using a mini sputter coater at room temperature. Ag-CNT coatings were fabricated using a magnetron sputtering (Teer Coatings Ltd), a deposition time of 10 min, and a pure silver target. DLC-CNT films were deposited using the rf PECVD, 170℃, a deposition time of 30 min, and methane (10 sccm) as carbon source.

Pt-CNT composite coating

Several attempts have been made to explore the fabrication of the CNTs reinforced nanocomposite coatings using both PVD and CVD. Figure 4. 42 (a) shows the morphologies of the Pt-CNT composite coating. It can be seen that the composite coating is not very dense due to the low sputtering rate of Pt. The vertically aligned structure of the CNTs was broken because of the impact of the Pt nanoparticles. Figure 4. 42 (b) shows the TEM image of a CNT fully coated by the Pt nanoparticles with the size around 10 nm.

In this case, it is verified that the Pt nanoparticles can penetrate into the CNT film to form a Pt-CNT composite nanostructure, but the continuous impacts from the Pt nanoparticles can break the aligned structure of the CNTs. In addition, the low sputtering rate of Pt makes it difficult to fabricate a fully-composited coating. Due to the impact effects, freestanding CNTs are easy to be damaged by the particles during the sputtering process. Thus, this process is not capable to fabricate a well-composited coating even with a low-density CNT film.

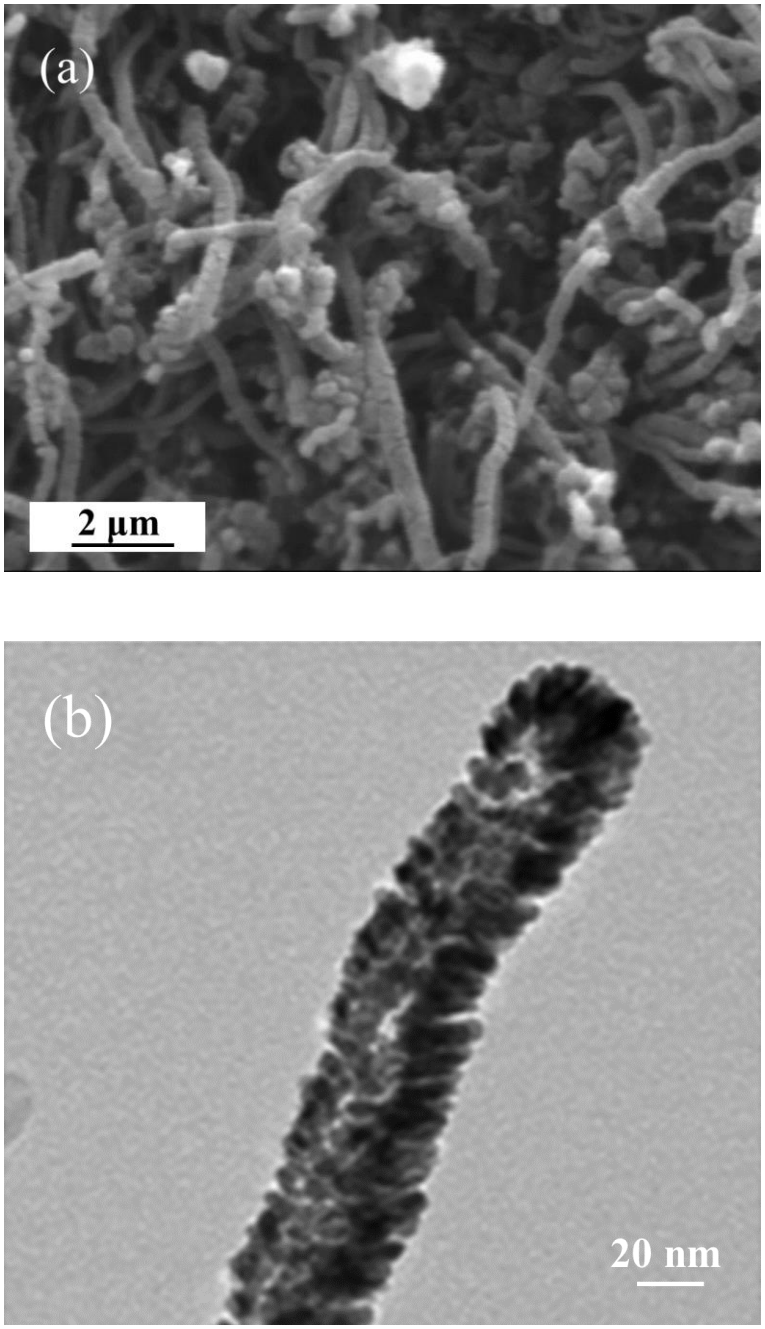

Figure 4. 42 (a) SEM image of the surface morphology of the Pt-CNT coating, (b) TEM image of single CNT coated with Pt nanoparticles

Ag-CNT composite coating

The Ag-CNT composite coating was deposited by a PVD sputtering process, in which Ag particles are sputtered off from the target and deposited on the CNT surface directly. The granular surface of Ag coating is shown in Figure 4. 43 (a), and the Si substrate and the underneath VACNT film can be seen in Figure 4. 43 which shows a cross

sectional view. Large silver particles cannot penetrate into the CNT film and form a Ag layer on the top of the CNTs shown in Figure 4. 43 (b). The thicknesses of the Ag layer and the CNT layer are around 2 μm and 1.2 μm, respectively.

The Ag layer has a coarse columnar structure, while the vertically aligned structure of the CNTs can be clearly viewed. An abrupt interface is observed but no Ag particles are found in the CNT layer because of their large size. Mechanical bonds were formed between these two layers due to the impact effects of the Ag particles.

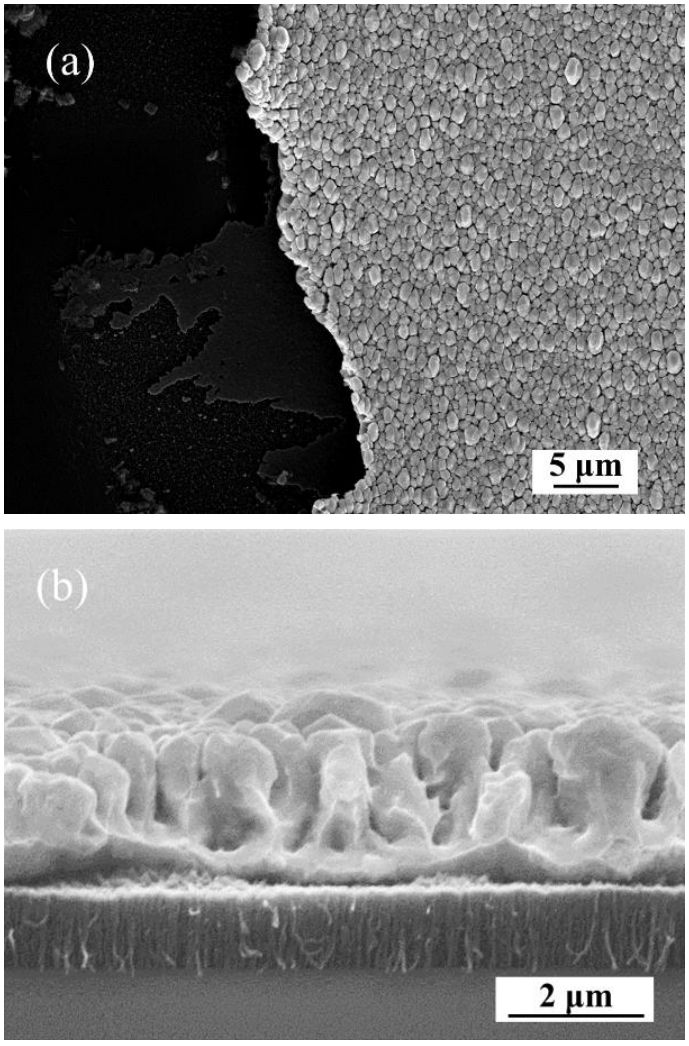

Figure 4. 43 SEM images of the Ag-CNT composite coating. (a) morphologies of the cracked Ag-CNT coating; (b) cross-section view of the Ag-CNT coating

DLC-CNT composite coating

Unlike the sputtering process, volatile precursors in the CVD process could penetrate into the CNT film and coat the CNTs. However, the DLC matrix prefers to accumulate on the tips of the CNTs when the CNT film has a high density. Figure 4. 44 shows the cross-section views of DLC-CNT composite coatings generated from two types of VACNT films. Figure 4. 44 (a) shows a composite structure with a surface amorphous carbons layer on the top of the CNT film. This composite coating was deposited on the high-density VACNT film grown from the SS catalyst film. Chemical bonds between the amorphous carbon and the CNTs are expected to form during the CVD deposition process. However, the amorphous carbon is limited at the top area due to the high density of the CNTs.

On the other hand, there are more inter-CNT spacing in the low-density CNT film, which makes it easier for the carbon species to diffuse into the CNT layer. Figure 4. 44(b) shows the cross-section image of the DLC-CNT film deposited from the low-density VACNT film. It can be seen that a columnar-like structure have been formed and it is difficult, if not impossible, to distinguish the CNTs from the carbon coating. Clearly, a CNT reinforced carbon-based nanocomposite coating has been successfully generated.

Raman spectra of the DLC-CNT composite coating

The Raman spectra of the DLC film, the CNT film, and the DLC-CNT nanocomposite coating are compared in Figure 4. 45. The DLC coating has overlapped D band and G band due to its amorphous structure and their intensity ratio is 0.58. Unlike the DLC coating, separated D band and G band can be clearly seen from the multi-walled CNTs and the intensity ratio is 0.85. For the DLC-CNT nanocomposite coating, its Raman

spectrum is a combination of the amorphous carbon and the CNTs and the intensity ratio I_D/I_G is 0.71. Even though the amorphous carbon layer was deposited on the CNT film, the Raman features from the DLC-CNT nanocomposite coating are similar to that of CNT film.

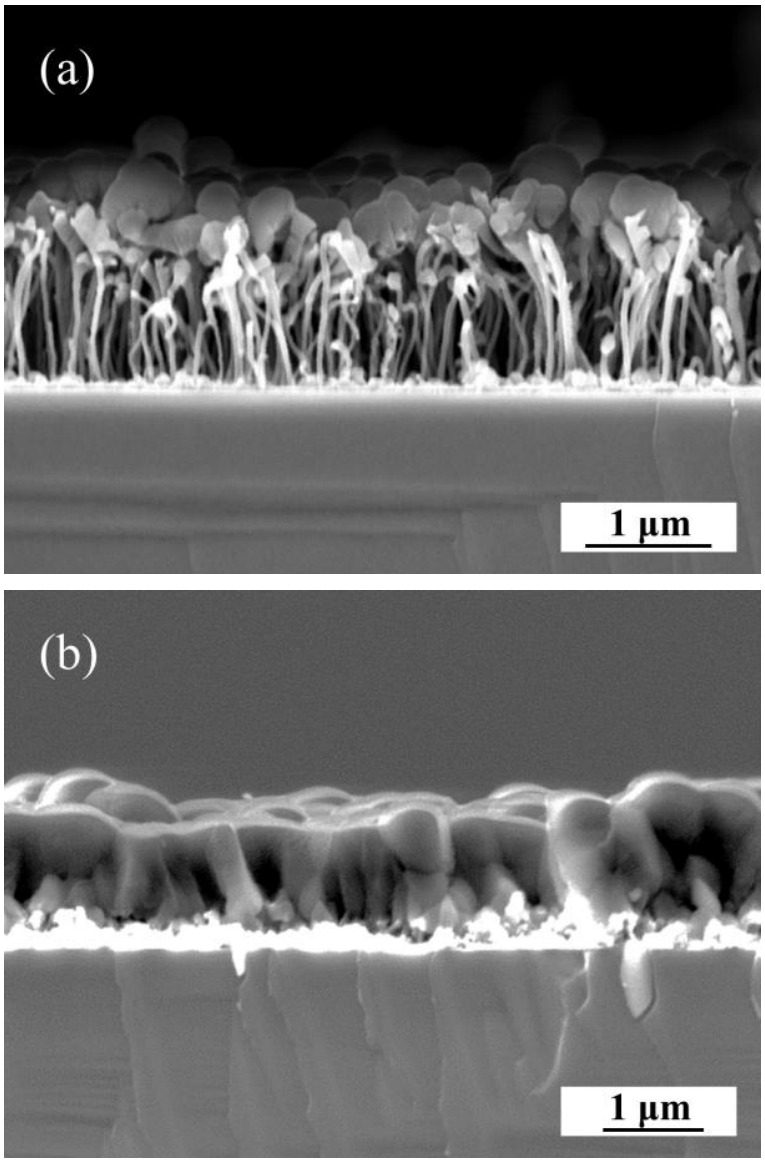

Figure 4. 44 Cross-section SEM images of the DLC-CNT composite coatings deposited bases on the (a) high-density VACNT film and (b) low-density Ag-VACNT film

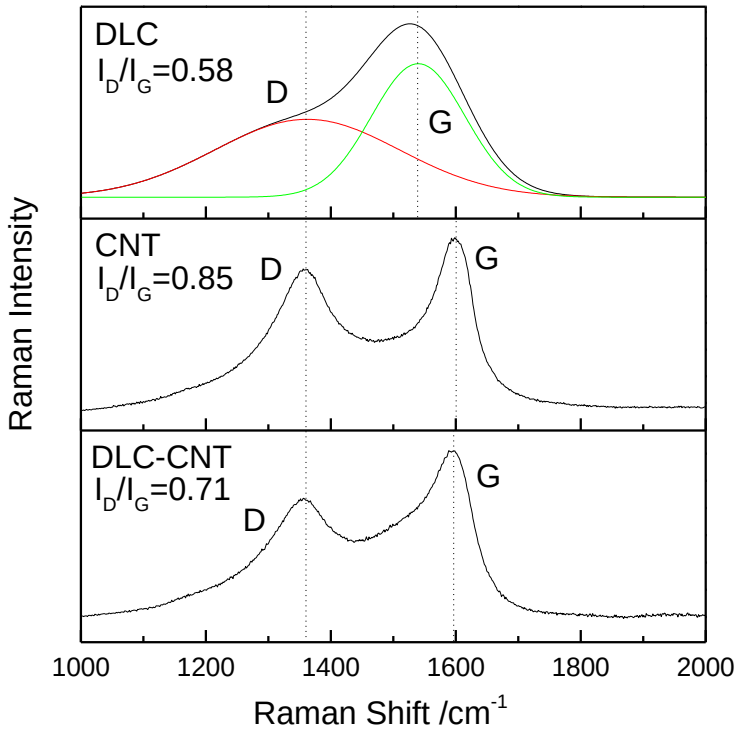

Figure 4. 45 Comparison of the Raman spectra between the DLC film, the CNT film grew from Ag-SS and the DLC-CNT composite coating grew from the low-density CNT film

Wettability of the DLC-CNT composite coating

The wettability of the CNT related coatings has been studied. The variation of the contact angles is mainly influenced by the morphologies of the coatings because all the surfaces consisted of amorphous carbon which should have similar chemical status. The pure DLC coating is very flat with a roughness of 4 nm and its contact angle is around 91º. For the DLC-CNT composite coating deposited from the high-density VACNT films, a relatively rough surface was formed because the amorphous carbon was mainly attached to the tips of the CNTs, thus resulting in a high contact angle 145º. For the DLC-CNT composite coating deposited from the low-density VACNT films, the amorphous carbon can fully fill in the gap of the low-density VACNT film to form a nanocomposite coating with a relatively low roughness and hence its contact angle is around 115º.

Electrical properties of the DLC-CNT composite coating

As mentioned in Chapter 3, the electrical properties of the as-deposited coatings were measured by the four-probe tester and the results are summarized in Table 4. 7. It can be seen that the VACNT film and the Ag impregnated VACNT film has a very low resistivity of 0.43 kΩcm and 0.007 kΩcm respectively, and their square resistances is 8.36 kΩ/□ and 135 Ω/□, respectively. The low resistivity of the VACNT films indicates that the CNTs have an excellent electrical conductivity. The conductivity of the VACNT film and Ag-VACNT film are 2.36×10^{-3} S/cm and 0.15 S/cm, respectively. It is clear that the Ag impregnated VACNT film has a lower resistivity and a better conductivity than the VACNT film probably due to the contribution of Ag.

Unlike the pure DLC coating which is nonconductive, both the DLC-CNT composite coatings deposited from the high density (DLC-CNT-High) and low-density VACNT films (DLC-CNT-Low) are conductive. The resistivity of the DLC-CNT-High and DLC-CNT-Low coatings is 23.2 kΩcm and 55.3 kΩcm, and their square resistances are 212.6 kΩ/□ and 623.5 kΩ/□ respectively. The conductivities of these two DLC-CNT composite coatings are 0.63×10^{-4} S/cm and 1.64×10^{-5} S/cm, respectively.

Table 4. 7 Electrical conductivity properties of the as-deposited coatings

Sample	Resistivity	Conductivity	Square resistance
VACNT	0.43 kΩcm	2.36×10^{-3} S/cm	8.36 kΩ/□
Ag-VACNT	0.007 kΩcm	0.15 S/cm	135 Ω/□
DLC-CNT-High	23.2 kΩcm	0.63×10^{-4} S/cm	212.6 kΩ/□
DLC-CNT-Low	55.3 kΩcm	1.64×10^{-5} S/cm	623.5 kΩ/□
DLC	-	-	-

Clearly, the novel CNT reinforced DLC-matrix nanocomposite coatings possess a much high electrical conductivity as compared with conventional DLC, which is non-conductive. Therefore, such novel CNT reinforced DLC-matrix nanocomposite coatings could be used as multi-functional coatings for some special applications.

4.6 Active screen plasma co-alloying in methane ambient

Active screen plasma co-alloying (ASPCA) technique has been developed for the deposition of Ag wire reinforced composite coatings. Pure Ag lid and 316 SS mesh lid were applied as the alloying sources in an ambient of CH_4 and H_2. Details of the active screen settings and the deposition processes are described in Section 3.3.1. To investigate the effect of the deposition conditions on the formation of Ag wire reinforced composite coatings, a series of experiments were designed, and the parameters are listed in Table 4. 8.

Table 4. 8 Deposition parameters of the active screen plasma co-alloying processes

Code	Pressure	Temperature	Time	CH_4	H_2	Distance
A1	1 mbar	420℃	20 h	1.5%	98.5%	20mm
A2	3 mbar	420℃	20 h	1.5%	98.5%	20mm
A3	1mbar/3mbar	420℃	2h +18 h	1.5%	98.5%	20mm
A4	1mbar/3mbar	420℃	2h +18 h	3%	97%	20mm
A5	1mbar/3mbar	420℃	2h +18 h	1.5%	98.5%	10mm
A6	1mbar/3mbar	420℃	2h +18 h	1.5%	98.5%	30mm

4.6.1 Surface morphologies

The morphologies of the composite coatings deposited by the ASPCA technique are shown in Figure 4. 46, which are significantly influenced by the deposition conditions. Figure 4. 46 (a) shows the surface morphology of the composite coating synthesised at 1 mbar for 20h (A1). Some large particles are distributed on the surface of the substrate. The hollow cathode effect during the process was very strong due to the low gas

pressure, and hence lots of stainless-steel nanoparticles and Ag particles were sputtered off from the active screen lids, but no continuous coating was formed in this case.

For the coating deposited at 3 mbar for 20 h (A2), large agglomerations can be clearly seen on the sample surface. These particles are much larger than that formed for A1 composite coating. No wires could be observed on the surface of the A2 composite coating.

Wire-shaped structures embedded in the matrix of the composite coating can be observed from the surface of A3 composite coating, as exemplified in Figure 4. 46 (c). The length of these wires is varied from 1 to 10 μm. These wires are mainly formed with Ag and stainless-steel particles as verified by EDS in the subsequent session.

Figure 4. 46 (d) presents the surface morphology of the A4 composite coating synthesised with a high fraction (3%) of methane. Ag wires were also formed during the deposition process, but a thick carbon-rich layer seems to be formed due to the high amount of carbon source. Although the growth mechanism of the Ag wires during the sputtering process is not fully understood, these SEM observations indicate that the deposition conditions for A3 and A4 are suitable for the growth of Ag wires; a lower percentage of methane (1.5%) would produce a better Ag wires reinforced composite coating.

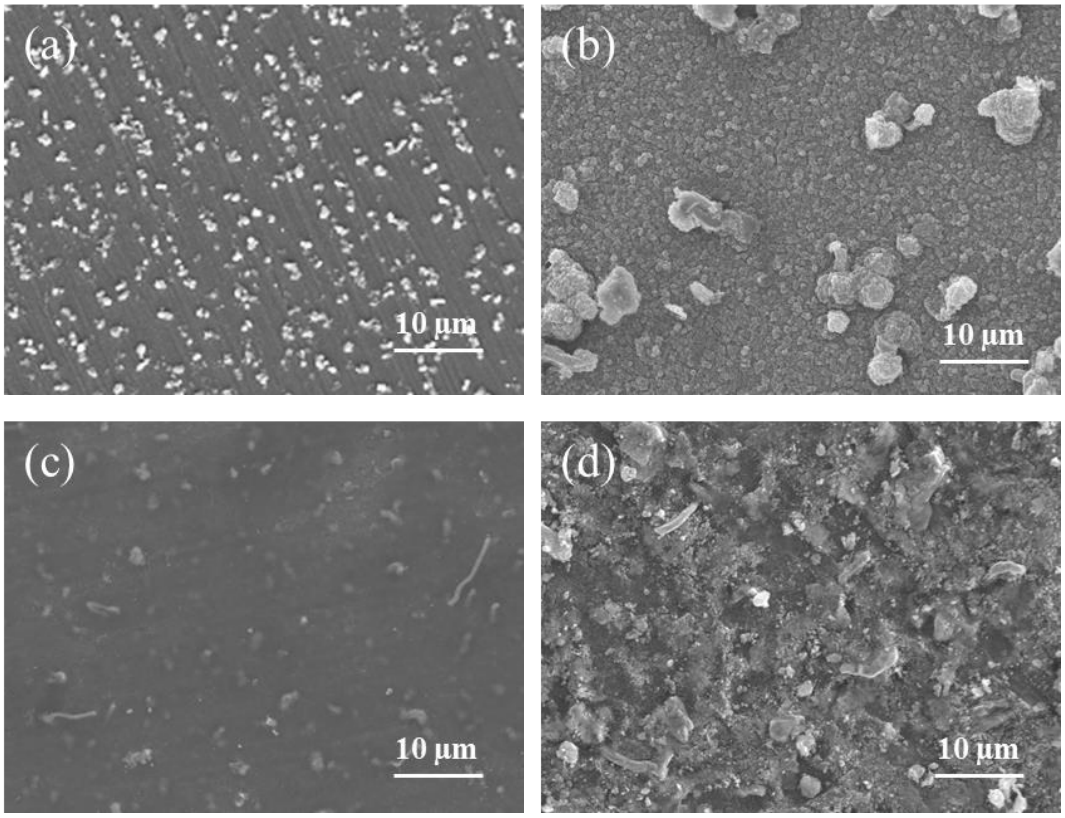

Figure 4. 46 Surface morphologies of the composite coating deposited by ASPA technique. (a) A1: low pressure 1 mbar; (b) A2: high pressure 3 mbar; (c) A3: 1mbar/3 mbar and 1.5% methane; (d) A4: 1 mbar/3 mbar and 3% methane

EDS mapping has been carried out to study the element distribution on the composite coating. Figure 4. 47 and Figure 4. 48 show the EDS mapping results of the A3 and A4 composite coatings. Beside the SEM image, element mappings of Ag, C, Fe, Ni, and Cr are acquired. The bright areas shown in Figure 4. 47 (b) and Figure 4. 48 (b) are corresponding to the Ag rich areas. It is verified that the wire structures are composed of Ag by the comparison between the SEM image and the Ag EDS mapping. Beside these Ag wires and clusters, nanoparticles were also sputtered off from the Ag lid and randomly distributed in the composite coating.

Figure 4. 47 (c) and Figure 4. 48 (c) show the distribution of carbon in the selected area, and a low amount of carbon is detected at the Ag rich area. EDS mappings of Fe, Ni, Cr are shown in Figure 4. 47 (d)&(e)&(f) and Figure 4. 48 (d)&(e)&(f). It seems that

the stainless-steel nanoparticles are well distributed in the composite coating surface. However, there are some dark areas in the mapping of Fe, Ni, Cr, which are corresponding to the Ag rich areas. This indicates that the wires and clusters formed on the composite surface are mainly composed of Ag, and the matrix of the composite coating contains carbon, Ag and stainless-steel nanoparticles.

The above results have revealed that the Ag wires reinforced composite coating deposited under A3 conditions exhibited a good Ag-reinforced composite structure and a smooth surface. Thus, composite coatings A5 and A6 are deposited using the similar parameters but with different deposition distances between the sample surface and the active screen lid. The surface morphologies and cross-section view of A3, A5 and A6 composite coatings are compared in Figure 4. 49. It seems that the deposition distance does not have an appreciable effect on the formation of the Ag wires. Ag wires can be observed in all those three composite coatings. However, the length and thickness of the Ag wires are not uniform, and the length of the Ag wires ranged from 10 μm to around 2 μm. The thickness variation of these curly Ag wires implies that most probably these Ag wires are not a single crystal, which is different from those single crystalline Ag nanowires grown through the chemical process [106, 164].

Figure 4. 49 (b)&(d)&(e) show the cross-section views of the composite coatings, and their thicknesses are 2.11 μm (A3), 3.04 μm (A5) and 1.87 μm (A6). This indicates that a shorter deposition distance would lead to a thicker composite coating. Besides, the A3 & A5 composite coatings exhibit good adhesion to the substrate, while the A6 composite coating is partially delaminated after the sample preparation, indicating that a long deposition distance can reduce the adhesion of the composite coating to the substrate.

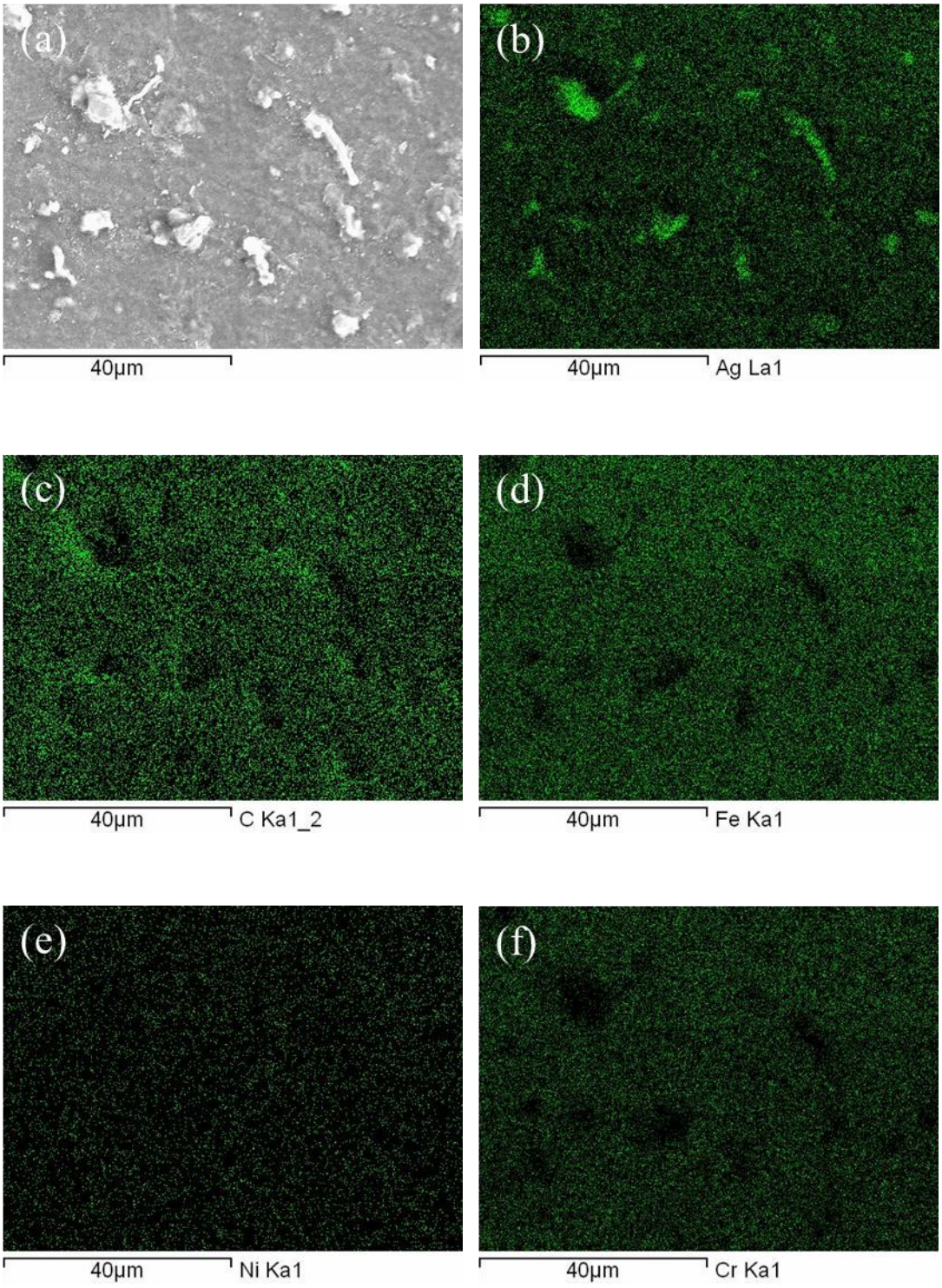

Figure 4. 47 EDS mapping of the A3 composite coating. (a) SEM image; (b) mapping scan of Ag; (c) mapping scan of C; (d) mapping scan of Fe; (e) mapping scan of Ni; (f) mapping of Cr

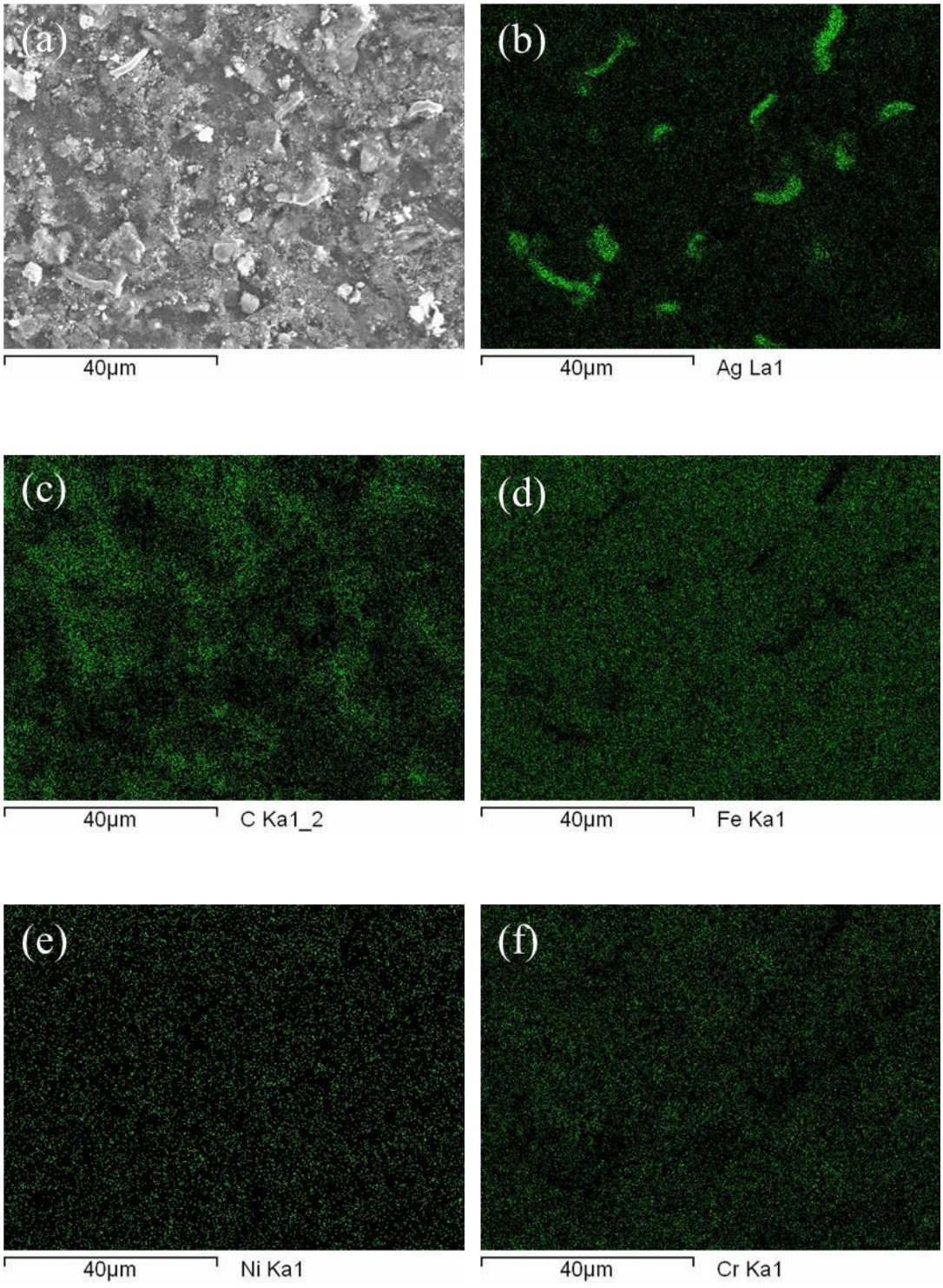

Figure 4. 48 EDS mapping of the A4 composite coating. (a) SEM image; (b) mapping scan of Ag; (c) mapping scan of C; (d) mapping scan of Fe; (e) mapping scan of Ni; (f) mapping scan of Cr

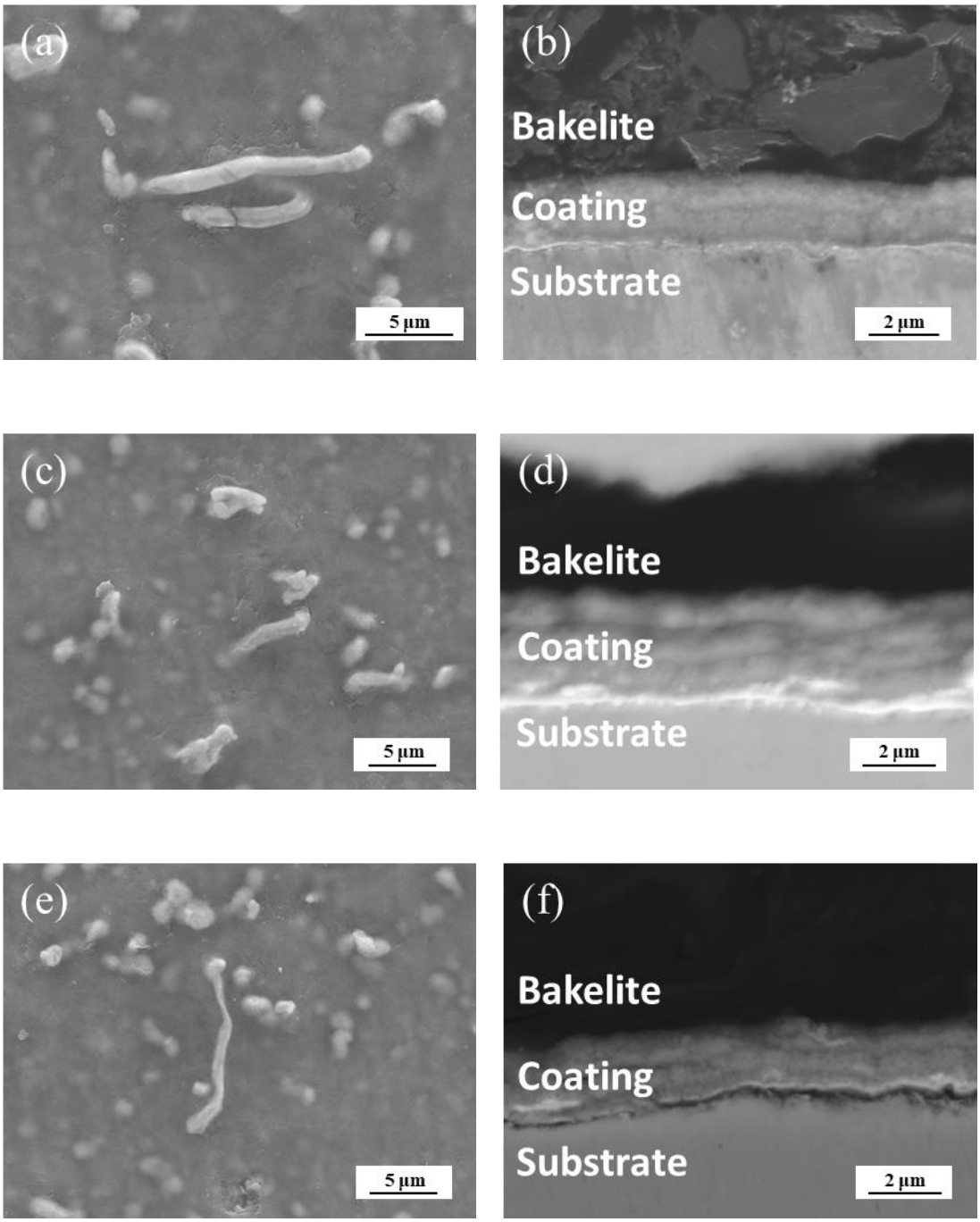

Figure 4. 49 Surface morphologies and cross-section views of the Ag wires reinforced composite coatings. A3: (a) & (b); A5: (c) & (d); A6: (e) & (f)

4.6.2 Phase identification

The phase components of the composite coatings (A3, A5, A6) and the stainless-steel substrate were investigated by XRD and the corresponding spectra are shown in Figure 4. 50. Typical peaks (111), (200) and (220) of the γ-phase for the face-centred cubic (fcc) structured austenitic stainless steel were detected from the 316 SS substrate. As shown in Figure 4. 50, the XRD patterns of the composite coatings (A3 & A5 & A6) are very similar, indicating that the change of the deposition distance does not affect the phases with the composite coatings.

The γ-phase peaks were also detected from the Ag reinforced composite coating, which may come from the composite coating and the substrate in view of the thinness of the composite coating. No peaks for chromium carbides could be detected, which indicates that the SS nanoparticles sputtered from the 316 SS screen and lid did not react with the carbon precursor during the deposition process at 420℃. Beside the γ-phase, peaks at around 38.2°, 44.5°, 64.7°, 77.7° and 82.0° can match the (111), (200), (220), (222), and (311) peaks of pure Ag.

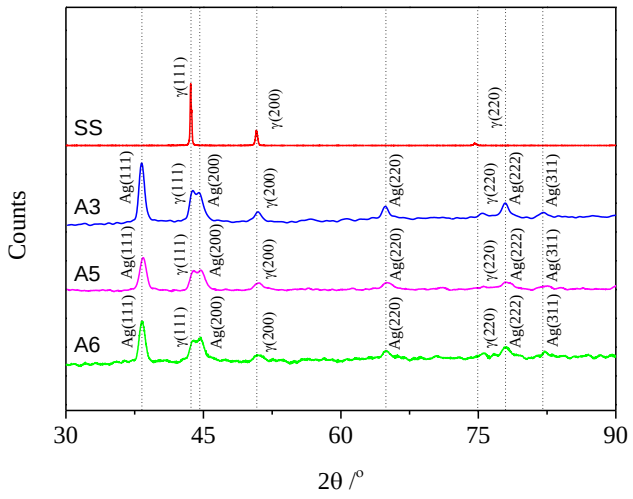

Figure 4. 50 XRD results of the untreated 316 stainless steel and the A3, A5 and A6 composite coating with Ag wires

4.6.3 Chemical state

The surface chemical states of the Ag wire reinforced A3 composite coating has been investigated by X-ray photoelectron spectroscopy (XPS). The spectra were collected from the as-deposited surface and the sublayer by etching for 60s with Ar ions in order to compare the chemical state variation of the composite coating. Figure 4. 51 shows the survey spectra and high-resolution spectra of Ag 3d, C 1s, and Fe 2p. The survey spectra shown in Figure 4. 51 (a) indicate that the chemical states are different before and after etching. After etching, more peaks were detected from the surface which indicates that there is an oxide layer formed at the surface and an obvious peak for O 1s can be viewed from the unetched surface (see Figure 4. 51 (a))

Figure 4. 51 (b) shows the high-resolution Ag spectra from the composite coating. Peaks belong to Ag $3d_{5/2}$ at 368.2 eV and Ag $3d_{3/2}$ at 374.3 eV were detected from the coating surface before and after etching. These two peaks prove that the Ag detected from the composite coating has a valence of zero, indicating that the wires are formed with pure Ag.

Figure 4. 51 (c) shows the C 1s spectra of the composite coating. The peak at 284.6 eV detected from both the unetched and the etched coating surface can be assigned to the C-C bond. Besides, a shoulder peak at 286.2 eV corresponding to the C-O bond was only detected from the unetched surface, which may be due to the reactions between the surface carbon and oxygen in the ambient, while no such C-O peak can be detected from the composite coating after etching.

Figure 4. 51 (d) shows the high-resolution spectra of iron, and very weak peaks for Fe were detected before etching. Clear peaks at 706.7 eV and 720.0 eV are corresponding

to Fe^0, indicating that the SS nanoparticles had not reacted with the carbon during the deposition process, which is consistent with the XRD results.

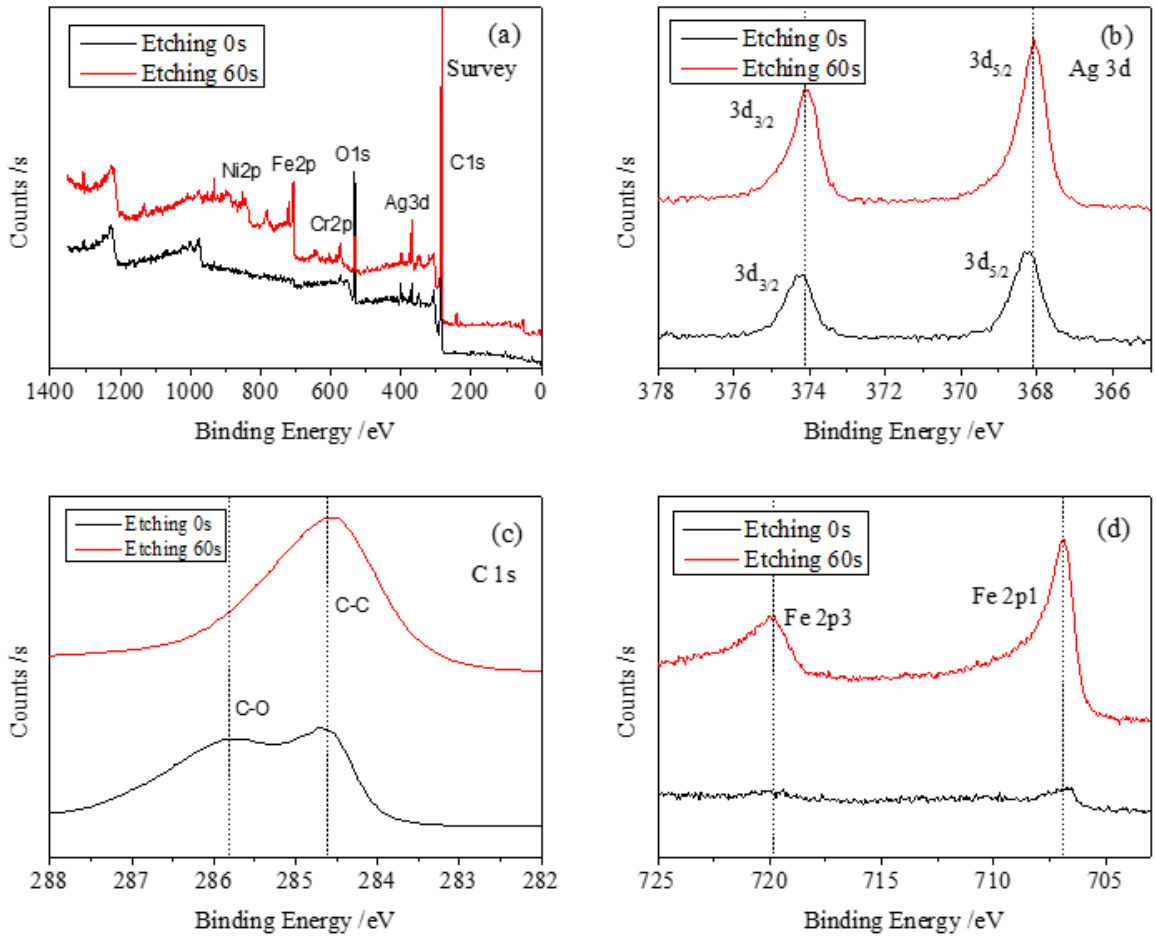

Figure 4. 51 XPS spectra of the Ag wire reinforced composite coating (A3). (a) survey of the Ag wire reinforced composite coating; (b) Ag 3d spectra; (c) C 1s spectra; (d) Fe 2p spectra

4.6.4 Raman spectroscopy

In order to investigate the microstructures of these carbon rich composite coatings, Raman analysis has been conducted and the Raman spectra are shown in Figure 4. 52. D peak and G peak at around 1355 cm^{-1} and 1590 cm^{-1} respectively were detected from all those composite coatings, which verified the existence of carbon in the composite coatings. The high D peak indicates that there are lots of defects formed in the coatings during the plasma deposition process. Unlike the diamond-like carbon films which have

overlapped D peak and G peak [165], the D peak and G peak, in this case, are separated from each other, indicating that carbon in these composite coatings has a different structure as compared with the hard amorphous carbon.

No peak shift was observed from these Raman spectra due to the similar deposition processes. However, the band intensity ratios (I_D/I_G) of the composite coatings are varied from 1.02 to 1.15. It is known that the band intensity ratios (I_D/I_G) are an indication of defects in the coatings. The experimental results have revealed that a low-intensity ratio can be achieved when the deposition processes were carried out with a high percentage of methane (A4) or with a small deposition distance (A6).

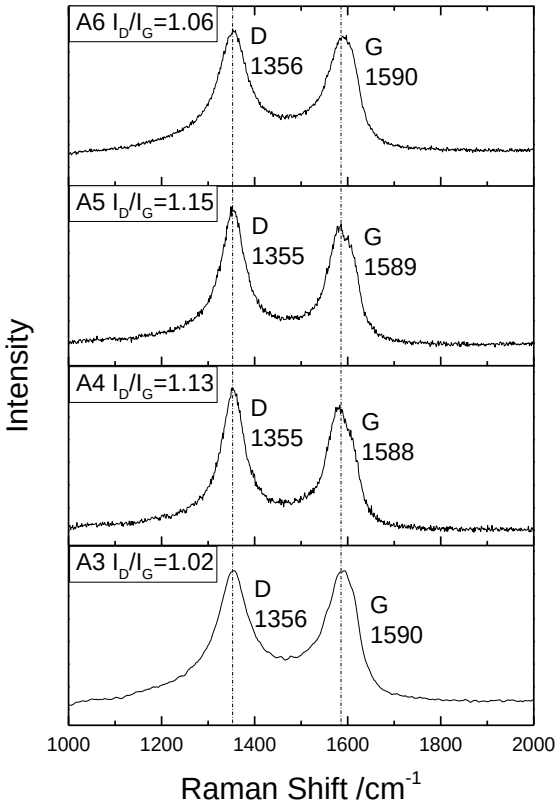

Figure 4. 52 Raman spectra of the Ag wires reinforced composite coatings (A3, A4, A5 and A6). The positions of D peak and G peak are marked, and the intensity ratios are calculated and presented in the image

4.6.5 Contact angle and hardness

The contact angle of the Ag wires reinforced composite coatings were measured to evaluate their wettability, which is influenced by the physical and chemical status of the surfaces. As shown in Figure 4. 53, the polished stainless-steel substrate surface presents a contact angle around 96^{o} which is relatively hydrophobic, while the contact angles of the Ag wires reinforced composite coatings are 55^{o}, 59^{o}, and 63^{o} for A3, A5, A6, respectively. This indicates that these composite surfaces are hydrophilic. The variations of contact angles between the composite surfaces may be caused by the roughness, and the corresponding average roughness (Ra) of the composite coatings are 573 nm (A3), 616 nm (A5) and 551 nm (A6), respectively.

The microhardness of the Ag wires reinforced composite coatings are measured under the load of 50 g. Figure 4. 53 shows that the hardness of the composite surfaces (~500 $HV_{0.05}$) is higher than that of the stainless-steel substrate (~245 $HV_{0.05}$). The hardness enhancement of the composite surface may be due to the diffusion of carbon into the substrate.

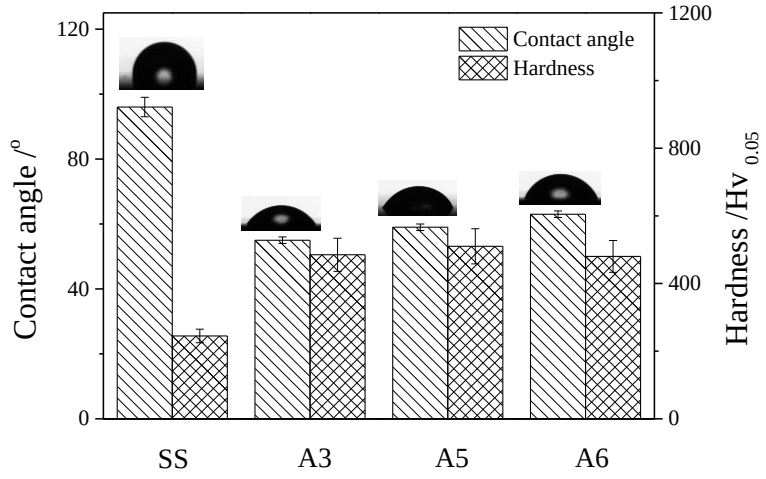

Figure 4. 53 Contact angles between distil water and the different surfaces to evaluate the wettability of the composite surfaces, and optical images of the water droplets are inserted

4.6.6 Adhesion-abrasion resistance against Al

It is known that Ag is a solid lubricant and hence could be used to reduce adhesion and friction of steel surface. Therefore, reciprocating sliding friction tests have been carried out against an Al counterpart pin. Figure 4. 54 shows the friction coefficients of the A3 composite coating compared to that of uncoated SS substrate under dry sliding condition. After a couple of initial strokes, the friction coefficients of polished SS started to rise from 0.15 to 0.45 and then fluctuated largely throughout the test. This is a clear indication of stick-slip caused by the strong adhesion between the SS and Al. In addition, the friction heat generated by the high friction would reduce the strength of aluminium alloys and hence increase adhesion further, thus leading to excessive materials transfer. This adhesion behaviour of ductile materials reflects the similar trends obtained from the previous friction coefficient analysis [166].

However, the interface friction coefficient was greatly reduced when the metal was coated with the Ag wires impregnated composite coating. The friction coefficient was 0.17 in the first 5 cycles and it slowly climbed to 0.25 after 25-50 strokes which are believed to be caused by the slow run-in between aluminium and the coating. Then, the friction coefficient of the composite coating against Al remained low (0.25) throughout the test.

The wear tracks formed during the tests were studied using SEM and TEM and the results are shown in Figure 4. 55. It can be seen from Figure 4. 55 (a) that at the wear surface of the Ag wire reinforced composite coating, the original features of the silver wires and silver particles are still clearly visible and there is no transfer of aluminium onto the coating surface. Some horizontal scratches in the sliding direction appeared on the composite coating surface after 500 strokes of the reciprocating sliding test.

Cross-sectional microstructure analysis inside the wear track and the elements measured by EDX from the wear track and the Al pin surface are shown in Figure 4. 55 (c)&(d)&(e).

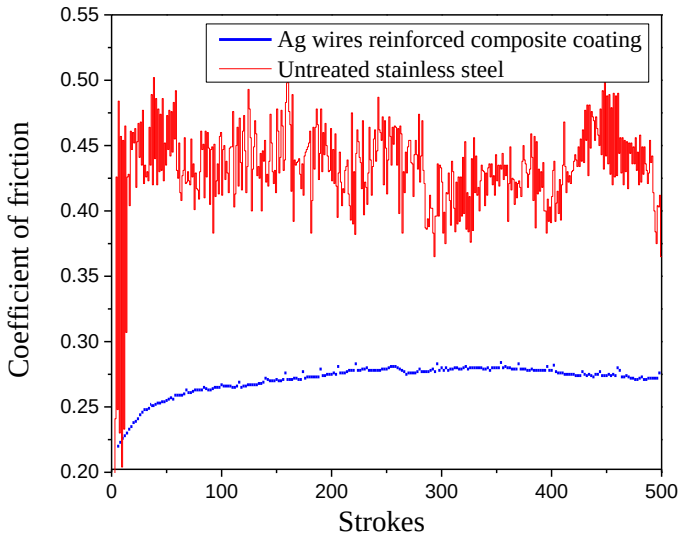

Figure 4. 54 Friction coefficient between conformal-contacted Al and nano-Ag/C coating sliding surfaces

Table 4. 9. The thickness of the carbon rich layer is significantly reduced on the top of the coating and the silver wire appears plastic deformed. The EDS results show that the transfer layers formed on Al pin mainly consist of carbon, whereas the wear track on the coating consists of reduced amount of C and increased amount of O. Although the Ag wires were deformed as compared to the as-treated coating, the high-magnification TEM image in Figure 4. 55 (e) shows that the fine Ag particles are free from damage as evidenced by their original spherical shape. The transformation of carbon phases on the sliding surface can be evidenced by the post-wear Raman spectrums in Figure 4. 56, showing the increased intensity of G peaks in the wear track as compared to the D-peak dominated spectrum of the original coating.

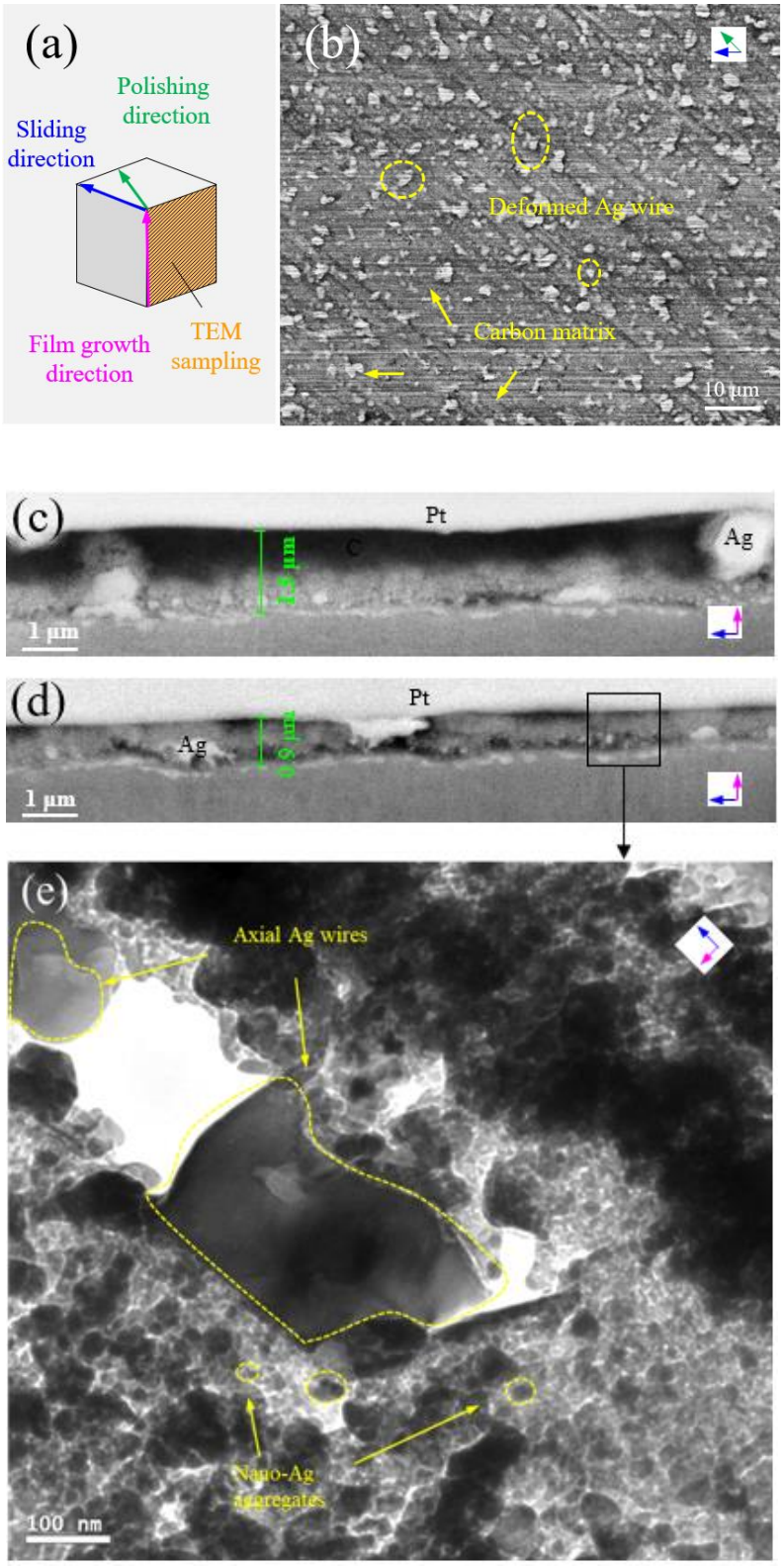

Figure 4. 55 (a) illustration of film growing and sampling orientations, (b) post-wear surface morphology of nano-Ag/C coating showing lines of scratches and plastic deformed Ag wires, cross-sectional SEM images of (c) as-treated coating and (d) wear track, (e) TEM of wear track showing cross-section of nano-Ag wire

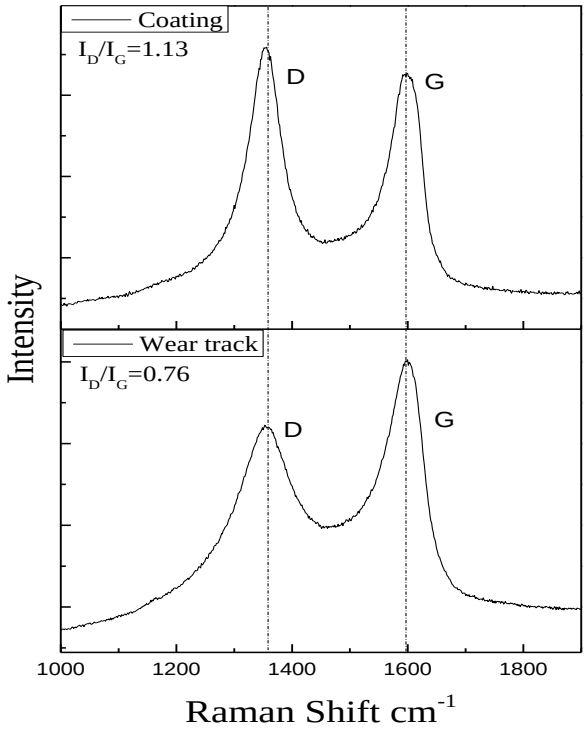

Figure 4. 56 Peak fits of Raman spectrum on the areas of as-treated surface and wear track

Table 4. 9 Elemental distribution on the surface of frictional counterparts

	C	O	Mg	Al	Si	Cr	Fe	Ni	Ag
Al pin	8.23	3.06	0.53	84.02	3.66	0.00	0.51	-	0.00
Al wear area	43.87	4.94	0.35	44.53	1.73	0.63	2.84	-	1.11
nano-Ag/C	23.56	1.87	-	0.00	0.25	8.61	26.29	3.57	34.78
Wear track	17.14	3.02	-	0.00	0.25	8.69	26.94	3.44	39.73

4.6.7 Antibacterial properties

Antibacterial tests were carried out to evaluate the bacterial inhibition performance of the Ag wires impregnated composite coatings. The experimental details are described in Section 3.3.1. Both Gram-negative P. gingivalis and Gram-positive S. epidermidis

bacteria were used to study the antibacterial effect of the Ag wires impregnated composite surfaces.

Figure 4. 57 shows the colonies of the Gram-negative P. gingivalis on the tryptone soya agar plates after incubation. Each spot inside the plate represents for one colony of P. gingivalis. As there is no antibacterial effect of the glass slide control sample, most of the P. gingivalis are alive after 5h contact. Huge amount of *P. gingivalis* colonies were grown, which almost cover the whole agar plate, can be viewed in Figure 4. 57 (a).

In contrast, Figure 4. 57 (b) shows the colonies of *P. gingivalis* after contact with the Ag impregnated composite coating. The colonies are much less compared to that of the control, indicating the inhibition effect of the composite coating. The colonies in each plate were counted to calculate the antibacterial efficiency of the Ag impregnated composite coating to *P. gingivalis* and the quantitative results are shown in Figure 4. 59 (92.2%).

Figure 4. 57 P. gingivalis colonies on the soya agar plates after 5 h contact with (a) glass and (b) Ag impregnated composite coating

In addition to the Gram-negative bacteria (P. gingivalis), Gram-positive bacteria (S. epidermidis) was also used to study the antibacterial activity of the Ag wires reinforced composite coating. Figure 4. 58 shows the S. epidermidis colonies on the soya agar plates after the antibacterial tests. The test conditions are as same as the antibacterial tests to P. gingivalis. The colonies of S. epidermidis after contact with the control glass are spread over the whole soya agar plate as shown in Figure 4. 58 (a). On the other hand, few colonies of S. epidermidis are shown in Figure 4. 58 (b), because they were incubated from the suspension after contact with the Ag impregnated coating. The antibacterial efficiency of the composite coating to S. epidermidis is 95%, which is slightly higher compared to that of the P. gingivalis (Figure 4. 59).

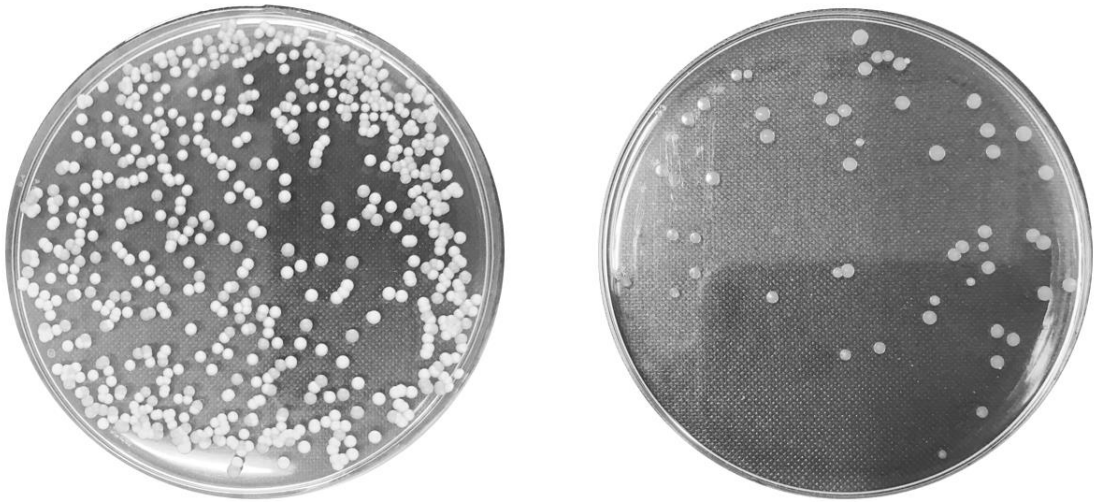

Figure 4. 58 S. epidermidis colonies on the soya agar plates after 5 h contact with (a) glass and (b) Ag impregnated composite coating

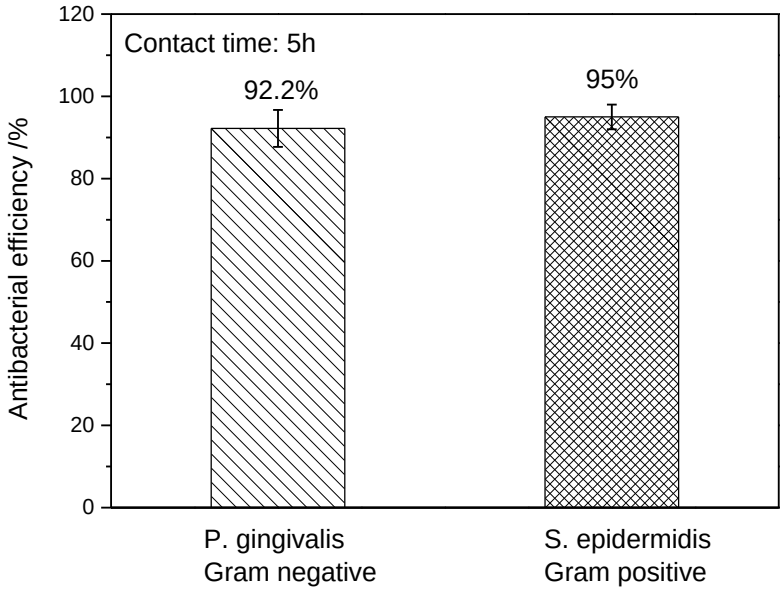

Figure 4. 59 Antibacterial efficiency of the Ag impregnated composite coating

4.7 Active screen plasma co-alloying in a nitrogen ambient

As described in Section 3.3.2, plasma co-alloying in nitrogen ambient has also been investigated using a double glow plasma sputtering process with the same active screen settings as for the plasma co-alloying in methane ambient reported in the last section. However, the bias on the active-screen and the workable/samples can control separately. The specific deposition conditions are summarised in Table 4. 10.

Table 4. 10 Sample codes and the duplex plasma treatment conditions for the Ag impregnated composite surfaces

Code	Substrate	Voltage		Distance	Pressure	Temperature	Gases		Time
		Bottom	Top				N_2	H_2	
M0	316SS	-	-	-	-	-	-	-	-
M1	316SS	200V	520V	25cm	1mbar	420℃	25%	75%	20h
M2	316SS	220V	510V	20cm	1mbar	420℃	25%	75%	20h
M3	316SS	240V	500V	15cm	1mbar	420℃	25%	75%	20h

During the treatment, both Ag and SS particles can be sputtered from the silver plate and the stainless-steel active screen lids to form a Ag impregnated SS layer; meanwhile, nitrogen ions within the plasma surrounding the samples will react with the stainless-steel particles and the excessive nitrogen will diffuse into the stainless-steel substrate to form the S-phase layer. In this case, the 'sputtering and deposition' mechanism can be applied to explain the formation of the S-phase [87].

4.7.1 Surface morphology & layer structure

The surface morphologies of the as-deposited functionally graded composite surfaces are shown in Figure 4. 60 (a)&(b)&(c), and the cauliflower-like surfaces are the result of the sputtering process. Figure 4. 60 (d)&(e)&(f) show the cross-sectional images of the functionally graded composite surfaces after etching by HCl + HNO_3 + H_2O (2:1:1) solution. The interfaces between the composite surface layer, the S-phase sublayer, and the substrate can be distinguished. The thicknesses of the Ag impregnated composite layers are all about 2 μm. The thick S-phase layers formed beneath the composite coating layers are featureless, indicating that the nitrogen supersaturated S-phase layer can withstand the attack from the acid solution during etching. However, some etching craters can be viewed in the 316 SS substrate, which indicates that the corrosion resistance of the S-phase layer is better than that of the 316 SS substrate. Confocal 3D images of the composite surfaces are shown in Figure 4. 60 (g)&(h)&(i), and the average surface roughness (Ra) of M1, M2, and M3 is 452 nm, 223 nm, and 124 nm, respectively.

The deposition process of the Ag impregnated SS layer is mainly determined by the bias on the active screen and on the samples as well as the sputtering distance between the top lids and the samples. It has been found that the higher the bias applied to the lid targets, the more and larger Ag and SS particles would be sputtered from the silver plate

and the SS lid. However, the bias applied to the samples also forms a sputtering effect, which can remove some low energy particles and promote the formation of a dense coating. It can be seen that M1 has a rough surface with large Ag particles impregnated in the surface layer. Even though the sputtering distance for M3 is smaller than that for M1 and M2, the thicknesses of the surface composite layer for these three samples are similar due to the high bias applied to the M3 samples. Beside the large Ag particles, Ag nanoparticles were also formed during the sputtering process.

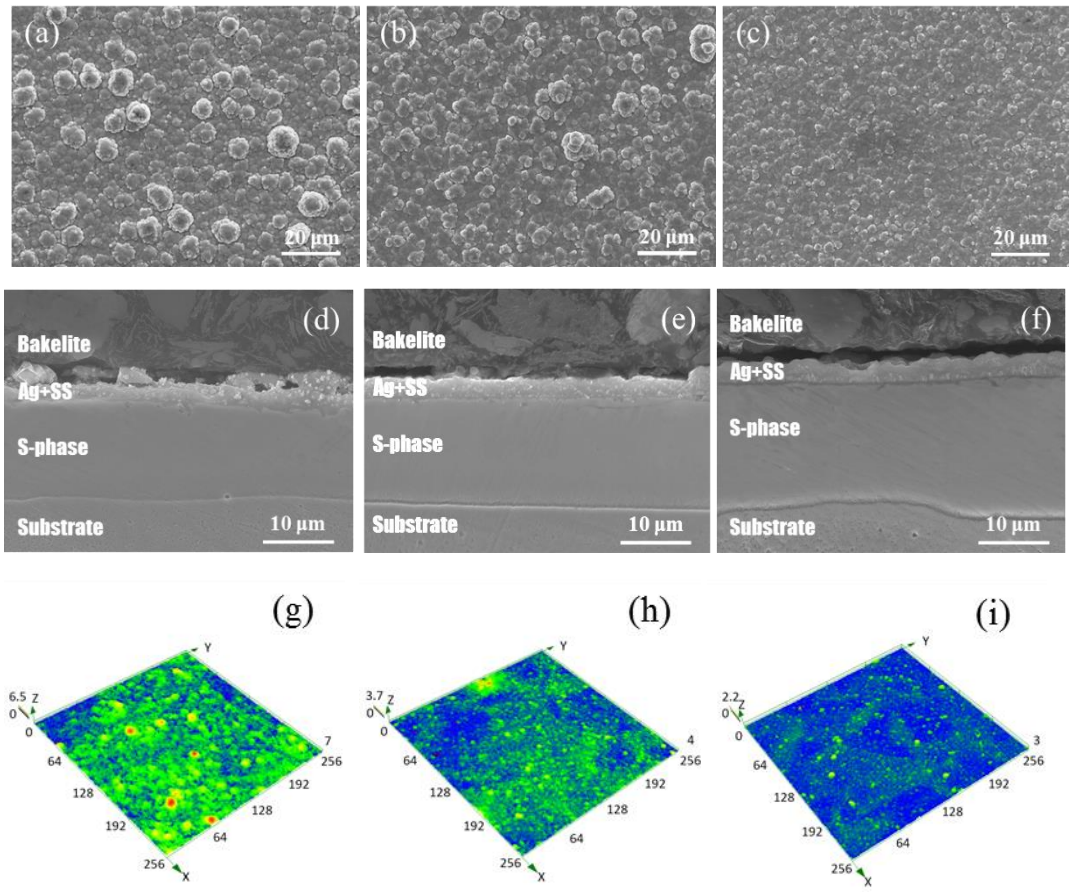

Figure 4. 60 Surface Morphologies, cross-sectional views and confocal 3D images of as deposited functionally graded composite surfaces: (a), (d), (g) for M1; (b), (e), (h) for M2; (c), (f), (i) for M3

4.7.2 Depth distribution of silver and nitrogen

The depth distributions of silver and nitrogen in the composite surfaces are studied using GDOES. Figure 4. 61 presents the depth profiles of nitrogen and silver within the deposited composite surfaces measured by GDOES. The double glow plasma co-alloying treatment is a synergy of the plasma sputtering process and the plasma nitriding process. However, the sputtering process may interfere with the adsorption and diffusion of nitrogen. Thus, a graded distribution of nitrogen will be generated within the composite coating and the S-phase layer beneath. It is shown in Figure 4. 61(a) that the distribution of nitrogen could be divided into two parts. Near the surface within the first part, the nitrogen content is high but reduces rapidly; the nitrogen content within the second part reduces gradually with the depth. The changing point of the nitrogen slopes can be recognized as the interfaces between the surface composite coating and the S-phase case in view of the cross-sectional layer structures shown in Figure 4. 61.

For composite surface M1, the amount of nitrogen is higher in the coating, but lower in the S-phase compared to that in M2 and M3, which may be due to the long-sputtering distance and the interference of the large Ag particles. The content of Ag is found to be influenced by the sputtering distance. It can be seen that the amount of Ag in M3 is higher than that in M1 and M2 because of the short sputtering distance, even though the bias applied to M3 was higher than to M1 and M2. It also noted from Figure 4. 61 (b) that all three Ag depth profiles present two peak values one at the surface and the other at the coating/S-phase interface. This can be attributed to the difference in the sputtering rate of silver, which should be related to the hollow-cathode effect formed between the Ag plate and the 316 SS mesh lids. The composite coating was formed layer by layer from the co-sputtering process, and more Ag particles were sputtered

from the Ag plate at the beginning and ending stage of the coating process most probably caused by the unstable and violent hollow-cathode effect when turned on and turned off the powers. In this study, the surface Ag rich layer is beneficial for the antibacterial activity, which will be reported in Section 4.7.8.

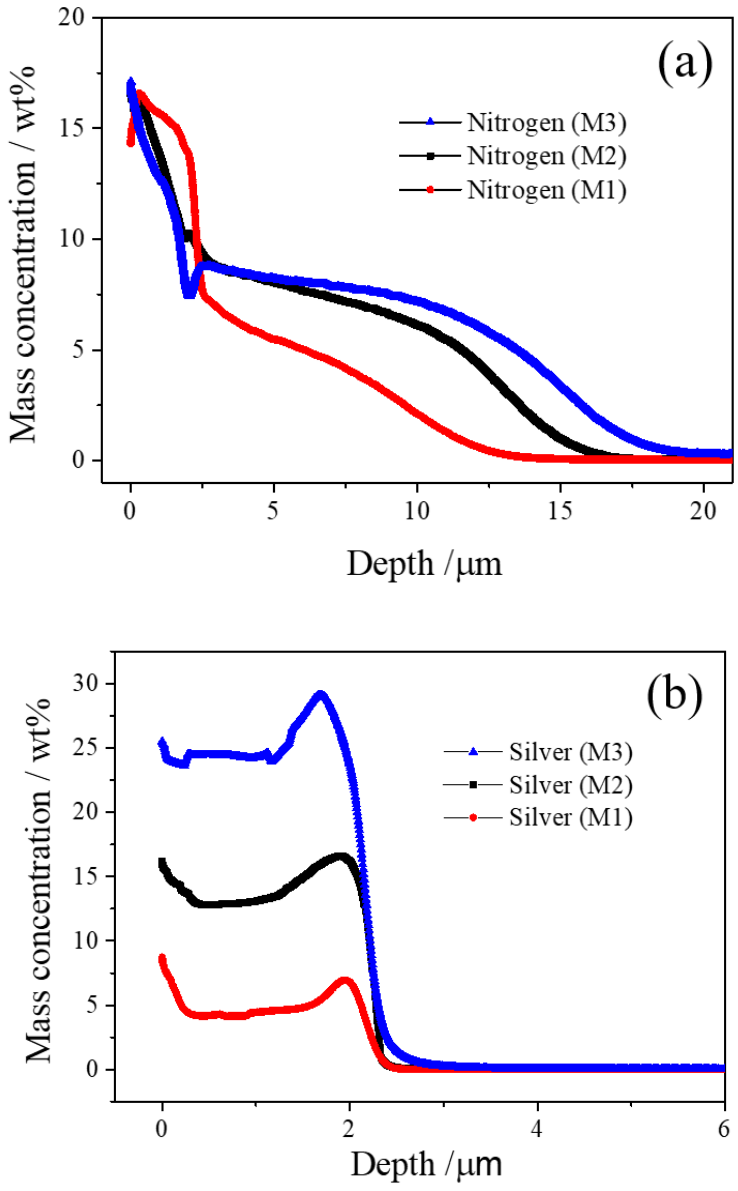

Figure 4. 61 Depth profiles of (a) nitrogen and (b) silver in the composite surfaces, measured by glow discharge optical emission spectroscopy (GDOES)

4.7.3 Contact angle and microhardness

The wettability of the composite surfaces has been investigated by measuring their contact angles, which is mainly determined by their chemical composition and surface roughness of the surface. A contact angle lower than 90^{o} indicates that the surface is hydrophilic [167]. A low contact angle is good for antibacterial activity because it can improve aqueous dispersion. Figure 4. 62 shows the contact angles of the as-treated samples and one untreated one as the control. It can be seen that the as-polished SS sample is relatively hydrophobic with a contact angle of about 96^{o}. The functionally graded composite surfaces have lower contact angles around 60^{o}. This could be partially attributed to the high nitrogen content in these composite coating surfaces, which can form a covalent bond with water [168, 169] and partially attributed to the increased surface roughness by the plasma treatment. Small differences in the contact angle can be observed between the composite surfaces due to their roughness variance. It seems that the rougher the composite coating surface, the smaller the contact angle and hence the better the wettability.

Hardness results are also shown in Figure 4. 62 and it is clear that the hardness of the functionally graded composite surfaces (>650 $HV_{0.05}$) is much higher than that of the untreated stainless steel (245 $HV_{0.05}$). Hardness is correlated with the mechanical properties of the composite coating layer and the S-phase layer. The hardness enhancement is mainly due to the S-phase sublayer, which can provide a high load bearing capacity for the composite surface layer. Besides, the quality of the composite coating layer also has an influence on the hardness. This is evidenced by that fact that the hardness of the three composite surfaces increased with the bias applied to the samples. This because a high bias to the samples can eliminate large Ag particles, thus making the coating layer denser and improving the overall hardness.

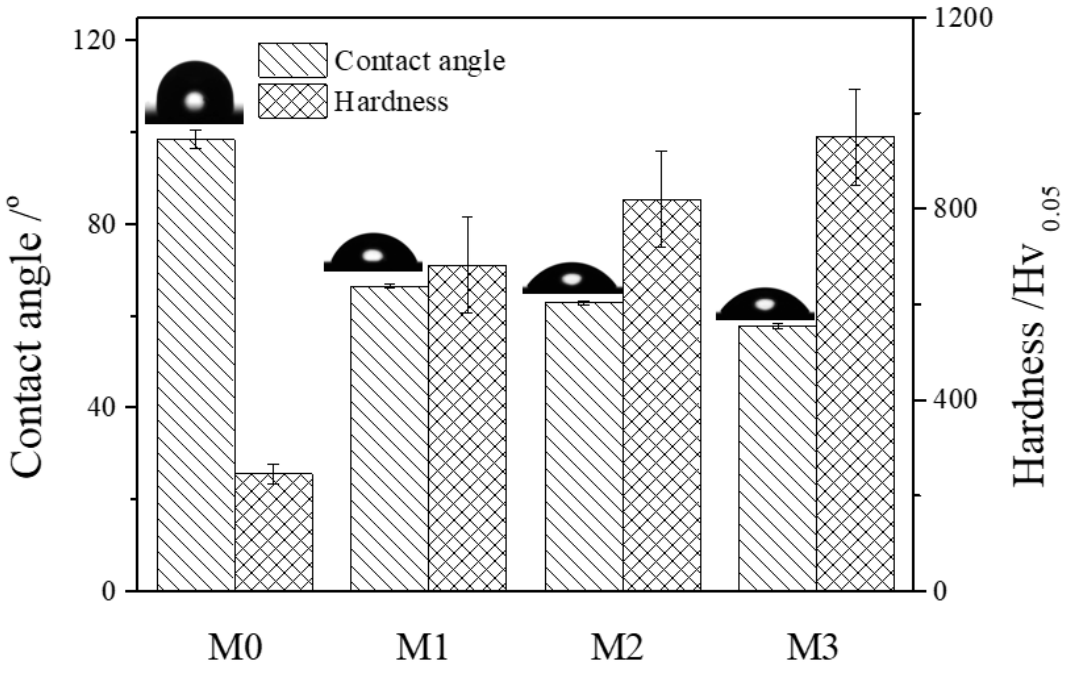

Figure 4. 62 Contact angles and microhardness of the as-deposited functionally graded composite surfaces with the untreated substrate for comparison

4.7.4 X-ray diffraction analysis

The XRD results of the functionally graded composite and the untreated surfaces are shown in Figure 4. 63. Typical γ(111), γ(200) and γ(220) peaks detected from the untreated surface confirm the fcc structured austenitic stainless steel substrate. The XRD patterns of the composite surfaces show the phases related to Ag and stainless steel. Peaks for Ag are clearly identified and no peaks for other Ag compounds are found in the XRD patterns, which indicates that Ag is inert during the sputtering and nitriding processes at 420℃. It is known that the antibacterial property is provided by the impregnated Ag particles, and so there is no reduction in the antibacterial activity by the deposition process. However, the austenitic stainless-steel phases cannot be found in the composite surfaces, because nitrogen has diffused into both the sputtered SS particles and the substrates during the double glow plasma co-alloying process. The

saturated nitrogen atoms can cause lattice expansion within the SS, which induced peak left shift [170, 171]. Thus, hard SS particles can be formed during the double glow plasma co-alloying process. Regarding the relative amount of the Ag and SS particles within the composite coating, the intensities of the Ag and S-phase peaks vary between different samples. No peaks for chromium nitride can be detected within the composite coating, which can cause degradation of the corrosion resistance [172]. Thus, this indicates that there is no precipitation of chromium nitride at 420℃.

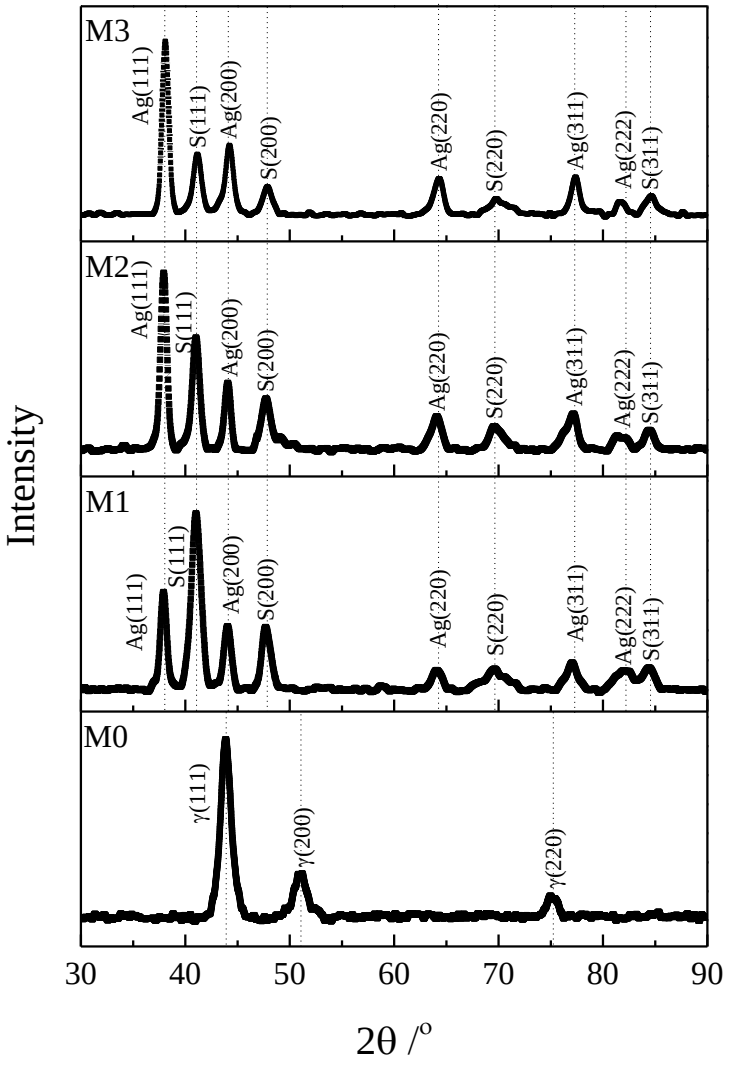

Figure 4. 63 XRD patterns of the untreated SS surface and the plasma treated functionally graded composite surfaces

4.7.5 XPS analysis

XPS has been used to study the chemical status of the extreme outer surface which interacts with the environment directly. In this study, XPS has been used to investigate the chemical status of the Ag impregnated composite surface. This is important for advancing scientific understanding of the mechanism involved in double glow plasma co-alloying and for interpreting the antibacterial results to be reported in Section 4.7.8.

High resolution XPS spectra of Ag 3p, N 1s, Fe 2p and Cr 2p are shown in Figure 4. 64. Two etching cycles (60s for each cycle) by Ar ions are used to verify the consistence of the chemical status. As can be seen from Figure 4. 64, the spectra from the 3 scans overlap well with each other, indicating that the chemical status of the near surface is uniform and stable.

Two obvious peaks belonging to $Ag3d_{3/2}$ and $Ag3d_{5/2}$ can be found at 373.8 eV and 367.8 eV in the Ag 3p spectra, which are attributed to Ag and AgO, respectively. The appearance of AgO may be due to the reaction between Ag and O_2 in the ambient air. The N 1s spectra exhibits two pronounced peaks at 396.4 eV and 400.6 eV, which correspond to iron nitride and nitrogen [173, 174], respectively. Gammon *et al.* suggested that the component at 400.6 eV may come from N in a pyrrole-like configuration [175]. This indicates that some of the chemisorbed nitrogen atoms may have reacted with Fe in the SS particles while others are interstitial atoms in the matrix to form the S-phase.

Peaks for Fe $2p_{3/2}$ and Fe $2p_{1/2}$ can be found at 711.0 eV and 724.8 eV attributing to Fe^{3+} and Fe^{2+} [173], respectively. However, a weak peak at 706.7 eV attributed to Fe^{0} can be distinguished in the Fe 2p spectra. This is due to the 'sputtering and deposition' mechanism for the formation of the S-phase [92]. Chromium atoms substitute the lattice

positions of the iron atom in stainless steel and their valence states are counted as zero. However, the XPS results indicate that the surface chromium atoms transferred into trivalent states [176]; two broad peaks located at 576.7 eV and 586.7 eV in the Cr 2p spectrum correspond to Cr $2p_{3/2}$ and Cr $2p_{1/2}$ of Cr^{3+} [177], which are helpful to prohibit corrosion.

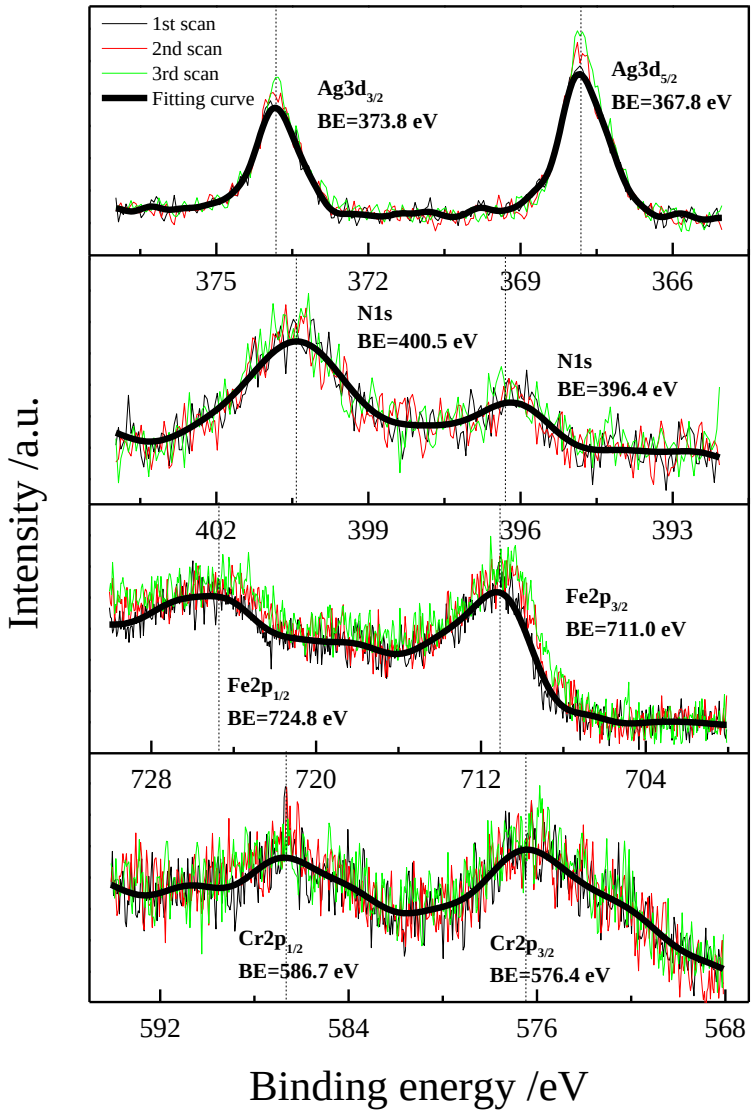

Figure 4. 64 High resolution XPS spectra of Ag 3d, N 1s, Fe 2p and Cr 2p of Ag impregnated functionally graded composite coating

4.7.6 Scratch resistance

Scratch testing can be used to assess the quality and adhesion of the composite coating layer. In this study, the scratch resistance of the Ag impregnated surface layer is essential to keep its antibacterial function. Thus, the durability of the coating has been evaluated by progressively increasing load during the scratch tests from 1 N to 10 N. The normal load on the indenter is transferred to the front half of the tip and will cause bending of the coating. When the internal stress is sufficient, cracks tend to initiate at defect sites within the coating and then propagate to cause coating failure [178]. Figure 4. 65 (a) shows the applied normal load, recorded tangential load and acoustic emission signals during the scratch tests, and the insert image is a typical scratch track on M1. It can be seen that all three composite coatings presented excellent scratch resistance, while no obvious change of the slope of the tangential force during the progressive load scratch tests and no peeling off occurred.

Acoustic emission signals were also recorded which detect the generation of cracks and can be used to evaluate the quality of the coating. The acoustic emission signals of S1 are higher than that of the S2 and S3 because more large Ag particles were impregnated in S1 which may decrease the scratch resistance of the composite coating. Several tensile cracks can be found within the track while there is no buckling. It suggests that the composite surface may have failed due to cohesive failure by through-thickness cracking (Figure 4. 65 (b)).

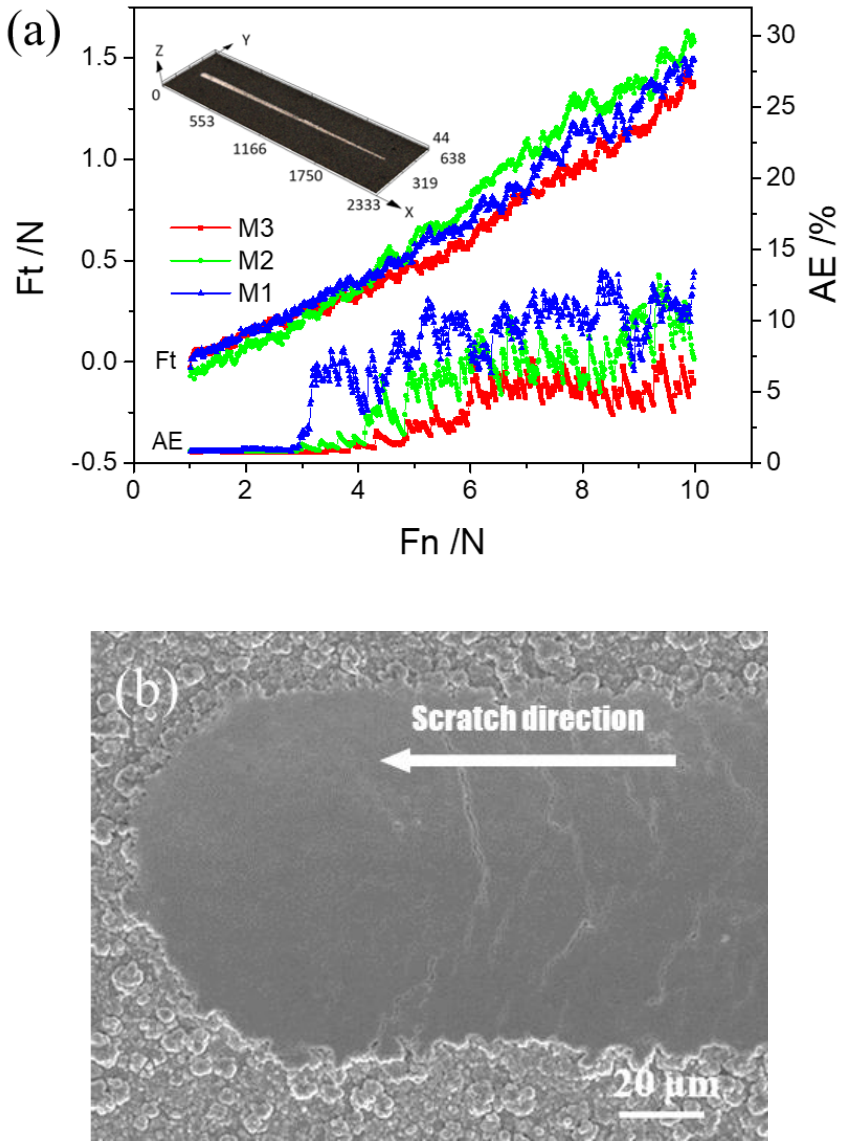

Figure 4. 65 Scratch tests under progressive increasing load from 1N to 10N. (a) normal loads Fn, tangential loads Ft and acoustic emission signals during the scratch tests; the insert shows a 3D scratch track. (b) SEM image of the scratch track at the ending position

4.7.7 Wear resistance

Wear of bio-functional surfaces is inevitable during service and wear resistance is important for a long-lasting antibacterial composite surfaces. Previous studies indicated that a hard S-phase layer can enhance the load bearing capacity of the composite surface and then improve the wear resistance under dry friction conditions [77, 78, 98]. In this study, the in vitro study of the bio-functional composite surfaces has been carried out

within Ringer's solution to simulate the body fluid environment, and the load, frequency and time of the tests are 5 N, 5 Hz and 10 min, respectively. Figure 4. 66 (a) shows that the three composite surfaces present similar friction coefficients against a Si_3N_4 ceramic ball but their friction coefficients are clearly lower than that of the stainless-steel surface under the same tribological conditions.

Besides, the wear rate of the untreated stainless steel is larger compared to that of the composite surfaces (Figure 4. 66 (b)). In comparison, the wear tracks of the untreated stainless-steel surface and the composite surface (M1) are shown in Figure 4. 67 (a)&(b) respectively, and the EDS results of the selected positions are summarised in Table 4. 11, which are helpful for understanding the wear mechanisms involved.

Rough surfaces with deeply scratch grooves and peeled-off craters are observed from the wear track on the surface of the stainless steel (See Figure 4. 67 (a)), while the wear track of the composite surface is more uniform. It can be seen that the adhesive mode [179] has dominated the wear of the untreated stainless steel surface. On the other hand, shallow scratch grooves formed on the Ag impregnated composite surface indicate the mild abrasive mode of wear on the composite surfaces. This is because the composite coating layer is formed by hard nitride stainless steel nanoparticles and soft Ag particles; the former can reduce the generation of abrasives due to high hardness and the letter could prevent material transfer between the friction pair due to its solid lubricant nature. In addition, the hard S-phase sublayer can provide high load bearing capacity for the composite surface, thus improving the wear resistance.

Ringer's solution may have also acted as a corrosive agent during the friction tests. However, no corrosion occurred on the composite surface during the corrosion-wear

tests. This is because the low temperature nitriding process can avoid the precipitation of chromium nitrides [92].

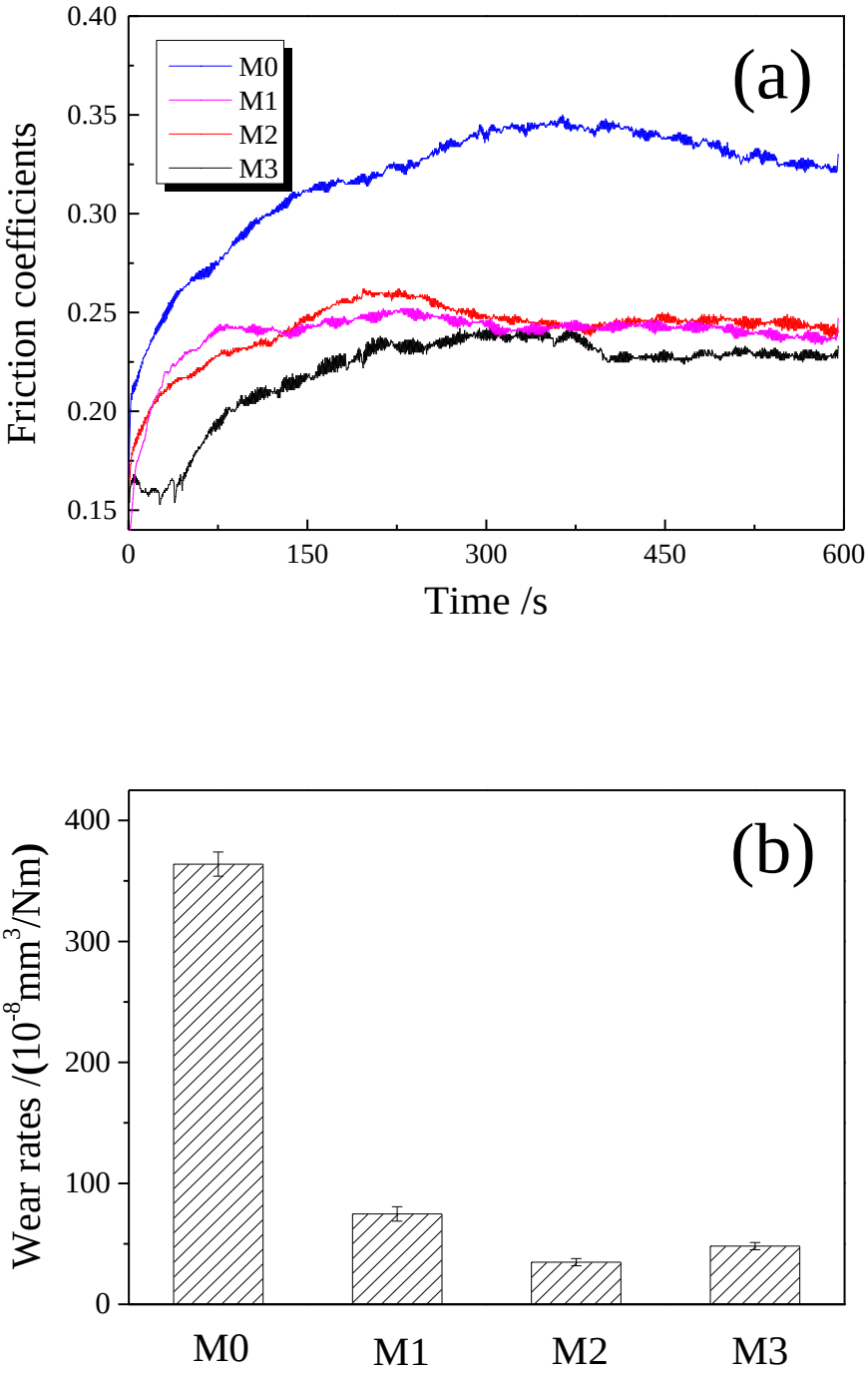

Figure 4. 66 Friction coefficients and wear rates of the untreated surface and the composite surface under the lubrication of Ringer's solution (5 N, 5 Hz, 10 min)

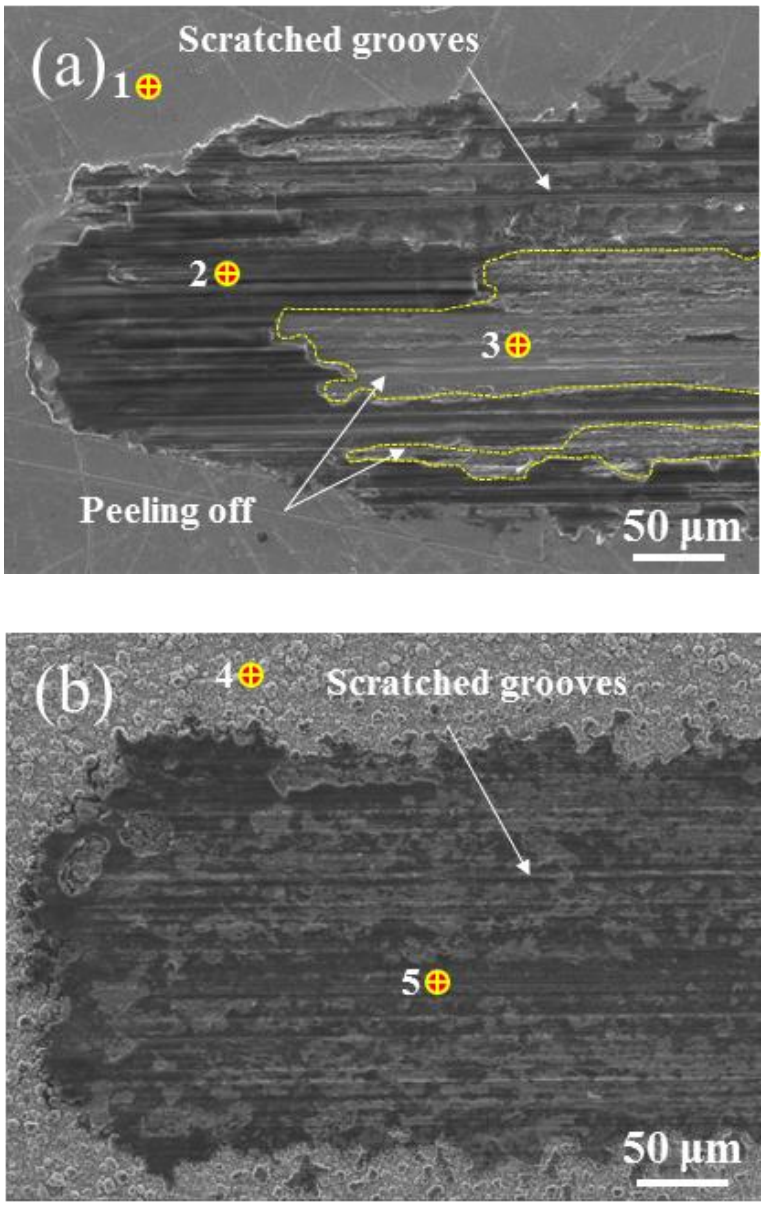

Figure 4. 67 Morphologies of the wear tracks of (a) untreated SS surface and (b) Ag impregnated composite surface, carried out in a Ringer's solution

Table 4. 11 EDS results for the points shown in Figure 4.67 (at. %)

Point	Fe %	Ni %	Cr %	Ag %	Si %	O %
1	66.59	8.36	19.14	0	0.87	1.79
2	28.22	4.08	8.04	0	13	45.17
3	50.77	7.12	14.33	0	1.31	23.6
4	56.89	6.43	13.6	18.36	0.76	1.92
5	29.62	2.95	5.26	13.61	5.66	42.46

4.7.8 Antibacterial properties

The antibacterial activities of as-deposited functionally grade composite surfaces and controls to Gram-negative bacteria (*E. coli*) have been investigated using a spread plate method. Colonies formed from viable *E. coli* after 5 h contact with the surfaces are shown in Figure 4. 68 and the numbers of colonies are used to quantitatively evaluate the antibacterial activities of the surfaces. Figure 4. 69 shows that the surviving number of *E. coli* after 5 h contact decreased as a function of the silver contents. Control surfaces with 0% of silver exhibited a colony forming units (CFU) of 267.4. The composite surface with a low content of Ag (8 wt. %) presented a reduced average number of CFU of 69.5, whereas for the composite surfaces with a higher silver level of 15 wt. % & 25 wt. %), the surviving number of the CFU further reduced to 4.25 and 3.07, respectively.

The antibacterial process is influenced by various factors such as the content of antibacterial agents, contact time, surface roughness and so on [98]. In this study, the composite surfaces are formed by sputtered Ag and SS particles. However, to our knowledge, the SS nanoparticles do not have antibacterial activity. Thus, the antibacterial property should be attributed to the Ag particles. Though the antibacterial mechanism of Ag is not fully understood, a common view is that the higher the content of Ag, the higher the antibacterial efficacy [180]. However, as Ag is a noble metal, a balance between the content of Ag and the antibacterial efficacy is needed for commercial applications.

Previous studies have indicated that the inactivation rate increases with the contact time, and typically 3-6 hour is sufficient to distinguish the antibacterial efficacy of the Ag impregnated material [77, 181]. In this study, the contact time was set to 5 h to evaluate the antibacterial properties of the composite surface. It can be seen from Figure 4. 68

that the Ag impregnated surfaces showed a much better antibacterial activity than the control. However, the results also indicated that the antibacterial efficiency is related to the percentage of Ag on the surface. Low Ag content surface may take a longer time to inactivate the same amount of bacteria but the composite surface with about 15% Ag has similar antibacterial activity as the surface with about 25% Ag.

To determine the statistically significant difference between these samples, a one-way analysis of variance (ANOVA) was used to understand the antibacterial performances and the multiple comparison table is shown in Table 4. 12. As we can see that the significance values between the control sample (S0) and the silver impregnated samples (S1, S2, and S3) are 0.047, 0.003 and 0.007, which are below 0.05. Therefore, there are statistically significant differences in the antibacterial performances during the 5h contacts between the untreated control (M0) and all the treated samples (M1, M2, and M3). On the other hand, all the significance values between the silver impregnated samples are larger than 0.05, which indicates that there is no statistical difference between these functional surfaces. However, these significance values are calculated from limited numbers of tests, more tests should be carried out in future work in order to guarantee the reliability of these results.

Surface roughness not only has an influence on bacteria adherence but also directly affects the contact angle of the surface. However, the effect of surface roughness would be marginal in our antibacterial tests. Firstly, the size of the *E. coli* NCTC 10418 is about 2 μm, which is much larger than the roughness of the composite surfaces. The roughness difference between the composite surfaces has a limited effect on bacterial adherence. In addition, 5 h is enough for the fully contact between bacteria and surfaces, and thus surface roughness would play a minor role in the antibacterial tests.

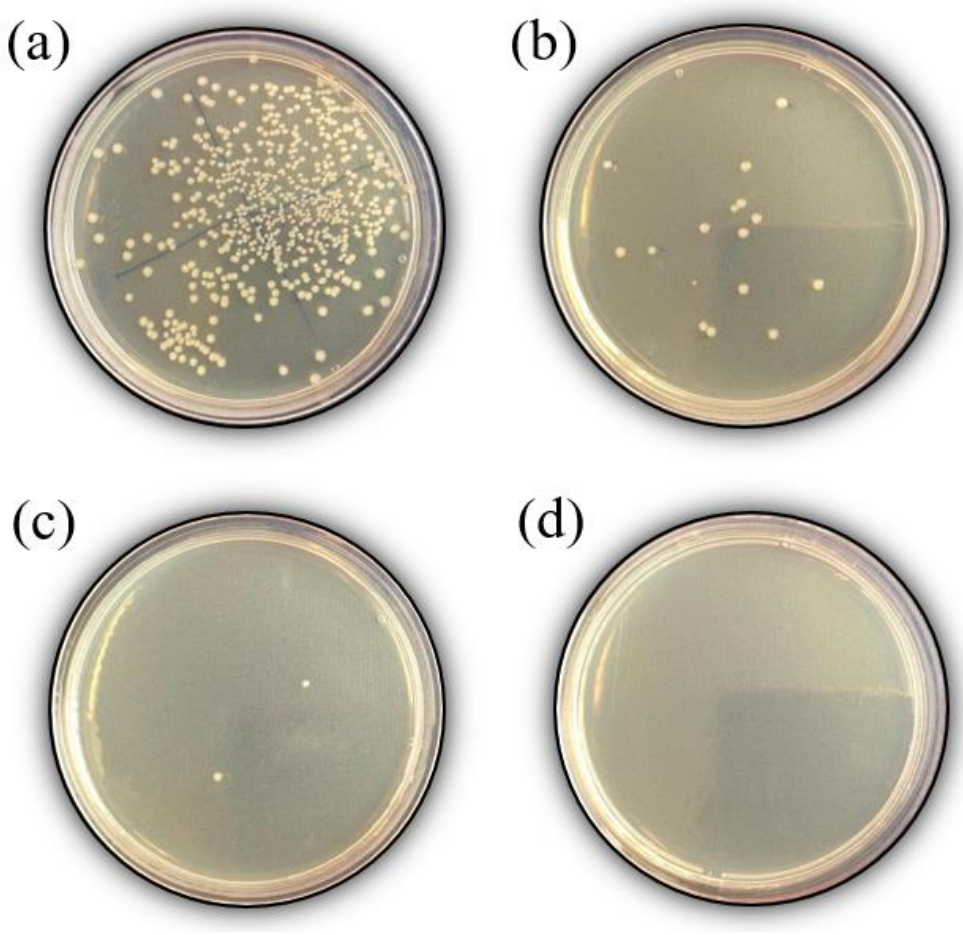

Figure 4. 68 Colonies on the tryptone soya agar plates after 5 h contact with the control and functionally graded composite surfaces, the fewer colonies, the better antibacterial activity. (a) M0; (b) M1; (c) M2; (d) M3

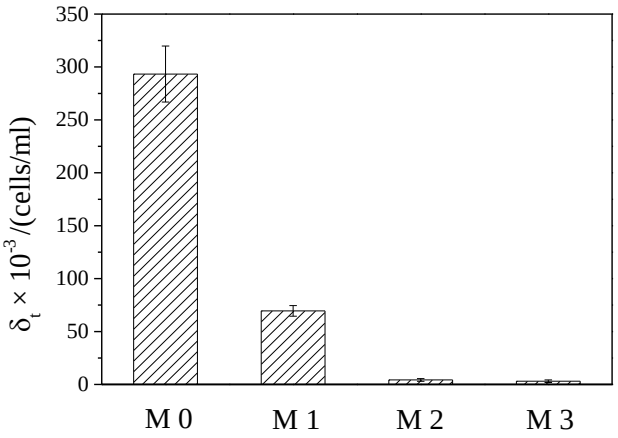

Figure 4. 69 Surviving number of bacteria δt (*E. coli* NCTC 10418) after 5 h contact with Ag impregnated composite surface and control surface

Table 4. 12 One-way analysis of the variance (ANOVA) of antibacterial results

(I) Group		Mean Difference (I-J)	Std. Error	Sig.	95% Confidence interval	
					Lower Bound	Upper Bound
S0	S1	289.000*	73.398	.007	67.78	510.22
	S2	289.611*	67.003	.003	87.67	491.56
	S3	223.667*	73.398	.047	2.45	444.89
S1	S0	-289.000*	73.398	.007	-510.22	-67.78
	S2	.611	67.003	1.0	-201.33	202.56
	S3	-65.333	73.398	.851	-286.55	155.89
S2	S0	-289.611*	67.003	.003	-491.56	-87.67
	S1	-.611	67.003	1.0	-202.56	201.33
	S3	-65.944	67.003	.809	-267.89	136.00
S3	S0	-223.667*	73.398	.047	-444.89	-2.45
	S1	65.333	73.398	.851	-155.89	286.55
	S2	65.944	67.003	.809	-136.00	267.89

*. The mean difference is significant at the 0.05 level

Chapter 5 Discussion

As described in Chapters 1 & 3, a series of research work has been conducted to develop advanced plasma surface engineering technologies based on active-screen plasma, plasma-enhanced chemical vapour deposition and double glow plasma techniques. It was the intent to use these techniques to develop novel multi-functional nanocomposite coatings reinforced by vertically aligned carbon nanotubes or silver wires.

A wide range of experimental results presented in the preceding chapter has provided a solid basis not only for plasma surface engineering technology innovation but also for advancing the scientific understanding of these techniques. Therefore, the interpretation and discussion in this chapter will focus on the mechanisms involved in the new plasma surface engineering techniques developed and in understanding the high anti-bacterial efficacy of the bactericidal surfaces generated from this research.

5.1 Mechanism of ASP co-sputtering process

Active screen plasma co-sputtering is an effective and convenient way for deposition of multielement thin films and composite coatings. In this study, this process has been utilised for preparation of different catalyst thin films, deposition of Ag contained composite coatings. A better understanding of this co-sputtering process is essential for optimising the deposition process.

Some preliminary experimental results (not presented in this thesis) revealed that stainless-steel nanoparticles could be sputtered off from the stainless-steel active screen. However, a very low sputter rate was generated due to the low density of the plasma. Thus, the hollow cathode effect has been applied to intensify the plasma density in order to enhance the sputter rate. As described in Section 3.1.2, the active screen has two parallel lids on top of samples with a fixed distance of 6 mm between them. In

order to allow the particles sputtered between the lids to reach the substrate, a mesh stainless-steel sheet was used as the bottom lid. During the sputtering process, hollow cathode effect will be generated between the lids under specific conditions and the enhanced plasma can increase the sputter rate. This simple approach provides a versatile way to prepare multifunctional surface layers by using different active screen lids for the co-sputtering process.

The hollow cathode effect is caused by the coalescing of negative glows, which can greatly rise the plasma density and light emission. Uncontrolled hollow cathode effect is commonly arisen in DC plasma treatment (nitriding and carburizing) in small holes and narrow channels, which can cause nonuniform heating or even damage the samples. In this research, the active screen co-sputtering technique makes use of the advantages of controlled hollow cathode effect in order to avoid the negative influences of hollow cathode effect, such as arcing, nonuniform heating, and edge effect [182, 183].

Hollow cathode effect is generally caused by the overlapping of glow discharges. Thus, fundamental knowledge of the glow discharge between two plan electrodes is helpful for the understanding of the co-sputtering process. The physical appearance of a glow discharge can be mainly divided into cathode dark space, negative glow, Faraday dark space and positive column [184]. Paschen's Law (Equation 7) presents a relationship for the glow discharge between the breakdown voltage, the pressure and the electrode separation distance [185]. Paschen's Law below provides a basic route to achieve the hollow cathode effect with a high density of the plasma, which is sufficient to sputter nanoparticles from the lids.

$$V_b = \frac{Bpd}{ln(Apd/ln[1+(1/\gamma)])} \quad (7)$$

where V_b is the breakdown voltage, p is the pressure inside the chamber, d is the distance between two electrodes, A, B, and γ are constants.

A schematic diagram of the active screen plasma co-sputtering process is shown in Figure 5. 1. The active screen lids are connected to the cathode during the sputtering process. Plasma is generated due to the chain reactions when power is turned on. Electrons are emitted from the active screen and collide with gases in the ambient to form gas ions. Continuous collisions within the chamber will lead to avalanche discharge.

Particles can be sputtered off from the active screen lids due to the bombardment of gas ions. It is noted that the size of the sputtered particles varies with the composition of the active screen lids, while the sputter rate is related to the density of the plasma. A high sputter rate can be generated in the area with a high density of the plasma. Thus, hollow cathode effect is essential to elevate the plasma density between the two active screen lids. Paschen's Law indicates that the breakdown voltage is mainly related to the gas pressure and the distance between the electrodes. Hollow cathode effect only generates at specific gas pressure and working power.

The plasma ambient in the chamber also affects the sputtering process. Neutral gases like hydrogen and argon only produce sputter effect without reacting with the sputtered particles. However, the situations are more complex when some reactive gases are introduced into the chamber, such as oxygen, nitrogen, and methane, which not only act as sputtering agents but also react with the particles. It has been reported that iron nitrides can be formed during the active screen plasma nitriding process [98].

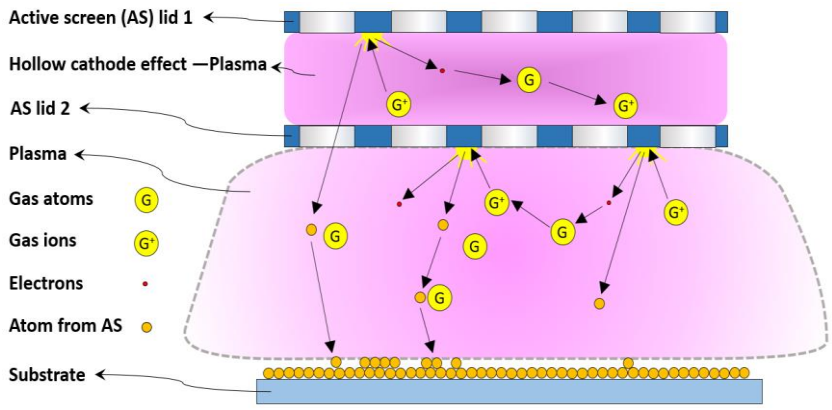

Figure 5. 1 Schematic diagram of the active screen plasma co-sputtering process

In this study, depositions were carried out under different gas pressure and power, which affected the status of plasma during the deposition processes. Figure 5. 2 shows the plasma field within the PECVD chamber under different deposition conditions. Figure 5. 2 (a) presents the status of methane plasma during the deposition of DLC with a pressure of 0.05 mbar and a power of 150 W. As no active screen was set between the electrodes, the grey plasma was dispersed between the two electrodes. The low density of the plasma is well suited for accelerating ions to form a dense solid film.

Figure 5. 2 (b) exhibits the sputtering process of the stainless-steel catalyst film, and two active screen lids were set on top of the samples which was connected to the cathode (1 mbar and 300W). A mixture of Ar and H_2 was used, leading to a pink colour plasma and strong hollow cathode effect was generated between the active screen lids and in the holes on the lids. The dense plasma generated in this situation is effective to promote the sputtering process for the deposition of catalyst films.

Figure 5. 2 (c) shows the plasma field of the failed attempt for the synthesis of CNTs, which was carried out under a chamber pressure of 1 mbar and power of 100 W in an ambient of C_2H_2, Ar, and H_2. Even though no strong hollow cathode effect was formed between the active screen lids, dense plasma layer was also generated near the lid

surfaces. This was caused by the high working power, and the strong etching effect of the plasma can inhibit the growth of CNTs. Thus, no CNTs were formed under this condition.

Figure 5. 2 (d) shows the plasma field during the successful synthesis of CNTs. The deposition was carried out under similar deposition parameters, but the working power is now 30 W. It is shown that a dense plasma ring was generated at the edge of the bottom electrode, while almost no plasma was formed on the active screen lids. In this case, the active screen has effectively blocked the plasma etching effect, which is benefited for the growth of CNTs. It is verified that CNTs can be successfully grown under this condition.

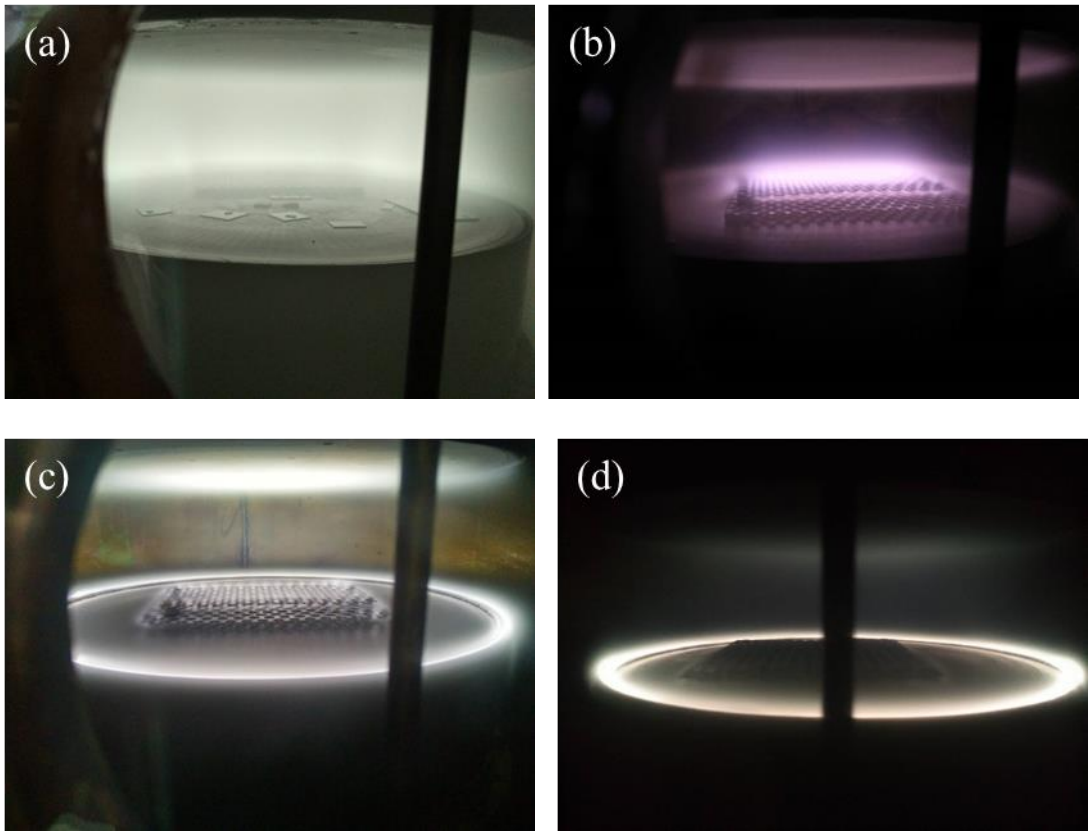

Figure 5. 2 Status of the plasma field under different conditions: (a) DLC coating; (b) SS catalyst films; (c) failure attempt for CNTs growth; (d) CNTs

The above discussion provides a basis for the understanding of the relationship between the plasma field and the deposition conditions. The plasma density is directly influenced by the gas pressure and working power, which will affect the sputtering and growth process. Hollow cathode effect can be generated in high pressure and high-power conditions, which can significantly promote the sputtering process. However, strong plasma should be avoided during the CNTs synthesis process, because the etching effect of the ions will inhibit the growth of CNTs.

5.2 Low-temperature synthesis of CNTs

5.2.1 Role of *in-situ* ASP setting

As has been reported in the preceding chapter, several types of CNTs, such as the VACNT film and free-standing CNTs, have been successfully deposited using the PECVD with purposely designed ASP setting at low temperature. TEM and Raman results have verified that all these CNTs are multiwalled CNTs.

As discussed in Chapter 2, the growth of CNTs has been widely studied in the past years, and different formation mechanisms were proposed to explain the growth process of CNTs depending on the growth methods used, such as arc discharge, laser ablation, or CVD [186-188]. The growth of CNTs in this study could be explained based on the vapour-liquid-solid mechanism [189].

It is generally agreed that the formation of CNTs is mainly due to the continuous precipitation of supersaturated carbon atoms which are released from decomposed hydrocarbons and then diffuse into the surface of the catalytic metal particles. The driven force for the diffusion of carbon atoms is ascribed to a temperature gradient. Therefore, sufficient energy is required for the continuous diffusion of carbon atoms. Consequently, the typical growth temperature for thermal CVD (T-CVD) is above 600℃, and the thermal energy is the single source for the decomposition and diffusion

processes.

In this study, CNTs have been successfully synthesised at temperatures between 400 ℃ and 500 ℃. This could be mainly attributed to the plasma effect brought from PECVD and the additional ASP setting within the PECVD chamber. First, plasma is effective in facilitating the ionization of the working gases used by promoting the dissociation of hydrocarbons, thus increasing the density of ions. Second, plasma has a heating effect which can provide more kinetic energy for the diffusion of carbon atoms [40, 47]. Therefore, the growth temperature used in this research can be much lower than in T-CVD and conventional PECVD [44, 47]. This is also supported by the fact that without the additional ASP settings, CNTs cannot be formed when using the same PECVD equipment with pre-prepared catalyst film.

However, plasma also has an etching effect which can restrict the growth of CNTs. The active screen installed in the PECVD facility between the two electrodes and connected to the bottom electrode has acted as a shield grid to filter or slow down the high-energy ions. This can lead to a desirably balanced function of the plasma, which is necessary for activating the growth process without causing undue ion etching. In addition, the thermal radiation from the active screen has contributed to the homogenous heating of the substrate surface [76].

Furthermore, it is known that the growth of CNTs occurs in the dark space with a strong electric field [184]. Ions are accelerated to bombard the cathode and secondary electrons are emitted, which accelerate through this space away from the cathode. The settings of the electrodes have a critical effect on the distribution of the plasma field. In this study, the active screen could be counted as an additional electrode, which can expand the cathode dark space to support the growth of CNTs. Clearly, the novel active screen setting within the PECVD chamber played a key role during the growth of CNTs

in terms of reducing the deposition temperature, avoiding undesirable plasma etching effect and expanding cathode dark space so as to support the growth of CNTs.

The conventional process for the synthesis of VACNT films normally consists of two separate steps: catalyst preparation and CNT growth. These steps are carried out in different facilities. Therefore, it is difficult, if not impossible, to avoid the contamination or oxidation of the catalyst during the sample transfer between the steps. In addition, this two-step process lowers the production efficiency.

The novel process developed from this research for the low-temperature *in-situ* synthesis of VACNT films combined the catalyst sputtering process with the CNT growth process, and the basic deposition process is schematically shown in Figure 5. 3. Because the catalyst sputtering and the CNT growth are carried out in the same equipment, the oxidation of the catalyst film during the sample transfer can be reduced. The formation of vertically aligned structures is attributed to the van der Waals forces between the CNTs during the growth process. As reported, the key to the successful cost-effective *in-situ* synthesis of VACNT films is to innovatively introduce the principle of ASP into PECVD. The novel design of ASP double lids can enhance the deposition of catalyst film using the hollow cathode effect and promote the growth of CNTs due to increased dissociation of carbon sources and reduced plasma etching effect.

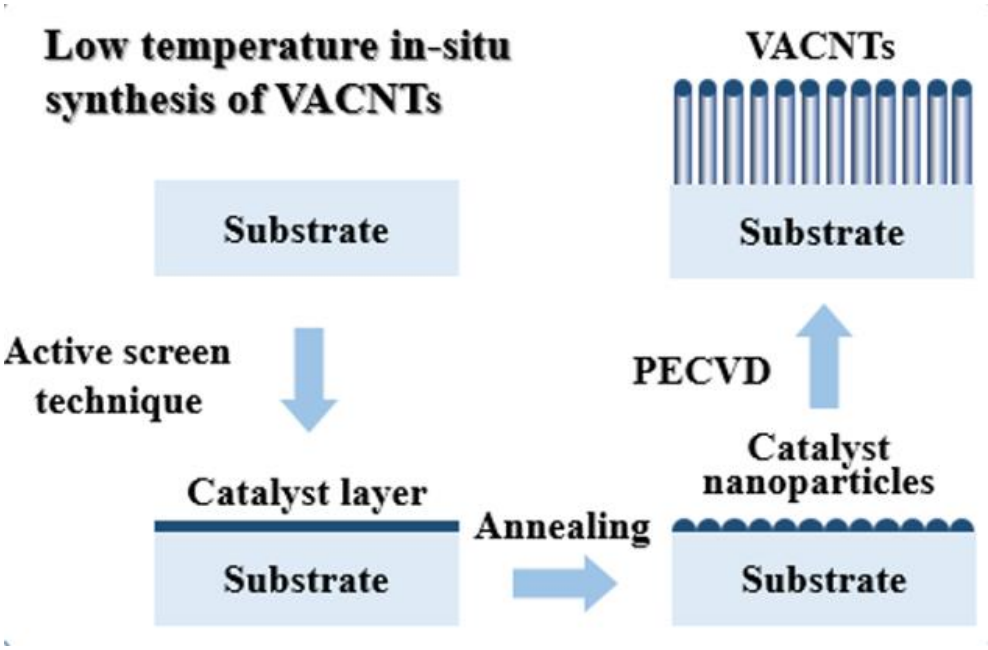

Figure 5. 3 Basic deposition process for the low-temperature *in-situ* synthesis of VACNTs

5.2.2 Growth of CNTs

Catalyst plays an important role in the growth of CNTs. Fe, Co, and Ni are common elements used as catalysts for the growth of CNTs due to their high activity to the carbon sources. However, some researchers indicated that some binary or multimetal alloy catalysts are more efficient for the growth of CNTs by increasing the rate of diffusion and reaction [190]. In this study, commercial 316 stainless-steel has been used for the growth of CNTs. In addition, noble element Ag can be added into the catalyst film to modify the growth of CNTs by changing the top active screen catalyst lids. The co-sputtering process in this study provides a cost-effective way to adjust the nuclei sites. It has been reported that some novel carbon materials like nanocoils or branched CNTs can be deposited from composite catalysts [191, 192].

In this study, TEM examination has revealed tip growth mode of CNTs, which may be related to the features of the catalyst nanoparticles deposited by co-sputtering. As shown in Figure 5. 4 (a), during the tip growth process, hydrocarbon was absorbed first

from the tip of catalyst particles, and then the precipitated carbon will push the catalyst nanoparticles up to form the CNT. The growth will be stopped when the catalyst nanoparticles fully covered by carbon and the absorption process is inhibited. However, it is difficult to determine when the growth will stop, which is related to the status of the catalyst and the deposition conditions.

The bottom growth of CNTs also happened in this study, though most of the CNTs were grown through the tip growth mode. It is known that bottom growth mode happens when the size of the catalyst particles is too large or there is a strong adhesion between the catalyst particles and the substrates. In some cases, metallic silicide can be generated between the catalysts and the Si substrate [193, 194], which can increase the adhesion. However, these interactions will cause deterioration of the catalysts and a typical solution is to add buffer layers, such as SiO_2, Ti, Al [195]. Gohier *et al.* [196] have indicated that the growth modes are determined also by the size of the catalyst particles, which is related to the thickness of the catalyst film.

As schematically shown in Figure 5. 4 (b), for the bottom growth mode, catalyst particle is seized on the substrate while hydrocarbon sources are absorbed by the catalyst particles in the bottom. The CNT is pushed up by the precipitated carbon. A closed carbon cap will be formed on one end of the CNT.

However, most of the CNTs observed by TEM in this research have catalyst nanoparticles embedded at their tips, indicating that the growth of CNTs in this research is dominated by the tip-growth mode. This can be explained by the fact that the catalyst nanoparticles deposited by the ASP process are very small with relatively low adhesion to the substrate, which are easy to be lifted during the growth process of CNTs.

Beside the CNTs, CNFs have also been formed when the Ag-SS catalyst film is used. It is supposed that these CNFs are formed based on a bottom growth mode as

schematically shown in Figure 5. 4 (c) because no catalyst particles can be found within the CNFs. The growth process should be similar to that of the bottom CNT growth as shown in Figure 5. 4 (c), but the mechanism for the formation of CNFs would be different. As discussed in Chapter 2 that a CNT rather than a CNF would be preferentially formed if carbon atoms can be supplied rapidly [38, 44, 47]. It is known that Ag has no catalytic effect for the growth of CNTs. Therefore, compared with the SS catalyst film, the Ag-SS composite catalyst film should have a weaker catalytic effect and hence insufficient carbon atoms are available for the growth of CNTs.

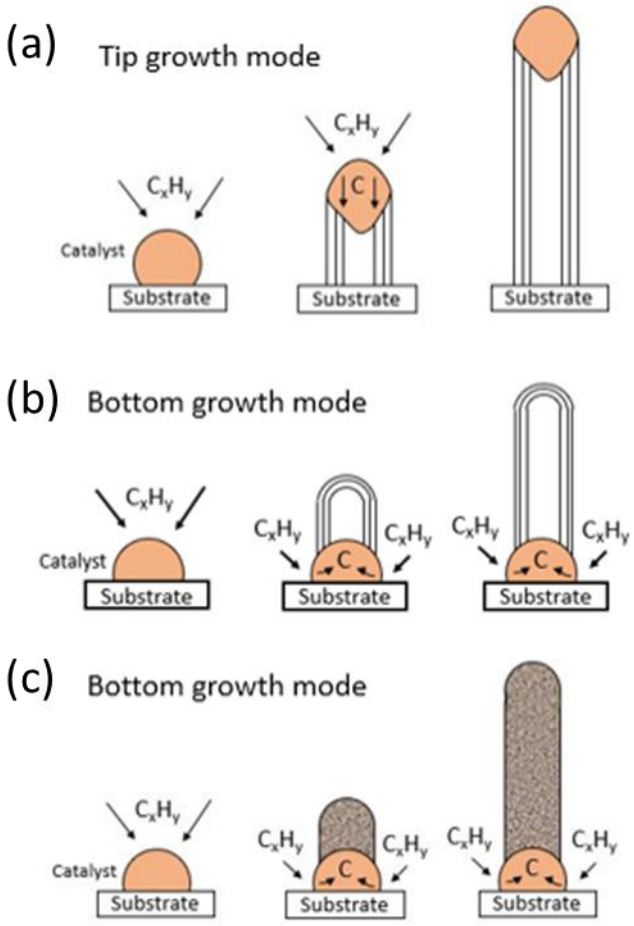

Figure 5. 4 Schematic diagrams of (a) the tip growth mode and the bottom growth modes of (b) CNTs and (c) CNFs

As reported above, the ASP technique has provided a novel approach for cost-effective

deposition of catalyst films. However, the solution-based process could be more convenient to coat catalyst films on large surfaces or 3D surfaces. Nitrate of Fe, Co and Ni can be used for the growth of CNTs. However, aggregates were formed during the drying process, which also prohibit the full interaction between the catalyst and the carbon sources. Thus, catalyst films deposited by the solution process are not suitable for the synthesis of VACNT films on large surfaces.

On the other hand, catalyst films deposited on the micro-sphere by the solution process have been proved to be feasible for the growth of VACNT films. When the metal balls and the hollow glass balls are ultrasonically washed with the catalyst suspension, a uniform catalyst film can be coated on their surfaces due to surface tension.

5.3 Formation mechanism of the metal wires

As has been reported, Ag wire reinforced composite coating can be acquired by the one-step low-temperature active screen plasma carburizing process. Solid Ag wires are formed during the deposition process with the diameter in micron scale. In this section, in order to have a better understanding of the formation mechanism of Ag wires during a sputtering process, the fundamentals of the growth 1D structures are briefly discussed. Furthermore, the formation mechanism of the Ag nanowires through the wet-chemistry synthesis is also discussed. The microstructure of the Ag wires is carefully studied so as to figure out the growth mechanism. In addition, the formation of Cu wires reinforced composite coating using the similar deposition process will be discussed for comparison.

5.3.1 Growth of Ag wires

As discussed in Chapter 2, several strategies have been developed to synthesise the metal wires. In this study, the growth of Ag wires is similar to the spontaneous growth process for the 1D structures. It is known that the reduction of Gibbs free energy or

chemical potential are the driven force for the spontaneous growth of wires. Anisotropic growth is generated due to the growth speed variation along different crystal directions. For the solution-based process to synthesise Ag nanowires, $PtCl_2$ is used as growth seeds, and $AgNO_3$ is reduced as Ag source [106]. However, there are no obvious seeds for the growth Ag wires during the co-sputtering process.

Besides, a capping agent like polyvinyl pyrrolidone (PVP) is commonly used to block some growth surface in order to get the anisotropic growth of metal wires. Thus, single crystallinity of the metal wire is usually formed through the solution-based process. It is not clear what is the driven force for the preference growth of the Ag wires during the co-sputtering process. The existence of the methane plasma to some extent may serve a similar purpose to PVP.

Similar to the solution-based growth, there should be a nucleation process at the beginning stage of the sputtering process for the formation of the Ag wires because Ag wires were only generated at the silver-rich area. As seen in Figure 4. 49, large Ag particles were formed beside the Ag wires, indicating that there is a driven force to promote the aggregation of the sputtered Ag particles. However, some of the sputtered Ag particles aggregated as a big Ag particle, while others accumulated into a Ag wire. Thus, there should be something prohibit the homogeneous nucleation of the Ag particles.

As have been reported in Section 4.1, Ag particles with different sizes can be sputtered off from the Ag lid (target) even just using the hydrogen plasma and some of the Ag particles are as large as 1μm. Figure 5. 5 shows that Ag particles are homogeneously distributed on the surface of the substrate with no sign of Ag wires. It seems that the hydrogen plasma has just played a role of impacting and eroding the Ag target to generate Ag particles. It has verified that beside these observed large Ag particles, Ag

nanoparticles are also generated during the sputtering process (Figure 4. 4). However, no Ag wires could be found when the treated is carried out in the ambient of hydrogen plasma. This indicates that the ambient of the plasma will determine the reaction within the plasma chamber, and pure hydrogen plasma is not feasible for the synthesis of Ag wires.

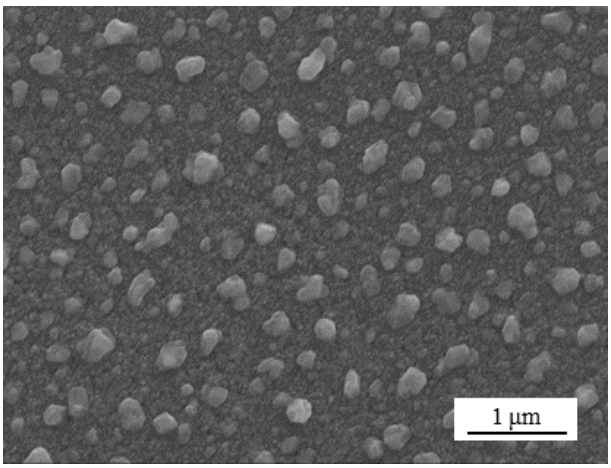

Figure 5. 5 Ag-SS catalyst film deposited using the active screen plasma technique under 200ºC for 10 min in an ambient of H_2

In addition to hydrogen, a gas mixture of H_2 and N_2 (75% and 25%) has also been used for the sputtering process to investigate the influence of nitrogen plasma. Cauliflower morphologies of the deposited composite coating are shown in Figure 5. 6, and it can be seen that large agglomerates composed of Ag and stainless-steel particles are formed during the sputtering process. This indicates that no wires can form in the nitrogen/hydrogen plasma. The reaction between the nitrogen and the stainless-steel has led to the formation of a nitrogen-rich composite coating, while the interaction between nitrogen and Ag particles is limited if any as revealed by the XPS analysis results (Figure 4. 64).

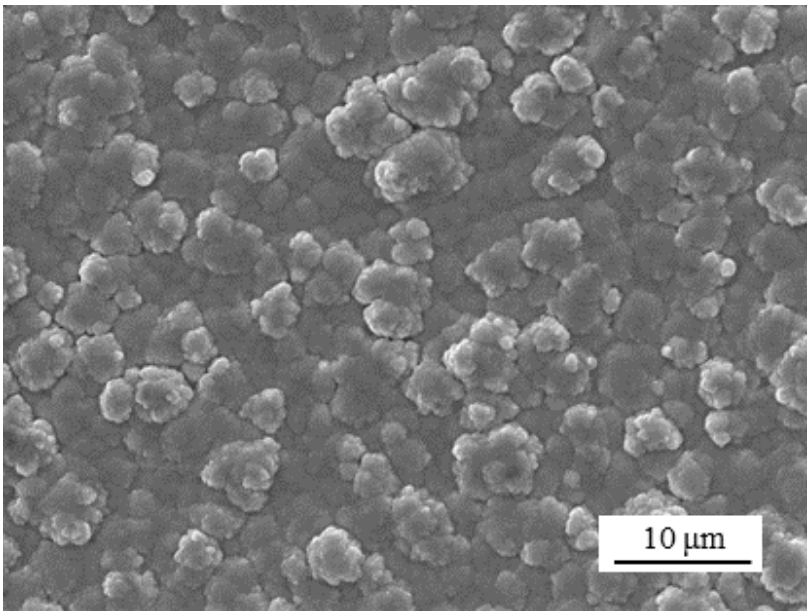

Figure 5. 6 Surface morphology of the Ag-SS composite coating deposited in an ambient of H_2 and N_2 (75% and 25%) at 420°C 20h

As reported in Section 4.6, Ag wires can be formed when methane is used for active-screen plasma co-sputtering. As shown in Figure 5. 7, Ag wires are formed in the ambient of CH_4 and H_2 (1.5% and 98.5%). The Ag wires are randomly distributed on the surface of the coating layer with varying shapes and sizes; large Ag particles are also formed and embedded in the composite coating. However, unlike the sputtering process in the ambient of nitrogen, no large agglomerates are generated after 20h sputtering, and these Ag particles are separated from each other. The as-grown Ag wires are not as straight as those deposited by the wet-chemical process. Figure 5. 3 (b) clearly shows a bent piece of Ag wire with the varying diameter at different positions. This morphology implies that most probably the as-deposited Ag wire is not a single crystal.

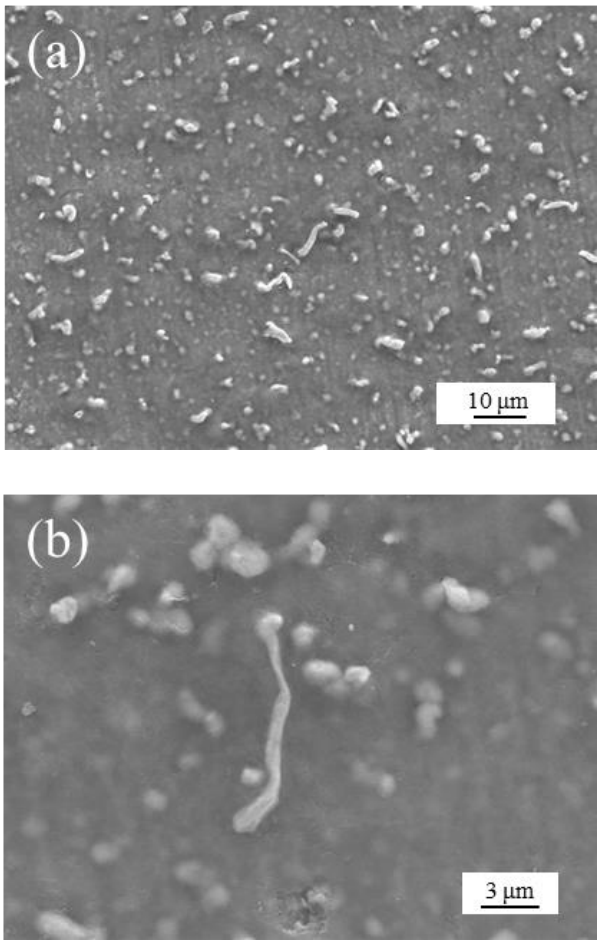

Figure 5. 7 SEM images of the Ag wires reinforced composite coating deposited in an ambient of CH_4 and H_2 (1.5% and 98.5%) at 420°C 20h

TEM investigation has been further conducted to study the structure of the Ag wires. As revealed by the SEM results (Figure 5. 7 (b)), the sizes of these Ag wires are at the micron scale, which are too large to be directly used as TEM samples. To prepare suitable TEM samples, some debris are scratched off from the composite coating and adhere to a TEM Cu grid with a carbon film. A relatively small piece of Ag wire has been found after several trials and the TEM images of a break Ag wire are shown in Figure 5. 8.

It is shown in Figure 5. 8 (a) that the Ag wire is not straight, and the diameter of the thin rod area is around 0.65 μm. The right end of the Ag wire is thicker than the rod area, which is supposed to be the 'root' of the Ag wire. Some nanoparticles are found to be attached on the surface of the Ag wire, and the size of these nanoparticles ranges

from 5 nm to 50 nm as shown in Figure 5. 8 (b). The microstructure of the Ag wire cannot be viewed directly because the Ag wire is too thick for the electron beam to transmit.

Figure 5. 8 (c) shows that several large agglomerates of nanoparticles are formed at the edge of the 'root' area. These agglomerates are not as dense as the Ag wire, but it is believed that these supplements could be helpful for thickening the Ag wire. The SAD pattern is shown in Figure 5. 8 (d) indicates that these agglomerates are formed with Ag nanoparticles and stainless-steel nanoparticle.

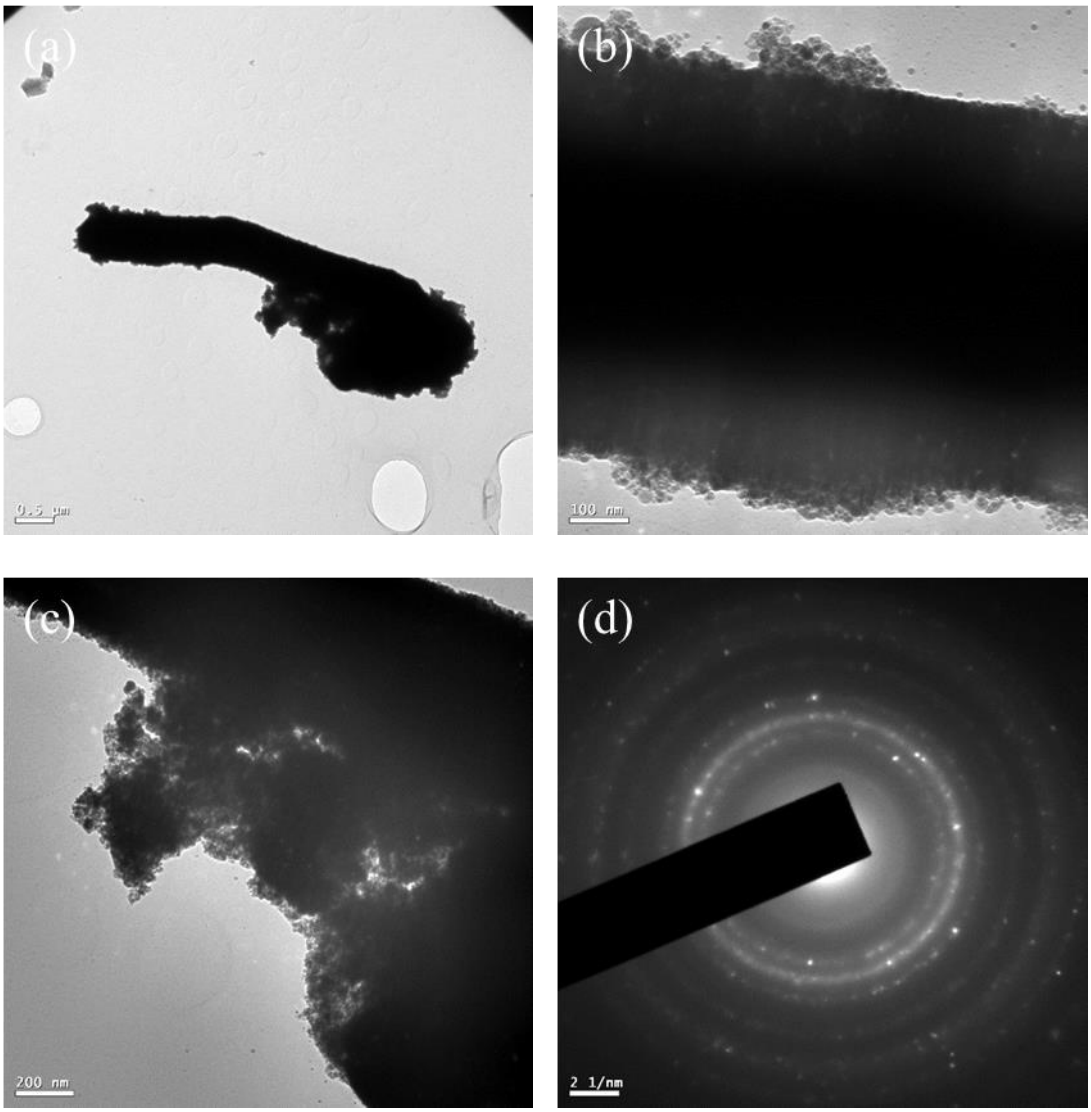

Figure 5. 8 TEM images of the as-deposited Ag wire, (a)&(b)&(c) are morphologies of the Ag wire; (d) SAD pattern of the selected area in (c)

Based on the microstructures of the Ag wires and the discussion above, a growth mode is proposed to explain the formation mechanism of the Ag wire. Figure 5. 9 depicts the schematic diagram of the proposed formation process of a Ag wire. It is noted that although both Ag and stainless-steel nanoparticles are generated during the co-sputtering process, the Ag nanoparticles are agglomerated to form some large Ag clusters which are building blocks for the growth of the Ag wire.

Unlike the continuous growth of the Ag clusters in the ambient of nitrogen, the size of the Ag particles could be limited by the existence of carbon although the function of the carbon plasma is still not clear. Ag clusters condense on the sample surface and the continuously generated Ag clusters will attach to the preferred growth plane, thus driving the growth of the Ag wires (Figure 5.9).

Along with the axial growth of the Ag wire, Ag clusters and nanoparticles are also adsorbed on the surface of the Ag wire to make it thicker. In the meantime, the incorporation of stainless steel nanoparticles sputtered from the SS lid within the Ag wire during the growth process would act as defects and affect the axial growth of the Ag wire. This would change the preferred growth orientation, thus resulting in the curly Ag wire. Besides, some of the large Ag particles may also play a role in adjusting the preferred orientation. It is thus supposed that the Ag wire is formed with a Ag crystalline core, while the continued adsorption (or deposition) of Ag clusters will induce the axial and radial growth. Though the effect of the carbon plasma is not clear, it is considered that the carbon ions may have a catalytic effect for the growth of Ag wires [197].

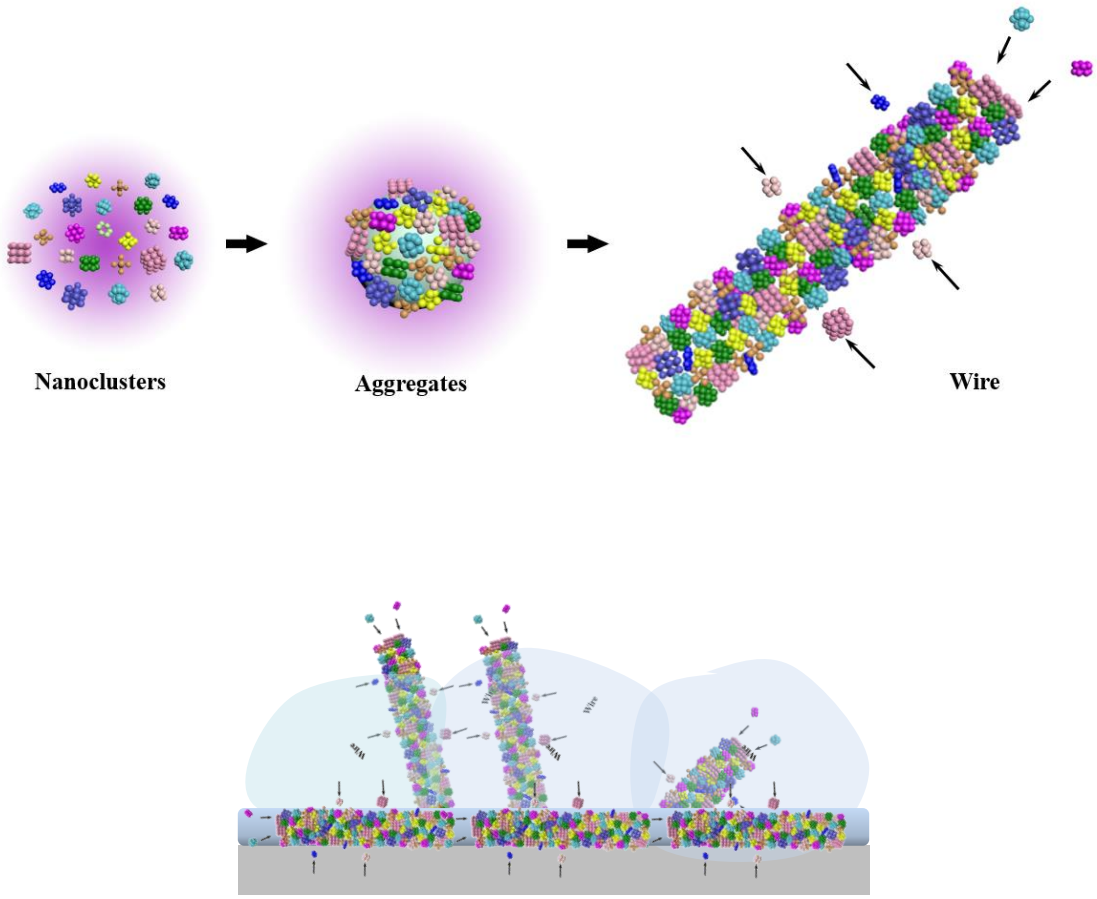

Figure 5. 9 Schematic diagram showing the growth mechanism of the Ag wires and the Ag wires reinforced composite coating

5.3.2 Growth of Cu wires

The active screen plasma carburizing process has been proved to be effective for the formation of Ag wires and a growth mode is proposed in the preceding section. In order to acquire more information to support this wire growth mechanism, a similar process has carried out to explore if Cu wires can be formed using the similar co-sputtering process. The active screen settings are similar to that used for the growth of Ag wire, but the Ag lid is replaced by a Cu and the sputtering processes are carried out at 1mbar for 2 h for heating and cleaning followed by co-sputtering at 3 mbar for 18 h in a gas

mixture of 1.5 %CH_4 + 98.5 %H_2 (i.e. A3 condition in Table 4.1). AISI 316 stainless steel dishes (Ø25.4×5 mm) were utilised as the substrate.

The surface morphologies of the as-deposited Cu reinforced composite coating are shown in Figure 5. 10. Some of the typical wire structures can be seen in Figure 5. 10 (a) and it is clear that the ASP co-sputtering process is also feasible for the production of Cu wires. However, different from the Ag wires that embedded inside the composite coating, these Cu wires are grown through the composite coating. The shapes of these Cu wires are different from each other. While some of them are thick and short with a diameter of 3 μm, others are long and thin with a length around 20 μm and a diameter of around 500 nm. The stubby Cu wires look similar to the Ag wires which are curly with varying diameters while the long and thin Cu wire looks like a long-thin straight stick.

An enlarged image of the root area of the long and thin Cu wire is shown in Figure 5. 10. The thick root grown from the composite coating revealed crystalline planes. This indicates that the Cu wire has a preferred growth orientation and the thin Cu rod is formed from the tip of the Cu root. Particles can be viewed on the surface of the Cu wire, which act as feeds for the growth of the Cu wire.

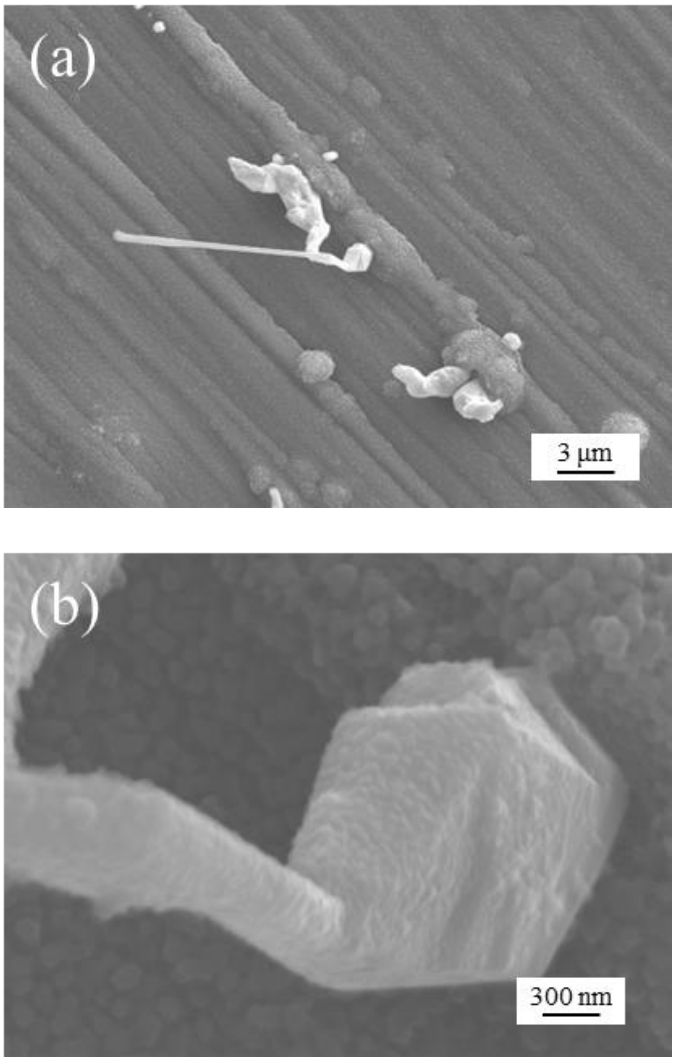

Figure 5. 10 SEM images of the surface morphologies of the Cu wire reinforced composite coating

EDS mappings of the composite coating have been conducted to investigate the element distribution of Cu, and Fe. Figure 5. 11 (a) shows an SEM image of Cu wire with a length of 12.3 μm and an average diameter of around 1.5 μm. The composition of the selected area is shown in Figure 5. 11 (b)&(c). Compare to the SEM image, it can be seen from Figure 5. 11 (b) that the wire area is rich in Cu and lean in Fe, verifying that this a Cu wire. Besides, Cu is also detected from the surface which indicates the sputtered Cu nanoparticles are distributed on the whole surface. Figure 5. 11 (c) shows the Fe mapping with few irons in the wire area, indicating that the wire is mainly formed with Cu.

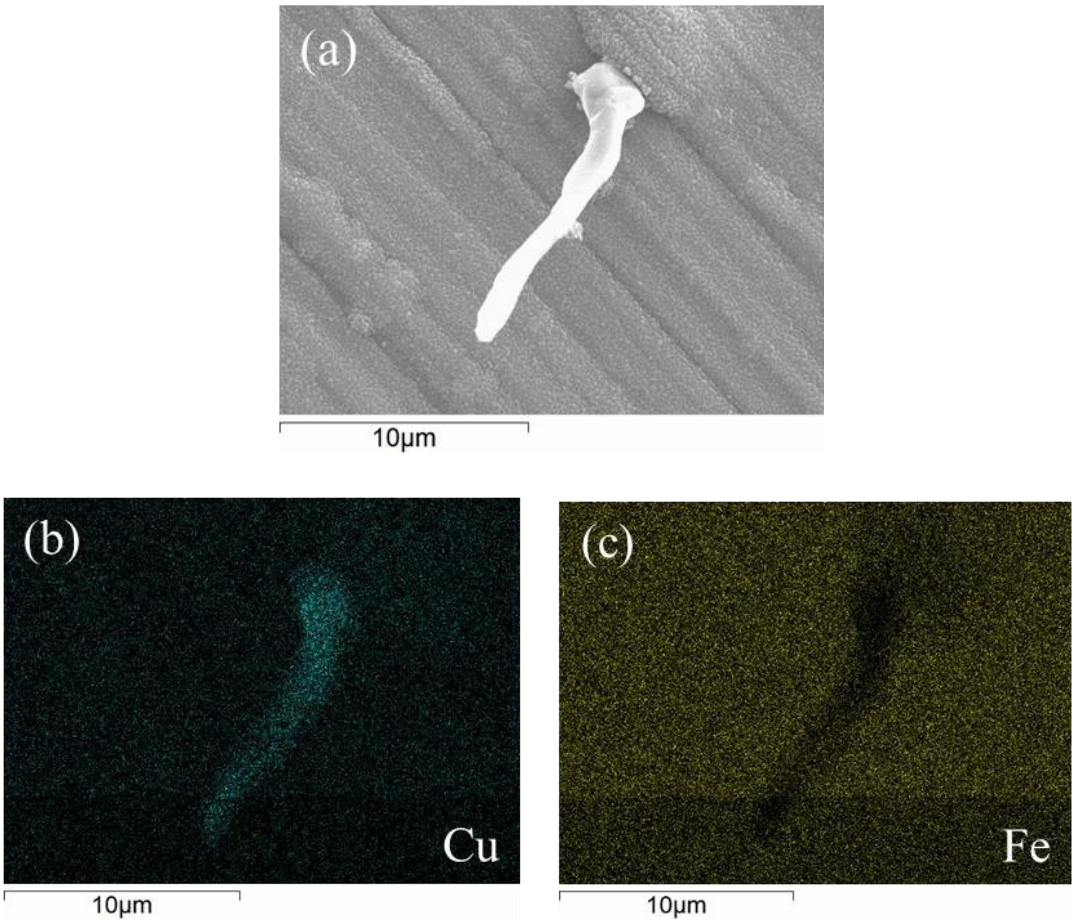

Figure 5. 11 EDS mapping of the Cu wire composite coating: (a) SEM image; (b) Cu mapping; (c) Fe mapping

Similar TEM sample preparation method as for Ag wire has been used to prepare Cu wire TEM samples, and Figure 5. 12 shows a Cu wire on the TEM grid. The stick part of the Cu wire is long and straight with a diameter of 0.6 μm whilst the root area of the Cu wire is thick with diameter of around 1.2 μm. Figure 5. 13 shows nanoparticles slicked onto the surface of the Cu wire with an average size of about 10 nm, and some nanoparticles can be viewed inside the edge of the Cu wire.

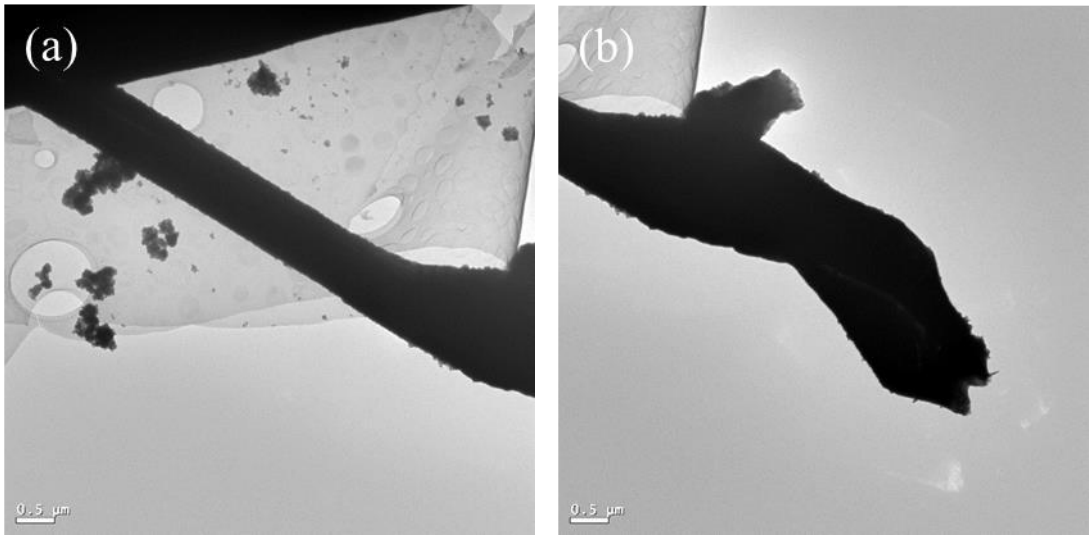

Figure 5. 12 TEM images of the as-deposited Cu wire

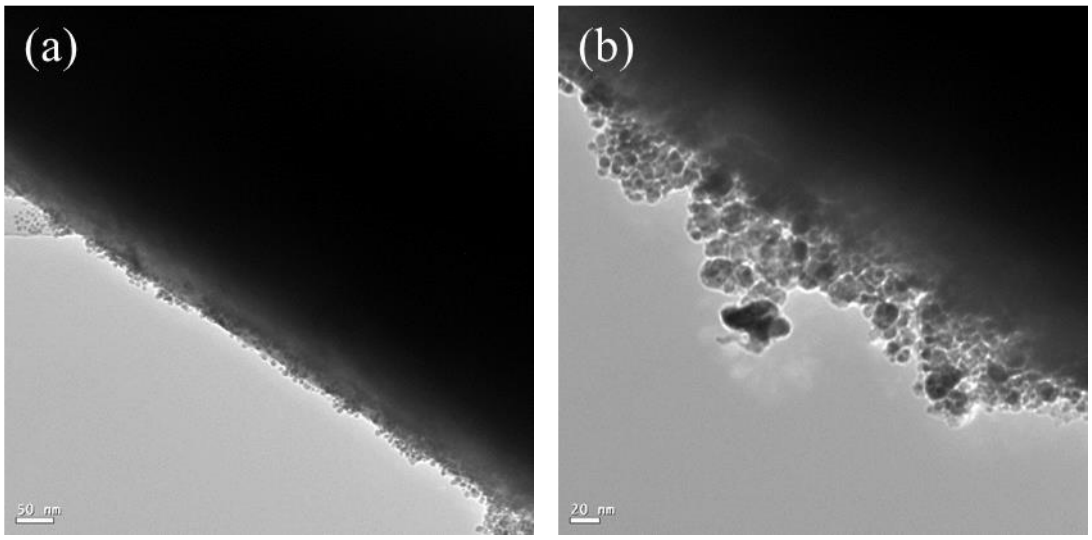

Figure 5. 13 TEM images of the nanoparticles on the surface of the Cu wire

Consequently, the above supplementary study on the formation of Cu wire during ASP co-sputtering supports the growth mechanism proposed in the last section for the growth of Ag wire. Cu cluster was formed with the Cu nanoparticles and acted as a seed for the growth of Cu wire at the beginning. The continuously absorbed Cu nanoclusters will accumulate on the preferred orientation to feed the growth of the Cu wire. The formation mechanism of the stubby Cu wires may attribute to the defects within the Cu

wire caused by the stainless-steel nanoparticles, leading to the bending Cu wires. On the other hand, large Cu clusters may also affect the preferred growth direction of the Cu wire.

However, the formation mode of the long and straight Cu wire might be slightly different from that for the thick Cu or Ag wires. This could be attributed to the difference in the sputtering behaviour of Ag and Cu under the same plasma co-sputtering process. It has been observed that some large Ag particles are in micron scale while most of the Cu particles are in nanoscale. Thus, whilst the growth of Ag wire could be interrupted by the large Ag particle, these Cu nanoparticles would have less effect on the change of the preferred growth orientation of the Cu wire. Hence, long and straight Cu wires can be formed during the ASP co-sputtering process.

In short, based on the SEM and TEM observations, a vapour-solid mechanism has been proposed to explain the formation of Ag wires and Cu wires during the active screen plasma carburizing process.

5.4 Formation of fibre reinforced composite coatings

As discussed in Section 2.1, stimulated by the excellent properties of one-dimensional (1D) fibres reinforced bulk composite materials, 1D fibres reinforced composite coating has drawn the attention of some researchers. Although painting or electroplating was applied to fabricate 1D composite coatings by adding fibres into the solvents, aggregation of the thin fibres can degrade the uniformity of the coatings. In this study, novel approaches have been developed for the generation of 1D fibres reinforced composite coatings using the PECVD method and the ASP technique.

5.4.1 CNTs reinforced composite coatings

As described in Chapter 3, the CNTs reinforced composite coatings have developed using a two-step strategy, and Figure 5. 14 shows the schematic diagram of the two-

step process.

Vertically aligned CNTs are produced as the reinforcements and PECVD or PVD is applied for the formation of the composite coating. The experimental results reported in Chapter 4 demonstrate that the thickness and the density of the VACNT film can greatly affect the formation of the composite coatings.

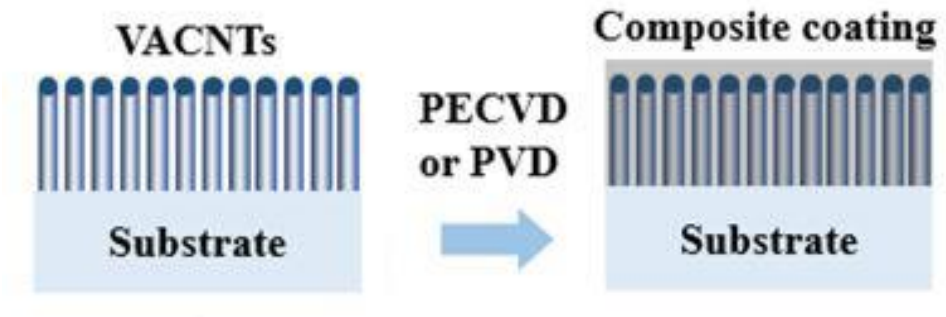

Figure 5. 14 Schematic diagram of the CNTs reinforced composite coating

As shown in Figure 4. 7, the VACNTs grown from stainless-steel catalyst films are densely packed. This would be a barrier for the diffusion or penetration of the matrix materials into the CACNT film. Furthermore, for a given density, it is difficult to fill all the gaps between the CNTs if the CNTs are too long.

The results of the Pt-CNT and Ag-CNT composite coatings have demonstrated that the sputtering PVD process is not suitable for the deposition of fully composited structures. This is because the large particles sputtered from the Pt and Ag targets are difficult, if not impossible, to penetrate the dense VACNT film.

The Ag-CNT produced by sputtering PVD has resulted in a double layer structure (Figure 4. 43) with a mechanical bonding formed between the sputtered layer and the VACNT layer. On the other hand, the sputtered Pt nanoparticles can penetrate into the VACNT film. However, many of these nanoparticles will accumulate on the tips of the CNTs without the formation of a continuous layer on the top of the VACNT film.

Clearly, a dense CNT reinforced composite coating cannot be produced using the sputtering PVD of Ag or Pt on the VACNT film. However, the relatively porous double layer surface composite structure could be used in sensors or energy storages in view of their large surface areas and high conductivity [198].

The PECVD process provides a feasible way for the two-step formation of the CNT reinforced composite coating because the vapour phase could diffuse through the gaps without damaging the vulnerable CNTs. However, densely packed CNTs also can cause accumulation of a surface layer. Thus, decreasing the density of the VACNT film is the key to the formation of the fully composited coating. In this study, a novel composite Ag-SS catalyst film has been developed to decrease the density of the VACNT film. The noble element Ag can inhibit the growth of CNTs because Ag does not have a catalytic effect for CNT growth.

Fully reinforced DLC-CNT composite coating has been achieved by the continuous diffusion of amorphous carbon into the low-density VACNT film, thus forming a columnar structured nanocomposite coating. The reinforcements have provided the composite coating with significantly increased electrical conductivity. This could pave the way for the functional application of the CNT reinforced nanocomposite coating.

It should be admitted that the adhesion of the CNT reinforced nanocomposite coating to the substrate is not as good as that of commercial DLC coatings. Hence, further explorations are required to enhance the bonding of the composite coating, for instance, the use of an interface binding layer (such as Cr or Ti).

5.4.2 Metal wires reinforced composite coating

As has been reported, *in-situ* Ag wires reinforced composite coatings have been successfully produced using the ASP co-sputtering technique. This one-step deposition process makes it possible to achieve the metal wires reinforced composite coating with

the metal wires randomly formed within the composite coating without further modification. These metal wires not only act as reinforcements but also equip the composite coating with some novel functional properties, such as antibacterial property, antiadhesive property, and low friction coefficient. However, there are still some limitations to the ASPC deposition process. For example, the shape and the distribution of the Ag wires are difficult to control. Therefore, further work is required to optimise the process.

The ASP co-sputtering process has provided a feasible way for the deposition of metal wires reinforced composite coating. This is evidenced by the fact that other than the Ag wires, Cu wires can be also formed by using a Cu lid. However, no stainless-steel wires can be observed. This implies that only some elements are available for the formation of the metal wires. It is speculated that Au wires could be produced using the same or similar ASP co-sputtering process in view of its similar periodic table position and hence chemical properties as for Ag and Cu.

The matrix of the composite coating is mainly composed of carbon, stainless-steel, and Ag nanoparticles. The carbon plasma has played an important role in the deposition of the composite coating. In addition to the catalytic effect of the carbon plasma, solid carbon is also generated from the hydrocarbon source as the matrix. Raman spectra have revealed that graphite-like carbon other than diamond-like carbon has led to the relative soft carbon layer.

5.5 Bactericidal surfaces

Two types of bactericidal surfaces have been developed from this study, which are the VACNT films and the Ag contained composite coatings. These surfaces have proved to be effective to kill some pathogenic microorganisms after contact for several hours.

As discussed in Chapter 2, bacteria can be killed through physical and chemical

processes. Mechanical damage to the cell walls of the microbes via scratching or rupturing during the contact process is the main mechanism for the physical killing process. The chemical antibacterial process is more complex, in which the active chemical agents can inhibit or regulate enzymes for cell wall biosynthesis, protein synthesis, nucleic acid metabolism or repair. In addition, the chemical agents can also disrupt the structure of cell membrane.

5.5.1 VACNT antibacterial surfaces

Carbon allotropes are formed with sp^2 and sp^3 bonds between the carbon atoms, such as graphene, CNT, and fullerene. Carbon nanomaterials have been developed as biomaterials, energy storage materials and electrical materials. With the increasing applications of carbon nanomaterials, their interactions with living tissue and cells have come into focus. Some researchers found that carbon nanomaterials have moderate toxic to eukaryotic and prokaryotic cells [199, 200].

On the other hand, nanomaterials have also provided antibacterial means for combating bacterial-related infections and food poison. A number of antibacterial tests were carried out in a liquid dispersion or in the biological medium to investigate the applications of carbon nanomaterials for wastewater treatment or other distribution systems [201].

The antibacterial activity of carbon nanomaterials is widely studied, and three main antibacterial approaches are proposed to explain their antibacterial activities, which are mechanical, reactive oxygen species, and photocatalytic activity [202]. These antibacterial actions are related to the features of the specific carbon nanomaterials.

In this study, the antibacterial performances of the VACNT films developed from the research are evaluated with the contact antibacterial tests. The bacteria are directly contacted with the CNT tips because the VACNTs are perpendicular to the substrate.

The forces of gravity and flow motion are considered as the driven forces for the interactions between the bacteria and the CNTs. Therefore, the CNTs can damage the cell membrane as nano-darts and the sharp tips of the CNTs can easily penetrate the cell membrane [149, 150].

As shown in Figure 4.22, the pristine VACNT film is hydrophobic with a contact angle of 160°. However, when post-treated by nitrogen plasma, the contact angle of the N-VANCT film is dramatically reduced to 15° leading to a superhydrophilic nature even though they have almost the same appearance. This is attributed to the defects and functional groups generated by the etching process.

However, as evidenced in Figures 4.23 and 4.24, both the VACNT film and N-AVCNT film possess almost the same antibacterial efficacy to both Gram-negative *E. coli* and Gram-positive S. epidermidis although their wettability and surface chemistry are different. This clearly indicates that either surface wettability or surface chemistry or surface energy has limited, if any, effect on the antibacterial efficacy of VACNTs to both Gram-negative *E. coli* and Gram-positive S. epidermidis.

Therefore, the high antibacterial efficacy of VACNTs to *E. coli* and *S. epidermidis* should be attributed to the physical contact killing mechanism and the killing of these bacteria is dominated by the physical contact mode, whilst the variation of the chemical states and wettability has limited influence on the antibacterial process.

The contact killing process combines the role of gravity and the sharp nanofeatures. Figure 5. 15 shows the schematic diagram of the interaction between a bacterial cell and different surfaces. It is understandable that a large contact surface between the bacterial cell and the surface can decrease the contact pressure. Hence, the bacterial cells will not be ruptured on a flat surface (Figure 5. 15 (a)) or a rough surface (Figure 5. 15 (b)). On the other hand, high contact pressure will be generated at the tips

of the sharp nanostructures, thus leading to the rupture of the cell wall (Figure 5. 15 (c)).

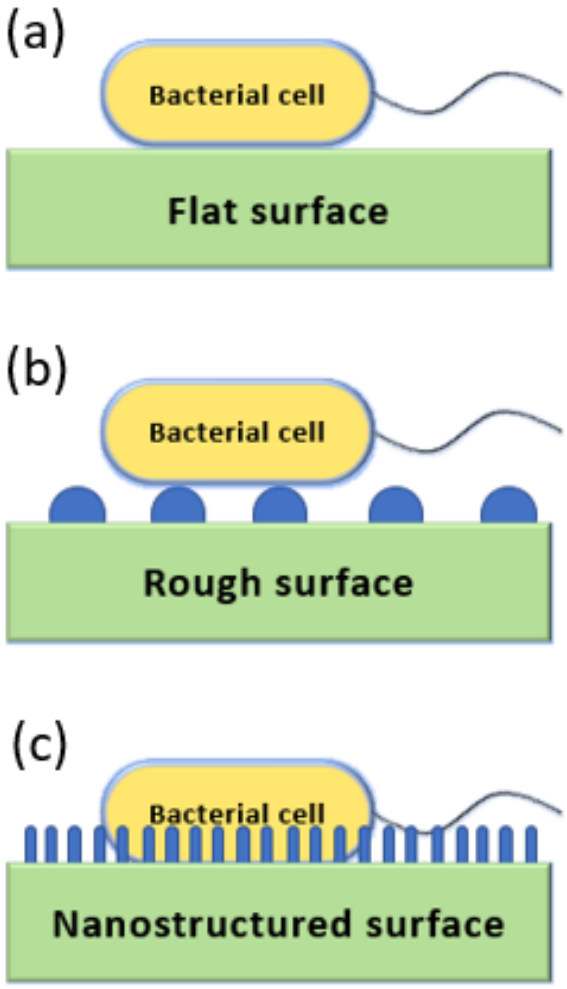

Figure 5. 15 Schematic diagram of the bacterial cell on (a) flat surface; (b) rough surface, and (c) nanostructured surface

Actually, the VACNT films have similar surface morphologies to some natural antimicrobial surfaces of insects, such as gecko skin [136], Sand dragonfly [203], and Megapomponia intermedia [204]. These natural bactericidal surfaces are also formed with nanopillars to protect them from pathogenic bacteria. It is reported that these surfaces have the ability to kill bacteria upon contact.

It is also of great interest to compare the killing rate after 5 h contact of the VACNT

films to the gram-negative *E. coli* (around 99.5%) with that to the gram-positive S. epidermidis (about 88.5%). Clearly, the VACNT films are more effective in killing the Gram-negative *E. coli* than killing the gram-positive S. epidermidis. This is consistent with the results reported by Hasan *et al.* [138] that the thickness of the cell membrane is the primary factor which determines the viability of bacteria through the contact killing process. It is known that the thickness of the peptidoglycan cell wall of the Gram-positive bacteria is about 4 times that of the Gram-negative bacteria. Hence, the Gram-positive bacteria have a higher survivability during the contact with the nanostructured surface due to their thicker rigid peptidoglycan cell walls as compared with the Gram-negative bacteria.

The above findings are also supported by the work by Liu *et al.* [150] who stimulated the penetrate cell damage process using atomic force microscopy with a 2 nm sharp AFM tip to pierce both gram-positive and gram-negative bacteria under loads from 10 nN to 2000 nN. The results indicated that nano-pores only formed under high load, while the cytoplasm released leaving with a shrivelled cell. On the other hand, the continuously tapping at a low load also can introduce damage to the cell membrane, indicating that the contact antibacterial effect also can be attributed to a large number of interactions between the CNTs and the cell membranes. The force-distance curves indicated that due to the thick peptidoglycan protective layer, the gram-positive bacteria are less vulnerable to the physical damage than the gram-negative bacteria.

The antibacterial activity of the Ag-VACNT film is more complex because the VACNT film is embedded with Ag which is known as an antibacterial agent. As shown in Figure 4. 24, the average killing rate of the Ag-VACNT film to *E. coli* (99.57%) is higher than that of the VACNT film (99.49%) and N-VACNT film (99.31%); however, the difference in the antibacterial efficacy of these three CNT films is not significant

according to the statistics analysis using ANOVA (Table 4.5). It seems that doping of Ag has not increased the antibacterial efficacy of the VACNT film to *E. coli*. However, the killing rate of the Ag-VACNT film to *S. epidermidis* (90.7%), which is significantly higher than that for both the VACNT film (88.2%) and N-VACNT film (88.8%). This implies that doping of Ag can increase the antibacterial efficacy of the VACNT film to *S. epidermidis.*

The above seemingly contradicting effect of Ag doping on the antibacterial efficacy of VACNTs could be related to the type of bacteria used for the antibacterial tests. As has been discussed above, the antibacterial mechanism for both *E. coli* and *S. epidermidis* is dominated by the contact killing provided by the nano-sized tips of CNTs. However, the cell membrane of the Gram-positive *S. epidermidis* is much thicker than that of the Gram-negative *E. coli*. Therefore, it is reasonable to assume that it would take a longer time for the Gram-positive S. epidermidis to be penetrated by the CNTs than for the Gram-negative *E. coli*. Consequently, the anti-bacterial effect of Ag could be observed during the antibacterial test using the Gram-positive *S. epidermidis*.

5.5.2 Ag contained bactericidal surfaces

One significant problem encountered in metal medical devices is their weak resistance to the adhesion and growth of bacteria on their surfaces, which can cause cross contamination and post-operation infection. The emergence of some superbugs such as Methicillin-resistant *Staphylococcus aureus* (MRSA) makes Hospital-Acquired Infections (HAIs) one of the chief causes of death all over the world. Therefore, it is important to develop effective preventative technology to reduce bacterial adherence to the medical devices [134, 205].

Some inorganic antibacterial agents, such as silver, copper, and titanium dioxide, have been reported to be effective in killing several disease-causing bacteria including *E.*

coli, S. aureus, Pneumococcus, which can cause skin and wound infections [206]. However, bulk Ag or Cu are rarely used for medical devices and hospital equipment due to their low strength and poor wear resistance. Thus, Ag or Cu containing coatings are being widely researched to improve the antibacterial properties of medical devices [207].

Generally, most surgical tools such as surgical knives and scissors are made of stainless steel, which has high strength and excellent corrosion resistance. However, stainless steel has a weak resistance to pathogens which may lead to nosocomial infections during surgery [208]. Recent studies point to the development of long-lasting antibacterial materials instead of conventional short-life cleaning agents. Silver is well known for its excellent antibacterial properties, such as inhibition of bacteria adhesion, broad anti-bacterial spectrum, and persistent anti-bacterial activity, because silver ions which dissociate from silver nanoparticles can kill various bacteria by damaging the cell walls [206].

As has been reported in Sections 4. 6 and 4.7, Ag containing antibacterial stainless-steel surfaces have been generated from this research through the development of a novel active screen plasma co-sputtering processes. The experimental results have demonstrated that the structures and properties of the composite coatings are significantly influenced by the precursor gases (nitrogen or methane) used.

As reported in Section 4.6, the ASP technique has been proved to be effective to fabricate the Ag contained composite coating and Ag wires reinforced composite coatings have been formed in the plasma ambient of methane and hydrogen (Figure 4.4). As discussed in Section 5.3, The formation of the Ag wires could be attributed to the catalytic effect of the carbon species during the deposition process. However, no Ag wire structures have formed in the plasma ambient of nitrogen and hydrogen (see

Section 4.7) although Ag has been introduced into the composite coating dominated by SS sputtered off from the SS lid. Instead, an S-phase sublayer is formed beneath the Ag-containing composite coating (Figure 4. 60)

Clearly, different microstructures and layer structures have been formed when using different gases for the ASP treatment. This is because the ASP process used is, in essence, a hybrid process combining plasma co-sputtering and plasma carburizing/nitriding. Ag wires and Ag nanoparticles, as well as SS particles, are formed by the plasma co-sputtering; in the meantime, plasma carburizing (when using CH_4/H_2) or nitriding (when using N_2/H_2) occurs. During the plasma carburizing process, solid graphite-like carbon is formed but the interaction between the carbon and the Ag or the stainless-steel particles would be negligible since neither silver carbides nor chromium carbides could be detected by XRD and XPS. The formation of the graphite-like carbon matrix may have consumed most the carbon thus limited carbon could diffuse into the stainless-steel substrate. Thus, unlike conventional low-temperature plasma carburizing, no appreciable carbon S-phase layer could be identified beneath the Ag-containing composite coatings (Figure 4. 49 and Figure 4. 50).

In contrast, a composite surface containing a composite coating layer and a hard S-phase sublayer (Figure 4. 60) has been formed during the hybrid ASP process in the plasma ambient of nitrogen. The S-phase layer is a nitrogen interstitial supersaturated austenite layer [209], which can provide good load bearing capacity to the top composite coating due to its very high hardness (Figure 4. 62). Thus, the functionally graded composite surfaces could be ideal structures as durable long-lasting antibacterial surfaces. As reported in Sections 4.6 and 4.7, although the microstructure and the morphology of Ag produced are closely related to the gases used, the Ag-containing composite coatings produced by the novel hybrid ASP process possess remarkable

antibacterial efficacy. As demonstrated in Figure 4. 59, the Ag wires reinforced composite coating can effectively kill the gram-negative P. gingivalis and the gram-positive S. epidermidis after 5 h contact with the killing rates of 92.2% and 95%, respectively. Similarly, the Ag impregnated composite coatings deposited in the plasma ambient of nitrogen and hydrogen have also shown high antibacterial efficacy (Figure 4. 69).

The observed high antibacterial efficacy of the composite coatings should be attributed to the Ag embedded into the coating. As evidenced by the Ag EDS mapping (Figure 4. 47 and Figure 4. 48), large Ag particles are accumulated to form the Ag wires and Ag nanoparticles are homogeneously distributed in the surface produced by the hybrid ASP process using CH_4/H_2 gas mixture; when using a gas mixture of N_2/H_2, no Ag wires could be formed but a high level of Ag can be introduced into the composite coating (Figure 4. 61).

As discussed in Chapter 2, although Ag is a noble metal which is stable in water or acid, a small amount of Ag ions can be continuously released from the large Ag particles, which is a biochemically active agent for the antibacterial process [210]. These Ag ions can disturb the biochemical process of the cell through the interactions with proteins, nucleic acid, and cell membrane [211]. In addition, the reactive oxygen species were formed in the presence of silver for some cells [212]. Thus, the Ag ions can distract from the biological process through different approaches.

Chapter 6 Conclusions

In this research, a series of novel hybrid low-temperature plasma technologies have been developed to generate advanced to high-quality vertically aligned carbon nanotubes (VACNTs) and novel one-dimensional fibre reinforced multifunctional composite coatings. The microstructures of the advanced VACNTs and the novel one-dimensional fibre reinforced multifunctional composite coatings has been systematically characterised and their mechanical, tribological, biological and physical properties are fully investigated. The main conclusions of this study including the synthesis strategies, microstructure characterisation, and properties evaluation are summarised as follows:

(1) Stainless-steel thin catalyst films have been cost-effectively deposited using the advanced active screen plasma technique with a stainless-steel (SS) active screen in the plasma ambient of hydrogen. Thicknesses of the SS catalyst films vary from 20 nm to 100 nm with the deposition time and voltage.

(2) Ag-SS catalyst films have been successfully deposited using a plasma ambient of hydrogen and the novel active screen with double lids namely a top Ag lid and a bottom SS lid. An inter-lid spacing of 10mm generates a hollow-cathode effect resulting in the co-sputtering of both SS and Ag and an increase in the sputtering rate.

(3) Carbon nanotubes (CNTs) have been successfully deposited using the PECVD at a relatively low temperature (<500°C). The results indicate that the sputtered stainless-steel thin films are a suitable catalyst for the catalytic growth of CNTs; suitable deposition conditions are required to provide sufficient thermal energy, avoid strong plasma etching effect, and control the quantity of carbon sources. TEM results show that the as-deposited CNTs have a multiwalled structure due to the low

deposition temperature. This has also been verified by the Raman analysis results.

(4) The solution-based approach provides a feasible way to prepare catalysts on sophisticated surfaces and iron nitrate is proved to be viable for the growth of CNTs. The composite micro-balls (CNT-Ni and CNT-glass) have been produced by PECVD, which pave the way for the deposition of a homogeneous CNTs reinforced composite materials.

(5) Low-temperature *in-situ* growth of vertically aligned carbon nanotubes (VACNT) films has been successfully achieved using the novel hybrid plasma-assisted technology combining the active-screen catalyst sputtering process and the PECVD CNT growth process.

(6) The vertically aligned structures are formed due to the Van der Waals forces between the CNTs during the growth process. The growth temperature directly affects the length and diameter of the CNTs, and the high growth temperature will lead to thin and long CNTs. TEM investigation results indicate that the tip growth mechanism could be applied to explain the growth of the CNTs.

(7) The antibacterial performances of pristine VACNT film, Ag-VACNT film, and N-VACNT film have been evaluated, and all these three types of VACNT films exhibit high antibacterial efficacy to both the Gram-negative *E. coli* and gram-positive *S. epidermidis* after contact for 5h.

(8) The antibacterial results have also revealed that the chemical state and surface wettability of the VACNT film have limited, if any, influence on their antibacterial properties, even though the doping of nitrogen can convert the wettability of VACNT film from superhydrophobic to superhydrophilic. This implies that the physical contact killing mechanism could be used to explain the antibacterial performances and the sharp CNTs are considered as nanodarts to damage the cell

membranes.

(9) The density of the pre-deposited VACNT film directly affects the structure of the VACNT reinforced composite coatings. The high-density VACNT film grown form the stainless-steel catalyst film prohibited the composite process, leading to a bilayer structure. Ag embedded catalyst film can provide a convenient way to decrease the density of the VACNT films.

(10) The CNTs reinforced composite coatings have been explored through a two-steps strategy. The Pt-CNT and Ag-CNT composite coatings deposited through the PVD approach have demonstrated that the sputtering process is not feasible for the formation of a well-composited structure. Amorphous DLC coatings were deposited by PECVD, and the vapour phase can diffuse into the low-density VACNT film to form the DLC-CNT composite coating. The electrical conductivity of the DLC-CNT composite coating can be effectively increased due to the existence of CNTs and Ag particles.

(11) Ag wire reinforced composite coatings have been successfully fabricated using the novel hybrid plasma technology combining the active screen plasma co-sputtering process and plasma diffusion process in the plasma ambient of methane and hydrogen (i.e. plasma carburising). Ag wires are formed presumably due to the catalytic effect the carbon ambient, and a vapour-solid mechanism can be applied to explain the growth of the Ag wires.

(12) The matrix of the Ag wires reinforced composite coating is rich in carbon and the Ag wires reinforced composite coating has presented excellent tribological property especially in preventing the adhesion of ductile aluminium alloy. However, the formation of the solid carbon prohibits or retards the continuous diffusion of carbon into the stainless-steel substrate, and no obvious carbon S-phase layer can

be generated.

(13) Ag impregnated functionally grade composite surfaces have been also developed using the same hybrid plasma technology combining plasma co-sputtering of both SS and Ag and plasma diffusion but in the plasma ambient of nitrogen and hydrogen (i.e. plasma nitriding). The composite surface consists of a coating layer containing Ag and a hardened S-phase layer due to the continuous diffusion of nitrogen. The S-phase layer with high hardness provides a high load bearing capacity, which enhanced the scratch resistance and wear resistance of the composite surface.

(14) All the Ag contained composite surfaces exhibit excellent antibacterial performances because Ag ions can be released from the sputtered Ag particles within the composite coating. Beside the Ag wires, Ag nanoparticles are also formed within Ag wires reinforced composite coating, leading to excellent antibacterial activity to gram-negative P. gingivalis and gram-positive S. epidermidis.

Chapter 7 Suggested future work

In this study, some novel hybrid plasma technologies have been developed to cost-effectively deposit catalyst films with controlled composition and density for the generation of VACNT films, to generate VACNTs reinforced multifunctional composite coatings, and fabricate the novel metal wires reinforced composite coatings. The bio-inspired VACNT film could be used for waste water treatment due to its antibacterial activity and the CNTs reinforced composite coatings could be used for sensors because it can modify the electric property of the composite structure. The hybrid process for the growth of CNTs on particles in micron scales provides a novel approach for preparation of composite powders for thermal spray deposition. The metal wires reinforced composite coating could act as the new generation of self-lubricant coating. However, these plasma hybrid technologies and the composite coatings are still at their early stage and future work is needed to optimise the process and evaluate the performance of these novel functional coatings, and the topics below are suggested for further investigations:

(1) As Ag and Cu have proved to be feasible to form the corresponding metal wires in this study, other elements such as Au, Al and Zn are suggested to be investigated. This could help to advance the understanding of the formation mechanism of the metal wires.

(2) Antibacterial activity of the VACNT films and the Ag contained composite coatings was tested only against a limited number of bacteria, though excellent performances were achieved, it is suggested to carry out the antibacterial tests to a broad spectrum of bacteria and time-depending tests should be conducted to evaluate the antibacterial performances. Further characterisations of the killed bacteria are required to understand the antibacterial mechanisms involved.

References

1. Hull, D. and T.W. Clyne, *An introduction to composite materials*. Cambridge solid state science series. 1996.

2. Musil, J., *Hard nanocomposite coatings: Thermal stability, oxidation resistance and toughness.* Surface & Coatings Technology, 2012. **207**: p. 50-65.

3. Li, F., Y. Liu, C.B. Qu, H.M. Xiao, Y. Hua, G.X. Sui, and S.Y. Fu, *Enhanced mechanical properties of short carbon fiber reinforced polyethersulfone composites by graphene oxide coating.* Polymer, 2015. **59**: p. 155-165.

4. Archambault, G., B. Jodoin, S. Gaydos, and M. Yandouzi, *Metallization of carbon fiber reinforced polymer composite by cold spray and lay-up molding processes.* Surface & Coatings Technology, 2016. **300**: p. 78-86.

5. Kinoshita, H., I. Ippei, H. Sakai, and N. Ohmae, *Synthesis and mechanical properties carbon nanotube/diamond-like carbon composite films.* Diamond and Related Materials, 2007. **16**(11): p. 1940-1944.

6. Varshney, D., A.V. Sumant, B.R. Weiner, and G. Morell, *Growth of carbon nanotubes on spontaneously detached free standing diamond films and their field emission properties.* Diamond and Related Materials, 2012. **30**: p. 42-47.

7. Hu, H.Y., G. Chen, and J.Y. Zha, *Facile synthesis of CNTs-doped diamond-like carbon film by electrodeposition.* Surface & Coatings Technology, 2008. **202**(24): p. 5943-5946.

8. Nieto, A., J. Kim, O.V. Penkov, D.E. Kim, and J.M. Schoenung, *Elevated temperature wear behavior of thermally sprayed WC-Co/nanodiamond composite coatings.* Surface & Coatings Technology, 2017. **315**: p. 283-293.

9. Luo, X.X., Z.J. Yao, P.Z. Zhang, and D.D. Gu, *Al2O3 nanoparticles reinforced Fe-Al laser cladding coatings with enhanced mechanical properties.* Journal of Alloys and Compounds, 2018. **755**: p. 41-54.

10. Ma, W., R.Z. Ma, C.X. Wang, J.B. Liang, X.H. Liu, K.C. Zhou, and T. Sasaki, *A Superlattice of Alternately Stacked Ni-Fe Hydroxide Nanosheets and Graphene for Efficient Splitting of Water.* Acs Nano, 2015. **9**(2): p. 1977-1984.

11. Hu, C., Y.R. Niu, S.S. Huang, H. Li, M.S. Ren, Y. Zeng, X.B. Zheng, and J.L. Sun, *In-situ fabrication of ZrB2-SiC/SiC gradient coating on C/C composites.* Journal of Alloys and Compounds, 2015. **646**: p. 916-923.

12. Xu, L., X. Li, L. Ni, J. Shi, J. Hu, T. Li, Z. Feng, and D. Zhang, *Ablation behavior of functional gradient ceramic coating for porous carbon-bonded carbon fiber composites.* Corrosion Science, 2018.

13. Donnet, C. and A. Erdemir, *Historical developments and new trends in tribological and solid lubricant coatings.* Surface & Coatings Technology, 2004. **180**: p. 76-84.

14. Thostenson, E.T., Z.F. Ren, and T.W. Chou, *Advances in the science and technology of carbon nanotubes and their composites: a review.* Composites Science and Technology, 2001. **61**(13): p. 1899-1912.

15. Liu, B. and E.S. Aydil, *Growth of Oriented Single-Crystalline Rutile TiO2 Nanorods on Transparent Conducting Substrates for Dye-Sensitized Solar Cells.* Journal of the American Chemical Society, 2009. **131**(11): p. 3985-3990.

16. Li, S.B., P. Zhang, H. Chen, Y.F. Wang, D.T. Liu, J. Wu, H. Sarvari, and Z.D. Chen, *Mesoporous PbI2 assisted growth of large perovskite grains for efficient perovskite solar cells based on ZnO nanorods.* Journal of Power Sources, 2017. **342**: p. 990-997.

17. Karthik, K., S. Dhanuskodi, S.P. Kumar, C. Gobinath, and S. Sivaramakrishnan, *Microwave assisted green synthesis of MgO nanorods and their antibacterial and anti-breast cancer activities.* Materials Letters, 2017. **206**: p. 217-220.

18. Liu, X.H., T.T. Ma, L. Sun, Y.S. Xu, J. Zhang, and N. Pinna, *Enhancing the Lithium Storage Performance of Graphene/SnO2 Nanorods by a Carbon-Riveting Strategy.* Chemsuschem, 2018. **11**(8): p. 1321-1327.

19. Xia, Y.N., P.D. Yang, Y.G. Sun, Y.Y. Wu, B. Mayers, B. Gates, Y.D. Yin, F. Kim, and Y.Q. Yan, *One-dimensional nanostructures: Synthesis, characterization, and applications.* Advanced Materials, 2003. **15**(5): p. 353-389.

20. Gojny, F.H., M.H.G. Wichmann, U. Kopke, B. Fiedler, and K. Schulte, *Carbon nanotube-reinforced epoxy-compo sites: enhanced stiffness and fracture toughness at low nanotube content.* Composites Science and Technology, 2004. **64**(15): p. 2363-2371.

21. Kauffman, D.R. and A. Star, *Carbon nanotube gas and vapor sensors.* Angewandte Chemie-International Edition, 2008. **47**(35): p. 6550-6570.

22. Liu, G.D., Y.H. Lin, Y. Tu, and Z.F. Ren, *Ultrasensitive voltammetric detection of trace heavy metal ions using carbon nanotube nanoelectrode array.* Analyst, 2005. **130**(7): p. 1098-1101.

23. Wang, J., *Carbon-nanotube based electrochemical biosensors: A review.* Electroanalysis, 2005. **17**(1): p. 7-14.

24. Fan, S.S., M.G. Chapline, N.R. Franklin, T.W. Tombler, A.M. Cassell, and H.J. Dai, *Self-oriented regular arrays of carbon nanotubes and their field emission properties.* Science, 1999. **283**(5401): p. 512-514.

25. Saito, Y. and S. Uemura, *Field emission from carbon nanotubes and its application to electron sources.* Carbon, 2000. **38**(2): p. 169-182.

26. Liu, C., F. Li, L.P. Ma, and H.M. Cheng, *Advanced Materials for Energy Storage.* Advanced Materials, 2010. **22**(8): p. E28-+.

27. Lee, S.M. and Y.H. Lee, *Hydrogen storage in single-walled carbon nanotubes.* Applied Physics Letters, 2000. **76**(20): p. 2877-2879.

28. Tang, H., J.H. Chen, Z.P. Huang, D.Z. Wang, Z.F. Ren, L.H. Nie, Y.F. Kuang, and S.Z. Yao, *High dispersion and electrocatalytic properties of platinum on well-aligned carbon nanotube arrays.* Carbon, 2004. **42**(1): p. 191-197.

29. Dai, H.J., E.W. Wong, and C.M. Lieber, *Probing electrical transport in nanomaterials: Conductivity of individual carbon nanotubes.* Science, 1996. **272**(5261): p. 523-526.

30. Ushio, M., D. Fan, and M. Tanaka, *A Method of Estimating the Space-Charge Voltage Drop for Thermionic Arc Cathodes.* Journal of Physics D-Applied Physics, 1994. **27**(3): p. 561-566.

31. Sari, A.H., A. Khazali, and S.S. Parhizgar, *Synthesis and characterization of long-CNTs by electrical arc discharge in deionized water and NaCl solution.* International Nano Letters, 2018. **8**(1): p. 19-23.

32. Chen, J.K., X.C. Gui, Z.Q. Lin, Z.K. Tang, M.M. Lee, A. Wokaun, and T. Lippert, *Pulsed ultra-violet laser interactions with ultra-low-density porous carbon nanotube sponges.* Carbon, 2015. **93**: p. 604-610.

33. Yuge, R., F. Nihey, K. Toyama, and M. Yudasaka, *Preparation and Characterization of Newly Discovered Fibrous Aggregates of Single-Walled Carbon Nanohorns.* Advanced Materials, 2016. **28**(33): p. 7174-+.

34. Wang, X.F., H.J. Li, M.J. Li, C.P. Li, H.L. Dai, and B.H. Yang, *Synthesis and characterization of graphene-based nanostructures by electron-assisted hot filament plasma CVD.* Diamond and Related Materials, 2018. **86**: p. 179-185.

35. Lee, C.J. and J. Park, *Growth model of bamboo-shaped carbon nanotubes by thermal chemical vapor deposition.* Applied Physics Letters, 2000. **77**(21): p. 3397-3399.

36. Siegal, M.P., D.L. Overmyer, and P.P. Provencio, *Precise control of multiwall carbon nanotube diameters using thermal chemical vapor deposition.* Applied Physics Letters, 2002. **80**(12): p. 2171-2173.

37. Dillon, A.C., A.H. Mahan, P.A. Parilla, J.L. Alleman, M.J. Heben, K.M. Jones, and K.E.H. Gilbert, *Continuous hot wire chemical vapor deposition of high-density carbon multiwall nanotubes.* Nano Letters, 2003. **3**(10): p. 1425-1429.

38. Choi, Y.C., D.J. Bae, Y.H. Lee, B.S. Lee, G.S. Park, W.B. Choi, N.S. Lee, and J.M. Kim, *Growth of carbon nanotubes by microwave plasma-enhanced chemical vapor deposition at low temperature.* Journal of Vacuum Science & Technology A, 2000. **18**(4): p. 1864-1868.

39. Pitkanen, O., N. Halonen, A.R. Leino, J. Maklin, A. Dombovari, J.H. Lin, G. Toth, and K. Kordas, *Low-Temperature Growth of Carbon Nanotubes on Bi- and Tri-metallic Catalyst Templates.* Topics in Catalysis, 2013. **56**(9-10): p. 522-526.

40. Teo, K.B.K., D.B. Hash, R.G. Lacerda, N.L. Rupesinghe, M.S. Bell, S.H. Dalal, D. Bose, T.R. Govindan, B.A. Cruden, M. Chhowalla, G.A.J. Amaratunga, J.M. Meyyappan, and W.I. Milne, *The significance of plasma heating in carbon nanotube and nanofiber growth.* Nano Letters, 2004. **4**(5): p. 921-926.

41. Bower, C., W. Zhu, S.H. Jin, and O. Zhou, *Plasma-induced alignment of carbon nanotubes.* Applied Physics Letters, 2000. **77**(6): p. 830-832.

42. Hofmann, S., B. Kleinsorge, C. Ducati, A.C. Ferrari, and J. Robertson, *Low-temperature plasma enhanced chemical vapour deposition of carbon nanotubes.* Diamond and Related Materials, 2004. **13**(4-8): p. 1171-1176.

43. Boskovic, B.O., V. Stolojan, D.A. Zeze, R.D. Forrest, S.R.P. Silva, and S. Haq, *Branched carbon nanofiber network synthesis at room temperature using radio frequency supported microwave plasmas.* Journal of Applied Physics, 2004. **96**(6): p. 3443-3446.

44. Wang, H.Y. and J.J. Moore, *Low temperature growth mechanisms of vertically aligned carbon nanofibers and nanotubes by radio frequency-plasma enhanced chemical vapor deposition.* Carbon, 2012. **50**(3): p. 1235-1242.

45. Meyyappan, M., *A review of plasma enhanced chemical vapour deposition of carbon nanotubes.* Journal of Physics D-Applied Physics, 2009. **42**(21).

46. Wang, H.Y. and J.J. Moore, *Different growth mechanisms of vertical carbon nanotubes by rf- or dc-plasma enhanced chemical vapor deposition at low temperature.* Journal of Vacuum Science & Technology B, 2010. **28**(6): p. 1081-1085.

47. Hofmann, S., C. Ducati, J. Robertson, and B. Kleinsorge, *Low-temperature growth of carbon nanotubes by plasma-enhanced chemical vapor deposition.* Applied Physics Letters, 2003. **83**(1): p. 135-137.

48. Hofmann, S., C. Ducati, B. Kleinsorge, and J. Robertson, *Direct growth of aligned carbon nanotube field emitter arrays onto plastic substrates.* Applied Physics Letters, 2003. **83**(22): p. 4661-4663.

49. Boskovic, B.O., V. Stolojan, R.U.A. Khan, S. Haq, and S.R.P. Silva, *Large-area synthesis of carbon nanofibres at room temperature.* Nature Materials, 2002. **1**(3): p. 165-168.

50. Kang, H.S., H.J. Yoon, C.O. Kim, J.P. Hong, I.T. Han, S.N. Cha, B.K. Song, J.E. Jung, N.S. Lee, and J.M. Kim, *Low temperature growth of multi-wall carbon nanotubes assisted by mesh potential using a modified plasma enhanced chemical vapor deposition system.* Chemical Physics Letters, 2001. **349**(3-4): p. 196-200.

51. Kojima, Y., S. Kishimoto, and T. Mizutani, *Low-temperature growth of carbon nanotubes by grid-inserted plasma-enhanced chemical vapor deposition.* Japanese Journal of Applied Physics Part 1-Regular Papers Brief Communications & Review Papers, 2007. **46**(12): p. 8000-8002.

52. Jang, I., H.S. Uh, H.J. Cho, W. Lee, J.P. Hong, and N. Lee, *Characteristics of carbon nanotubes grown by mesh-inserted plasma-enhanced chemical vapor deposition.* Carbon, 2007. **45**(15): p. 3015-3021.

53. Show, Y., *Selective growth of carbon nanotube at low temperate using triode type plasma enhanced CVD method.* Diamond and Related Materials, 2011. **20**(7): p. 1081-1084.

54. Chhowalla, M., K.B.K. Teo, C. Ducati, N.L. Rupesinghe, G.A.J. Amaratunga, A.C. Ferrari, D. Roy, J. Robertson, and W.I. Milne, *Growth process conditions of vertically aligned carbon nanotubes using plasma enhanced chemical vapor deposition.* Journal of Applied Physics, 2001. **90**(10): p. 5308-5317.

55. Show, Y., Y. Yabe, T. Izumi, and H. Yamauchi, *Development of triode type RF plasma enhanced CVD equipment for low temperature growth of carbon nanotube.* Diamond and Related Materials, 2005. **14**(11-12): p. 1848-1851.

56. Show, Y. and N. Fukuzumi, *Selective growth of CNT by using triode-type radio frequency plasma chemical vapor deposition method.* Diamond and Related Materials, 2007. **16**(4-7): p. 1106-1109.

57. Ryu, K.M., M.Y. Kang, Y.D. Kim, and H.T. Jeon, *Low-temperature growth of carbon nanotube by plasma-enhanced chemical vapor deposition using nickel catalyst.* Japanese Journal of Applied Physics Part 1-Regular Papers Brief Communications & Review Papers, 2003. **42**(6a): p. 3578-3581.

58. Zhang, L., Z.R. Li, Y.Q. Tan, G. Lolli, N. Sakulchaicharoen, F.G. Requejo, B.S. Mun, and D.E. Resasco, *Influence of a top crust of entangled nanotubes on the structure of vertically aligned forests of single-walled carbon nanotubes.* Chemistry of Materials, 2006. **18**(23): p. 5624-5629.

59. Robertson, J., G. Zhong, S. Hofmann, B.C. Bayer, C.S. Esconjauregui, H. Telg, and C. Thomsen, *Use of carbon nanotubes for VLSI interconnects.* Diamond and Related Materials, 2009. **18**(5-8): p. 957-962.

60. Okita, A., A. Ozeki, Y. Suda, J. Nakamura, A. Oda, K. Bhattacharyya, H. Sugawara, and Y. Sakai, *Analysis of oxidation state of multilayered catalyst thin films for carbon nanotube growth using plasma-enhanced chemical vapor deposition.* Japanese Journal of Applied Physics Part 1-Regular Papers Brief Communications & Review Papers, 2006. **45**(10b): p. 8323-8329.

61. Lee, K.M., H.J. Han, S.H. Choi, K.H. Park, S. Oh, S. Lee, and K.H. Koh, *Effects of metal buffer layers on the hot filament chemical vapor deposition of nanostructured carbon films.* Journal of Vacuum Science & Technology B, 2003. **21**(1): p. 623-626.

62. Ng, H.T., B. Chen, J.E. Koehne, A.M. Cassell, J. Li, J. Han, and M. Meyyappan, *Growth of carbon nanotubes: A combinatorial method to study the effects of catalysts and underlayers.* Journal of Physical Chemistry B, 2003. **107**(33): p. 8484-8489.

63. Cassell, A.M., Q. Ye, B.A. Cruden, J. Li, P.C. Sarrazin, H.T. Ng, J. Han, and M. Meyyappan, *Combinatorial chips for optimizing the growth and integration of carbon nanofibre based devices.* Nanotechnology, 2004. **15**(1): p. 9-15.

64. Delzeit, L., C.V. Nguyen, B. Chen, R. Stevens, A. Cassell, J. Han, and M. Meyyappan, *Multiwalled carbon nanotubes by chemical vapor deposition using multilayered metal catalysts.* Journal of Physical Chemistry B, 2002. **106**(22): p. 5629-5635.

65. Baker, R.T.K., *Catalytic Growth of Carbon Filaments.* Carbon, 1989. **27**(3): p. 315-323.

66. Liu, B.L., W.C. Ren, L.B. Gao, S.S. Li, S.F. Pei, C. Liu, C.B. Jiang, and H.M. Cheng, *Metal-Catalyst-Free Growth of Single-Walled Carbon Nanotubes.* Journal of the American Chemical Society, 2009. **131**(6): p. 2082-+.

67. Zeng, Z.Y. and J.H. Lin, *Metal-catalyst-free growth of carbon nanotubes/carbon nanofibers on carbon blacks using chemical vapor deposition.* Rsc Advances, 2014. **4**(76): p. 40251-40258.

68. Wei, Y.Y., G. Eres, V.I. Merkulov, and D.H. Lowndes, *Effect of catalyst film thickness on carbon nanotube growth by selective area chemical vapor deposition.* Applied Physics Letters, 2001. **78**(10): p. 1394-1396.

69. Rizzo, A., R. Rossi, M.A. Signore, E. Piscopiello, L. Capodieci, R. Pentassuglia, T. Dikonimos, and R. Giorgi, *Effect of Fe catalyst thickness and C2H2/H-2 flow rate ratio on the vertical alignment of carbon nanotubes grown by chemical vapour deposition.* Diamond and Related Materials, 2008. **17**(7-10): p. 1502-1505.

70. Jung, D., J.H. Kim, K.H. Lee, L.J. Overzet, and G.S. Lee, *Effects of pre-annealing of Fe catalysts on growth of spin-capable carbon nanotubes.* Diamond and Related Materials, 2013. **38**: p. 87-92.

71. Ren, Z.F., Z.P. Huang, J.W. Xu, J.H. Wang, P. Bush, M.P. Siegal, and P.N. Provencio, *Synthesis of large arrays of well-aligned carbon nanotubes on glass.* Science, 1998. **282**(5391): p. 1105-1107.

72. Zhang, C., R. Xie, B. Chen, J. Yang, G. Zhong, and J. Robertson, *High density carbon nanotube growth using a plasma pretreated catalyst.* Carbon, 2013. **53**: p. 339-345.

73. Mehn, D., A. Fonseca, G. Bister, and J.B. Nagy, *A comparison of different preparation methods of Fe/Mo/Al2O3 sol-gel catalyst for synthesis of single wall carbon nanotubes.* Chemical Physics Letters, 2004. **393**(4-6): p. 378-384.

74. Xu, C.B. and J. Zhu, *One-step preparation of highly dispersed metal-supported catalysts by fluidized-bed MOCVD for carbon nanotube synthesis.* Nanotechnology, 2004. **15**(11): p. 1671-1681.

75. Li, C.X., *Active screen plasma nitriding - an overview.* Surface Engineering, 2010. **26**(1-2): p. 135-141.

76. Li, C.X., J. Georges, and X.Y. Li, *Active screen plasma nitriding of austenitic stainless steel.* Surface Engineering, 2002. **18**(6): p. 453-458.

77. Dong, Y., X. Li, T. Bell, R. Sammons, and H. Dong, *Surface microstructure and antibacterial property of an active-screen plasma alloyed austenitic stainless steel surface with Cu and N.* Biomedical Materials, 2010. **5**(5).

78. Dong, Y.C., X.Y. Li, R. Sammons, and H.S. Dong, *The Generation of Wear-Resistant Antimicrobial Stainless Steel Surfaces by Active Screen Plasma Alloying with N and Nanocrystalline Ag.* Journal of Biomedical Materials Research Part B-Applied Biomaterials, 2010. **93b**(1): p. 185-193.

79. Tan, J., T. Yu, B. Xu, and Q. Yao, *Microstructure and wear resistance of nickel-carbon nanotube composite coating from brush plating technique.* Tribology Letters, 2006. **21**(2): p. 107-111.

80. Schittenhelm, H., D.B. Geohegan, G.E. Jellison, A.A. Puretzky, M.J. Lance, and P.F. Britt, *Synthesis and characterization of single-wall carbon nanotube-amorphous diamond thin-film composites.* Applied Physics Letters, 2002. **81**(11): p. 2097-2099.

81. Chiba, K. and M. Tada, *Buffered internal stresses in diamond-like carbon films reinforced with single-walled carbon nanotubes.* Thin Solid Films, 2012. **520**(6): p. 1993-1996.

82. Li, H.J., Z.S. Chen, K.Z. Li, Q.L. Shen, Y.H. Chu, and Q.G. Fu, *Wear behavior of SiC nanowire-reinforced SiC coating for C/C composites at elevated temperatures.* Journal of the European Ceramic Society, 2013. **33**(15-16): p. 2961-2969.

83. Eichhorn, H., K.H. Schoenbach, and T. Tessnow, *Paschen Law for a Hollow-Cathode Discharge.* Applied Physics Letters, 1993. **63**(18): p. 2481-2483.

84. Lisovskiy, V.A., S.D. Yakovin, and V.D. Yegorenkov, *Low-pressure gas breakdown in uniform dc electric field.* Journal of Physics D-Applied Physics, 2000. **33**(21): p. 2722-2730.

85. Li, C.X., T. Bell, and H. Dong, *A study of active screen plasma nitriding.* Surface Engineering, 2002. **18**(3): p. 174-181.

86. Gallo, S.C. and H.S. Dong, *On the fundamental mechanisms of active screen plasma nitriding.* Vacuum, 2009. **84**(2): p. 321-325.

87. Zhao, C., C.X. Li, H. Dong, and T. Bell, *Study on the active screen plasma nitriding and its nitriding mechanism.* Surface & Coatings Technology, 2006. **201**(6): p. 2320-2325.

88. Ahangarani, S., A.R. Sabour, F. Mahboubi, and T. Shahrabi, *The influence of active screen plasma nitriding parameters on corrosion behavior of a low-alloy steel.* Journal of Alloys and Compounds, 2009. **484**(1-2): p. 222-229.

89. Nii, H. and A. Nishimoto, *Surface modification of ferritic stainless steel by active screen plasma nitriding.* International Symposium on Materials Science and Innovation for Sustainable Society: Eco-Materials and Eco-Innovation for Global Sustainability (Eco-Mates 2011), 2012. **379**.

90. Chiu, L.H., Y.Y. Su, F.S. Chen, and H. Chang, *Microstructure and Properties of Active Screen Plasma Nitrided Duplex Stainless Steel.* Materials and Manufacturing Processes, 2010. **25**(5): p. 316-323.

91. Nagatsuka, K., A. Nishimoto, and K. Akamatsu, *Surface hardening of duplex stainless steel by low temperature active screen plasma nitriding.* Surface & Coatings Technology, 2010. **205**: p. S295-S299.

92. Li, C.X. and T. Bell, *Corrosion properties of active screen plasma nitrided 316 austenitic stainless steel.* Corrosion Science, 2004. **46**(6): p. 1527-1547.

93. Gallo, S.C. and H. Dong, *Study of active screen plasma processing conditions for carburising and nitriding austenitic stainless steel.* Surface & Coatings Technology, 2009. **203**(24): p. 3669-3675.

94. Saeed, A., A.W. Khan, F. Jan, M. Abrar, M. Khalid, and M. Zakaullah, *Validity of "sputtering and re-condensation" model in active screen cage plasma nitriding process.* Applied Surface Science, 2013. **273**: p. 173-178.

95. Gallo, S.C. and H. Dong, *New insights into the mechanism of low-temperature active-screen plasma nitriding of austenitic stainless steel.* Scripta Materialia, 2012. **67**(1): p. 89-91.

96. Li, C.X. and T. Bell, *Potential of plasma nitriding of polymer for improved hardness and wear resistance.* Journal of Materials Processing Technology, 2005. **168**(2): p. 219-224.

97. Li, C.X., H. Dong, and T. Bell, *A feasibility study of plasma nitriding of steel with an oxide layer on the surface.* Journal of Materials Science, 2006. **41**(18): p. 6116-6118.

98. Dong, Y., X. Li, L. Tian, T. Bell, R.L. Sammons, and H. Dong, *Towards long-lasting antibacterial stainless steel surfaces by combining double glow plasma silvering with active screen plasma nitriding.* Acta Biomaterialia, 2011. **7**(1): p. 447-457.

99. Lin, K.J., X.Y. Li, L.H. Tian, and H.S. Dong, *Active screen plasma surface co-alloying of 316 austenitic stainless steel with both nitrogen and niobium for the*

application of bipolar plates in proton exchange membrane fuel cells. International Journal of Hydrogen Energy, 2015. **40**(32): p. 10281-10292.

100. Lin, K.J., X.Y. Li, L.H. Tian, and H.S. Dong, *Active screen plasma surface co-alloying treatments of 316 stainless steel with nitrogen and silver for fuel cell bipolar plates.* Surface & Coatings Technology, 2015. **283**: p. 122-128.

101. Lin, K.J., X.Y. Li, Y. Sun, X. Luo, and H.S. Dong, *Active screen plasma nitriding of 316 stainless steel for the application of bipolar plates in proton exchange membrane fuel cells.* International Journal of Hydrogen Energy, 2014. **39**(36): p. 21470-21479.

102. Nishimoto, A., H. Nii, R. Narita, and K. Akamatsu, *Simultaneous duplex process of TiN coating and nitriding by active screen plasma nitriding.* Surface & Coatings Technology, 2013. **228**: p. S558-S562.

103. Cvelbar, U., Z.Q. Chen, M.K. Sunkara, and M. Mozetic, *Spontaneous Growth of Superstructure alpha-Fe2O3 Nanowire and Nanobelt Arrays in Reactive Oxygen Plasma.* Small, 2008. **4**(10): p. 1610-1614.

104. Lee, W.C., K. Kim, J. Park, J. Koo, H.Y. Jeong, H. Lee, D.A. Weitz, A. Zettl, and S. Takeuchi, *Graphene-templated directional growth of an inorganic nanowire.* Nature Nanotechnology, 2015. **10**(5): p. 423-428.

105. Chauvin, A., N. Stephant, K. Du, J.J. Ding, I. Wathuthanthri, C.H. Choi, P.Y. Tessier, and A.A. El Mel, *Large-Scale Fabrication of Porous Gold Nanowires via Laser Interference Lithography and Dealloying of Gold-Silver Nano-Alloys.* Micromachines, 2017. **8**(6).

106. Sun, Y.G., B. Gates, B. Mayers, and Y.N. Xia, *Crystalline silver nanowires by soft solution processing.* Nano Letters, 2002. **2**(2): p. 165-168.

107. Bonet, F., K. Tekaia-Elhsissen, and K.V. Sarathy, *Study of interaction of ethylene glycol/PVP phase on noble metal powders prepared by polyol process.* Bulletin of Materials Science, 2000. **23**(3): p. 165-168.

108. Silvert, P.Y., R. HerreraUrbina, N. Duvauchelle, V. Vijayakrishnan, and K.T. Elhsissen, *Preparation of colloidal silver dispersions by the polyol process .1. Synthesis and characterization.* Journal of Materials Chemistry, 1996. **6**(4): p. 573-577.

109. Silvert, P.Y., R. HerreraUrbina, and K. TekaiaElhsissen, *Preparation of colloidal silver dispersions by the polyol process .2. Mechanism of particle formation.* Journal of Materials Chemistry, 1997. **7**(2): p. 293-299.

110. Zhang, W.J., Y. Liu, R.G. Cao, Z.H. Li, Y.H. Zhang, Y. Tang, and K.N. Fan, *Synergy between Crystal Strain and Surface Energy in Morphological Evolution of Five-Fold-Twinned Silver Crystals.* Journal of the American Chemical Society, 2008. **130**(46): p. 15581-15588.

111. Li, Y., X.Y. Yang, Y. Feng, Z.Y. Yuan, and B.L. Su, *One-Dimensional Metal Oxide Nanotubes, Nanowires, Nanoribbons, and Nanorods: Synthesis,*

Characterizations, Properties and Applications. Critical Reviews in Solid State and Materials Sciences, 2012. **37**(1): p. 1-74.

112. Lee, S.T., N. Wang, Y.F. Zhang, and Y.H. Tang, *Oxide-assisted semiconductor nanowire growth.* Mrs Bulletin, 1999. **24**(8): p. 36-42.

113. Wagner, R.S. and W.C. Ellis, *Vapor-Liquid-Solid Mechanism of Single Crystal Growth (New Method Growth Catalysis from Impurity Whisker Epitaxial + Large Crystals Si E).* Applied Physics Letters, 1964. **4**(5): p. 89-&.

114. Wu, Y.Y. and P.D. Yang, *Direct observation of vapor-liquid-solid nanowire growth.* Journal of the American Chemical Society, 2001. **123**(13): p. 3165-3166.

115. Hsu, Y.J. and S.Y. Lu, *Vapor-solid growth of Sn nanowires: Growth mechanism and superconductivity.* Journal of Physical Chemistry B, 2005. **109**(10): p. 4398-4403.

116. Tripathy, A., P. Sen, B. Su, and W.H. Briscoe, *Natural and bioinspired nanostructured bactericidal surfaces.* Advances in Colloid and Interface Science, 2017. **248**: p. 85-104.

117. Swartjes, J.J.T.M., P.K. Sharma, T.G. van Kooten, H.C. van der Mei, M. Mahmoudi, H.J. Busscher, and E.T.J. Rochford, *Current Developments in Antimicrobial Surface Coatings for Biomedical Applications.* Current Medicinal Chemistry, 2015. **22**(18): p. 2116-2129.

118. Beveridge, T.J., *Use of the Gram stain in microbiology.* Biotechnic & Histochemistry, 2001. **76**(3): p. 111-118.

119. Brown, L., J.M. Wolf, R. Prados-Rosales, and A. Casadevall, *Through the wall: extracellular vesicles in Gram-positive bacteria, mycobacteria and fungi.* Nature Reviews Microbiology, 2015. **13**(10): p. 620-630.

120. Tiller, J.C., C.J. Liao, K. Lewis, and A.M. Klibanov, *Designing surfaces that kill bacteria on contact.* Proceedings of the National Academy of Sciences of the United States of America, 2001. **98**(11): p. 5981-5985.

121. Liau, S.Y., D.C. Read, W.J. Pugh, J.R. Furr, and A.D. Russell, *Interaction of silver nitrate with readily identifiable groups: relationship to the antibacterial action of silver ions.* Letters in Applied Microbiology, 1997. **25**(4): p. 279-283.

122. Jeon, H.J., S.C. Yi, and S.G. Oh, *Preparation and antibacterial effects of Ag-SiO2 thin films by sol-gel method.* Biomaterials, 2003. **24**(27): p. 4921-4928.

123. Lee, D., R.E. Cohen, and M.F. Rubner, *Antibacterial properties of Ag nanoparticle loaded multilayers and formation of magnetically directed antibacterial microparticles.* Langmuir, 2005. **21**(21): p. 9651-9659.

124. Liu, W., Y.A. Wu, C. Wang, H.C. Li, T. Wang, C.Y. Liao, L. Cui, Q.F. Zhou, B. Yan, and G.B. Jiang, *Impact of silver nanoparticles on human cells: Effect of particle size.* Nanotoxicology, 2010. **4**(3): p. 319-330.

125. Choi, O. and Z.Q. Hu, *Size dependent and reactive oxygen species related nanosilver toxicity to nitrifying bacteria.* Environmental Science & Technology, 2008. **42**(12): p. 4583-4588.

126. Kuo, Y.C., J.W. Lee, C.J. Wang, and Y.J. Chang, *The effect of Cu content on the microstructures, mechanical and antibacterial properties of Cr-Cu-N nanocomposite coatings deposited by pulsed DC reactive magnetron sputtering.* Surface & Coatings Technology, 2007. **202**(4-7): p. 854-860.

127. Adams, L.K., D.Y. Lyon, and P.J.J. Alvarez, *Comparative eco-toxicity of nanoscale TiO2, SiO2, and ZnO water suspensions.* Water Research, 2006. **40**(19): p. 3527-3532.

128. Cho, M., H. Chung, W. Choi, and J. Yoon, *Linear correlation between inactivation of E-coli and OH radical concentration in TiO2 photocatalytic disinfection.* Water Research, 2004. **38**(4): p. 1069-1077.

129. Rincon, A.G. and C. Pulgarin, *Use of coaxial photocatalytic reactor (CAPHORE) in the TiO2 photo-assisted treatment of mixed E-coli and Bacillus sp and bacterial community present in wastewater.* Catalysis Today, 2005. **101**(3-4): p. 331-344.

130. Fu, G.F., P.S. Vary, and C.T. Lin, *Anatase TiO2 nanocomposites for antimicrobial coatings.* Journal of Physical Chemistry B, 2005. **109**(18): p. 8889-8898.

131. Applerot, G., A. Lipovsky, R. Dror, N. Perkas, Y. Nitzan, R. Lubart, and A. Gedanken, *Enhanced Antibacterial Activity of Nanocrystalline ZnO Due to Increased ROS-Mediated Cell Injury.* Advanced Functional Materials, 2009. **19**(6): p. 842-852.

132. Applerot, G., N. Perkas, G. Amirian, O. Girshevitz, and A. Gedanken, *Coating of glass with ZnO via ultrasonic irradiation and a study of its antibacterial properties.* Applied Surface Science, 2009. **256**(3): p. S3-S8.

133. Hu, H., W. Zhang, Y. Qiao, X. Jiang, X. Liu, and C. Ding, *Antibacterial activity and increased bone marrow stem cell functions of Zn-incorporated TiO2 coatings on titanium.* Acta Biomaterialia, 2012. **8**(2): p. 904-915.

134. Glinel, K., P. Thebault, V. Humblot, C.M. Pradier, and T. Jouenne, *Antibacterial surfaces developed from bio-inspired approaches.* Acta Biomaterialia, 2012. **8**(5): p. 1670-1684.

135. Cloutier, M., D. Mantovani, and F. Rosei, *Antibacterial Coatings: Challenges, Perspectives, and Opportunities.* Trends in Biotechnology, 2015. **33**(11): p. 637-652.

136. Watson, G.S., D.W. Green, L. Schwarzkopf, X. Li, B.W. Cribb, S. Myhra, and J.A. Watson, *A gecko skin micro/nano structure - A low adhesion, superhydrophobic, anti-wetting, self-cleaning, biocompatible, antibacterial surface.* Acta Biomaterialia, 2015. **21**: p. 109-122.

137. Ivanova, E.P., J. Hasan, H.K. Webb, V.K. Truong, G.S. Watson, J.A. Watson, V.A. Baulin, S. Pogodin, J.Y. Wang, M.J. Tobin, C. Lobbe, and R.J. Crawford, *Natural Bactericidal Surfaces: Mechanical Rupture of Pseudomonas aeruginosa Cells by Cicada Wings.* Small, 2012. **8**(16): p. 2489-2494.

138. Hasan, J., H.K. Webb, V.K. Truong, S. Pogodin, V.A. Baulin, G.S. Watson, J.A. Watson, R.J. Crawford, and E.P. Ivanova, *Selective bactericidal activity of nanopatterned superhydrophobic cicada Psaltoda claripennis wing surfaces.* Applied Microbiology and Biotechnology, 2013. **97**(20): p. 9257-9262.

139. Ivanova, E.P., J. Hasan, H.K. Webb, G. Gervinskas, S. Juodkazis, V.K. Truong, A.H.F. Wu, R.N. Lamb, V.A. Baulin, G.S. Watson, J.A. Watson, D.E. Mainwaring, and R.J. Crawford, *Bactericidal activity of black silicon.* Nature Communications, 2013. **4**.

140. Nowlin, K., A. Boseman, A. Covell, and D. LaJeunesse, *Adhesion-dependent rupturing of Saccharomyces cerevisiae on biological antimicrobial nanostructured surfaces.* Journal of The Royal Society Interface, 2015. **12**.

141. Fisher, L.E., Y. Yang, M.F. Yuen, W.J. Zhang, A.H. Nobbs, and B. Su, *Bactericidal activity of biomimetic diamond nanocone surfaces.* Biointerphases, 2016. **11**(1).

142. May, P.W., M. Clegg, T.A. Silva, H. Zanin, O. Fatibello, V. Celorrio, D.J. Fermin, C.C. Welch, G. Hazell, L. Fisher, A. Nobbs, and B. Su, *Diamond-coated 'black silicon' as a promising material for high-surface-area electrochemical electrodes and antibacterial surfaces.* Journal of Materials Chemistry B, 2016. **4**(34): p. 5737-5746.

143. Diu, T., N. Faruqui, T. Sjostrom, B. Lamarre, H.F. Jenkinson, B. Su, and M.G. Ryadnov, *Cicada-inspired cell-instructive nanopatterned arrays.* Scientific Reports, 2014. **4**.

144. Chan, C.M.N., A.M.C. Ng, M.K. Fung, H.S. Cheng, M.Y. Guo, A.B. Djurisic, F.C.C. Leung, and W.K. Chan, *Antibacterial and photocatalytic activities of TiO2 nanotubes.* Journal of Experimental Nanoscience, 2013. **8**(6): p. 859-867.

145. Wang, X.L., F. Yang, W. Yang, and X.R. Yang, *A study on the antibacterial activity of one-dimensional ZnO nanowire arrays: effects of the orientation and plane surface.* Chemical Communications, 2007(42): p. 4419-4421.

146. Wang, Y.C., Y. Wu, F. Quadri, J.D. Prox, and L. Guo, *Cytotoxicity of ZnO Nanowire Arrays on Excitable Cells.* Nanomaterials, 2017. **7**(4).

147. Kang, S., M. Pinault, L.D. Pfefferle, and M. Elimelech, *Single-walled carbon nanotubes exhibit strong antimicrobial activity.* Langmuir, 2007. **23**(17): p. 8670-8673.

148. Kang, S., M. Herzberg, D.F. Rodrigues, and M. Elimelech, *Antibacterial effects of carbon nanotubes: Size does matter.* Langmuir, 2008. **24**(13): p. 6409-6413.

149. Liu, S.B., L. Wei, L. Hao, N. Fang, M.W. Chang, R. Xu, Y.H. Yang, and Y. Chen, *Sharper and Faster "Nano Darts" Kill More Bacteria: A Study of Antibacterial Activity of Individually Dispersed Pristine Single-Walled Carbon Nanotube.* Acs Nano, 2009. **3**(12): p. 3891-3902.

150. Liu, S.B., A.K. Ng, R. Xu, J. Wei, C.M. Tan, Y.H. Yang, and Y.A. Chen, *Antibacterial action of dispersed single-walled carbon nanotubes on Escherichia coli and Bacillus subtilis investigated by atomic force microscopy.* Nanoscale, 2010. **2**(12): p. 2744-2750.

151. Choi, Y.C., Y.M. Shin, Y.H. Lee, B.S. Lee, G.S. Park, W.B. Choi, N.S. Lee, and J.M. Kim, *Controlling the diameter, growth rate, and density of vertically aligned carbon nanotubes synthesized by microwave plasma-enhanced chemical vapor deposition.* Applied Physics Letters, 2000. **76**(17): p. 2367-2369.

152. DiLeo, R.A., B.J. Landi, and R.P. Raffaelle, *Purity assessment of multiwalled carbon nanotubes by Raman spectroscopy.* Journal of Applied Physics, 2007. **101**(6).

153. Rajesh, J.A. and A. Pandurangan, *Lanthanum nickel alloy catalyzed growth of nitrogen-doped carbon nanotubes by chemical vapor deposition.* Rsc Advances, 2014. **4**(39): p. 20554-20566.

154. Antunes, E.F., A.O. Lobo, E.J. Corat, V.J. Trava-Airoldi, A.A. Martin, and C. Verissimo, *Comparative study of first- and second-order Raman spectra of MWCNT at visible and infrared laser excitation.* Carbon, 2006. **44**(11): p. 2202-2211.

155. Baro, M., D. Gogoi, A.R. Pal, N.C. Adhikary, H. Bailung, and J. Chutia, *Pulsed PECVD for Low-temperature Growth of Vertically Aligned Carbon Nanotubes.* Chemical Vapor Deposition, 2014. **20**(4-6): p. 161-169.

156. Mattia, D., M.P. Rossi, B.M. Kim, G. Korneva, H.H. Bau, and Y. Gogotsi, *Effect of graphitization on the wettability and electrical conductivity of CVD-carbon nanotubes and films.* Journal of Physical Chemistry B, 2006. **110**(20): p. 9850-9855.

157. Tian, W.L., H.Y. Li, B.C. Qin, Y.Q. Xu, Y.C. Hao, Y.P. Li, G.X. Zhang, J.F. Liu, X.M. Sun, and X. Duan, *Tuning the wettability of carbon nanotube arrays for efficient bifunctional catalysts and Zn-air batteries.* Journal of Materials Chemistry A, 2017. **5**(15): p. 7103-7110.

158. Feng, X., Y. Huang, and A.J. Rosakis, *On the Stoney formula for a thin film/substrate system with nonuniform substrate thickness.* Journal of Applied Mechanics-Transactions of the Asme, 2007. **74**(6): p. 1276-1281.

159. Janssen, G.C.A.M., M.M. Abdalla, F. van Keulen, B.R. Pujada, and B. van Venrooy, *Celebrating the 100th anniversary of the Stoney equation for film stress: Developments from polycrystalline steel strips to single crystal silicon wafers.* Thin Solid Films, 2009. **517**(6): p. 1858-1867.

160. Cordill, M.J., D.F. Bahr, N.R. Moody, and W.W. Gerberich, *Adhesion measurements using telephone cord buckles.* Materials Science and Engineering a-Structural Materials Properties Microstructure and Processing, 2007. **443**(1-2): p. 150-155.

161. Lee, K.R., Y.J. Baik, and K.Y. Eun, *Stress Relief Behavior of Diamond-Like Carbon-Films on Glasses.* Diamond and Related Materials, 1993. **2**(2-4): p. 218-224.

162. Moon, M.W., H.M. Jensen, J.W. Hutchinson, K.H. Oh, and A.G. Evans, *The characterization of telephone cord buckling of compressed thin films on substrates.* Journal of the Mechanics and Physics of Solids, 2002. **50**(11): p. 2355-2377.

163. Liu, H., S.H. Li, J. Zhai, H.J. Li, Q.S. Zheng, L. Jiang, and D.B. Zhu, *Self-assembly of large-scale micropatterns on aligned carbon nanotube films.* Angewandte Chemie-International Edition, 2004. **43**(9): p. 1146-1149.

164. Sun, Y.G., Y.D. Yin, B.T. Mayers, T. Herricks, and Y.N. Xia, *Uniform silver nanowires synthesis by reducing AgNO3 with ethylene glycol in the presence of seeds and poly(vinyl pyrrolidone).* Chemistry of Materials, 2002. **14**(11): p. 4736-4745.

165. Modabberasl, A., P. Kameli, M. Ranjbar, H. Salamati, and R. Ashiri, *Fabrication of DLC thin films with improved diamond-like carbon character by the application of external magnetic field.* Carbon, 2015. **94**: p. 485-493.

166. Dong, Y.C., K.L. Zheng, J. Fernandez, X.Y. Li, H.S. Dong, and J.G. Lin, *Experimental investigations on hot forming of AA6082 using advanced plasma nitrocarburised and CAPVD WC: C coated tools.* Journal of Materials Processing Technology, 2017. **240**: p. 190-199.

167. Liu, H., L. Feng, J. Zhai, L. Jiang, and D.B. Zhu, *Reversible wettability of a chemical vapor deposition prepared ZnO film between superhydrophobicity and superhydrophilicity.* Langmuir, 2004. **20**(14): p. 5659-5661.

168. Xiao, K., L.X. Ding, G.X. Liu, H.B. Chen, S.Q. Wang, and H.H. Wang, *Freestanding, Hydrophilic Nitrogen-Doped Carbon Foams for Highly Compressible All Solid-State Supercapacitors.* Advanced Materials, 2016. **28**(28): p. 5997-+.

169. Wang, J.W., B.D. Mao, J.L. Gole, and C. Burda, *Visible-light-driven reversible and switchable hydrophobic to hydrophilic nitrogen-doped titania surfaces: correlation with photocatalysis.* Nanoscale, 2010. **2**(10): p. 2257-2261.

170. Stinville, J.C., P. Villechaise, C. Templier, J.P. Riviere, and M. Drouet, *Lattice rotation induced by plasma nitriding in a 316L polycrystalline stainless steel.* Acta Materialia, 2010. **58**(8): p. 2814-2821.

171. Gontijo, L.C., R. Machado, E.J. Miola, L.C. Casteletti, N.G. Alcantara, and P.A.P. Nascente, *Study of the S phase formed on plasma-nitrided AISI 316L*

stainless steel. Materials Science and Engineering a-Structural Materials Properties Microstructure and Processing, 2006. **431**(1-2): p. 315-321.

172. Esfandiari, M. and H. Dong, *Improving the surface properties of A286 precipitation-hardening stainless steel by low-temperature plasma nitriding.* Surface & Coatings Technology, 2007. **201**(14): p. 6189-6196.

173. Wang, X., W.T. Zheng, H.W. Tian, S.S. Yu, W. Xu, S.H. Meng, X.D. He, J.C. Han, C.Q. Sun, and B.K. Tay, *Growth, structural, and magnetic properties of iron nitride thin films deposited by dc magnetron sputtering.* Applied Surface Science, 2003. **220**(1-4): p. 30-39.

174. Quesada-Cabrera, R., C. Sotelo-Vazquez, J.A. Darr, and I.P. Parkin, *Critical influence of surface nitrogen species on the activity of N-doped TiO2 thin-films during photodegradation of stearic acid under UV light irradiation.* Applied Catalysis B-Environmental, 2014. **160**: p. 582-588.

175. Gammon, W.J., O. Kraft, A.C. Reilly, and B.C. Holloway, *Experimental comparison of N(1s) X-ray photoelectron spectroscopy binding energies of hard and elastic amorphous carbon nitride films with reference organic compounds.* Carbon, 2003. **41**(10): p. 1917-1923.

176. Hanawa, T., S. Hiromoto, A. Yamamoto, D. Kuroda, and K. Asami, *XPS characterization of the surface oxide film 316L stainless steel samples that were located in quasi-biological environments.* Materials Transactions, 2002. **43**(12): p. 3088-3092.

177. Bondarenko, V., S. Kaciulis, A. Plesanovas, V. Volkov, and G. Zacharova, *Photoelectron-Spectroscopy of the Poly-Vanadium Transition-Metal Acids.* Applied Surface Science, 1994. **78**(1): p. 107-112.

178. Bull, S.J., *Failure Modes in Scratch Adhesion Testing.* Surface & Coatings Technology, 1991. **50**(1): p. 25-32.

179. Kazerooni, N.A., M.E. Bahrololoom, M.H. Shariat, F. Mahzoon, and T. Jozaghi, *Effect of Ringer's Solution on Wear and Friction of Stainless Steel 316L after Plasma Electrolytic Nitrocarburising at Low Voltages.* Journal of Materials Science & Technology, 2011. **27**(10): p. 906-912.

180. Zhang, W., Y.J. Luo, H.Y. Wang, J. Jiang, S.H. Pu, and P.K. Chu, *Ag and Ag/N(2) plasma modification of polyethylene for the enhancement of antibacterial properties and cell growth/proliferation.* Acta Biomaterialia, 2008. **4**(6): p. 2028-2036.

181. Ip, M., S.L. Lui, V.K.M. Poon, I. Lung, and A. Burd, *Antimicrobial activities of silver dressings: an in vitro comparison.* Journal of Medical Microbiology, 2006. **55**(1): p. 59-63.

182. Janosi, S., Z. Kolozsvary, and A. Kis, *Controlled hollow cathode effect: New possibilities for heating low-pressure furnaces.* Metal Science and Heat Treatment, 2004. **46**(7-8): p. 310-316.

183. Little, P.F. and A. Vonengel, *The Hollow-Cathode Effect and the Theory of Glow Discharges.* Proceedings of the Royal Society of London Series a-Mathematical and Physical Sciences, 1954. **224**(1157): p. 209-227.

184. Melechko, A.V., V.I. Merkulov, T.E. McKnight, M.A. Guillorn, K.L. Klein, D.H. Lowndes, and M.L. Simpson, *Vertically aligned carbon nanofibers and related structures: Controlled synthesis and directed assembly.* Journal of Applied Physics, 2005. **97**(4).

185. Roth, J.R., *Industrial plasma engineering*. 1995, Bristol ; Philadelphia: Institute of Physics Pub. v. <1 >.

186. Gamaly, E.G. and T.W. Ebbesen, *Mechanism of Carbon Nanotube Formation in the Arc-Discharge.* Physical Review B, 1995. **52**(3): p. 2083-2089.

187. Scott, C.D., S. Arepalli, P. Nikolaev, and R.E. Smalley, *Growth mechanisms for single-wall carbon nanotubes in a laser-ablation process.* Applied Physics a-Materials Science & Processing, 2001. **72**(5): p. 573-580.

188. Kumar, M. and Y. Ando, *Chemical Vapor Deposition of Carbon Nanotubes: A Review on Growth Mechanism and Mass Production.* Journal of Nanoscience and Nanotechnology, 2010. **10**(6): p. 3739-3758.

189. Tessonnier, J.P. and D.S. Su, *Recent Progress on the Growth Mechanism of Carbon Nanotubes: A Review.* Chemsuschem, 2011. **4**(7): p. 824-847.

190. Shen, W., Y. Wang, X. Shi, N. Shah, F. Huggins, S. Bollineni, M. Seehra, and G. Huffman, *Catalytic nonoxidative dehydrogenation of ethane over Fe-Ni and Ni catalysts supported on Mg(Al)O to produce hydrogen and easily purified carbon nanotubes.* Energy & Fuels, 2007. **21**(6): p. 3520-3529.

191. Liao, X.Z., A. Serquis, Q.X. Jia, D.E. Peterson, Y.T. Zhu, and H.F. Xu, *Effect of catalyst composition on carbon nanotube growth.* Applied Physics Letters, 2003. **82**(16): p. 2694-2696.

192. Fu, X., L.J. Pan, D.W. Li, N. Zhou, and Y.M. Sun, *Controlled synthesis of carbon nanocoils with selective coil diameters and structures by optimizing the thickness of catalyst film.* Carbon, 2015. **93**: p. 361-369.

193. Jung, Y.J., B.Q. Wei, R. Vajtai, and P.M. Ajayan, *Mechanism of selective growth of carbon nanotubes on SiO2/Si patterns.* Nano Letters, 2003. **3**(4): p. 561-564.

194. Yang, J.W., S. Esconjauregui, A.W. Robertson, Y.Z. Guo, T. Hallam, H. Sugime, G.F. Zhong, G.S. Duesberg, and J. Robertson, *Growth of high-density carbon nanotube forests on conductive TiSiN supports.* Applied Physics Letters, 2015. **106**(8).

195. Wu, W.Y., F.Y. Teng, and J.M. Ting, *The effect of an Al underlayer on Fe-Si thin film catalysts for the improved growth of carbon nanotubes.* Carbon, 2011. **49**(13): p. 4589-4594.

196. Gohier, A., C.P. Ewels, T.M. Minea, and M.A. Djouadi, *Carbon nanotube growth mechanism switches from tip- to base-growth with decreasing catalyst particle size.* Carbon, 2008. **46**(10): p. 1331-1338.

197. Yin, Y.D., G.T. Zhang, and Y.N. Xia, *Synthesis and characterization of MgO nanowires through a vapor-phase precursor method.* Advanced Functional Materials, 2002. **12**(4): p. 293-298.

198. Gallo, S.C., X.Y. Li, K. Futterer, C.A. Charitidis, and H.S. Dong, *Carbon Nanofibers Functionalized with Active Screen Plasma Deposited Metal Nanoparticles for Electrical Energy Storage Devices.* Acs Applied Materials & Interfaces, 2017. **9**(27): p. 23195-23201.

199. Yang, K., Y.J. Li, X.F. Tan, R. Peng, and Z. Liu, *Behavior and Toxicity of Graphene and Its Functionalized Derivatives in Biological Systems.* Small, 2013. **9**(9-10): p. 1492-1503.

200. Jia, G., H.F. Wang, L. Yan, X. Wang, R.J. Pei, T. Yan, Y.L. Zhao, and X.B. Guo, *Cytotoxicity of carbon nanomaterials: Single-wall nanotube, multi-wall nanotube, and fullerene.* Environmental Science & Technology, 2005. **39**(5): p. 1378-1383.

201. Gong, J.L., B. Wang, G.M. Zeng, C.P. Yang, C.G. Niu, Q.Y. Niu, W.J. Zhou, and Y. Liang, *Removal of cationic dyes from aqueous solution using magnetic multi-wall carbon nanotube nanocomposite as adsorbent.* Journal of Hazardous Materials, 2009. **164**(2-3): p. 1517-1522.

202. Maas, M., *Carbon Nanomaterials as Antibacterial Colloids.* Materials, 2016. **9**(8).

203. Nowlin, K., A. Boseman, A. Covell, and D. LaJeunesse, *Adhesion-dependent rupturing of Saccharomyces cerevisiae on biological antimicrobial nanostructured surfaces.* Journal of The Royal Society Interface, 2015. **12**(102).

204. Kelleher, S.M., O. Habimana, J. Lawler, B. O'Reilly, S. Daniels, E. Casey, and A. Cowley, *Cicada Wing Surface Topography: An Investigation into the Bactericidal Properties of Nanostructural Features.* Acs Applied Materials & Interfaces, 2016. **8**(24): p. 14966-14974.

205. Hasan, J., R.J. Crawford, and E.P. Lvanova, *Antibacterial surfaces: the quest for a new generation of biomaterials.* Trends in Biotechnology, 2013. **31**(5): p. 31-40.

206. Chernousova, S. and M. Epple, *Silver as Antibacterial Agent: Ion, Nanoparticle, and Metal.* Angewandte Chemie-International Edition, 2013. **52**(6): p. 1636-1653.

207. Campoccia, D., L. Montanaro, and C.R. Arciola, *A review of the biomaterials technologies for infection-resistant surfaces.* Biomaterials, 2013. **34**(34): p. 8533-8554.

208. Faure, E., C. Falentin-Daudre, T.S. Lanero, C. Vreuls, G. Zocchi, C. Van De Weerdt, J. Martial, C. Jerome, A.S. Duwez, and C. Detrembleur, *Functional Nanogels as Platforms for Imparting Antibacterial, Antibiofilm, and Antiadhesion Activities to Stainless Steel.* Advanced Functional Materials, 2012. **22**(24): p. 5271-5282.

209. Liu, R., X.Y. Li, X. Hu, and H.S. Dong, *Surface modification of a medical grade Co-Cr-Mo alloy by low-temperature plasma surface alloying with nitrogen and carbon.* Surface & Coatings Technology, 2013. **232**: p. 906-911.

210. Glover, R.D., J.M. Miller, and J.E. Hutchison, *Generation of Metal Nanoparticles from Silver and Copper Objects: Nanoparticle Dynamics on Surfaces and Potential Sources of Nanoparticles in the Environment.* Acs Nano, 2011. **5**(11): p. 8950-8957.

211. Kokura, S., O. Handa, T. Takagi, T. Ishikawa, Y. Naito, and T. Yoshikawa, *Silver nanoparticles as a safe preservative for use in cosmetics.* Nanomedicine-Nanotechnology Biology and Medicine, 2010. **6**(4): p. 570-574.

212. Carlson, C., S.M. Hussain, A.M. Schrand, L. K. Braydich-Stolle, K.L. Hess, R.L. Jones, and J.J. Schlager, *Unique Cellular Interaction of Silver Nanoparticles: Size-Dependent Generation of Reactive Oxygen Species.* The Journal of Physical Chemistry B, 2008. **112**(43): p. 13608-13619.